Laser Powder Bed Fusion of Scalmalloy (Al-4.6Mg-0.6Sc-0.3Zr): Formation Mechanism of Bimodal Grain Structure and Fatigue Behaviour of the Alloy

Polina Chernyshova

A thesis submitted to Auckland University of Technology in fulfilment of the requirements for the degree of Doctor of Philosophy (PhD)

2025

School of Engineering, Computer and Mathematical Sciences

List of Publications

1. Chernyshova, P., Guraya, T., Martinez-Amesti, A., Andonegi, H., Singamneni, S., & Chen, Z. W. (2023). On the Mechanism of Formation of Bimodal Grain Structure in Al–4.5 Mg–0.7 Sc–0.3 Zr Alloy Processed by Laser Powder Bed Fusion. *Advanced Engineering Materials*, *25*(13), 2300135.
2. Chernyshova, P., Guraya, T., Singamneni, S., Zhu, T., & Chen, Z. W. (2021). Fatigue crack growth behavior of Al-4.5 Mg-0.6 Sc-0.3 Zr alloy processed by laser powder bed fusion. *Journal of Materials Engineering and Performance*, *30*(9), 6743-6751.

Abstract

Scalmalloy® is a relatively new and high strength aluminium alloy with a distinctive bimodal microstructure consisting of equiaxed and columnar grains, when processed through Laser Powder Bed Fusion (LPBF) additive manufacturing or 3D printing. The formation of this bimodal grain structure during LPBF allows the alloy to be 3D printable, without forming hot cracks. Hot cracking during LPBF of the traditional high strength aluminium alloys largely prevents these alloys from being 3D printable. However, the mechanism of the bimodal grain structure of Scalmalloy during LPBF has not been fully understood. For applications of high strength aluminium alloys, fatigue properties are particularly important for ensuring reliability in industries like aerospace and automotive, where lightweight and durable materials are essential. However, despite the significant research on Scalmalloy LPBF, the fatigue behaviour of the alloy is not fully understood.

Thus, the aim of this PhD research is to reveal and thus to understand the solidification behaviour during LPBF of Scalmalloy leading to the formation of the bimodal grain structure and the crack growth behaviour of the alloy under cyclic loading.

In the first part of this research (on solidification behaviour), the partitioning of elements in the alloy and forming of various particles during LPBF solidification were experimentally determined. It is found that strong and weak segregation of Mg and Sc, respectively, occurs in the final solidification areas of the fine- and equiaxed-grain regions. The coarser and columnar grain regions show weak segregation of Mg and no Sc segregation. A priori knowledge on the Al–Sc eutectic reaction based on the known phase system and its dependence on cooling rates, and the well-known thermal and solidification conditions related to the track location during LPBF is used to ascertain the mechanism of formation of the bimodal grain structure. The mechanism suggested is substantiated by the location-dependent elemental distributions and the various particles that are observed.

In the second part of this research, how LPBF defects affect the fatigue life of the alloy in both as-built (AB) and heat-treated (T5) samples and also in various crack directions (CD) and build directions (BD) has been studied. This part in turn has necessarily been divided into two sections to form a more complete understanding of the fatigue behaviour of the alloy. In section one, threshold stress intensity factor (ΔK_{th}) values of the alloy were determined. This mechanic approach provides a base that the boundary of fatigue limit/strength as a function of defect size can be determined. In section two, tests were conducted so that S-N (stress and number to failure) curves can be drawn. Following the tests, surface and sub-subsurface defects (referring to the distance to the sample surface) on fracture surfaces were observed and the sizes were measured, for the understanding of how the surface and subsurface defects of the samples affect the fatigue strength of the alloy processed by LPBF.

For the ΔK_{th} study, experimentally, FCG tests with R=0.1 have been conducted using samples with crack growth direction normal, parallel or 45° to build direction, meaning CD⊥BD, CD//BD and ∠CD/BD=45°,

respectively. Tested sample conditions include LPBF with a room temperature base plate or a heated base plate and as-built state or heat-treated state. FCG tests reveal a narrow range of ΔK_{th} values, 1.3–1.4 MPa·m$^{1/2}$, across all loading directions relative to the build direction, attributed to minimal orientation effect of roughness-induced crack closure. Heat treatment (T5) and variations in build plate temperature (180°C and room temperature) show negligible effects on FCG rates, as the grain morphology has changed little and thus crack paths remain smooth. Paris law parameters (C and m) are comparable to those of conventional aluminium alloys.

In the S-N study, fatigue strength tests with R=0.1 are carried out using two different groups, namely, AB group and T5 group. For each group, there are CD⊥BD and CD//BD samples. Thus, in total, there are four types of samples. As expected, defects affect the fatigue strength significantly. It has been found, however, that LD and T5 have not affected the fatigue strength significantly, although CD//BD may have displayed a lower fatigue strength due to them possibly having defects of large sizes as the size of a defect is orientation dependent. Using the Kitagawa-Takahashi (K-T) approach, given that ΔK_{th} is not affected significantly by T5 and BD and given the sizes of defects on fracture surfaces measured, how the defect size affects the fatigue life of the samples has been explained. It has been further found that, due to the presence of defects, the fatigue strength at $N \geq 10^7$ range 95-125MPa, defects size dependent. The defect size range of mostly 60-150μm measured in the fracture surfaces of the S-N tested is consistent with the defect size range that is LPBF track size specific. It can be suggested that, through examining the data in the K-T diagram, the fatigue strength of a short crack sample is ~140MPa (stress range).

Acknowledgement

My deepest gratitude goes to Professor Zhan Chen, my primary supervisor. His support, wise critiques, generous investment of time, patience, and willingness to share his knowledge have shaped this research. I am very thankful for his regularly staying on campus for thesis discussions after my work hours, arranging online meetings while on holiday, remaining available almost 24/7 and coming to the University on the weekends and public holidays to discuss and advance this study. His dedication and high standards consistently pushed me to refine every aspect of the work, for which I am profoundly thankful.

I am equally grateful to Professor Sarat Singamneni, my secondary supervisor, whose guidance on the fundamentals of the LPBF process and readiness to produce samples made this study possible. His steady encouragement and practical insight were invaluable.

My sincere appreciation extends to Professor Teresa Guraya (Department of Mining and Metallurgical Engineering and Materials Science, University of the Basque Country, Bilbao, Spain) for conducting the TEM work, including EDS and diffraction data, which made a significant contribution to this research.

Special thanks are due to Senior Technician Mark Masterton, for his remarkable skill in keeping the equipment running smoothly, his patient guidance in the lab and a sense of humour that made even the longest experimental days enjoyable.

I would also like to thank Yuan Tao, SEM Research Officer, for her expert assistance with SEM and her readiness to answer every question.

Lastly but not the least, to my family: my husband Bagrat Chachava for his constant motivation and willingness to help whenever needed; my parents, Anna and Igor, and my brother Ivan, for their support and encouragement throughout this journey; and my wonderful daughter Sofia, whose presence inspires me daily to learn and grow. This achievement would not have been possible without your love, help, support and belief in me.

Table of Contents

List of Figures

List of Tables

Nomenclature

AB	As-built
AH	As-hatched
AM	Additive Manufacturing
ASTM	American Society for Testing and Materials
BD	Build direction
C (grain region)	Columnar (grain region)
CD	Crack direction
CD//BD	Crack direction is parallel to the building direction
CD⊥BD	Crack direction is perpendicular to the building direction
CG	Coarse-grained (region)
CI	Crack-initiating (defect)
CM	Chemically milled
COD	Crack Opening Displacement
CT	Compact-tension (specimen)
$D0_{23}$	Ordered tetragonal AB_3 structure
E (grain region)	Equiaxed (grain region)
EBSD	Electron Backscatter Diffraction
EDX / XEDS	Energy-Dispersive X-ray Spectroscopy
FCG	Fatigue Crack Growth
FCC	Face-Centred Cubic crystal structure
FG	Fine-grained region
FEG-TEM	Field-Emission-Gun TEM
H	Horizontal build direction
HAZ	Heat-affected zone
HC	Heat-conduction mode
HIP	Hot-Isostatic Pressing
HCF	High Cycle Fatigue
HT	Heat treatment
KH	Keyhole (deep-penetration) mode
K-T diagram	Kitagawa–Takahashi diagram
LCF	Low Cycle Fatigue
LPBF	Laser Powder Bed Fusion
LOF	Lack of Fusion
$L1_2$	Ordered cubic AB_3 intermetallic structure
MM	Mechanically milled

PD	Parallelly deposited
RT	Room Temperature
SEM	Scanning Electron Microscope
SADP / TEM-SADP	Selected-Area Diffraction Pattern
SLM	Selective Laser Melting
STEM-EDS	Scanning TEM with Energy-Dispersive X-ray
S-N curve	Wöhler (fatigue) curve
S/L	Solid–liquid interface
T5	One-step heat treatment
T6	Two-step heat treatment
TD	Transversely deposited
TEM	Transmission Electron Microscope
TEM-FFT	Transmission Electron Microscopy image – Fast Fourier Transform analysis
TEM-SADP	Transmission Electron Microscopy image – Selective Area Diffraction Pattern
UTS (MPa)	Ultimate Tensile Strength
V	Vertical build direction
YS (MPa)	Yield Strength
a (mm)	Crack size in CT samples
√area (μm)	Defect size, Murakami's parameter
a_0 (μm)	El Haddad parameter
B (mm)	Thickness of CT sample
C ((mm cycle^{-1})/(MPa √m)^m)	Paris-law parameter
C (mm^{-1})	Normalised K-gradient
C_0 (%)	Average composition of the alloy
C_L (%)	Concentration of an element in liquid
C_S (%)	Concentration of an element in solid
C_{SM} (%)	Composition of solid material
C_E (%)	Composition of the eutectic phase
d (mm)	Hatch distance
d_{hkl} (nm)	Interplanar spacing for Miller index
da/dN (mm/cycle)	Crack growth rate
dT/dt	Cooling rate
ΔK (MPa √m)	Stress intensity factor
ΔK_{eff} (MPa √m)	Effective stress intensity factor
ΔK_{th} (MPa √m)	Threshold intensity factor

$\Delta\sigma$ (MPa)	Stress range
$\Delta\sigma_e$ (MPa)	Limiting threshold (fatigue limit of un-notched sample)
$\Delta\sigma_{w0}$ (MPa)	Fatigue strength of machined specimens without defects
E ($J \cdot mm^{-3}$)	Volumetric energy density
ε (%)	Elongation to failure
f (Hz)	Frequency
F (MPa)	Applied load during FCG test
Fw	Geometric factor in Murakami √area equation
G	Temperature Gradient
h, k, l	Miller indices
HV	Vickers hardness
k	Equilibrium partition coefficient
K_C (MPa √m)	Critical stress-intensity factor
L (mm)	Camera length (diffraction)
λ (nm)	Electron wavelength
m	Paris-law exponent
N	Load cycles
P (W)	Laser Power
R	Solidification front
R	Stress ration
R (mm)	Radius from centre spot to diffraction peak
Ra (µm)	Surface roughness
σ_a (MPa)	Stress amplitude
σ_{max} (MPa)	Maximum stress
σ_{min} (MPa)	Minimum stress
σ_m (MPa)	Mean stress
σ_w (MPa)	Fatigue strength
σ_y (MPa)	Yield strength
t (mm)	Layer thickness
θ	Angle between solidification front and scan direction
V_s ($mm \cdot s^{-1}$)	Scanning speed
W (mm)	Width of CT sample

Attestation of Authorship

I hereby declare that this submission is my own work and that, to the best of my knowledge and belief, it contains no material previously published or written by another person (except where explicitly defined in the acknowledgements), nor used artificial intelligence tools or generative artificial intelligence tools (unless it is clearly stated, and referenced, along with the purpose of use), nor material which to a substantial extent has been submitted for the award of any other degree or diploma of a university or other institution of higher learning.

Auckland

Signature:

Name: Polina Chernyshova

Chapter 1 - Introduction

1.1 Laser Powder Bed Fusion (LPBF)

Today, additive manufacturing (AM) is attracting an increasing amount of industry interest and enables the fabrication of complex parts (see Figure 1.1) with significantly improved performance, such as weight, functional integration, structural optimisation, or thermal behaviour (1). The principles of AM technologies are founded on the idea that rather than removing material, as is done in traditional manufacturing processes like cutting or grinding, more material is added together to create a three-dimensional item. Direct digital manufacturing, rapid prototyping, generative manufacturing and 3D printing are all synonyms for additive manufacturing. The term "additive manufacturing" has become the de facto term for manufacturing using such technologies, because AM technologies have a long history dating back to the mid-1980s with the introduction of stereolithography and because they are currently quickly making their way into industrial applications (2).

.

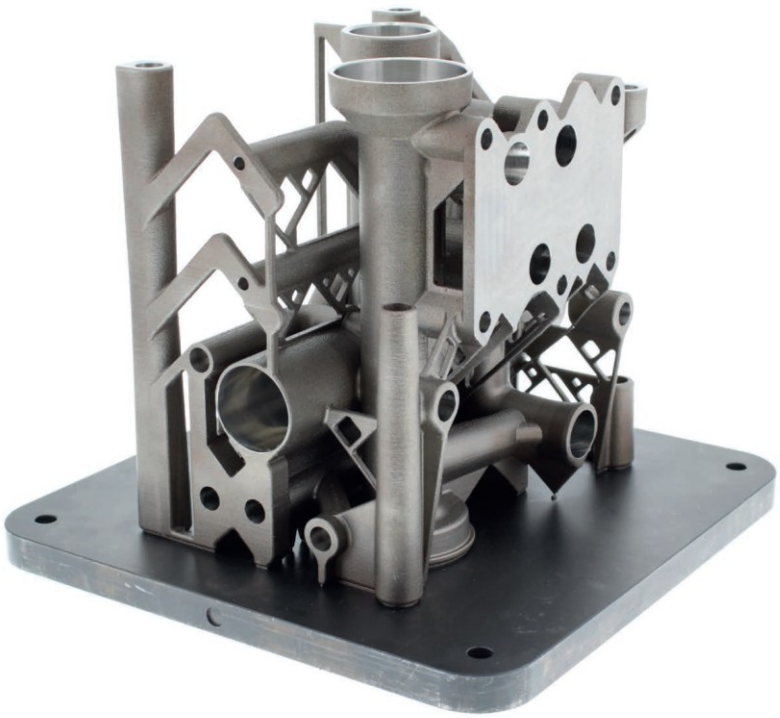

Figure 1.1. Parts produced by 3D printing (3).

Laser Powder Bed Fusion (LPBF) or Selective Laser Melting (SLM) is a major additive manufacturing process that has earned great interest in industry and science. This process enables the production of lightweight complicated parts without specific tooling (4). Moreover, it was widely reported that LPBF enables resources saving, leading to eco-design optimization and reduces toxic chemicals (5). A schematic representation of the

LPBF process is presented in Figure 1.2. A powder bed is created by raking powder across the work area. The energy source (laser beam) is programmed to provide energy to the powder bed to melt the powder along the path of the beam. After a layer has been built, powder is raked across the bed for the building of the next layer, and the process is repeated to print a solid 3-D part. The process is thus able to produce parts with high-resolution features and internal passages, and to maintain dimensional control.

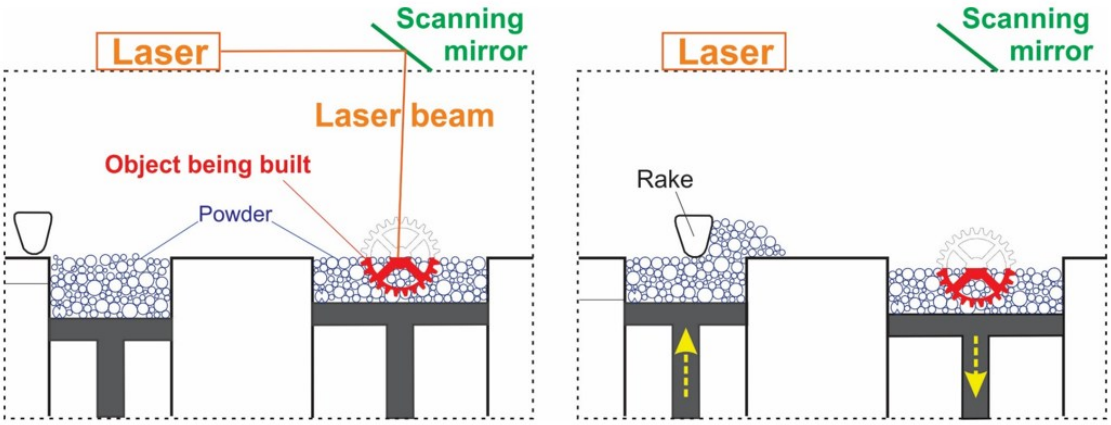

Figure 1.2. Schematic illustration showing the steps of laser powder bed fusion (LPBF) process a) Scanning/melting and solidification, b) Power spreading.

The impacts of various printing parameters on the quality of parts using various materials have been examined by numerous researchers (6), (7), (8). Laser power (P), scanning speed (v_s), hatch spacing (d) between two adjacent laser scan tracks and layer thickness (t), as illustrated in Fig. 1.3, are the most crucial LPBF processing factors. Volumetric energy density (E, J/mm^3) that used most frequently in LPBF literature is defined as:

$$E = \frac{P}{v_s \times d \times t} \quad \text{Equation 1}$$

The formula shows that several parameter combinations can produce the same energy density. The process parameters have an impact on the stability of the melt pools generated during LPBF (9). For example, the breadth and depth of a melt pool are influenced by the laser power and scan speed, whereas the length of the track is determined by the laser power and material absorptivity (10).

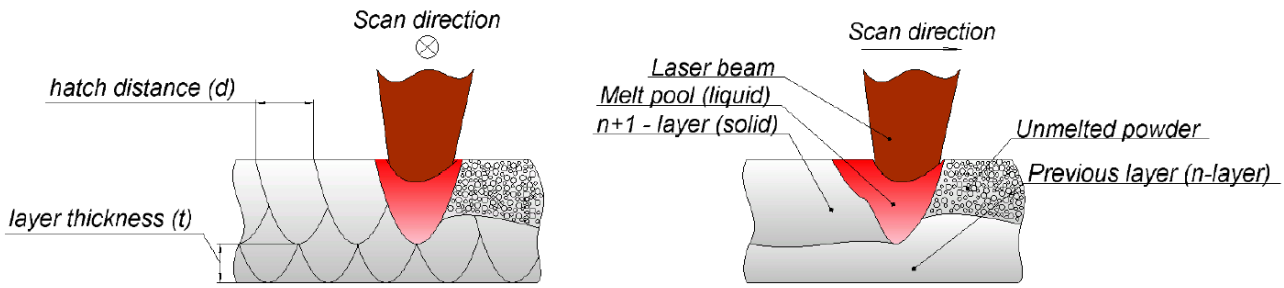

Figure 1.3. Schematic representation of layer-by layer process.

For parts produced by LPBF, there are a number of important defects that can influence quality and reliability (11). Microstructural defects in LPBF include three main types, namely: (1) lack of fusion (LOF), (2) gas pores, and (3) keyhole pores. There have been many studies conducted to reveal how defects may form during LPBF and how LPBF parameters relate to the level of defects (12), (13). A schematic illustration of keyhole and LOF pore formation during LPBF is shown in Figure 1.4. It has been well understood that LOF occurs when the laser energy is not sufficient to fully melt the powder so that a melt track does not completely overlap with the previous one. However, when the laser energy input is too high, evaporation of the melt occurs, leading to the formation of keyhole pores shown in Figure 1.4 (14).

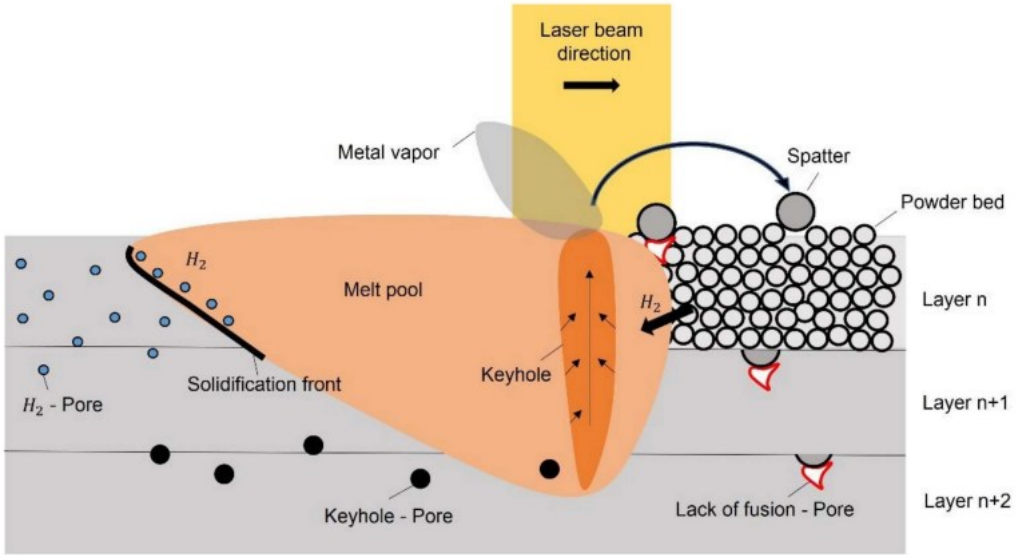

Figure 1.4. Schematic illustration of keyhole pores and LOF forming during LPBF (15).

Shrestha et al. (16) have conducted research on the influence of LPBF parameters on the defect formation for Inconel 625. It has been shown that lower (20.31 J/mm^3) and upper (162.5 J/mm^3) ranges of volumetric energy densities of their study both resulted in high porosity, however the nature of porosity for lower and upper set of energy density is different. At low energy densities, lack of fusion is formed, while keyhole pores are formed at higher energy densities (Fig. 1.5). Figure 1.5 shows three micrographs of samples produced with different scan speeds, while laser power 195 W and hatch spacing 120µm remained constant. Figure 1.5 (a) is obtained from a sample fabricated with 375 mm/s scan speed, thus with the highest energy density in this study that resulted in the formation of keyhole pores inside of the tracks, while for sample produced with the lowest energy density (scan speed 1500 mm/s) the lack of fusion, located between the tracks, is observed (Fig. 1.5.(c)).

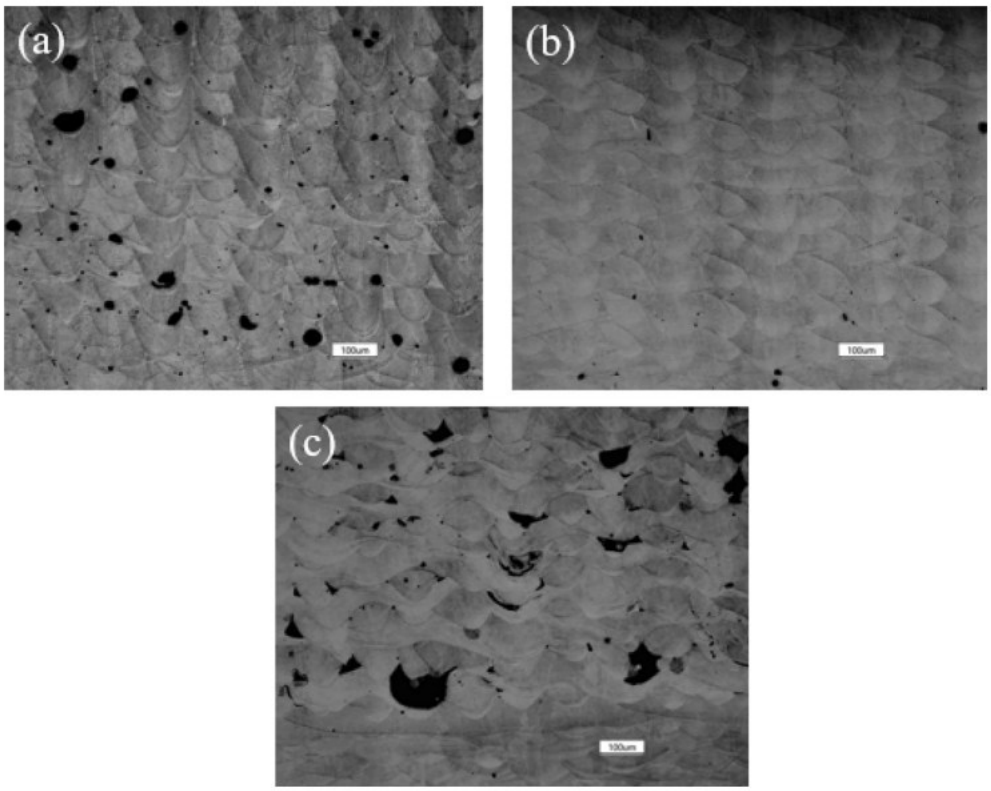

Figure 1.5. Optical microscope images of LPBF samples showing layers formed using power 195 W, 120 µm hatch spacing and (a) 375 mm/s, (b) 750 mm/s, (c) 1500 mm/s scan speeds (16).

Since LOF is caused by lack of complete melting and overlapping, it is expected that an increase in laser power (P) and a decrease in the speed of scanning (v) will melt more powder particles within a unit of time. The concept is the same as in conventional fusion welding, whereby the input of energy by the heat source is expressed by the ratio of P/v. However, during LPBF, the complete melting of powder particles is greatly dependent on the volume of material to be melted. Decreasing layer thickness (h) and inter-scanline (hatch) distance (d) is thus expected to enhance the complete melting of powder particles. The energy input per unit volume per unit time is a measure of the melting level and is commonly utilized to evaluate LPBF process parameters.

Because cooling rate is high (10^5–10^6 K/s) during LPBF (17), the solidified microstructures can be considerably different from the microstructures formed using traditional processing methods, as cooling rates are normally considerably lower. The very high cooling rates during solidification in LPBF result in a very fine microstructure, for example, submicron sizes of secondary dendrite arm spacings (18).

Aluminium alloys stand out as one of the primary material systems drawing significant interest in the LPBF research, earning preference for numerous high-value applications. They are positioned to be employed in applications where performance and light-weighting are required, because they offer a good compromise between strength and density and are also reasonably priced. Nowadays, aerospace and automobile products all incorporate aluminium components produced by LPBF (19). The microstructural improvement of Al (cast

alloys, in particular) after LPBF processing is another benefit. In the past, cast alloys have been strengthened by modifying their microstructures chemically while being cast.

Al alloys from the high-strength 2xxx and 7xxx series are widely used in aerospace and automotive industries but face challenges in LPBF due to hot cracking. Hot cracking can be either liquation cracking or solidification cracking. Liquation cracking occurs when intermetallic-phase particles at grain boundaries melt at temperatures above the eutectic point but below the alloy's solidus temperature. These particles cannot be completely dissolved during LPBF due to rapid heating, which results in forming liquid films that lead to cracks under tensile stress. In high strength Al alloys like AA7075 and AA2024, as in most unweldable alloys, cracks initiate in the final stage of solidification in semi-solid regions with low liquid fraction when liquid cannot effectively be fed to the shrinking space and thermal stress is built up to assist the crack propagation during LPBF (20), (21). Therefore, one of the solutions to this problem is developing a new alloy, specifically designed for LPBF process. Thus, Scalmalloy, a high-strength aluminium alloy, has been specially developed for aerospace applications and proven suitable for processing by LPBF (22).

1.2 Scalmalloy and its LPBF

Scalmalloy (Al-4.5Mg alloy with the additions of Sc and Zr), developed by Airbus Group Innovations for aerospace applications, is a member of the 5xxx series of aluminium alloys. This alloy is LPBF printable without hot cracking. When high strength and thermal conductivity are required, Scalmalloy may be used in place of titanium alloys in aerospace applications (23). According to the APWORKS data sheet (24), Scalmalloy's YS = 480 MPa, UTS = 520 MPa, while YS and UTS for high strength Al alloy 2024-T6 are 390 MPa and 470 MPa, respectively (25). Thus, Scalmalloy is a high strength aluminium alloy with better elongation than other aluminium alloys processed by LPBF, strong corrosion resistance and weldability (24).

The microstructure of LPBFed parts differs from the microstructure of parts obtained through conventional manufacturing techniques, such as rolling, casting and forging. Solidification mode mainly depends on the temperature gradient ($G = dT/dx$) and the solidification velocity ($V = dx/dt$) in the solidification front. Cooling rate ($dT/dt = G \cdot V$), on the other hand, determines the size of solidification microstructures. When the ratio of the thermal gradient and the velocity of solid-liquid front G/V increases, the solidification mode changes from dendritic to cellular and finally to planar crystal (Fig. 6). The size of the microstructure reduces as $G \cdot V$ increases.

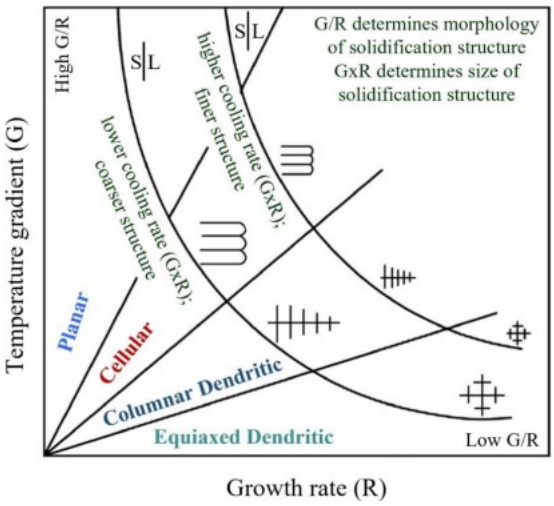

Figure 1.6. Map of solidification modes and microstructure sizes under various G and R values (26).

During LPBF, thermal gradients due to localized laser heating ranged 5–20 K/μm and cooling rates ranged 1–40 K/μs are high (27). When $G >> V$, the heat is extracted directionally, favoring columnar grain growth aligned with the heat flow. When G is not significantly larger than V, the cooling rate is high but still allows some instability in solidification front, leading to dendritic structures. Thus, the microstructure of printed parts mainly consists of cellular and columnar dendrite grains. (Fig. 1.7) and the latter easily enables hot cracking.

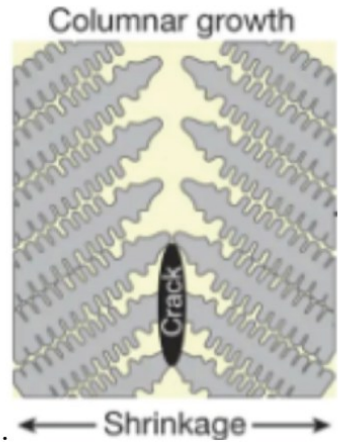

Figure 1.7. Hot cracking in columnar microstructure (28).

However, columnar grain growth, which occurs due to the steep thermal gradients with relatively lower solidification rates, is not the only condition for hot cracking. Another reason for hot cracking is liquid film formation that occurs in alloys with a wide solidification range, causing liquid films between dendrites/grains during cooling (Fig. 1.8). This is common for high strength Al alloys, such as Al7075 and Al6061, Ni-based superalloys (IN738) and high-strength steels. The residual liquid phase is trapped along grain boundaries and if the film is too thin, it can rupture creating a crack (29). Hot cracking can also be caused by shrinkage stress due to rapid cooling (30). LPBF cooling rates are around 10^5-10^6 and can induce high residual stress caused by thermal contraction mismatch. These stresses can exceed the fracture stress of the last solidifying grain boundaries and lead to crack propagation.

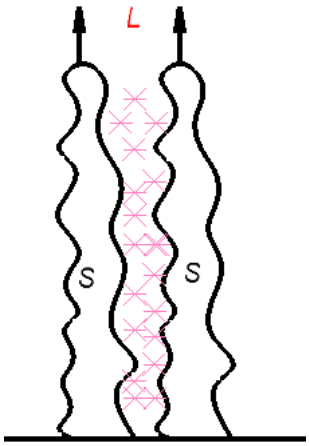

Figure 1.8. Schematic illustration showing liquid film forming between grains.

To eliminate hot cracking, the presence of equiaxed grains should be in the microstructure to interrupt the columnar grain growth and to prevent it from continuing to the next track, thus, equiaxed grains can act as a barrier for crack propagation. Scalmalloy's LPBF printability can therefore be attributed to its microstructure (31). Al-Mg alloy containing Sc and Zr processed by LPBF offers excellent properties in the as-built state ($\sigma_{0.2}$=300 MPa (32), due to the presence of very fine equiaxed grains in the microstructure. The alloy in as-built state has a duplex (bimodal) grain present in each track: region 1) fine, equiaxed grains (0.7 ±0.3 μm in diameter) adjacent and next to the track boundary; region 2) coarse, columnar grains (≈ 50 μm long) away from the boundary growing in the direction of heat flow (33), (34), (35), (36). The schematic illustration of the bimodal structure is provided below (Fig. 1.9)

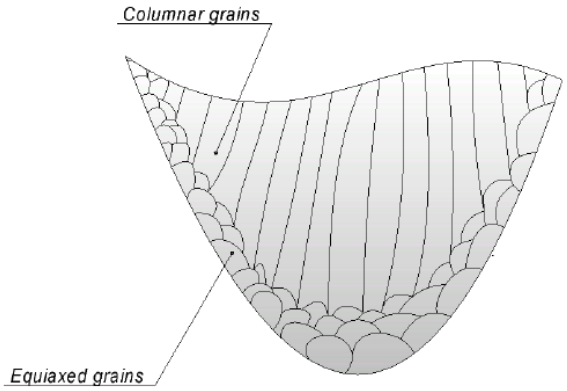

Figure 1.9. Schematic representation of bimodal structure.

To understand the significance of the bimodal grain structure in a track, it is helpful to compare it with the grain structure observed in a commonly used LPBF alloy. A suitable comparison can be made with Co-29Cr-6Mo, a well-established alloy in additive manufacturing that has typical cellular/dendritic microstructure. The comparison of printed Co-29Cr-6Mo microstructure and printed Scalmalloy microstructure is presented below (Fig. 1.10). In LPBF of Co-29Cr-6Mo, like most alloys, equiaxed grains do not form, and after epitaxial growth, cellular/dendritic grain growth continues to the top, resulting in a fully cellular/dendritic

microstructure. On the other hand, during LPBF of Scalmalloy, in each track, fine equiaxed grains form and grow next to and along the track boundary, followed by columnar grain growth. Thus, there are no continued columnar dendritic grains grown from one track/layer to another, therefore, there is no condition for hot cracking. It is now well understood that the alloy is amendable for processing by LPBF with the microstructure free of hot cracking, however the formation mechanism of bimodal microstructure is yet to be understood fully.

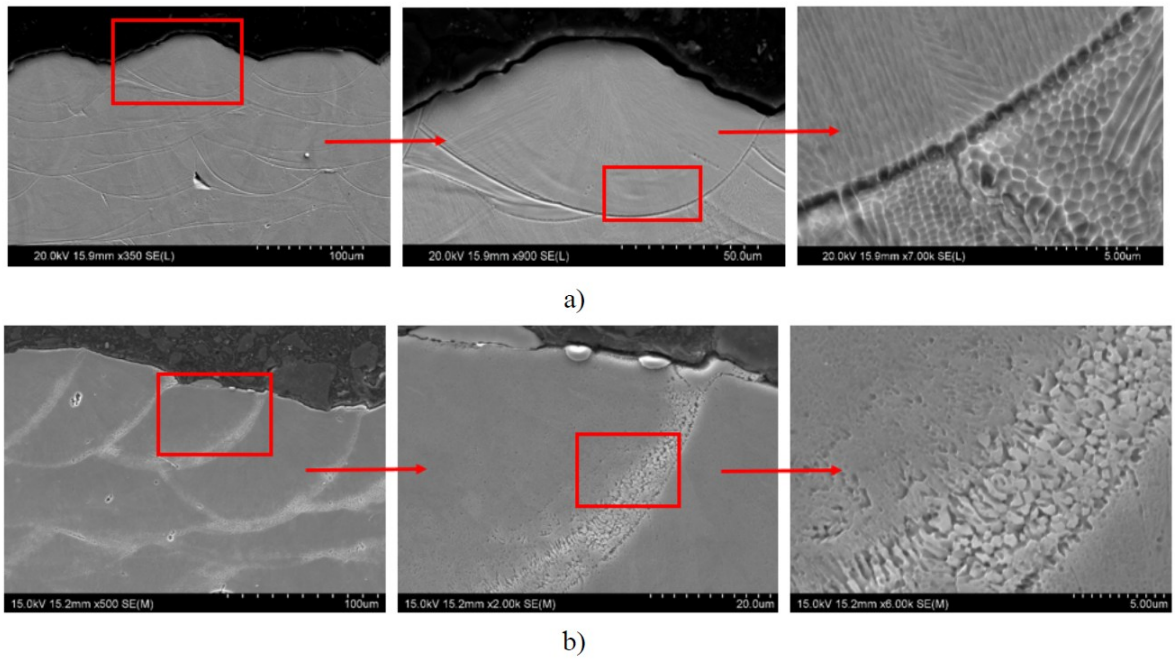

Figure 1.10. a) Microstructure of Co-29Cr-6Mo alloy samples processed by LPBF made in our lab (37). Columnar cellular morphology. b) Microstructure of Al-Mg-Sc-Zr alloy (Scalmalloy) samples processed by LPBF made in our preliminary work. Equiaxed grain region next and along the track boundary and columnar grain region away from the boundary inside the track = bimodal microstructure.

With a special blend of fracture toughness and high yield strength, Scalmalloy's hardening mechanism relies on both very small grain size during solidification and precipitation hardening via $Al_3(Sc_1; Zr_{1-x})$ (35). According to Spierings et. Al (35), to obtain high strength with UTS>520 MPa and YS>480 MPa heat treatment after printing is needed to result in precipitation hardening and the treatment should be holding the printed alloy between 325°C and 350 °C for 4 h to 10 h.

1.3 Mechanical properties under cyclic loading

Scalmalloy is a high-strength aluminium alloy and can be used for applications where cyclic loading is an important consideration, however, despite increased usage, the fatigue behaviour of LPBF-produced Scalmalloy is insufficiently understood, even after a decade of investigation. Metal fatigue is the major form of failure that occurs after the repetition of several cycles, from a few to millions, of stresses applied to the part. Breakages due to fatigue are very costly and many human lives have been lost because of unexpected failures or errors in the fatigue design process. Thus, fatigue characteristics can play a crucial role in some parts and require a deep understanding of the crack initiation and propagation mechanisms (38).

Fatigue loading is the repeated application of cyclic stress or strain, which is much lower than the stress required to cause failure during a single application of stress. In fatigue analysis, several key stress parameters are used to describe the cyclic loading conditions. The maximum stress (σ_{max}) is the highest stress level in a cycle, while the minimum stress (σ_{min}) is the lowest. The stress amplitude (σ_a) represents half of the total stress variation in a cycle and is calculated as:

$$\sigma_a = \frac{\sigma_{max} - \sigma_{min}}{2} \quad \text{Equation 2}$$

The stress range ($\Delta\sigma$) is simply the difference between the maximum stress and the minimum stress:

$$\Delta\sigma = \sigma_{max} - \sigma_{min} \quad \text{Equation 3}$$

The mean stress is the mean value of the maximum and minimum stress:

$$\sigma_m = \frac{\sigma_{max} + \sigma_{min}}{2} \quad \text{Equation 4}$$

The stress ratio (R) is the relationship between the minimum and maximum stress and is given by:

$$R = \frac{\sigma_{min}}{\sigma_{max}} \quad \text{Equation 5}$$

A positive R ratio (e.g., $0 < R < 1$) indicates tension-tension loading, while a negative R ratio ($R < 0$) indicates tension-compression loading (39).

Fatigue strength is described as the number of cycles to failure under a specific applied stress and the fatigue (endurance) limit can be found by constructing an S-N curve (fatigue curve, Wöhler curve) through fatigue testing. In a S-N curve, stress (can be maximum stress, stress range or stress amplitude in the vertical axis) is plotted as a function of cycle number to failure (horizontal axis). The figure below shows a typical S-N curve (Fig. 1.11). Tests are performed by applying cyclic loading on specimens until the failure of the specimen occurs. In some cases, the test is stopped after a very large number of cycles ($N>10^7$), meaning run-out, and the results are then interpreted as infinite life, thus the fatigue limit is determined.

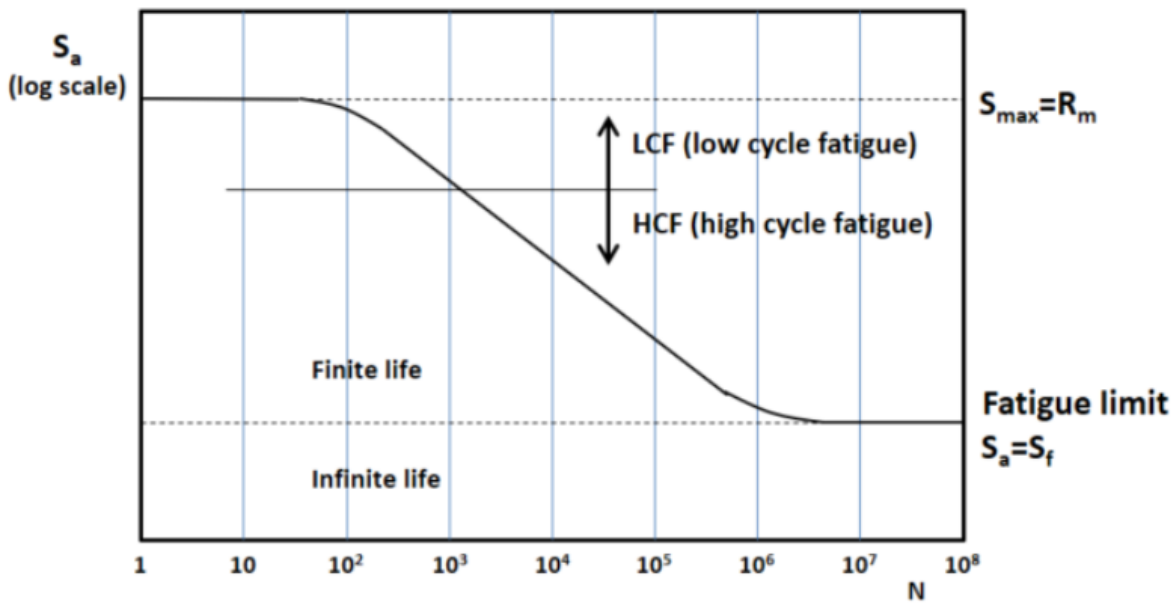

Figure 1.11. Typical S-N curve (38).

Many factors affect fatigue strength of materials, such as geometry of the sample, stress ratio, surface conditions, residual stresses and test environment. In High Cycle Fatigue (HCF) section of the S-N curve, applied stress is sufficiently low (lower than yield stress) and thus the specimen deforms elastically. Referring to Figure 1.11, between $N=10^3$ to $N=10^6$, log(S) decreases linearly with the increase in log(N). The Low Cycle Fatigue (LCF) region in Figure 1.11 refers to the data plot where applied stress is higher than the yields stress, thus the specimen plastically deforms during fatigue testing. However, the demarcation between LCF and HCF may not be clear. In conducting a fatigue test, ASTM E466 is normally followed.

The second important fatigue testing is one to determine the crack growth rate under cyclic loading when a long crack is present. This refers to as fatigue crack growth (FCG) testing. To conduct FCG tests, the ASTM E647 is followed (40). One of the commonly used type of FCG specimen is called compact tension (CT) specimens and the specimen size, notch and locations of the holes for loading pins as shown in Figure 1.12 are specified in the standard. The use of a notch is a crack to be generated first by load cycling so that crack growth under an applied condition (stress intensity factor) can occur.

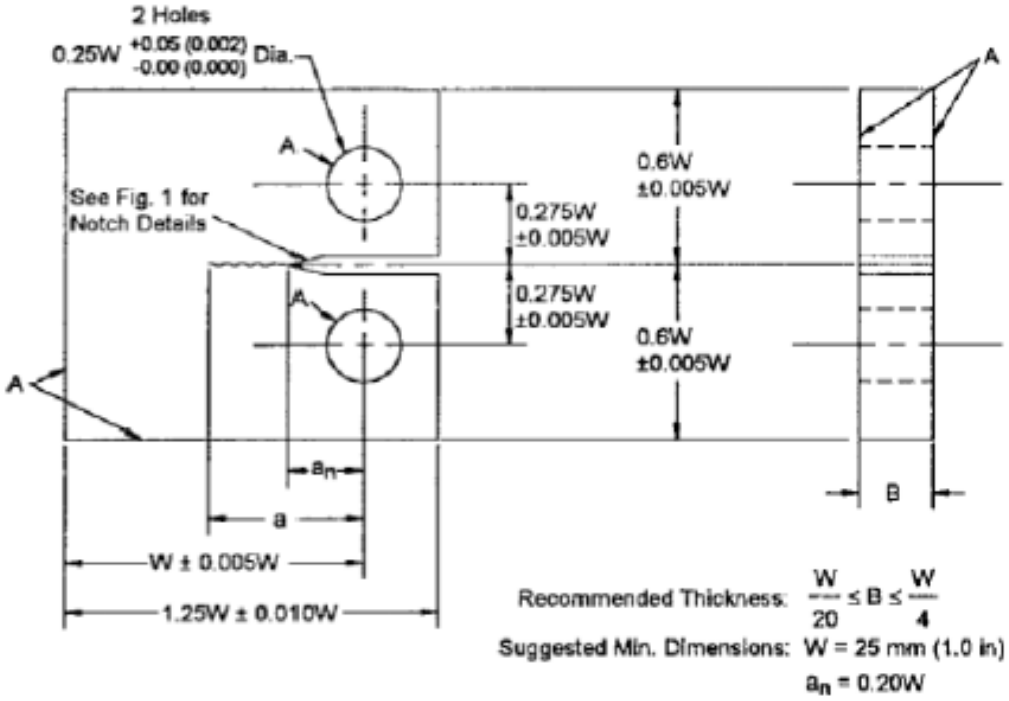

Figure 1.12. An example of a standard Compact-Tension (CT) specimen with dimensions indicated for FCG Testing as specified in ASTM E647 (41).

The results of tests as per ASTM E647 are presented in a graph plotting the crack growth rate (da/dN) as a function of the stress intensity factor range (ΔK) on a log-log scale (Fig. 1.13). The graph is divided into three regions, and each of them represents different crack growth behaviour when fatigue loading is applied. Region I (threshold region) is at the left side of the graph, this region represents the threshold intensity factor (ΔK_{th}) below which the crack does not grow. Region II (stable crack growth region) is in the middle section of the graph, where crack growth is stable and predictable. The relationship between log(da/dN) and log(ΔK) is approximately linear, following the Paris-Erdogan law:

$$\frac{da}{dN} = C\Delta K^m \qquad \text{Equation 6}$$

where a is the crack length and $\frac{da}{dN}$ is the increase in the crack length per cycle, C and m are material parameters and can be determined from linear region II of the graph. Region III (unstable crack growth region): located at the right side of the graph, near the critical stress intensity factor (K_C), which represents the material's fracture toughness. Crack growth becomes rapid and unstable, eventually leading to failure.

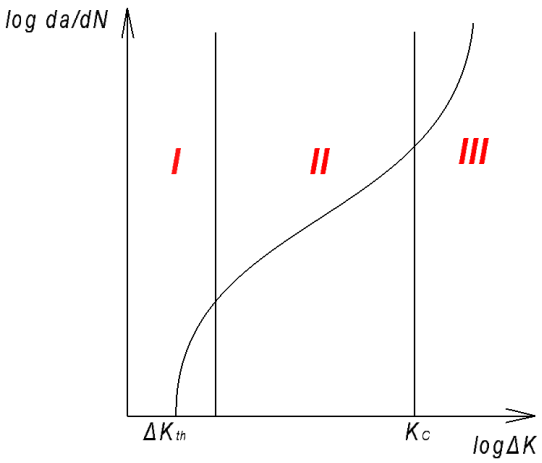

Figure 1.13. Typical plot of crack growth per cycle as a function of the stress intensity range showing the three regions.

To understand how defects and surface conditions affect fatigue performance, it's important to use a suitable model. For LPBF components with high-quality surface finishes, achieved through machining or polishing, fatigue performance is mainly influenced by internal defects rather than surface conditions (42). It is found that these internal defects, often located at the fracture surface edge (surface defects) or just below the surface (subsurface defects), behave like short cracks. Their size can be measured using Murakami's √area parameter, where √area is the square root of area of the defect that caused the failure. Furthermore, the relation between defect size and dynamic strength can be illustrated using the Kitagawa-Takahashi (K-T diagram (Fig. 1.14) (43) and a modified El-Haddad model (44).

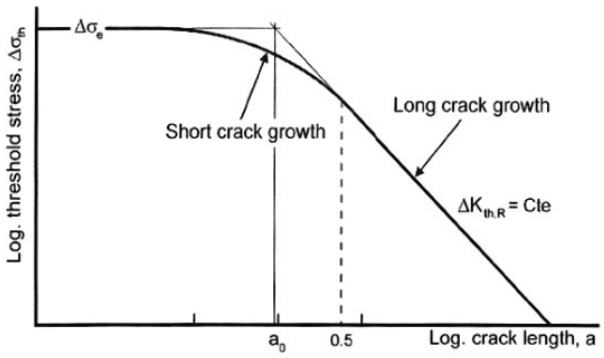

Figure 1.14. Schematic representation of the Kitagawa-Takahashi diagram (43).

For short cracks, there is a limiting threshold, $\Delta\sigma_e$, which closely matches the fatigue limit determined for smooth, unnotched specimens. The transition from short to long crack growth is defined by a specific crack length, known as the El Haddad parameter (a_0). This parameter can be determined using the following equation (44).

$$a_0 = \left(\frac{\Delta K_{th}}{\Delta\sigma_e}\right)^2 \frac{1}{\pi} \quad \text{Equation 7}$$

1.4 What this thesis covers

This PhD research investigates the solidification behaviour of Scalmalloy during LPBF and its influence on the resulting microstructure, with a particular focus on the formation of the bimodal grain structure that makes this alloy printable. The study first examines the elemental segregation and phase formation and growth during LPBF solidification, providing insights into the underlying mechanisms responsible for the unique microstructural characteristics observed in LPBF-processed Scalmalloy. Then, this research explores the crack growth behaviour of Scalmalloy when cyclic loading is applied, a critical factor in determining the alloy's fatigue performance and structural integrity in engineering applications. The diagram representing the scope of this thesis is presented below (Fig. 1.15)

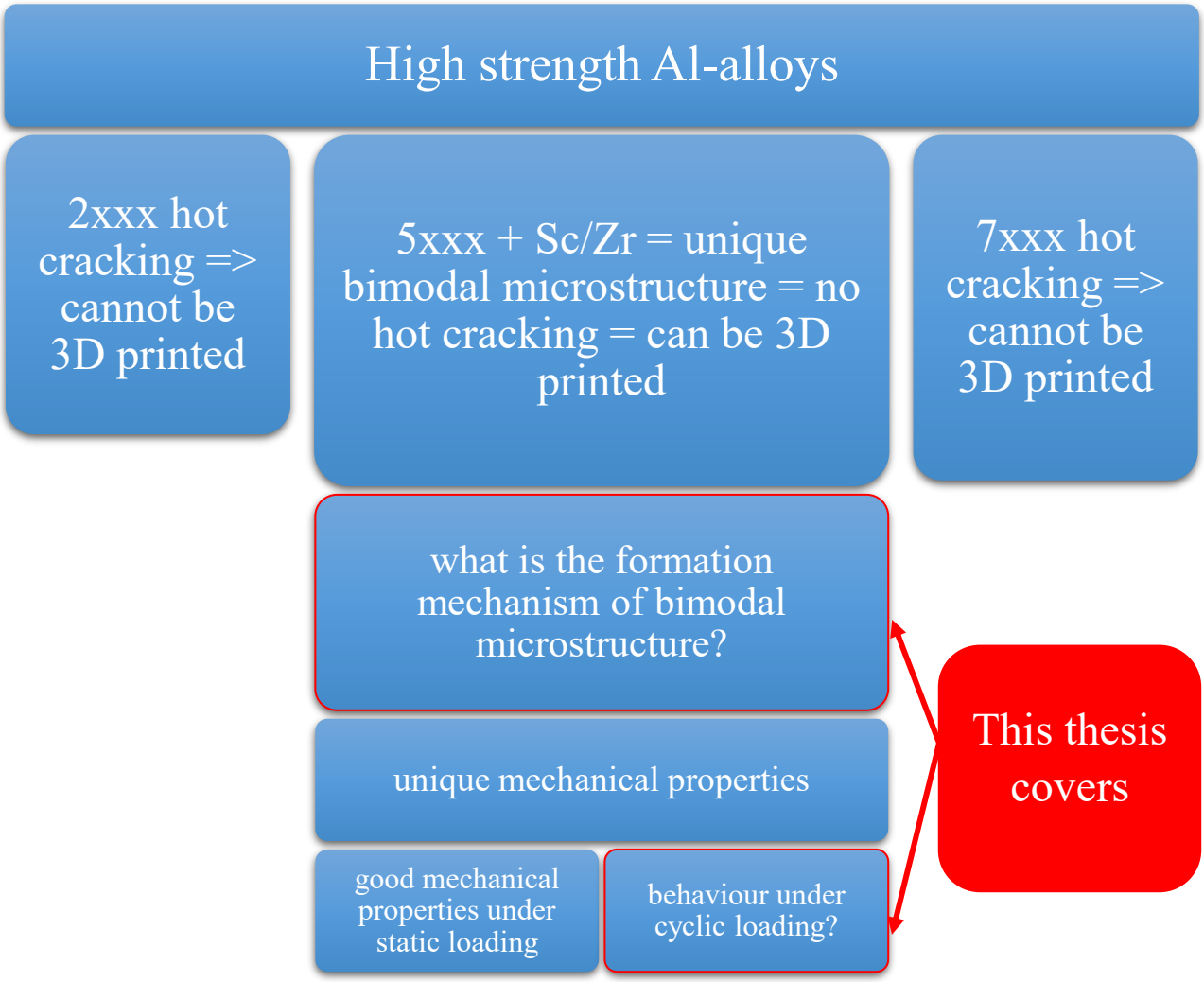

Figure 1.15. Scope of the Thesis.

Chapter 2 - Literature review and research questions

The review will first cover the research on solidification during LPBF of aluminium alloys, from the conventional castable alloy, through high strength Al-alloys that are not castable and thus not printable, to Scalmalloy that is printable. The review on solidification will then examine the Al-Mg-(Sc/Zr) phase systems and possible solidification paths relevant to Scalmalloy during LPBF. This is then followed by deeply analysing the literature on possible mechanisms of formation of bimodal grain structure during LPBF of Scalmalloy. The second aspect of the review will cover the Scalmalloy heat treatment condition and how it affects $Al_3(Sc,Zr)$ particles. Finally, research work on the fatigue behaviour of LPBF Scalmalloy will be reviewed in detail. The review on fatigue performance of LPBF Scalmalloy includes an assessment of its high cycle fatigue strength determined from S–N data, fatigue crack growth behaviour and corresponding threshold stress intensity factor (ΔK_{th}), as well as LPBF defects and their role analysed using the Kitagashi–Takahashi diagram.

2.1 Solidification

2.1.1 Grain structures in as-built state

Aluminium alloys are one of the extensively used metals in LPBF due to their lightweight, high strength and resistance to corrosion. The predominant aluminium alloys processed by LPBF have come from the Al-Si-Mg alloys, in which silicon serves as the main alloying element. Typical Al alloys produced by LPBF are AlSi12 and AlSi10Mg, where Si addition improves its castability (thus printability), and Mg addition for strengthening of the alloy through precipitation hardening and to a small extent solution hardening (45).

Thijs et al. (46) conducted a comprehensive study on the AlSi10Mg alloy, with a specific focus on how various scanning strategies could influence the microstructures. An image depicting the microstructure of an AlSi10Mg LPBFed component, both from a frontal and lateral perspective, can be seen in Figure 2.1. Across the melt pool, three distinct zones can be identified: a fine and a coarse cellular structure within the melt pool and a heat-affected zone (HAZ) surrounding the melt pool in the previously deposited layers. The solidification mode is mainly cellular, but dendrite side branches also have formed. It was also observed that due to the movement of the laser beam and the method of scanning, the thermal gradients and growth rates varied across the melt pool. Consequently, the fine of cells and textures changed throughout the cross-section of the track, leading to characteristic anisotropic mechanical behaviour in additively manufactured aluminium components (47).

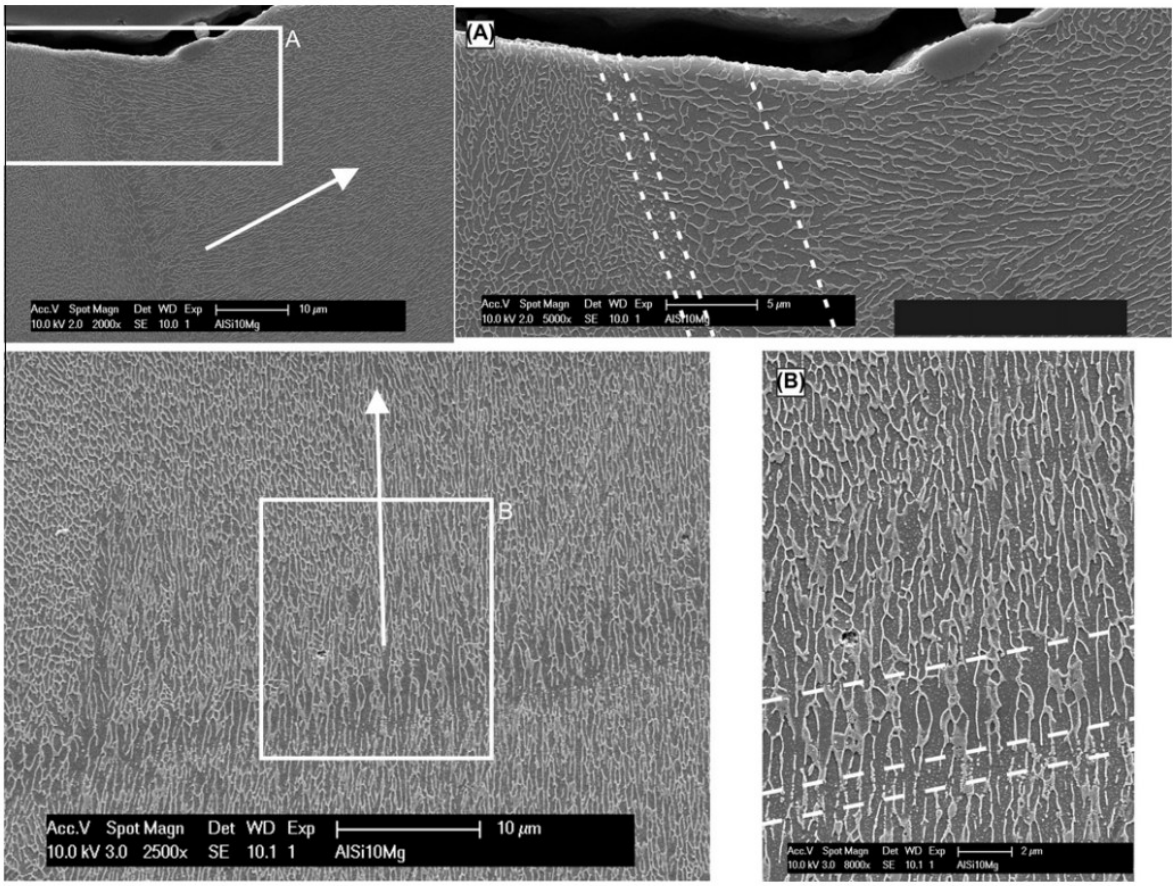

Figure 2.1. SEM micrographs taken in a LPBF AlSi10Mg sample: top micrographs taken from a track surface region and the bottom microstructure taken from a lower track boundary region, with arrows pointing to cellular growth directions (46).

SEM images showing microstructures of the samples made with differing orientations are presented in Figure 2.2 (48). These microstructures exhibit finely cellular dendrites. Within these images, the dark grey regions correspond to the α-Al phase, while the bright grey regions represent Al–Si eutectic. Notably, the microstructure in the z-axis direction differs when compared to that of the x-axis and y-axis directions, with the latter two displaying similar features. Specifically, in the parallel and perpendicular directions relative to the build direction, the eutectic structure of Al–Si is interlinked, forming a network.

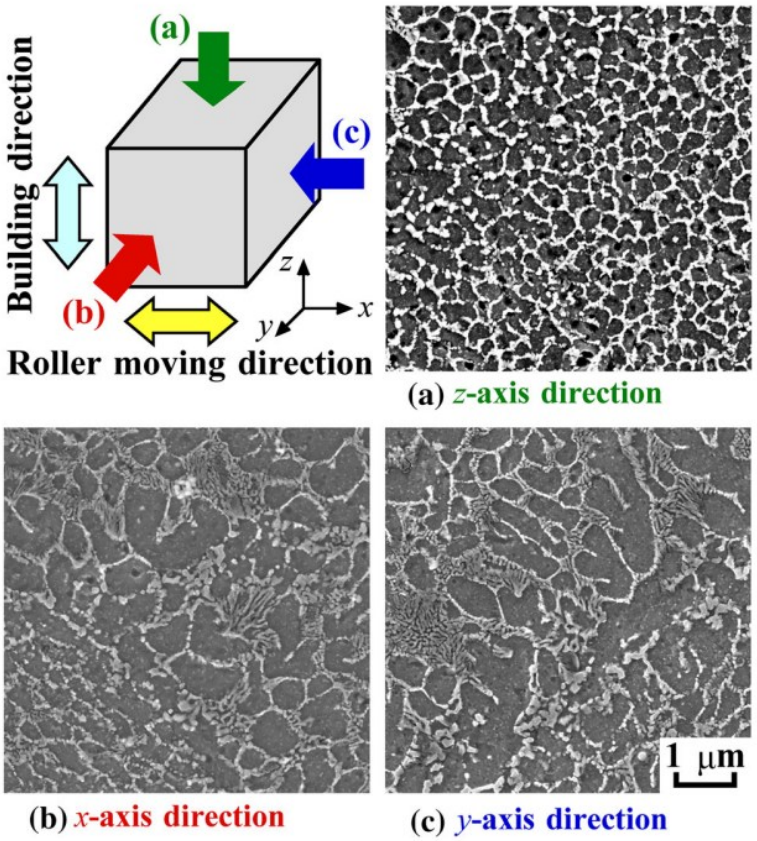

Figure 2.2. SEM images of a LPBF sample taken from various planes (48).

In order to achieve high strength in LPBFed Al alloys, efforts have been made to produce 2xxx, 6xxx, 7xxx series Al alloys by LPBF (49), (50), (51), (52). These alloys are widely used in the automotive and aerospace industries due to their exceptional strength-to-weight ratio, good corrosion resistance and favourable fatigue properties (53). However, LPBF-produced wrought aluminium alloys exhibit solidification cracks, making them less suitable for engineering applications (54), (31), (55). Contributing factors to susceptible hot-cracking and poor printability include (a) wide solidification temperature range, (b) poor liquid permeability and limited liquid supply at the final stage of solidification for backfilling the cracks, and (c) columnar solidification mode. Alloys with a large freezing range experience hot cracking as these alloys remain longer in the vulnerable state when inter-dendritic regions are effectively thin liquid films. During the solidification process, as solid fraction increases, liquid is present locally in some inter-dendritic pockets. When liquid is difficult to flow through the dendritic solid network under the condition of continued thermal contraction of the solid, hot tearing may readily occur (56). Moreover, the LPBF process creates specific solidification conditions that promote the development of long columnar grains in wrought aluminium alloys, thereby facilitating the initiation and spread of cracks along grain boundaries (49) (54). Examples of intergranular cracks for 2xxx and 7xxx Al alloys are provided below (Fig. 2.3, Fig 2.4).

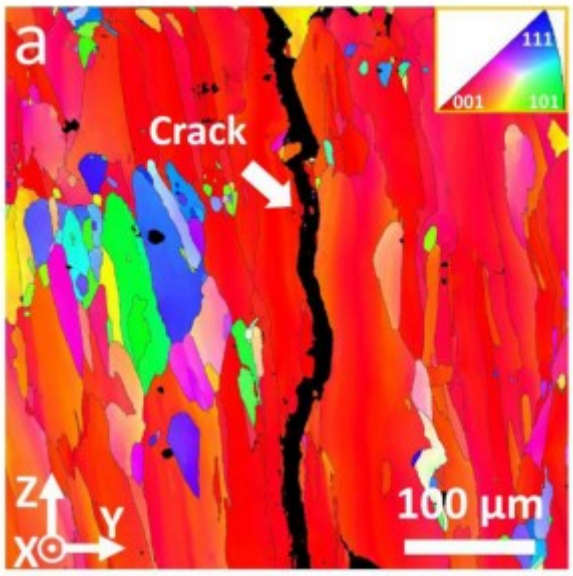

Figure 2.3. Hot crack propagating through the intergranular region in LPBF-processed 2024 aluminium alloy (49)

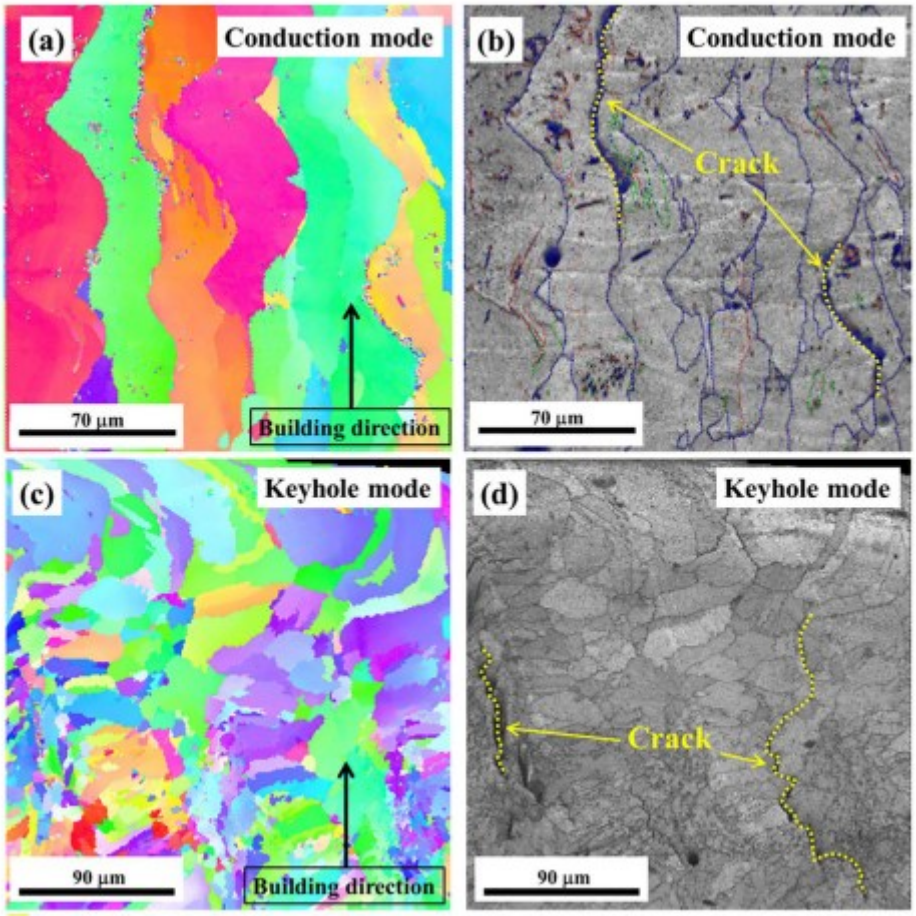

Figure 2.4. An intergranular crack in LPBF-processed AA7050 (54).

As for Scalmalloy, the addition of Scandium (Sc) and Zirconium (Zr) results in a bimodal (duplex) microstructure consisting of equiaxed and columnar grains. Schmidtke et al. (57) conducted research on the

alloy development based on very small additions of Sc (0.66 wt%) and Zr (0.37 wt%) to Al–4.5Mg (5xxx) alloy. These additions enabled the alloy to be age-hardenable, achieving a yield strength (YS, σ_y) of approximately 500 MPa in its peak-hardening state, while keeping the printed sample without hot cracking. However, the precise mechanism of bimodal microstructure formation that is hot crack free remains not fully understood. Spierings et al. conducted a number of studies (35), (36), (58), (59), (60) illustrating the presence of equiaxed-columnar bimodal structures within each printed track (see Fig. 2.5).

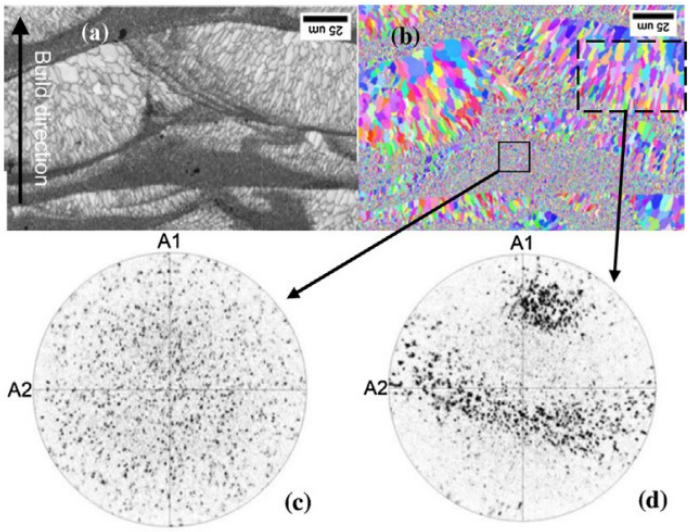

Figure 2.5. Microstructures of equiaxed and columnar grain regions. (a) shown in optical micrograph, (b) shown in EBSD orientation map, (c) pole figure in equiaxed grain region and (d) pole figure in columnar grain region (59).

It has been demonstrated that during solidification, two different structures are formed. In one type of structure, the material develops a long, narrow, grains that align with the build (z-) direction. In the other type of structure, the grains are much finer, arranged randomly, showing no clear pattern. This is confirmed by Figure 2.5.c, which indicates no preferred grain orientation for the equiaxed grains region and, in contrast, Figure 2.5.d shows that the columnar structure has a strong <100> orientation, roughly parallel to the build (z-) axis. Spierings et al.'s in (58) demonstrated an average thickness of a fine-grained (FG) region, or equiaxed grain region, of about 10 µm and a coarse-grained (CG) region, or columnar grain region, in size of approximately 20 µm. Also, it has been shown that the bimodal microstructure is fine-grained, with grain sizes ranging from 200 nm to less than 15 µm.

2.1.2 Phase diagrams and solidification path

Aluminium alloys that contain small scandium additions present improved properties in several fields. As underlined in the paper by Lee et al. (61), scandium, when added to aluminium, is a powerful dispersoid strengthener, grain refiner and recrystallisation inhibitor. Sc reduces hot cracking during welding and 3D printing and gives the highest increase of strengthening (per atomic percent) of any alloying metal when added to aluminium. The Al_3Sc dispersoid ($AuCu_3$-type phase) is coherent with the Al-matrix. To understand the

microstructure and mechanical properties of Aluminium alloys containing Sc, deep knowledge of the phase diagram and solidification process is required. The binary Al-Sc phase diagram is presented in Figure 2.6. It has been shown in (62), (63) that the limit solubility in Al-Sc phase diagram is 0.38 wt%, the eutectic temperature is 656-660°C, the eutectic point is 0.52-0.58 wt% Sc and the eutectic reaction is determined as L → (Al) + Al_3Sc.

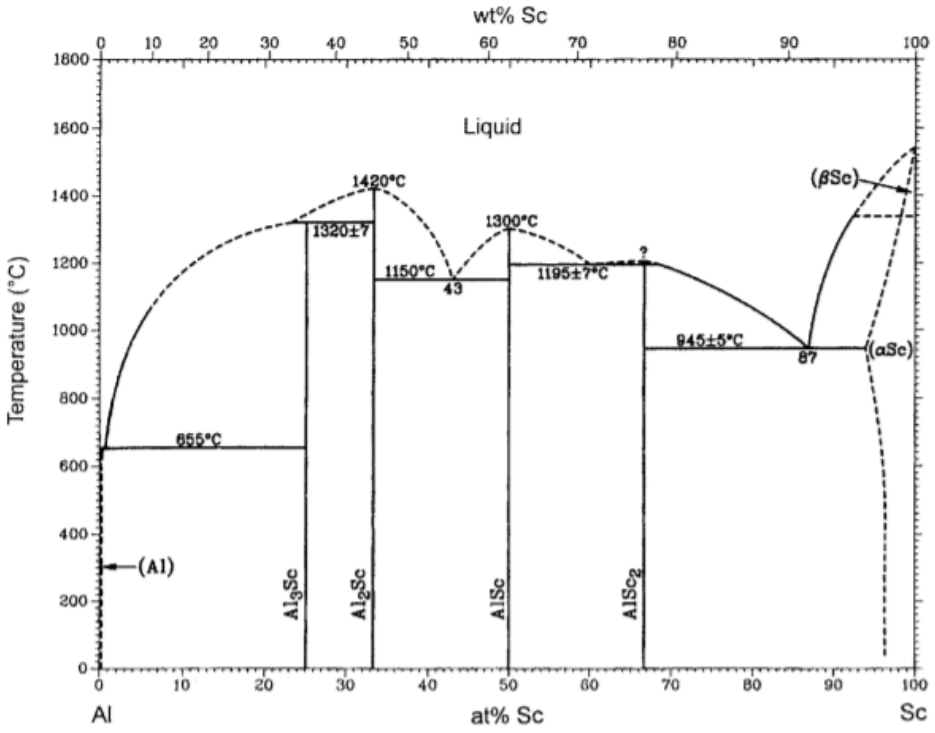

Figure 2.6. Binary Al-Sc phase diagram (63)

Zirconium, typically in the 0.1-0.3% range, is added to produce a fine precipitate of intermetallic particles. In the current research, Scalmalloy contains from 0.2% to 0.5% of Zr, as per the composition provided by the powder supplier (Table 3.1). In contrast to the Al-Sc alloy system, in the Al-Zr alloy system (referring to the Al-rich side), the peritectic reaction is promoted, creating the stable Al_3Zr phase that has DO_{23} crystal structure and exhibits a poor match with α-Al, where DO_{23} is a designation for a tetragonal crystal structure used to describe an ordered intermetallic phase. The influence of cooling rate on the solidification sequence of Al-Zr alloys has been studied by various researchers. Rapid solidification techniques like chill casting (64) and splat quenching (65) have been applied to study microstructures after solidification and the decomposition of Al+Zr solid solutions. Hori et al. (66) demonstrated the potential to control the formation of the primary phase (DO_{23} Al_3Zr) in the liquid phase, which helps to form the metastable $L1_2$ Al_3Zr phase (refer to Fig. 2.7). This transition leads to a grain structure refinement. Similar to the case of Sc, this effect can be attributed to the structure of the $L1_2$ Al_3Zr phase being similar to and α-Al. However, unlike Al-Sc alloys containing 0.7% Sc, which consistently form the $L1_2$ equilibrium phase across all cooling rates, the formation of $L1_2$ Al_3Zr intermetallic is limited to a narrow range of cooling rates and compositions, as depicted in Figure 2.7 (67).

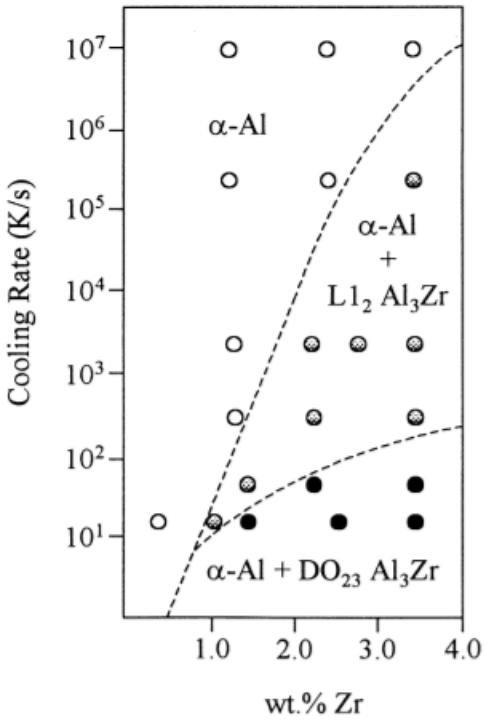

Figure 2.7. Map (cooling rate and Zr content) showing the conditions for forming primary metastable $L1_2$ Al_3Zr phase (67)

Wang et al. in (68) show that a eutectic reaction occurs in Al-Zr alloys under condition of cooling rates from 0.5 to 5 K/s during solidification. Zr-rich particles were detected to be present in grain boundaries and these particles were determined by electron diffraction analysis to be the tetragonal DO_{23} Al_3Zr phase. This is further supported by differential thermal analysis showing a peak at 658–659 °C, which is lower than the melting point of pure Al, thus indicating the presence of a eutectic reaction.

Scandium is shown to provide a strengthening effect for Al-Sc alloys with Sc>0.6%. However, when scandium is introduced in conjunction with zirconium, the modifying influence of scandium becomes evident at lower concentrations (Fig. 2.8). Zirconium is a common co-additive with scandium in Al alloys, employed to reduce the necessary quantity of the latter and enhance the stability of the dispersion-hardened structure. Extensive research has probed the isothermal section of Al-Sc-Zr phase diagram at 600°C across the entire phase diagram. This exploration revealed that the Al_3Sc phase can accommodate substantial amounts of Zr. Consequently, when both Scandium and Zirconium are added into an aluminium alloy, only a small amount, if any, of the Zirconium will form Al_3Zr particles. The remaining Zirconium will be dissolved into the Al_3Sc particles. Thus, it is more precise to refer to them as $Al_3(Sc_{1-x}Zr_x)$ particles or simply $Al_3(Sc,Zr)$ particles (69).

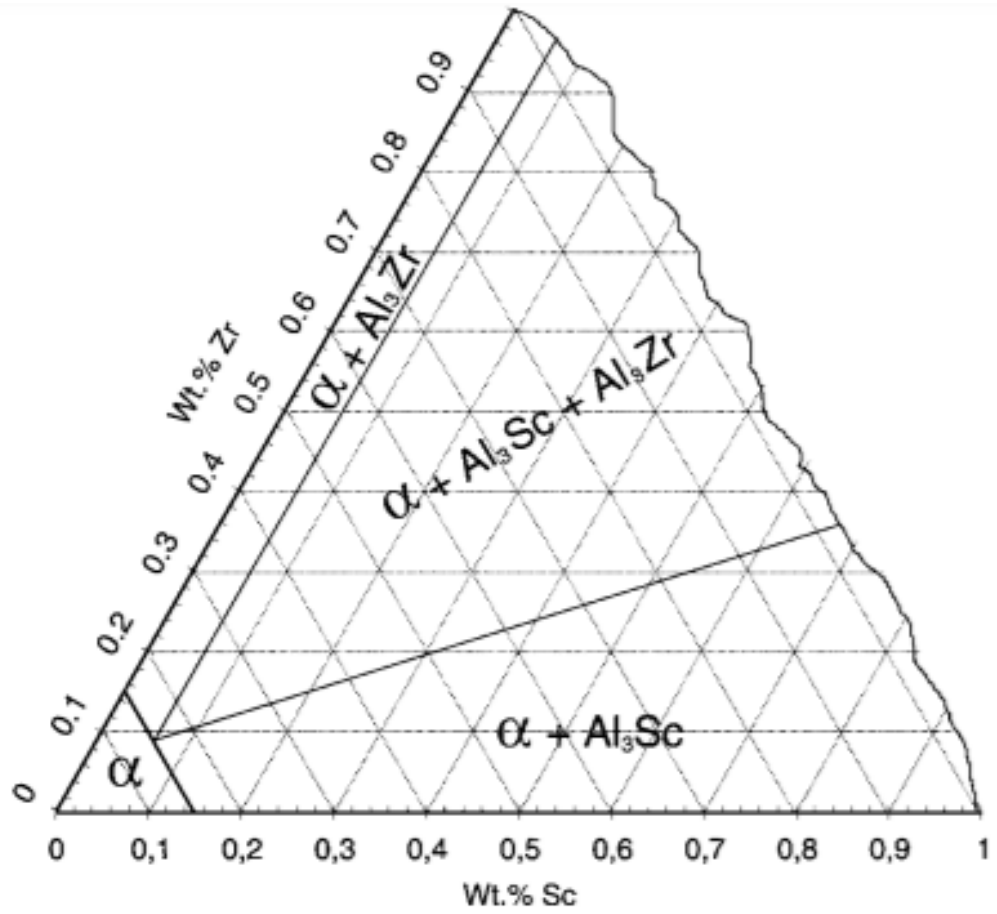

Figure 2.8. Al rich corner of Al–Sc–Zr phase diagram at 600°C (69).

Analysing these phase diagrams, it is important to understand how phases form during the solidification process, as their sequence influences the final microstructure and, subsequently, the mechanical properties of the alloy. The solidification path is the sequence of phase transformations, starting from the initial nucleation of primary solid phases, that occur during the solidification of liquid with decreasing temperature until a fully solid state. Samaras et al. in (70) has investigated the solidification path of Al-Mg-Sc-Zr using ThermoCalc software. The modelling has shown what phases occur at a certain temperature along the whole solidification path (Fig. 2.9, Table 2.1). According to the diagram presented in Figure 2.9, the Al_3Zr phase is solidified before FCC (688°C-639°C), facilitating heterogeneous nucleation sites for the main phase FCC (637°C) and modifying the as-cast grain structure. The Al_3Sc phase solidifies at 604°C, when 75% of FCC phase is solidified, and consequently its modifying effect is minor compared to Al_3Zr.

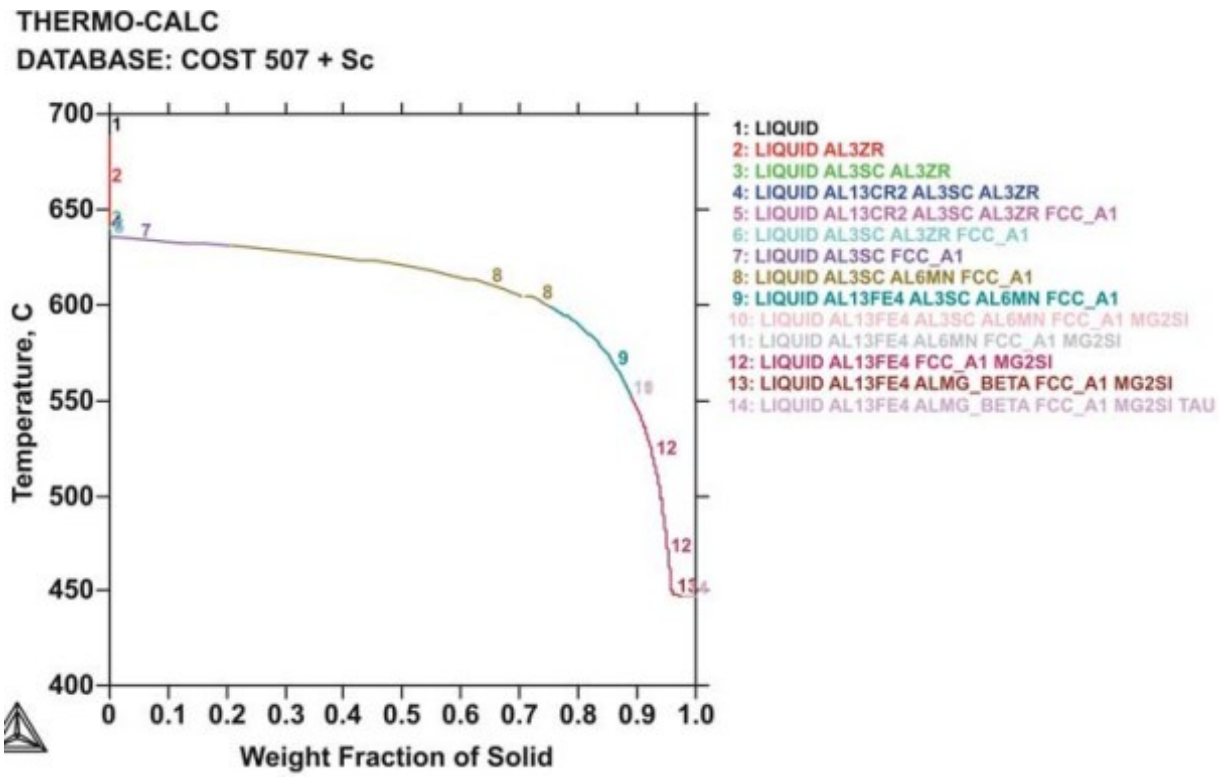

Figure 2.9. Solidification path of Al-4.5Mg-0.7Mn-0.4Sc-0.15Zr reported in (70).

Table 2.1. Phases reported in AA 5086 with addition of Sc and Zr (70).

Phase	Solubility Temperature	fraction at 25°C	Chemical Compo-sition	Comments
β–AlMg	228°C	10.2 at.%	63.23 wt.% Al 36.31 wt.% Mg 0.46 wt.% Zn.	
Al_6Mn	631°C	2.48 at.%	74.59 wt.% Al 19.28 wt.% Mn 6.13 wt.% Fe.	
Al_3Zr - 0.08%wt	687°C	0.0947 at.%	47.02 wt.% Al 52.98 wt.% Zr	exists with liquid at 638°C–687°C
Al_3Zr - 0.15%wt	738°C	0.18 at.%	Same	exists with liquid at 638°C–738°C
Al_3Sc - 0.1% wt	580°C	0.24 at.%	64.29 wt.% Al 35.71 wt.% Sc	
Al_3Sc - 0.4% wt	641°C	0.96 at.%	Same	

Another study (71) investigated the solidification path of Al alloy with the addition of Sc and Zr and showed that the liquidus temperature of the alloy is 688 °C (Fig. 2.10). The initial solid phase to occur within the molten material is Al_3Zr, which continues forming until it reaches 637 °C. At this temperature, the α phase commences its solidification. At this point, the primary Al_3Zr constitutes roughly 0.50 mass percent of the alloy. Being dispersed throughout the molten mixture, it offers various heterogeneous sites for initiating the solidification of the α phase. Notably, the primary Al_3Sc begins its formation at 604 °C, once about 70% of the matrix α phase has already solidified. Thus, in this scenario, it appears that the impact of Zr on refining the as-cast microstructure is more prominent than that of Sc. With higher Sc and Zr additions, these effects become more pronounced. For instance, introducing 0.40 mass percent Sc and 0.15 mass percent Zr into the base alloy results in a broader solidification range, initiating at 743 °C and concluding at 447.3 °C. Al_3Zr forms as the

first solid phase, followed by Al_3Sc, with the latter initiating solidification approximately 100 °C lower. It is important to note that, in this case, both of these phases begin solidifying before the matrix phase, thus providing the nucleation sites for microstructure refinement.

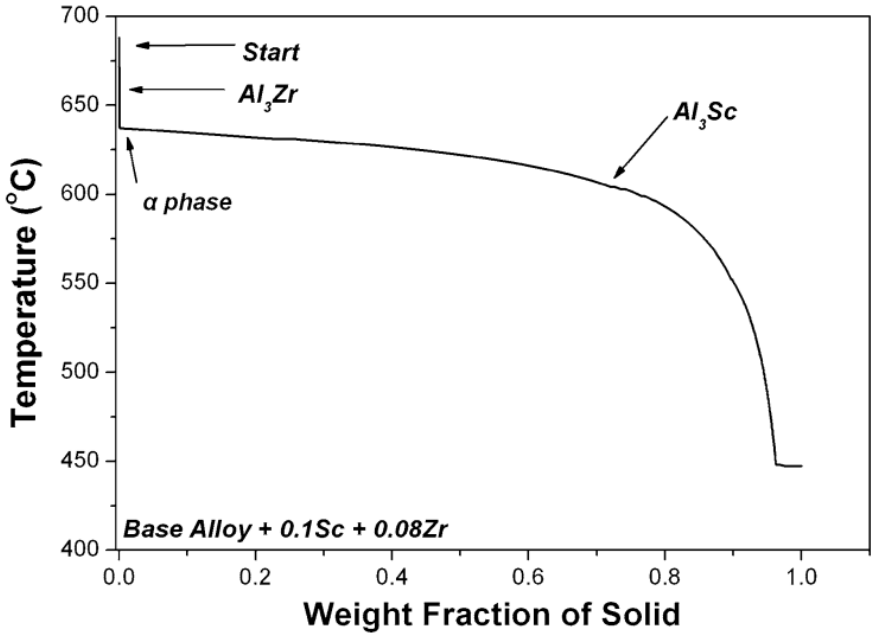

Figure 2.10. Solidification path of the Al-4.5Mg-0.1Sc-0.08Zr alloy predicted by Thermo-Calc calculation. Formation of the respective phase starts as pointed to by the arrows (71).

While the solidification path defines the sequence of phase transformations, it is equally important to analyse how these phases influence the final grain structure. In aluminium alloys with Sc and Zr additions, the early precipitation of Al_3Zr and Al_3Sc provides heterogeneous nucleation sites, refining the as-cast microstructure. However, during LPBF, cooling rates are high and up to $\approx 10^6$ K/s for aluminium. Thus, phase transformation during solidification is highly non-equilibrium, with the solidification path possibly departing from what may be predicted by the equilibrium phase diagrams significantly. Thus, the solidification path that leads to the formation of the bimodal grain structure during Scalmalloy LPBF needs to be considerably further studied.

2.1.3 Formation mechanisms of bimodal grains growth

The study of the formation mechanism of the bimodal microstructure in Scalmalloy processed by LPBF began as researchers observed peculiar grain structures unique to this advanced manufacturing process that has been widely reported (35), (36), (72). Initially, interest in Scalmalloy rose from its exceptional strength and ductility, making it a promising candidate for aerospace and high-performance applications. Experimental results have shown that adding Sc and Zr alloying elements causes precipitation of Al_3Sc and Al_3Zr, which act as grain refiners. This results in crack-free LPBF parts with high tensile strength. However, the mechanism of forming the bimodal structure is still not explained clearly (59).

In their research on LPBFed Scalmalloy, Spierings et al. (35), (36), (58), (59), (60) detected nanoparticles of $Al_3(Sc,Zr)$ within the size range of 30-100 nm. It was posited that these particles serve as nuclei for the development of equiaxed grains near the track boundary, as illustrated in Figure 2.11 (58). Both homogeneous (happens spontaneously within the liquid without any external surfaces) and heterogeneous (begins on a pre-existing surface) nucleation can produce new grains during solidification. As second-phase particles in the molten pool supply pre-existing surfaces, heterogeneous nucleation is more favourable than homogeneous nucleation as it requires less energy. If particles have a crystal structure and lattice parameters that are similar to those of the solidifying aluminium matrix, they can act as nucleation sites for new grains to grow. If nucleation sites are present, they can promote the formation of equiaxed grains, preventing the dominance of columnar growth (73). The origin of $Al_3(Sc,Zr)$ nanoparticles remains uncertain. Scheil simulations in study (58) have shown that these particles dissolve at temperature around ≈800 °C and growth of coarse columnar grains takes place. Thermal simulations, on the other hand, have demonstrated that temperatures below 800 °C within the melt-pool exist only in a relatively thin zone near the melt-pool, with an approximate thickness of ≈10 µm. This observation aligns with the fine-grained region seen in the microstructure. Thus, Spierings et al. have suggested that $Al_3(Sc,Zr)$ particles can survive in the melt region next to track boundary and later solidifies in equiaxed-grain solidification mode have come from the remelting of the previous track/layer.

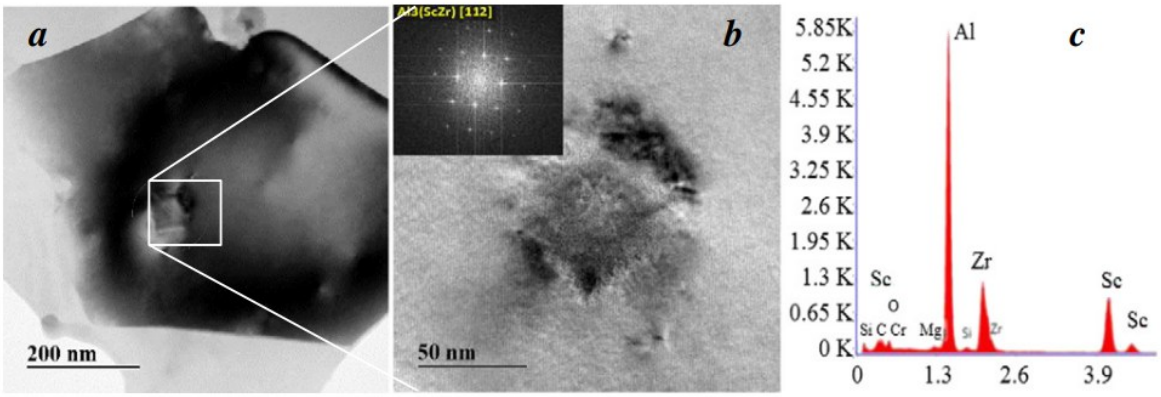

Figure 2.11. Cube-shaped $Al_3(ScZr)$ particle shown in a) BF-TEM image, (b) in a higher magnification image with FFT, c) EDS spectrum (58).

Spierings et al. (58) have suggested the role of $Al_3(Sc,Zr)$ particles as nucleation sites for equiaxed grain formation during LPBF, given that $Al_3(Sc,Zr)$ particles have been recognized for initiating equiaxed α-Al grain growth in conventional casting. However, it's important to note that equiaxed-grain formation during casting does not mean the presence of preexisting $Al_3(Sc,Zr)$ particles. Hyde et al. (74) illustrated the grain-refining effect of Al_3Sc during the solidification of Al–0.7wt%Sc alloy, which was initially melted and held at 750 °C. In this case, the melt temperature exceeded the liquidus temperature of the alloy, indicating that Al_3Sc particles do not exist in the melt. Instead, Al_3Sc nuclei have been formed directly from the melt pool as it has been cooled and solidified, providing the subsequent growth of equiaxed α-Al grains.

Therefore, the precise reason behind the belief that $Al_3(Sc,Zr)$ nuclei originate from the remelting of the previous layer or track to facilitate equiaxed grain formation during LPBF remains uncertain. This remelting mechanism, which leaves $Al_3(Sc,Zr)$ particles unmelted in the region adjacent to the track boundary, was subsequently proposed by Yang et al. (75). They succeeded in achieving an almost entirely equiaxed grain structure by elevating the applied energy density to 154.2 J/mm^3 and increasing the platform temperature to 200 °C. The authors have proposed that this achievement is attributed to a combination of reduced thermal gradients and enlarged remelting zone volumes, and effective grain refinement resulting from the addition of Sc, although the presence of Al_3Sc particles in equiaxed grain region has not been demonstrated (see Fig. 2.12).

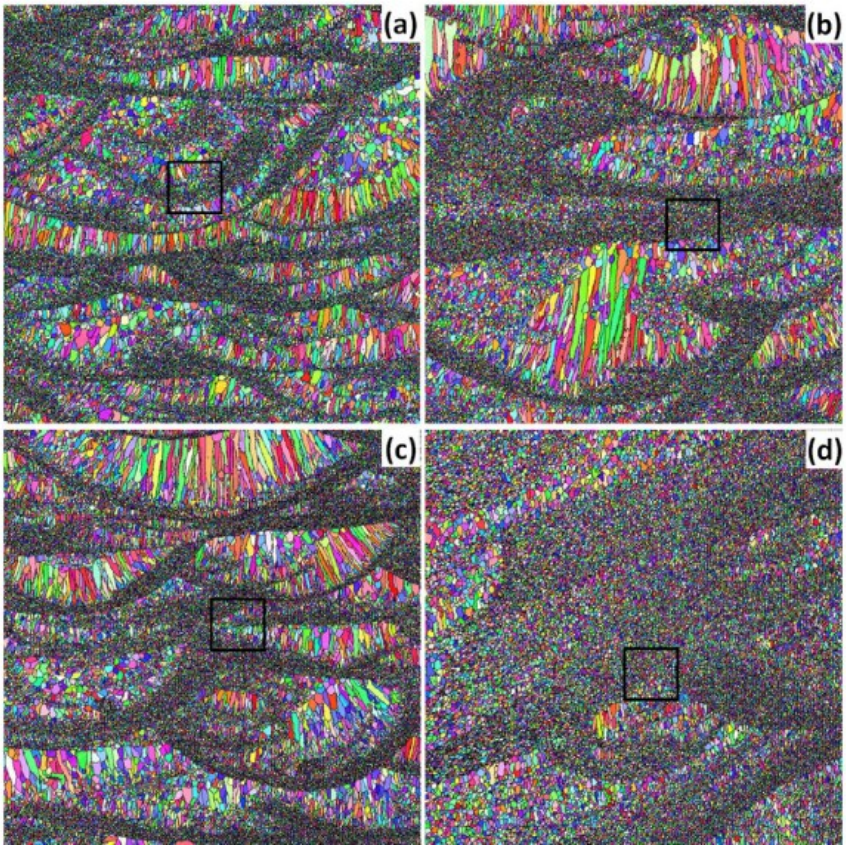

Figure 2.12. EBSD orientation maps of LPBF Scalmalloy samples with various laser energy and base plate temperature: (a) 77.1 J/mm^3 and 35 °C; (b) 154.2 J/mm^{3}and 35 °C; (c) 77.1 J/mm^3 and 200 °C; (d) 154.2 J/mm^3 and 200 °C (75).

The suggestion of the mechanism relating to remelting seems to be still prevailing, as described in a recent review specifically on LPBF of Sc-containing aluminium alloys (76). Ekubaru et al. (77) have recently demonstrated that controlling the hatch spacing can control the amount of equiaxed grains and thus manage the alloy's strength through grain-boundary strengthening (Fig. 2.13, 2.14). However, the role of unmelted particles in this mechanism remains unclear and requires further investigation.

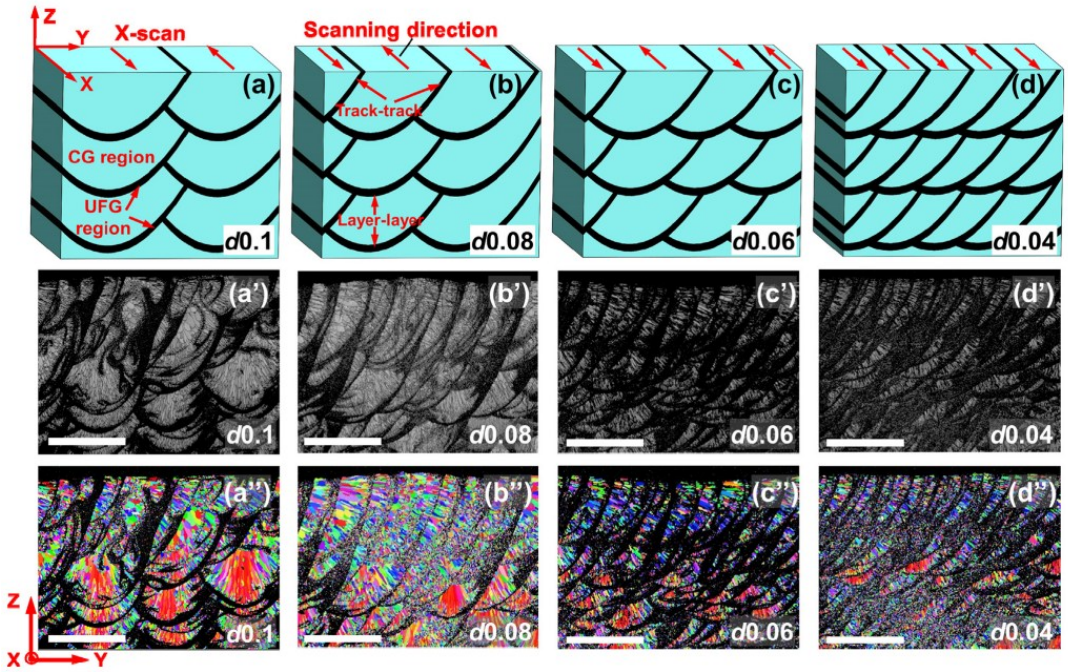

Figure 2.13. Schematic representation of scanning strategy and EBSD images for different hatch spacing set up, where d0.1, d0.08, d0.06 and d0.04 correspond to 0.1 mm, 0.08 mm, 0.06 mm and 0.04 mm hatch spacing. Scale bars: 200μm (77).

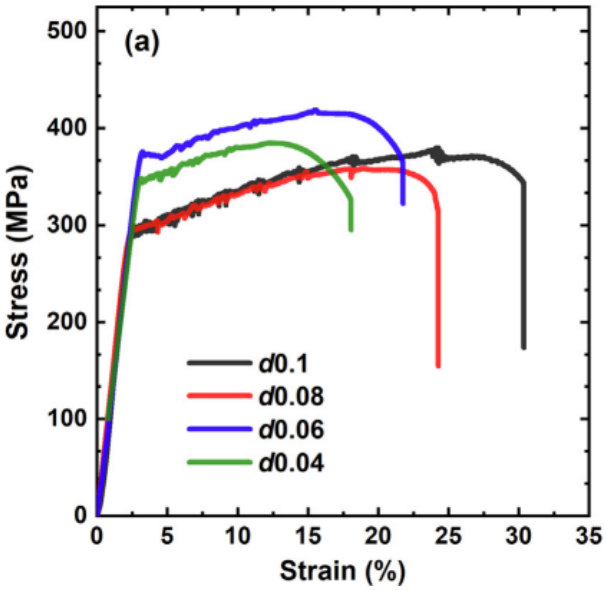

Figure 2.14. Corresponding tensile stress-strain curves demonstrating hardening effect for samples printed with higher hatch spacing (77).

Since Spierings et al.'s studies, there has continuously been a strong research effort on a number of aspects of LPBF of Al–Mg alloys containing various amounts of Sc and/or Zr (34), (78), (79), (80). Contents of Sc and Zr differ in various studies, so that the kinetics of forming Al_3(Sc,Zr) may differ. In Zhang et al.'s (78) study at a P/v = 0.18 J mm^{-1}, a small amount of coherent, spherical Al_3(Sc,Zr) precipitates with a radius of 10~40 nm were obtained at the bottom of molten pool, and very limited precipitates were found in the centre of the molten pool (Fig. 2.15), while no precipitates were observed throughout the matrix at P/v = 0.09 J mm^{-1} . The

author suggested it was probably attributed to the dramatic change of heat-mass transfer as well as the short liquid lifetime with the change of scan speed and subsequently P/v ratio.

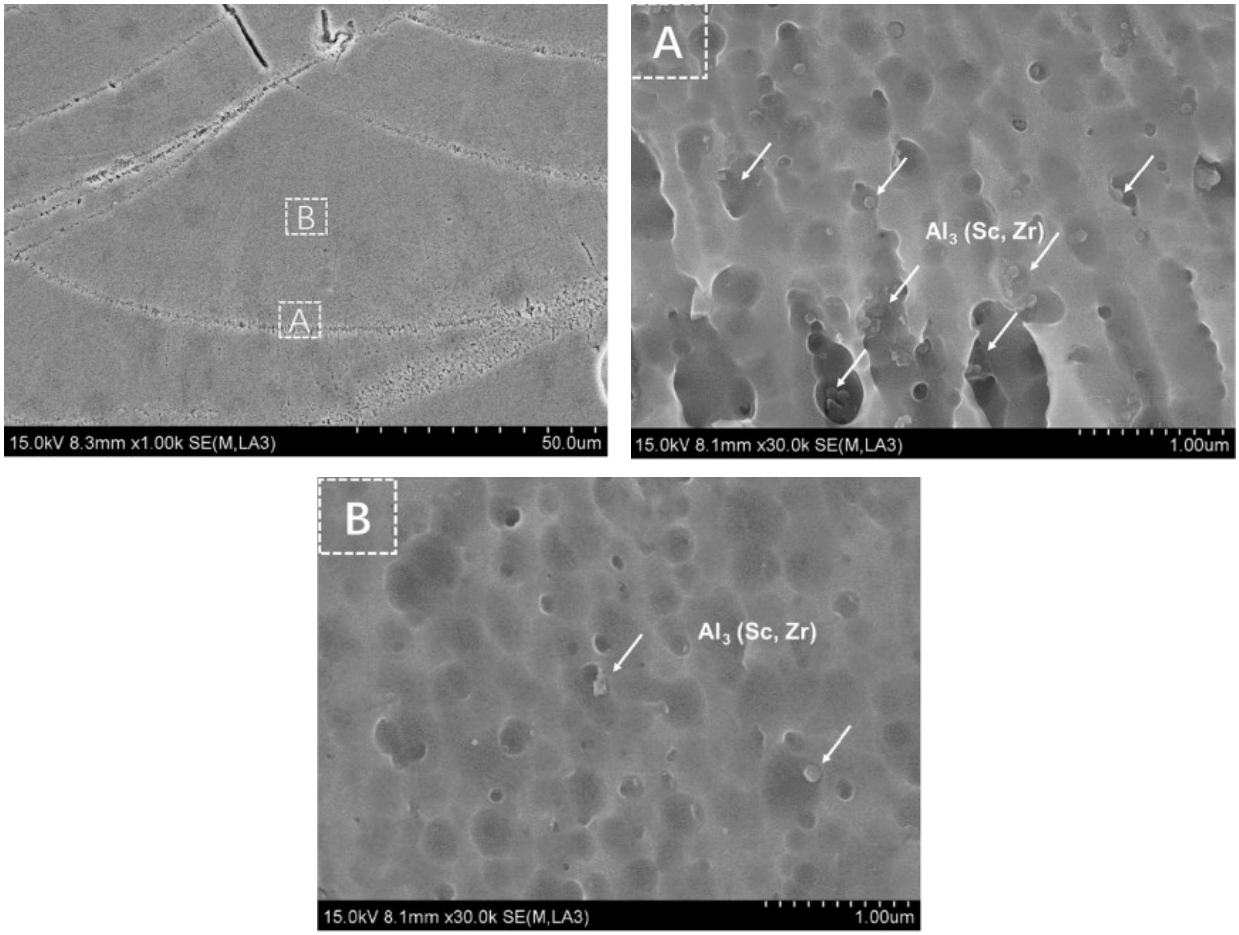

Figure 2.15. SEM micrographs taken from LPBF Al-Mg-Sc-Zr samples made using P/v = 0.18 J mm^{-1}, with Al_3(Sc,Zr) particles indicated by arrows (78).

In a contrasting study by Shi et al. (34) involving Scalmalloy processing at P/v values ranging from 0.07 to 0.62 J·mm^{-1} (with laser power ranging from 220 W to 370 W and scanning speed varying from 600 to 3000 mm/s), their scanning transmission electron microscope (STEM) analysis revealed the absence of detectable particles. Similarly, Churyumov et al. (80) found no Al_3(Sc,Zr) particles in their investigation. Even at P/v = 0.81 J·mm^{-1}, the examination of the microstructure using transmission electron microscopy (TEM) did not reveal any particles but only the aluminium solid solution (Fig. 2.16). The author proposes that the inability to identify those particles stems from a lower supersaturated solid solution of Mg, Sc, and Zr compared to prior studies.

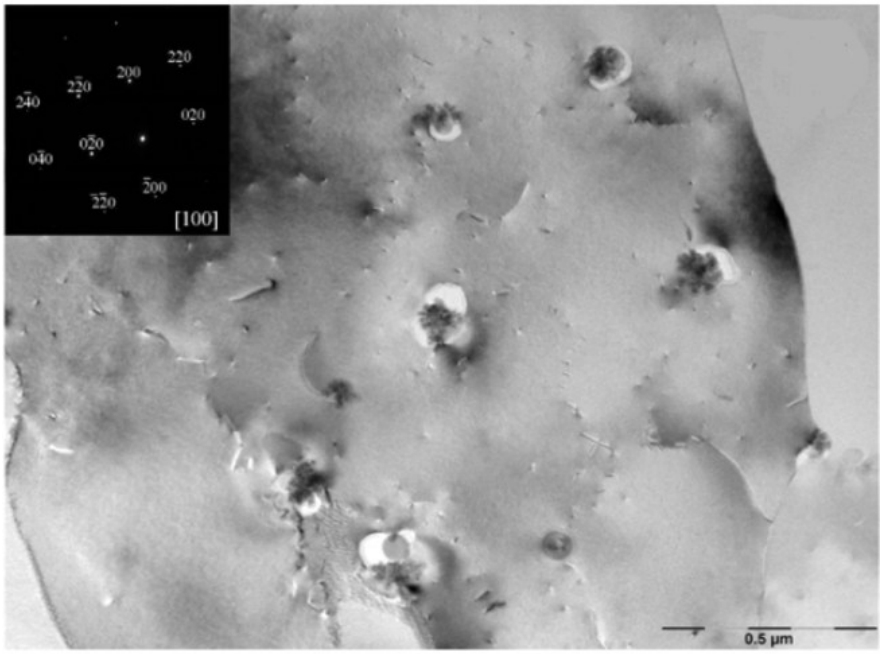

Figure 2.16. TEM microstructure of as-built sample produced using laser power 180 W and scanning speed 220 mm s^{-1} confirming lack of Al_3(Sc, Zr) particles (superstructure diffraction not observed in the diffraction pattern) (80).

Additionally, Ma et al. (79) analysed the microstructure and mechanical behaviour of an Al-4.0Mg-0.7Sc-0.4Zr-0.5Mn alloy produced by LPBF and samples for microstructural investigations and mechanical tests have been printed at P/v = 0.27 J·mm^{-1}. While the paper mainly focuses on the effects of bimodal microstructure on mechanical properties and describes the function of Al_3(Sc,Zr) particles as grain refiners, the authors do not, however, demonstrate the presence of these particles in the microstructure.

Analysing the previous studies, it can be noticed that there is no strong evidence to suggest that unmelted particles are the driving factor for equiaxed grain formation in LPBFed Scalmalloy. While some studies suggest their influence, clear experimental validation remains absent. A more thorough understanding of the role of Sc in forming the bimodal microstructure in Scalmalloy is thus important.

2.2 Precipitation hardening

It has been widely assumed that Al_3(Sc,Zr) particles act as nuclei for forming the equiaxed grains next to the track boundary. The original source of Al_3(Sc,Zr) nanoparticles, however, is less clear. This section is addressed with special focus on the literature reported the presence of Al_3(Sc,Zr) particles, their location within the melt pool, size and method of their detection. This section focuses on the precipitation behaviour of Scalmalloy, beginning with an examination of the state of hardening elements in the as-built condition, followed by a review of how Al_3(Sc, Zr) evolves during heat treatment.

2.2.1 State of hardening elements in as-built condition

Table 2.2 represents an overview of the existing work in the study of the state of $Al_3(Sc,Zr)$ particles in LPBFed Scalmalloy. The data are summarized from various sources in the literature and include the composition of the alloy, the process conditions (scan speed and power/speed ratio), and the measured particle size. Some papers report particle size and distribution in the equiaxed or columnar grain regions, however some papers report the absence of these particles. Various techniques, including TEM-FFT, SEM, STEM-EDS, and TEM-SADP, have been applied in the detection of the nanoscale precipitates.

Table 2.2. Summary of previous studies of $Al_3(Sc,Zr)$ particles state in as-built condition.

Mg - Sc - Zr	v, mm/s	P/v, J/mm	In equiaxed or columnar grain region	$Al_3(Sc,Zr)$ detection	Ref.
4.5-0.66-0.37	170-350 170	1.18-0.57 1.18	50nm in E GB 2-5nm in E	TEM-FFT	(58)
	>200	<1.00	None		(36)
4.2-0.4-0.2	1800	0.18	50-90nm mainly in E, but no small ones	SEM & TEM-FFT	(78)
3.4-1.08-0.23	600-3000	0.62-0.07	None	STEM-EDS	(34)
4.5-0.32-0.66	220	0.81	None	TEM-SADP	(80)
4.0-0.74-0.42	*1200*	0.27	None	TEM-EDS	(79)
4.5-0.51-0.07	500	0.40	They stated yes, 15-20nm but not shown in SADPs	TEM-SADPs, none show superstructure diffractions	(1)
4.7-0.72-0.33	1000	0.37	up to 100nm in E but no small ones	STEM-EDS+TEM-SADP	(81), (82)
4.5-0.66-0.33	1200	0.31	A single particle ~50nm in GB	TEM-SADP	(83)
4.6-0.69-0.39	No info	No info	A cluster with each up to 40nm	TEM-SADP	(84)

Although Mg concentration is just 3.4wt% in two of these investigations, it is close to 4.5wt% in many of them. According to several studies, the contents of Sc and Zr vary, which could affect how $Al_3(Sc,Zr)$ is being

formed. Heat input itself should have a closer relationship to the mode of solidification than the volumetric energy (E), which is frequently utilised in LPBF studies and equals the heat input divided by the product of hatch spacing and layer thickness. Thus, P/v values together with v values are listed in the table. These values correspond to those samples made for TEM analysis in the various studies. As listed in the table, the sizes of $Al_3(Sc,Zr)$ precipitates/dispersoids have been found either >50nm (large) or on average significantly less than 10nm (small).

Spierings et al. in (58) reported the presence of $Al_3(Sc,Zr)$ particles up to 100 nm in size in equiaxed grain region and assumed that these particles serve as the nucleation sites for the formation of equiaxed grains next to track boundaries, but further inside the track, the particles being dissolved lead to the growth of columnar grains (58). Also, Spierings et al. in (58) reported that Al_3Sc particles of <5nm size only precipitate at the low v value at 170 mm/s during LPBF (Fig. 2.17). This low v value, using the laser power (P) value of 200W corresponds to a heat input (P/v) value of 1.18 J/mm. Spierings et al. (36) point out that, for v > 200mm/s (P/v < 1 J/mm), supersaturation of Sc and Zr in Al-Mg forms instead of precipitating $Al_3(Sc,Zr)$ during LPBF solidification.

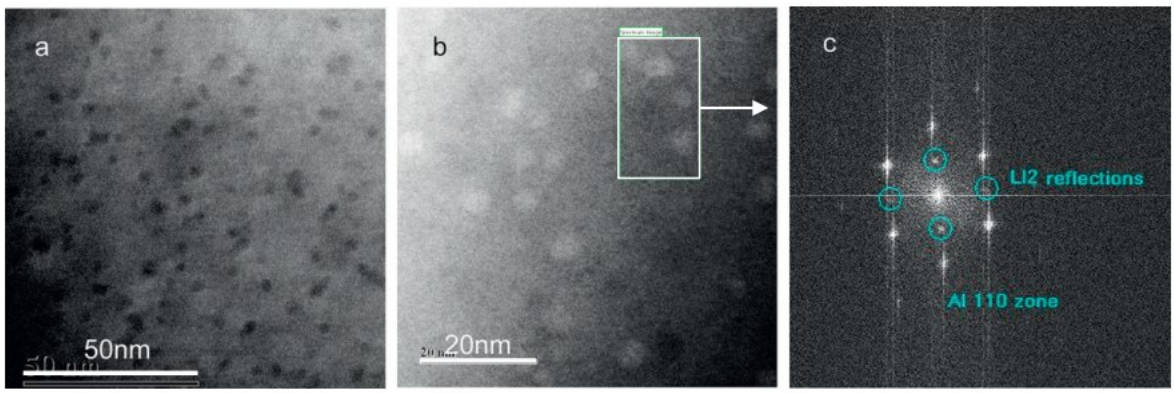

Figure 2.17. Nanostructure in equiaxed grain region of a sample made using scan speed at 170 mm/s: a) bright field STEM image, b) HR-TEM dark field image showing small <5 nm Al_3Sc particles, c) FFT image from b showing $L1_2$ reflections of Al matrix and of Al_3Sc particles (36).

The only research group reported the $Al_3(Sc,Zr)$ particles in size range of 15-20 nm is Kuo et al.'s (1), however, their TEM-SADPs do not show $Al_3(Sc,Zr)$ superstructure reflections (Fig. 2.18). Also, it has been stated in (79) that, while primary $Al_3(Sc,Zr)$ particles serve as a grain refiner and are primarily scattered within the grains, the Al_3Mg_2 and Al_6Mn precipitates are mostly distributed along the grain boundaries.

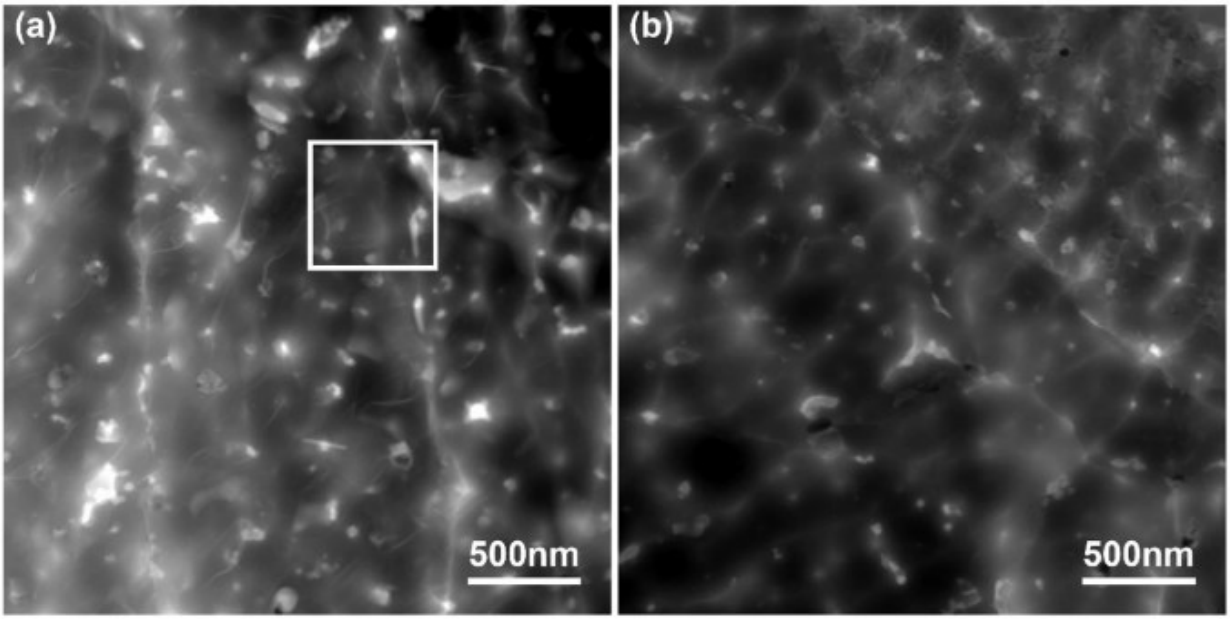

Figure 2.18. HAADF-TEM images of LPBF Al-Mg-Sc-Zr alloy: (a) in columnar grain regions and (b) in equiaxed grain regions (79).

Large Al_3(Sc,Zr) particles were also discovered in Zhang et al's (78) study utilising P/v=0.18 J/mm, whereas small Al_3(Sc,Zr) particles were not found in the as-built condition under this low heat input scenario. From Spierings et al. findings, it can be deduced that P/v<1 J/mm causes a lack of tiny Al_3(Sc,Zr) particles. Furthermore, there seems a lack of information on the partitioning Sc during LPBF, particularly relating to the mode of solidification. That the large (up to 100 nm) Al_3(Sc,Zr) particles are associated with the formation of thin equiaxed grain region next to track boundary is unnecessary, as these particles are not observed in some studies. Thus, the exact mechanism of solidification leading to the formation of bimodal microstructure appears not yet fully understood.

2.2.2 Evolution of Al_3(Sc, Zr) during heat treatment

The strengthening mechanism of Al-alloys with Sc, Zr additions is through the process precipitation hardening contributed from the formation of nano-scaled Al_3(Sc,Zr) particles. The high cooling rates used in LPBF process leave a large quantity of Sc and Zr in solid solution, which is accessible for the post-process heat- or HIP-treatment to precipitate finely dispersed, coherent Al_3Sc particles (60). Heat treatment of Scalmalloy is reported in a number of studies. In (23), (32), (85), (86), (87) it has been shown that the most appropriate regime to achieve the best combination of high strength and fracture strain is one-step heat treatment at 325°C for 4 hours after LPBF (in as-built state), without first solution treatment. This is referred to as one-step heat treatment. A one-step heat treatment can be compared to T5 heat treatment and thus termed T5 in this study. On the other hand, two-step heat treatment means the LPBF parts are solution treated normally at 540°C and then quenched, subsequently followed by aging at temperatures, for example, 300°C. The two-step heat treatment is thus T6 heat treatment.

Churyumov et al. in (80) have reported that due to the development of nanosized dispersoids, the YS and UTS dramatically increased after annealing and reached 424-438 MPa and 465-480 MPa, respectively. After two-stage annealing, the $Al_3(Sc,Zr)$ precipitates' homogeneous distribution causes a high value for the elongation. It was noted that the precipitation hardening effect for as-built Scalmalloy is quite pronounced at the temperature range 300–350°C during T5 aging treatment. The hardness increases because the precipitation of nanosized $Al_3(Sc,Zr)$ particles during aging from α-Al supersaturated solid solution occurs after LPBF. However, hardness reduction by aging at higher temperatures (than 360°C) can be explained by loss of coherency for nanosized $Al_3(Sc,Zr)$ precipitates when the particles reach their critical diameter (21.5 nm) at high temperatures (Fig. 2.19) (69).

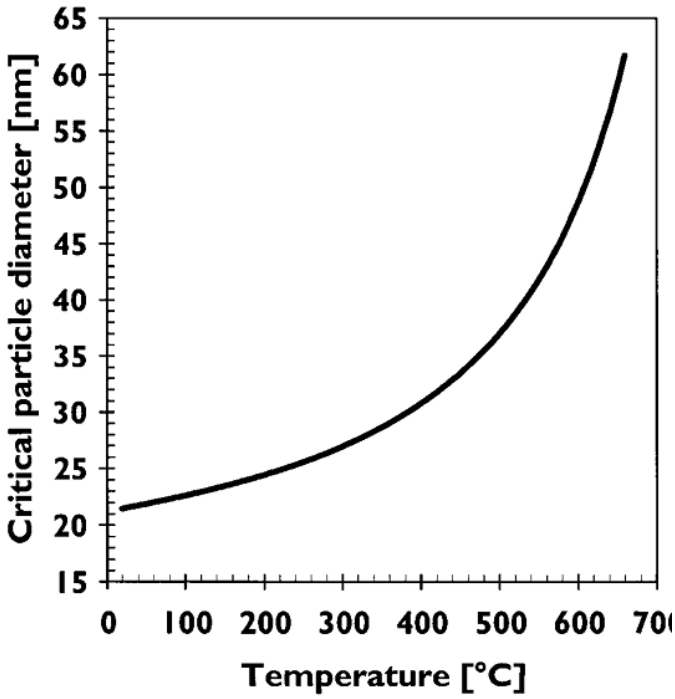

Figure 2.19. Approximately estimated critical diameter for introduction of dislocations on Al/Al_3Sc interface as a function of temperature (69).

Churyumov et al. in (80) also have reported the presence of nanosized $Al_3(Sc,Zr)$ precipices, formed in the supersaturated aluminium solid solution after one-step aging for 6h at 360 °C and two-step aging 300 °C for 3 h and then 360 °C for 4 h. The particles are predominantly on grain boundaries in the size of about 20-50 nm after one-stage annealing at 360 °C/6 h and 5-8 nm after two-stage annealing at 300 °C/3 h+360 °C/4 h (Fig. 2.20).

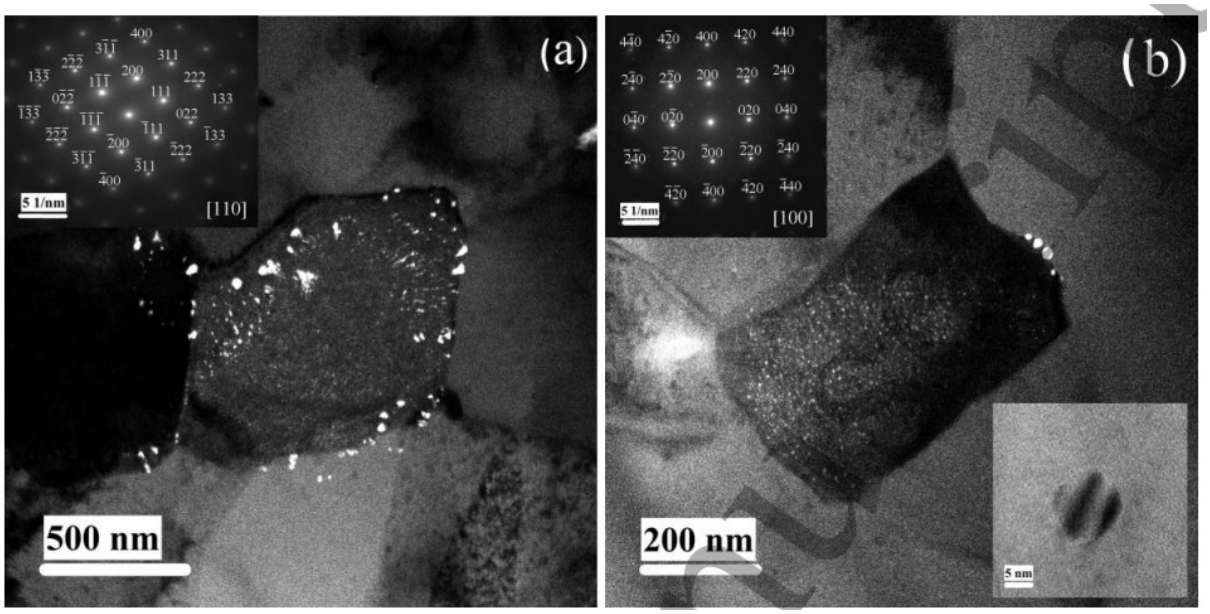

Figure 2.20. Microstructure shown in TEM (dark field) micrographs taken in samples made using P=180 W, v_s=220 mm/s, d=0.13 mm and after (a) one-stage aging (b) two-stage aging (80).

Croteau et al. (88) have shown that Al_3Zr precipitates in the alloy during T5 aging result in a ~40% increase in strength compared to the strength in as-built state. Koutny et al. (85) have compared mechanical properties after T5 (325°C/2h) heat treatment and T6 (540°C/1h with water quenching followed by 325°C/4h aging) heat treatment. Yield strength after T5 increased up to 540 MPa and after T6 up to 390 MPa. However, a significant loss in ductility after T6 is observed. The analysis of the microstructure of as-built samples and heat-treated ones has not been conducted, thus it is difficult to understand what sizes of precipitates have been achieved. Kuo et al. at (1) investigated the influence of heat treatment time on mechanical properties and precipitates behaviour and it was noted that after HT, the Al_3Sc precipitated consistently and increased (from 12.0 nm to 20.0 nm) with longer heat treatment times. Also, yield strength of LPBF Scalmalloy samples has considerably improved from 286.9 MPa to 455.8 MPa after 4 hours of aging at 325°C. Then, the yield strength decreased when the samples were aged for longer at that temperature. The size of precipitates after 4, 24 and 48 hours of aging at 325°C was stated to be 12.0 ± 0.1 nm, 18.3 ± 1.0 and 20.0 ± 0.3 correspondingly, however, SADPs have not confirmed the presence of particles (Fig. 2.21).

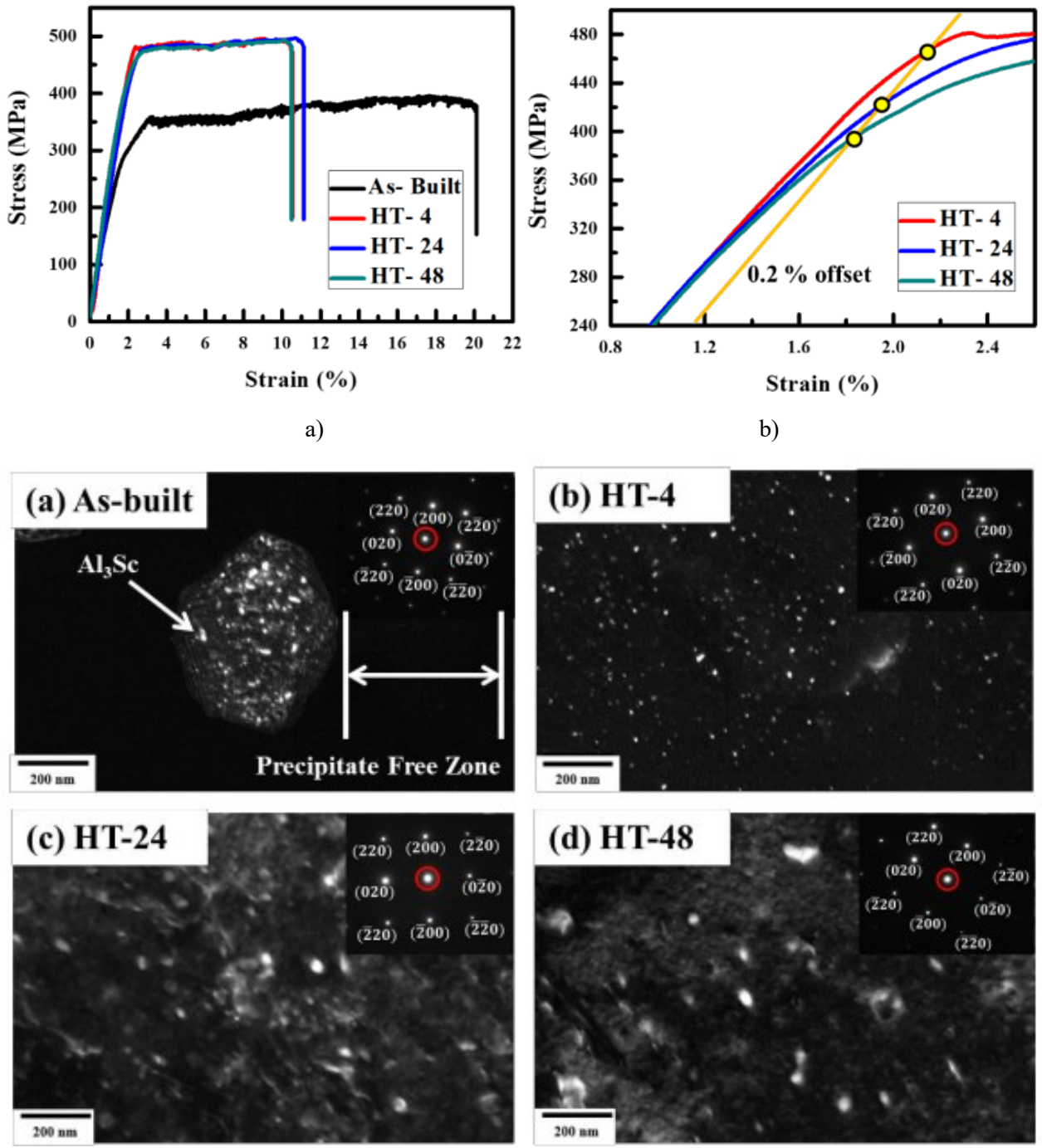

Figure 2.21. Tensile curves and TEM images with SADP: a) and b) tensile stress–strain curves of the as-built and heat-treated at 325°C for 4h (HT-4), 24h (HT-24) and 48h (HT-48) 3D-printed Scalmalloy samples, and (c) TEM images and the corresponding SADP (1).

Spierings et al. (60) suggested that due to the high cooling rates during LPBF, Sc and Zr largely remain in solid solution after solidification, and thus form precipitates during the post-LPBF heat- or HIP-treatment. The number density has increased from 0.5–1.0·10^{23} m^{-3} to values between ≈ 3·10^{23} m^{-3} and ≈ 5·10^{23} m^{-3} depending on the method of evaluation. The size of precipitates has been reported as ≈ 5nm. In a contradictory study by Shi et al. (34) involving Scalmalloy aged at 300°C for 12h, no traces of Zr- or Sc-rich particles have been found (Fig. 2.22). It has been also shown that after aging at 300°C for 12h, all samples (made with plate

temperature 35°C or 200°C, vertical or horizontal loading during tensile testing) reach almost the same tensile properties, with a yield strength of close to 460MPa.

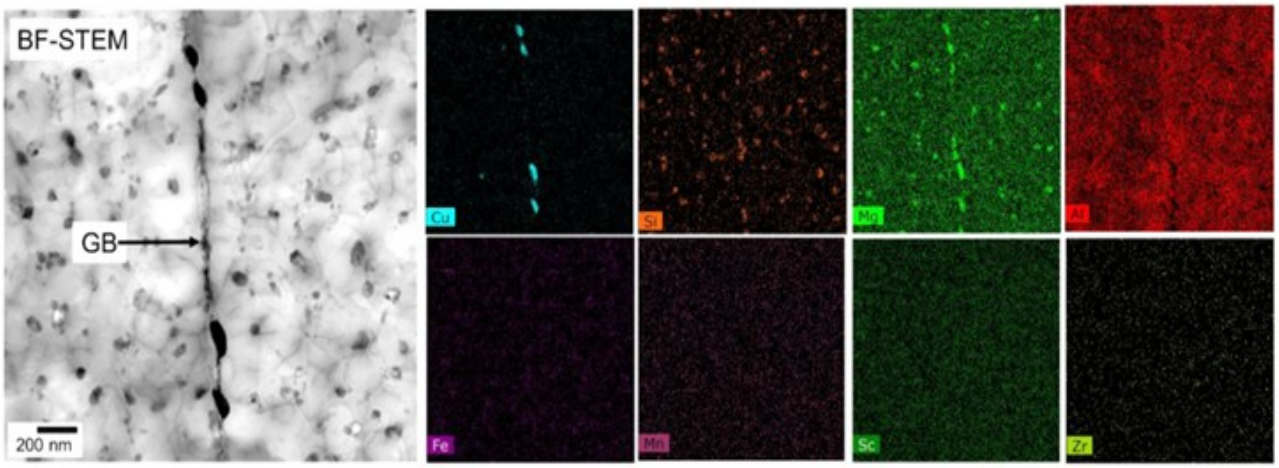

Figure 2.22. BF-STEM image of a LPBF Scalmalloy sample built using 35°C base plate and peak-aged at 300°C for 12 hours and the corresponding EDXS maps (34).

Zhao et al. in their study (89), investigated mechanical properties and the microstructure of Scalmalloy in as-built and after aging at 325°C for 4h. The UTS of about 350.14 ± 12.3 MPa and the ductility of about 25.3 ± 0.94% for as-fabricated samples, while a yield strength of up to 494.32 ± 4.16 MPa and a ductility of about 15 ± 1.27% after aging have been reported. They suggested that the increase in yield strength is from two sources, grain boundary strengthening and precipitation strengthening. After SEM and TEM analysis, numerous Al_3(Sc,Zr) particles have been found inside the grains. However, the size of these particles has not been reported.

The table below (Table 2.3) summarises studies that investigated precipitation behaviour after different heat treatments. It contains data on Mg-Sc-Zr alloys, including the composition, processing parameters, heat treatment conditions, mechanical properties and information related to the Al_3(Sc,Zr) particles, namely, their location and size. The heat treatment conditions range from 300°C to 360°C with different durations, however, the dominant regime used in most studies is aging at 325°C for 4 h. Observed particle sizes vary from particles in size of 1-3nm, 2-5nm, and <10nm to particles greater than 50nm, while some authors have reported no observed particles or have not provided sufficient evidence of their presence. The yield strength values range from 438 MPa to 500 MPa and, based on the available data, a clear correlation between particle size and mechanical properties cannot be established, as YS does not consistently increase or decrease with particle size.

Table 2.3. Information of detecting/determining $Al_3(Sc,Zr)$ precipitates/dispersoids in variousvs tudies of LPBF of Al-Mg alloys containing Sc and Zr after heat treatment.

Mg - Sc - Zr	v, mm/s	P/v, J/mm	HT Regime	In equiaxed (E) or columnar (C) grain region	YS, MPa	References
4.5-0.66-0.37	170 350	1.18 0.57	325°C4h 325°C4h	1-3nm in E 2-5nm in E		(60)
3.4-1.08-0.23	600-3000	0.62-0.07	300°C up to 12h	No particles observe	460	(34)
4.5-0.32-0.66	220	0.81	360°C4h 300°C3h+360°C4h	20-50 nm on GB (Small) <10nm in E	<438 <480	(80)
3.4-0.8-0.4	No info	No info	325°C4h	Yes, but no information on size Inside the grain	<500	(89)
4.5-0.51-0.07	500	0.40	325°C24h 325°C24h 325°C48h	They stated yes, 15-20nm but not shown in SADPs	<460	(1)

From data in Table 2.3, it has been shown in (87) that particles reached their critical size, however, the mechanical properties obtained in this research are lower than those reported in many others (36), (85), (90) even without age hardening. In (85), it has been shown that the parts after T5 heat treatment have better mechanical properties than those after T6 heat treatment. However, authors have not provided information on whether the size of precipitates after T6 (540°C/1h then 325°C/4h) can reach the size that corresponds to the maximum hardening according to the aging time-versus-hardening diagram. To summarize all the information, it can be stated that an appropriate regime of heat treatment that corresponds to the critical size and amount of precipitates, and subsequently to the maximum hardening, is still not fully clear.

2.3 Fatigue performance and failure mechanism

In this section, studies on fatigue strength and cyclic fatigue crack growth behaviour, particularly under high fatigue cycle (HFC) conditions, of Scalmalloy (or compositionally similar alloys) are reviewed. Available data on the stress-cycle life (S-N) plots will first be presented and compared. The limited data on crack growth rate (da/dN) as a function of intensity stress factor (ΔK) will then be discussed. Finally, the available studies on how LPBF defects of the alloy affect endurance limit (fatigue strength at $N \geq 10^7$ cycles), considering also threshold ΔK_{th}, are reviewed.

2.3.1 High cycle fatigue strength based on S-N data

Up to 2019, as Scalmalloy was still a new alloy, the fatigue behaviours/properties of Scalmalloy processed by LPBF had not been well studied. There had only been a few data points from fatigue testing of LPBF Scalmalloy (23), (91), from which S-N curves are not able to be drawn. Recent research endeavours have focused on conducting tests by four research groups to establish a more comprehensive set of S-N data for Scalmalloy and similar alloys. The review on this below will commence with an examination of data originating from tests carried out at an R-value of 0.1 from four separate research groups. Subsequently, a brief discussion will ensue regarding data obtained from tests conducted at an R-value of -1.

The first study of this series of investigations on S-N fatigue behaviour with a stress ratio (R) of 0.1 was undertaken by He et al. (92) (Group 1). Their chosen material, Al-5024 alloy, contained a relatively lower proportion of Sc at 0.26wt% and Zr at 0.09wt% in comparison to the composition of Scalmalloy, which contains slightly higher Sc and Zr, as shown in Table 3.1. The fatigue specimens they have tested are in the form of flat shapes, with the crack direction (CD) oriented parallel to the build direction (BD) during the LPBF process. The LPBF was conducted at a significantly higher laser energy level of 178 J/mm^3. Fatigue tests have been carried out with as-built (AB) samples, Hot Isostatic Pressing (HIP) or after two-step aging (OA2). In the HIP treatment, 100 MPa was applied at 325 °C for 4 h. In OA2 treatment, the samples were held at 300 °C for a duration of 5 min first and then quenched in water, followed by holding at 350 °C for 18 h. The experimental findings of He et al. are depicted in Figure 2.23, illustrating S-N curves alongside tensile testing data. Notably, the fatigue limit for as-built specimens has a maximum stress (σ_{max}) of 75MPa, or a stress amplitude (σ_a) of 34MPa. In contrast, specimens subjected to the HIP/aging process exhibit an improved fatigue strength, with a σ_{max} of 105MPa (σ_a=47MPa). For specimens subjected to the two-step aging treatment, the fatigue strength is equal to σ_{max}=90MPa (σ_a=41MPa).

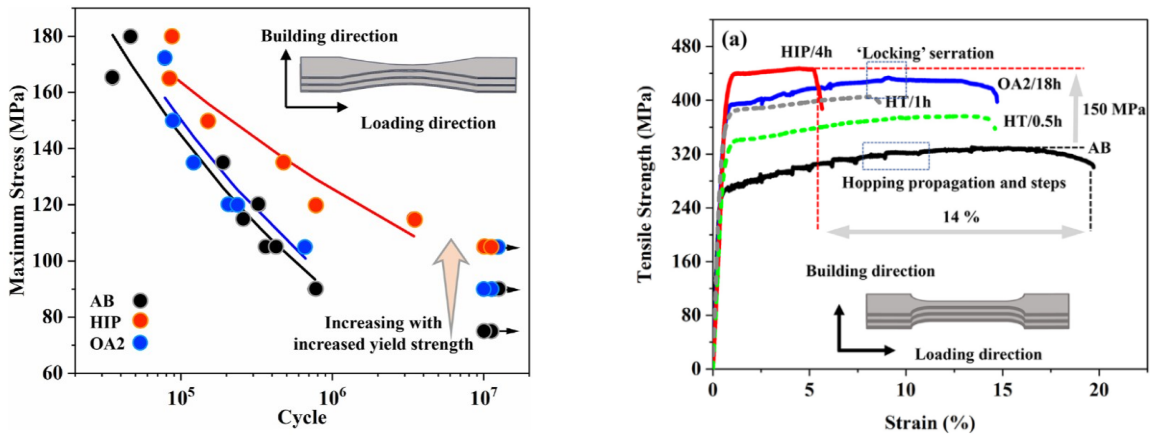

Figure 2.23. Test graphs of (a) fatigue stress-cycle tests and (b) tensile tests conducted on CD//BD flat samples by He et al. (92) with samples in three different conditions: as-built (AB), HIP/aged and two-step aging (OA2).

He et al. have noted that the enhancement in fatigue strength from as-built to two-step aged and finally to HIP/aged specimens mirrors the corresponding increase in yield strength of the LPBF alloy, transitioning from YS=236MPa, 380MPa and 414MPa respectively, as discerned from their tensile test data, as presented in Figure 2.23b. It has been widely reported that higher yield strength materials tend to have higher fatigue strength because they can better resist plastic deformation under cyclic loading and fitting relation between yield strength and fatigue strength has been found for AISI 4340 steel (Fig. 2.24) as $\sigma_w = 0.22 \times \sigma_y + 335$ (93). However, while yield strength and fatigue strength often increase together, this is not always the case as fatigue strength is heavily influenced by defects, inclusions, and surface roughness, which might not be accounted for in yield strength measurements (94).

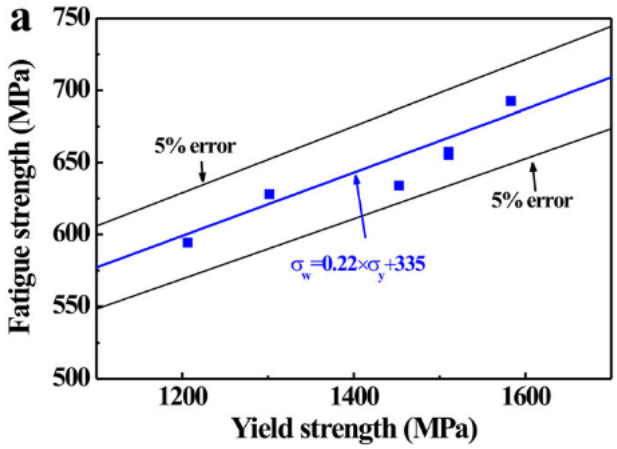

Figure 2.24. Very high-cycle fatigue strength vs. yield strength for AISI 4340 steel (93).

It is well-known that HIP is being used to achieve high densification of LPBFed parts reducing the number of defects in the material (95), leading to an increase in fatigue strength. Comparing the S-N curves, AB and aged (OA2) samples have similar fatigue strength values, but HIPed samples exhibit an enhancement in fatigue strength due to the reduced number of defects. Comparing the stress-strain curves, AB samples exhibit a significantly lower YS compared to HIP and OA2 samples. This indicates that while both HIP and aging increase YS, HIP also enhances fatigue strength by eliminating defects. Aging, however, is not able to alter the defect structure significantly, and consequently, is not able to enhance fatigue strength significantly.

In the second study of fatigue life of LPBF Scalmalloy, conducted by Qin et al. (96) (Group 2), an Al-Mg-Sc-Zr alloy with specific compositional proportions (4.74% Mg, 0.7% Sc, and 0.32% Zr) was studied. LPBF process was conducted with the following parameters: Laser Power = 370W, scan speed = 1000 mm/s, layer thickness = 30 µm, and hatch space = 0.12 mm, thereby an energy level is E_v = 103 Jmm^3. Subsequently, cylindrical samples are built in two distinct orientations: CD//BD and CD⊥BD. Samples are then aged at 325°C for 4 hours. Their fatigue and tensile data are presented in Fig. 2.25. Their tensile data show the typical aging response of the alloy and their fatigue data demonstrate a strong build orientation effect, with CD//BD samples showing higher (100MPa vs. 57MPa) fatigue strength at 10^7 cycles than CD⊥BD samples. It's worth noting the fatigue data in Fig. 2.25 are highly scattered, with the same fatigue life having stress amplitudes differing

by over 30% of magnitude. This reflects very high variability in material behaviour, which is not accounted for in the original work. Discrepancies of this type can be indicative of microstructural variability or process-introduced defects.

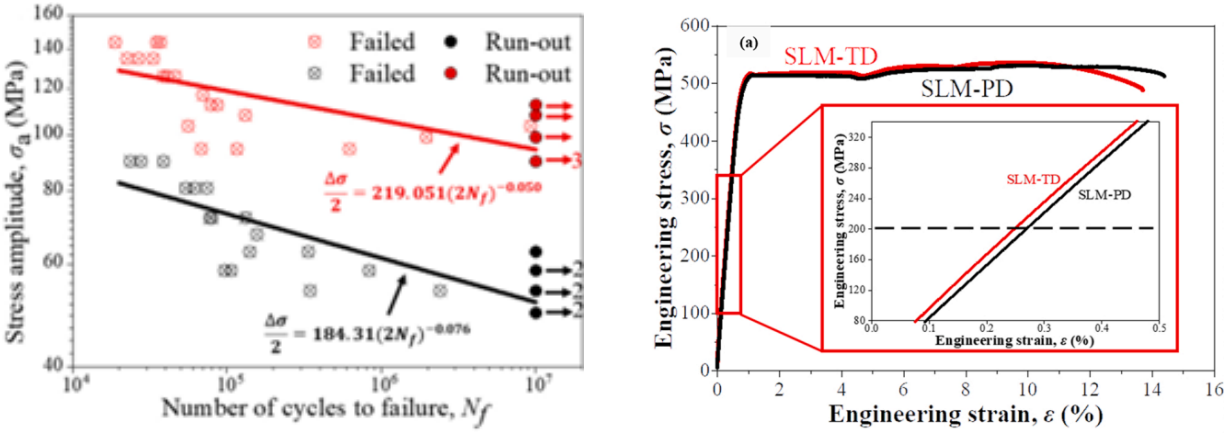

a. b)

Figure 2.25. (a) S–N data/curves (b) representative stress–strain curve from Qin et al. (96), where TD=CD//BD.

Although Qin et al. did not HIP their samples, for CD//BD samples, fatigue strength (σ_a=100MPa) from Qin et al. is significantly higher than that (from σ_a=41MPa) of the two-step aging samples from He et al. (Fig. 2.23). The reason for this difference is possibly due to the flat shape of the samples, which could lead to higher stress concentrations and reduced resistance to fatigue. Unlike cylindrical specimens, flat samples often have sharp edges or machined surfaces, which act as stress concentrators where fatigue cracks can initiate more easily. It has been shown by (97) that stress concentration near notches and edges reduces fatigue strength significantly because these locations experience localized stress peaks. Wen-Jie et al. (98) conducted the comparison fatigue tests on samples made of low carbon steel but in different shapes – thin-plate and sandglass shapes. It has been demonstrated that thin plate specimens have much lower fatigue strength compared to specimens in sandglass shapes (Fig. 2.26).

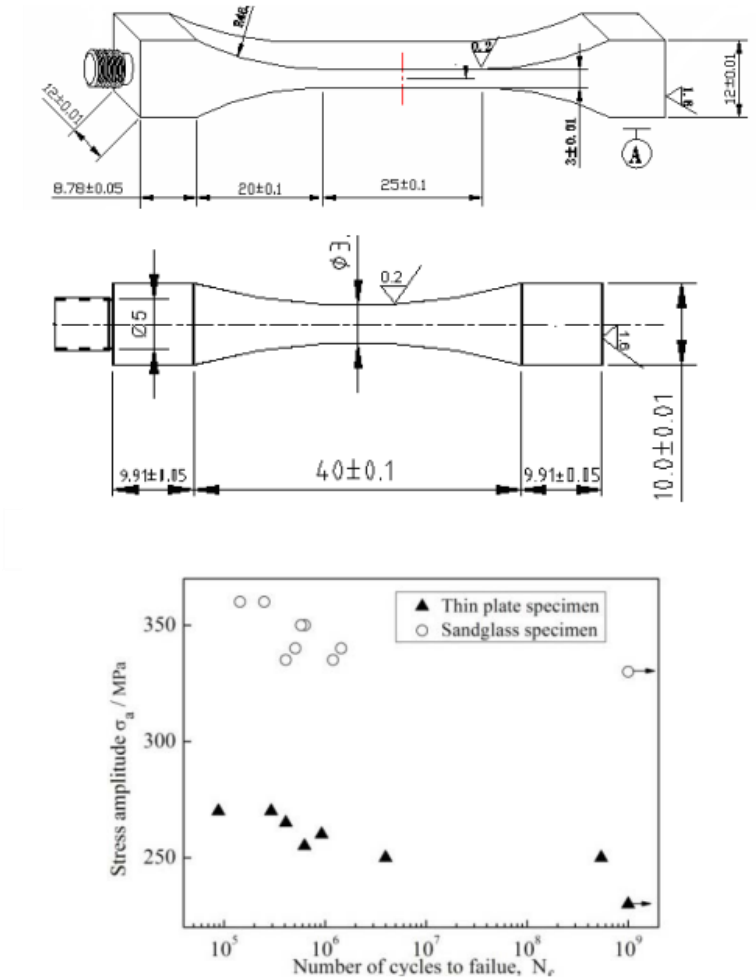

Figure 2.26. Fatigue test results for thin-plate and sandglass specimens (98).

In the second study, Qin et al. (99) (Group 2) further investigate the effect of HIP (100MPa at 325°C for 4 hours) on the fatigue strength of the CD⊥BD samples. Fig. 2.27 shows their tensile and fatigue data. The results showed that YS remains at a similar value after HT (DA) and HIP and is equal to 509.6±1.4 and 510.9±0.2, respectively. However, fatigue strength σ_a has changed dramatically and is 99.8 MPa after HIP compared to 57 MPa after Direct Aging. Clearly, HIP treatment has considerably increased the fatigue strength but this increase is not because of the difference in yield strength, as the yield strength values for the HIP samples are largely the same as the non-HIP samples. This finding is contradictory to what He et al. may have suggested on the effect of yield strength on fatigue strength. Also, it must be noted that the data points show significant scatter and at the same stress amplitude, different specimens fail at significantly different cycle counts. The authors have not provided the information on defect sizes for all specimens tested, however it can be suggested that the scatter is caused by variability in material defects.

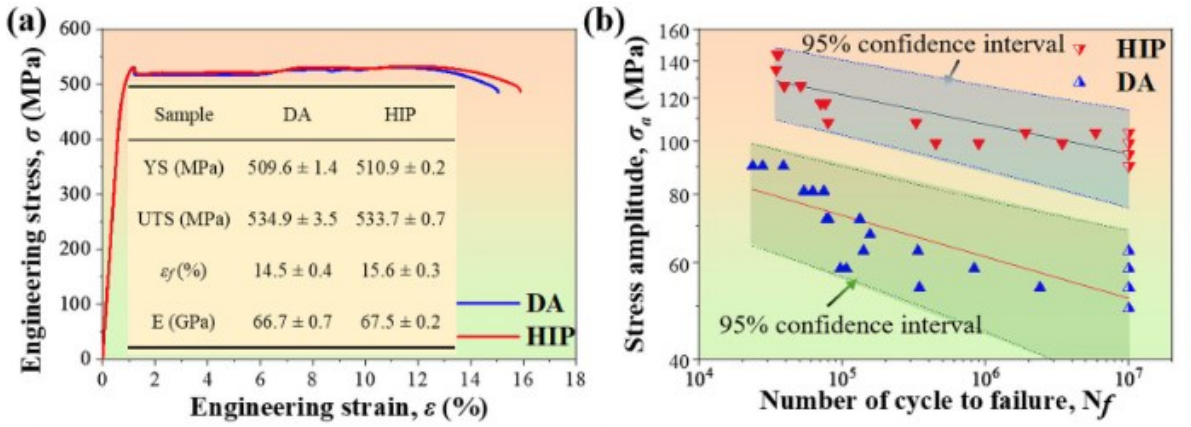

Figure 2.27. Mechanical properties of LPBF Scalmalloy either after aging or HIP shown in Qin et al.'s study: (a) engineering stress-strain curves and (b) S-N curves (99).

Raab et al. (100) (Group 3 for the 3rd series of the study) studied the fatigue behaviour of Scalmalloy, containing 0.78% Sc and 0.27% Zr produced by LPBF. They investigated four different surface conditions: the as-built state (with contour scan), as-hatched (without contour scan), chemically milled, and mechanically milled, as shown in Figure 2.28 (a) with fatigue test results are presented in Figure 2.28 (b). All tested samples have been heat-treated and HIPed. The HT has been conducted at a temperature of 325°C for 2 hours and HIP has been performed at the same temperature, but under a pressure of 1000 bar, with the intent of mitigating the potential influence of internal porosity on fatigue fracture behaviour.

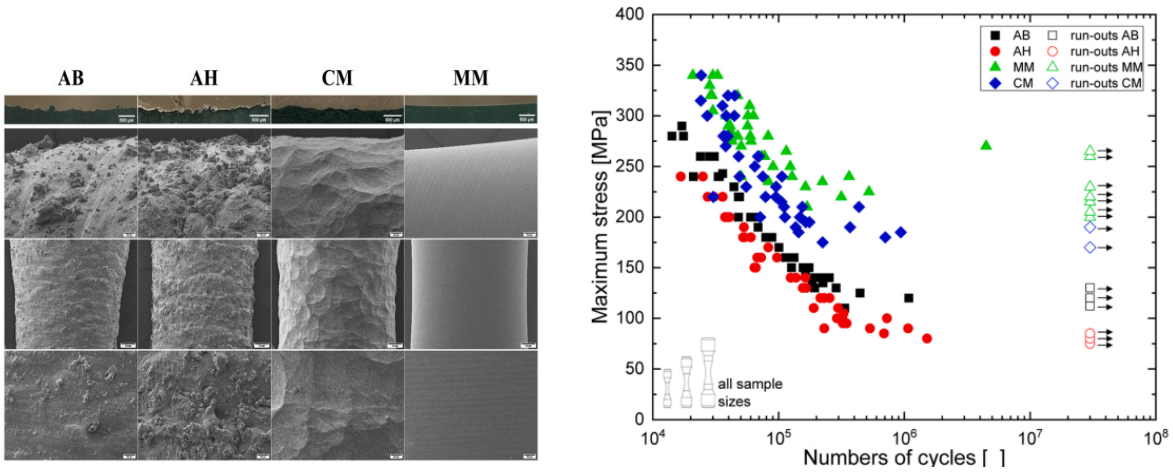

a) b)

Figure 2.28. a) surface conditions of samples b) S-N-curves for all surface modifications (100).

Four surface modifications have ranked in the following order, from the lowest to the highest fatigue strength (σ_{max}): as-hatched (AH, 85 MPa) < as-built (AB, 130 MPa) < chemically milled (CM, 170 MPa) < mechanically milled (MM, 265 MPa). The fatigue strength value attained for HIP-conditioned samples presented in (96), reported as 105 MPa, is in agreement with the fatigue strength value of 130 MPa for as-built samples with contour scan reported in (100).

Schimbäck et al. (group 4) in (101) and (102) investigated fatigue behaviour of samples produced from 4.5Mg-0.75Sc 0.35Zr-0.45Mn aluminium alloy and printed in a vertical direction. In these studies, two melting modes were compared – HC (heat conduction) mode and KH (keyhole/deep-penetration) mode by using two different laser spot sizes, with: P_L = 370W, v_s = 1000 mm/s, d_h = 100 µm and t_P = 30 µm. After the printing process, subsequent heat treatments for both tensile test and fatigue test samples at 325 °C/4 h without pressure (HT) and with pressure at 200 MPa (HIP) have been performed. The results of tensile tests are illustrated in Figure 2.29. In the HT state, a discrepancy between the HC and T modes is noticeable: the HC mode exhibits slightly higher strength but reduced ductility in comparison to the T mode. This trend persists even in the HIP-treated specimens, wherein the HC mode specimens experience superior mechanical properties with a yield strength of 519 MPa and an ultimate tensile strength of 524 MPa. From data presented, upper and lower yield strength can be observed showing the transition from the elastic to the plastic regime. It has been suggested that there is a correlation between yield-point phenomenon and grain size as it has been widely reported (103), (104).

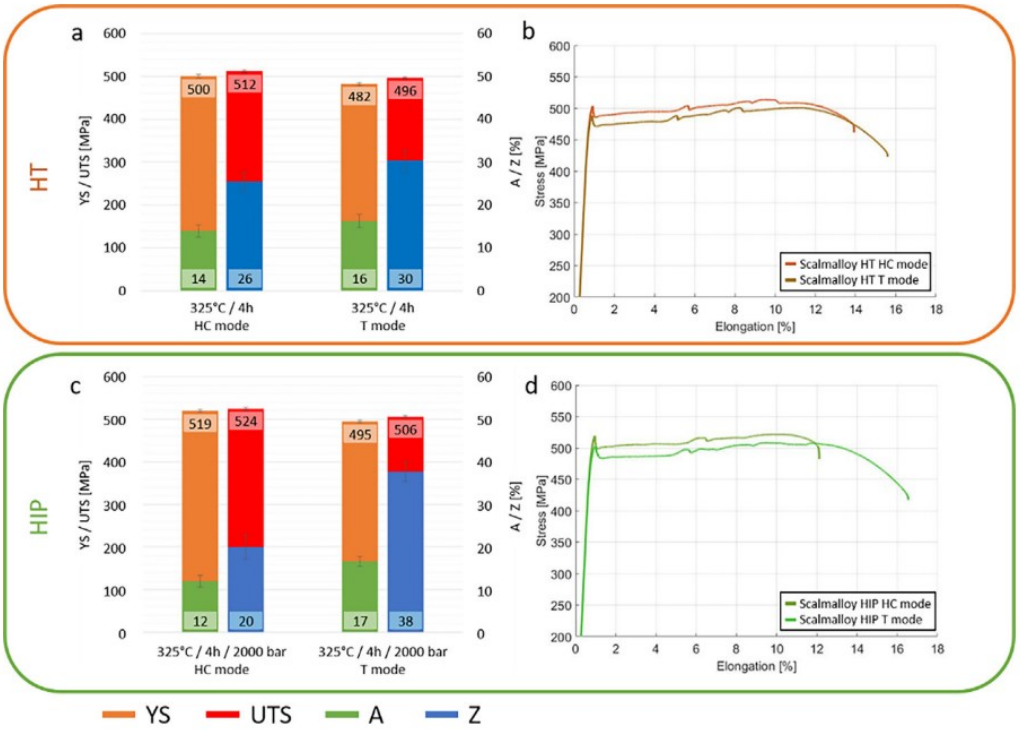

Figure 2.29. Tensile properties of LPBF Scalmalloy specimens with (a,c) data, (b,d) tensile curves (101).

For the high-cycle fatigue experiments, the findings are presented in Figure 2.30. S-N curves exhibit significant scatter, especially in the T mode HIP condition, where T_F3 sample possesses a notably lower fatigue limit around 230 MPa, whereas the T_F4 and the T_F3* samples under the same condition possess extremely high fatigue strengths of 350 MPa and 340 MPa, respectively. For the HC mode, the data are not adequate to establish a distinct fatigue limit because no samples survived the run-out. Also, HC_F4 sample (HIP in the HC mode) has failed at 2×10^5 cycles under 300 MPa, while the HC_F5 and the HC_F7 samples (also HIP in the HC mode) have failed after approximately 2×10^5 cycles under lower stress levels.

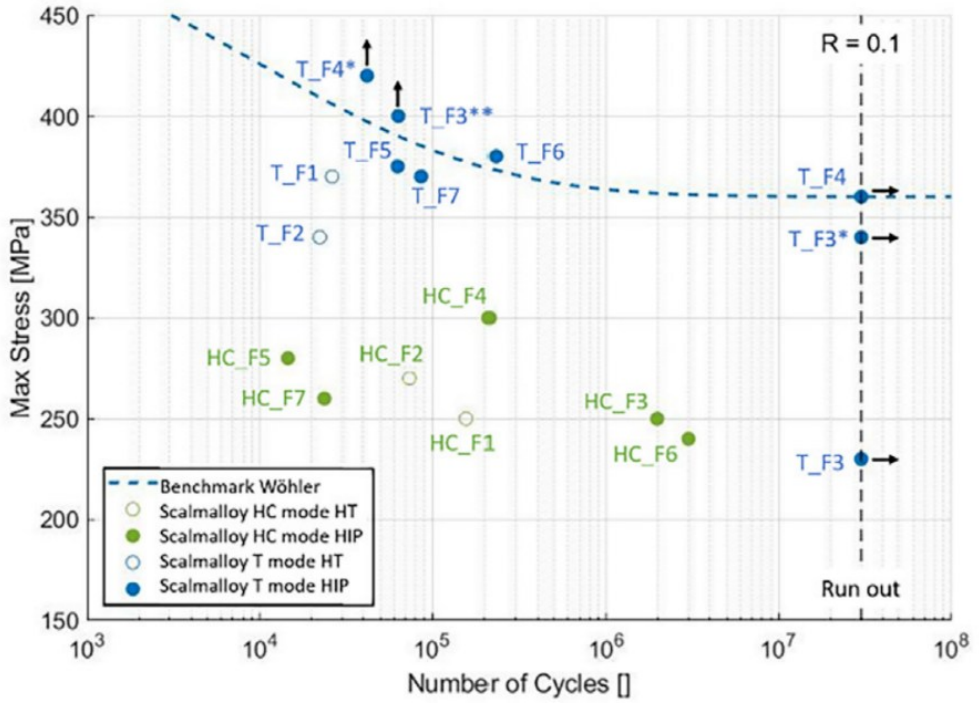

Figure 2.30. S-N plot for samples made using either HC mode or T mode and aged at 325 °C for 4 hours, either for HT only or for HIP (101).

Thus, the non-uniform trend of S-N curves indicates that the fatigue data do not follow the normal S-N behaviour (Fig. 1.11), where lower stress levels correspond to longer fatigue life and might be caused by the presence of local defects. Although HC mode fatigue specimens show a comparably high amount of scatters, it can be seen that samples produced in T mode have higher fatigue strength than those produced in HC mode. Also, a clear statement of the effectiveness of HIP treatment compared to HT on the fatigue strength cannot be made, as the number of specimens is not sufficient.

Table 2.4 presents a summarized compilation of fatigue data for Scalmalloy produced by LPBF at R=0.1, as reported in various research studies reviewed in detail above. Conditions include the information on build direction either vertical (V), where CD⊥BD, or horizontal (H), where CD//BD, heat treatment condition, surface condition for research by Raab & Bambach (100), and printing mode for research by Schimbäck et al. (101), (102). The corresponding fatigue strength is presented as strength amplitude (σ_a) or maximum strength (σ_{max}) at $N \geq 10^7$ cycles, as different studies reported their results using one of these conventions, thus converting either one of these ensures consistency. This summarized data provides a clear comparison of fatigue performance across different studies on LPBFed Scalmalloy.

Table 2.4. Summary of previous studies on fatigue behaviour of Scalmalloy (R=0.1).

Authors	Conditions	σ_a (10^7), MPa	σ_{max}(10^7), MPa
He et al., 2021 (92)	H & As-built (AB)	34	76
	H & HIP+aged, 100MPa, 325°C-4hrs (HIP)	47	104
	H & Age, 300°C-5mins+350°C-18hrs (OA2)	41	91
Qin et al., 2022,2022 (96), (99)	V & Age, 325°C-4hrs (TD)	57	126
	H & Age, 325°C-4hrs (PD or DA)	101	224
	V & HIP+Age, 100MPa, 325°C-4hrs (HIP)	100	222
Raab & Bambach, 2023 (100)	V, AH, Aged, 325°C-2hrs & 325°C-2hrs-100MPa (AH)	38	84
	V, AB, Aged, 325°C-2hrs & 325°C-2hrs-100MPa (AB)	59	131
	V, Ch-M, Aged, 325°C-2hrs & 325°C-2hrs-100MPa (CM)	77	171
	V, M-M, Aged, 325°C-2hrs & 325°C-2hrs-100MPa (MM)	119	264
Schimbäck et al., 2022, 2023 (101), (102)	V, HC & Aged, 325°C-4hrs (HC_F)	-	
	V, T & Aged, 325°C-4hrs (T_F)	-	
	V, HC & HIP+aged, 200MPa, 325°C-4hrs (HC_F)	90	200
	V, T & HIP+aged, 200MPa, 325°C-4hrs (T_F)	162	360

From Table 2.4, it can be noticed that studies are in agreement that fatigue strength significantly increases after HIP treatment compared to the as-built or heat-treated condition (He et al. (92) and Qin et al. (99)). However, magnitude of fatigue strength across all studies is pronounced and may vary significantly even for the samples with the same build directions and undergone the same treatment, for example, σ_{max} = 222 MPa from Qin et al. research (99) for vertically built samples after HIP, when in Schimbäck et al. study σ_{max} = 360 MPa (102) for the same build direction and treatment condition. Also, there is limited data for comparison of vertical and horizontal build directions and there is only one study comparing build direction effect (Qin et al. (96)), however, the authors have not provided the reasonable explanation of such pronounced difference between two build directions (σ_{max}=126 MPa for vertically built samples and σ_{max}=224 MPa for horizontally built samples), which creates uncertainty about comparison between horizontal and vertical orientations. Although there is a considerable variation in fatigue strength values, some studies have comparable results, such as the fatigue strength values obtained for HIPed samples in (96), which is 105 MPa, and the fatigue strength for as-built samples from (100), which is 130 MPa.

Other groups of researchers reported fatigue properties for Scalmalloy at R= -1. Although fatigue test results at R = 0.1 and R = -1 cannot be compared directly because they represent different loading conditions that significantly affect fatigue life, crack initiation, and growth behaviour, it provides a more comprehensive understanding of a material's fatigue behaviour. Stress ration R = 0.1 results in a positive mean stress $\sigma_m = \frac{\sigma_{max}+\sigma_{min}}{2}$ and the tensile loading is predominant, while R = -1 results in a fully reversed loading with zero mean stress. The increased mean stress at R = 0.1 reduces the fatigue life by speeding up the crack propagation, and for R = -1 the fully reversed loading increases the fatigue strength (105).

Muhammad et al. (106) compared fatigue strength of Al alloys, including Scalmalloy, with as-built surface and after machining (Fig. 2.31). The Scalmalloy processed using LPBF demonstrated significantly superior fatigue resistance when compared to other alloys, regardless of whether they were in their as-built or machined surface states. Additionally, it was observed that the fatigue stress amplitude (σ_a) for the machined surface Scalmalloy was approximately three times higher than that of the as-built surface, measuring 150 MPa compared to 50 MPa. This finding is in agreement with findings from Raab & Bambach, 2023 (100), where σ_a for as-built and machined samples are 59 MPa and 119 MPa, respectively, confirming the high dependency of fatigue strength from the surface roughness.

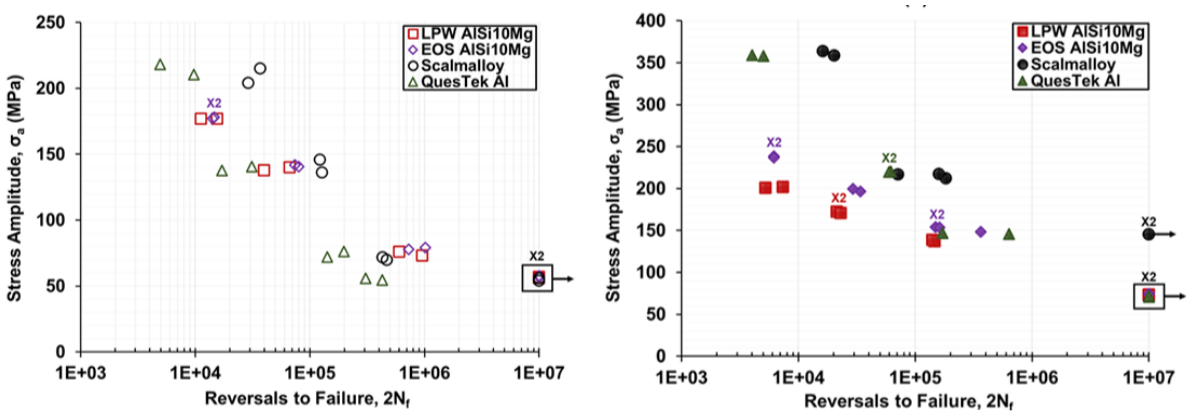

a) b)

Figure 2.31. S-N data of LPBF Al specimens in a) as-built and b) machined surface condition (106).

Study from Nezhadfar et al. (107) investigated the influence of build orientation on the fatigue properties of Al alloys, including Scalmalloy (Fig. 2.32). Scalmalloy specimens have been fabricated both vertically (CD⊥BD) and horizontally (CD//BD) and have been subjected to heat treatment at 325°C for a duration of 4 hours.

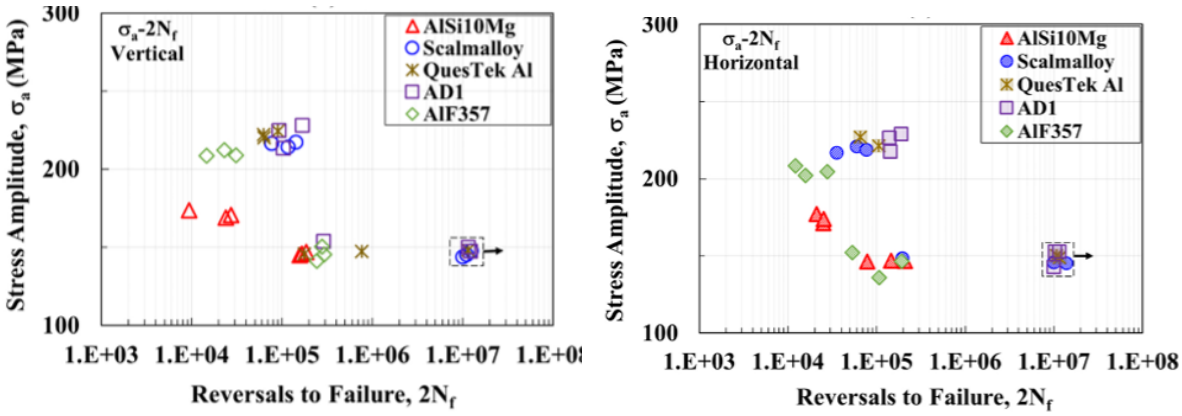

a) b)

Figure 2.32. Stress-life fatigue behaviour of a) vertical and b) horizontal LB-PBF Al specimens (107).

The results have revealed that Scalmalloy exhibits anisotropic behaviour in terms of fatigue strength, with both vertical and horizontal samples showing fatigue stress amplitudes of approximately 140 MPa, which is contradictory to what Qin et. al (96) have observed for their aged Scalmalloy samples tested at R=0.1. Moreover, scatter in fatigue life data is a key observation in both studies, but Qin et al. study has a much greater degree of variability in their fatigue results, with stress amplitudes varying by more than 30% for the same fatigue life.

Schneller et al. (108) investigated the influence of different heat treatments on fatigue properties. In this study, three groups of samples have been compared: base condition (BC) without post-process treatment, heat-treated (HT) at 300°C for 4 hours and HIP treated (HIP) at 300°C for 4 hours at 100 MPa. The comparison can be seen in Figure 2.33 below:

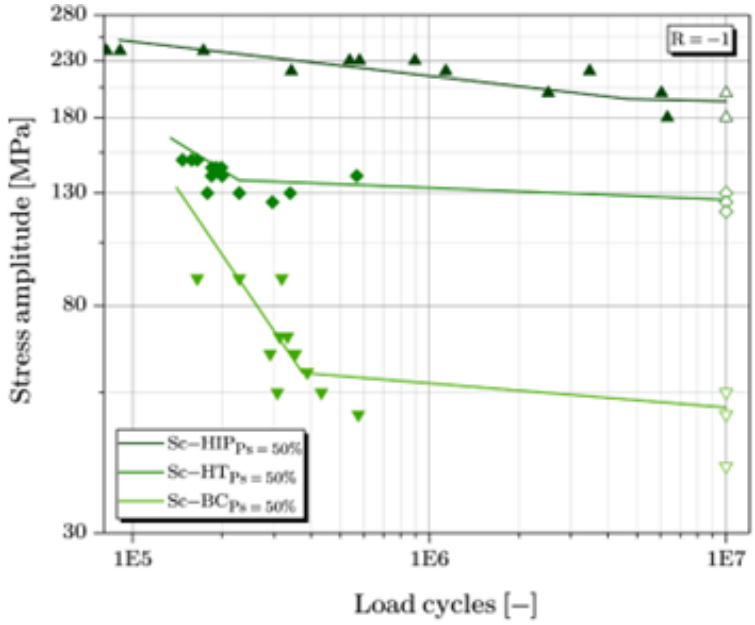

Figure 2.33. S-N curves for Scalmalloy tested at R=-1 (108).

It has been demonstrated that an improvement of fatigue performance by heat treatment is observed for Scalmalloy (+245%) and an increase of fatigue strength by applying HIP treatment to Scalmalloy is 374% compared to the base condition. The increase of fatigue strength after heat treatment or HIP is contradictory to what He et al. (92) observed in their study, where aged and HIPed samples experience increase of fatigue strength at 20% and 38% correspondingly.

Thus, the literature review on fatigue S-N curves for LPBFed Scalmalloy shows the significant variability in fatigue performance across different studies, demonstrating the strong influence of different factors such as heat treatment, build orientation, surface condition, and sample geometry. However, the high scatter in fatigue data across studies suggests that process-induced defects and microstructural heterogeneity play a significant role in fatigue failure.

2.3.2 Fatigue crack growth and threshold stress intensity factor

While there exists a substantial body of research showcasing S-N curves for LPBFed Scalmalloy, there is, as far as the author is aware, only a single study by Schimback et al. (102) currently available that provides da/dN versus ΔK curves. Also, it should be noted that the work of Schimback et al. was published two years after the FCG data presented in the current thesis had been published. In the investigation conducted by Schimback et al. (102), specimens of Scalmalloy were fabricated vertically (CD⊥LD) using LPBF and underwent HIP treatment at 325 °C/ 4h / 200 MPa. Testing was conducted at R ratios of 0.1 and 0.7. The resulting da/dN versus ΔK curves are presented in Figure 2.34.

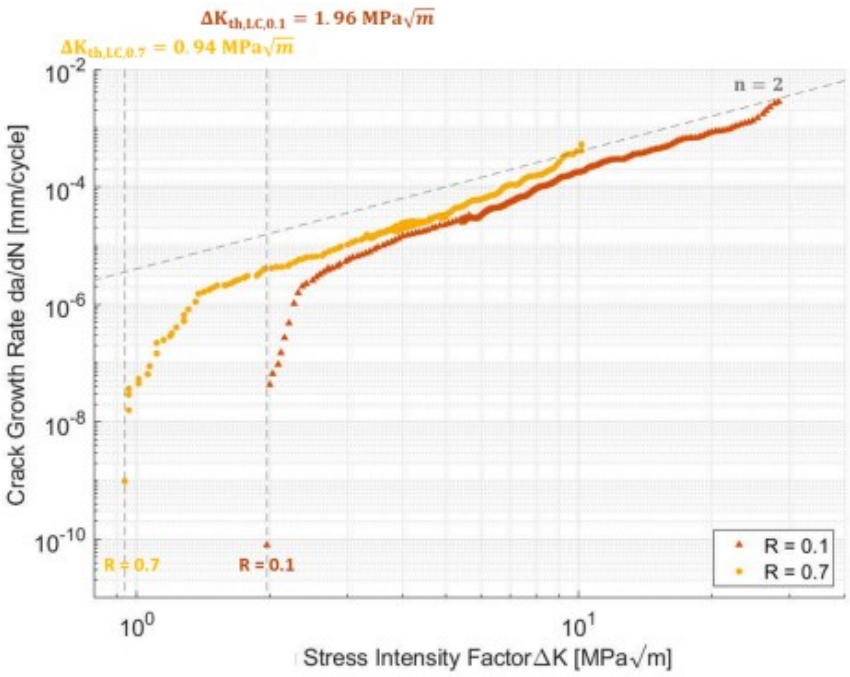

Figure 2.34. FCG data of Scalmalloy processed using LPBF (102).

Analysing the information presented in Figure 2.34, the author derived a Paris exponent (m) of approximately 2 (from the Paris-relation, Equation 6), which remains consistent regardless of the stress ratio applied. Additionally, the long crack threshold values for the stress intensity factor range (ΔK_{th}) exhibit a strong correlation with the applied stress ratio. Specifically, ΔK_{th} is equal to 2 MPa$\sqrt{m}$ for R = 0.1, while ΔK_{th} is 0.9 MPa$\sqrt{m}$ for R = 0.7. However, a closer look at the methodology makes these findings questionable. The authors loaded the specimens starting from ΔK = 0.5MPa$\sqrt{m}$, increasing the load step-wise by an increment of 0.2 MPa$\sqrt{m}$, while FCG tests as per ASTM E 647 should be conducted at K-decreasing mode first. This procedure starts by applying cyclic loading at a ΔK level equal to or greater than the ΔK value at the final stage of pre-cracking. Then, as the crack size increases, the cyclic load decreases until the low crack growth rate of interest is achieved. Once da/dN is close to 10^{-7} mm/cycle, K-increasing mode starts until the samples fracture. Also, the deviation from the classic fatigue crack growth models (Fig. 1.13) is observed as Paris Law Region is not linear for both curves with R=0.1 and R=0.7. Additionally, single data points for R = 0.1 and R = 0.7 at very low crack growth rates must be noted, which suggest limited data availability in the threshold regime.

Also, the crack growth path and crack closure mechanisms are presented in Figure 2.35. The crack closure effect refers to the phenomenon where the crack faces come into contact during part of the loading cycle, reducing the effective stress intensity factor (ΔK_{eff}) that drives crack propagation. Crack closure is caused by a number of mechanisms. Three are important: plasticity-induced, roughness-induced and oxide-induced (109). The microstructural features give rise to variations in crack path, which cause increased contact between the crack faces and hence lower the effective stress intensity at the crack tip. This mechanism is particularly critical in the regime around the ΔK_{th}, in which it can cause a drop in crack growth rate by enhancing crack resistance against opening and growth. It has also been shown that larger grains produce a rougher crack surface, which is conducive to crack closure, and thereby influences the effective crack propagation threshold (109). At lower R-ratios, significant crack closure occurs, increasing ΔK_{eff} required to propagate the crack, while higher R values (closer to 1) lead to reduced crack closure effect (110).

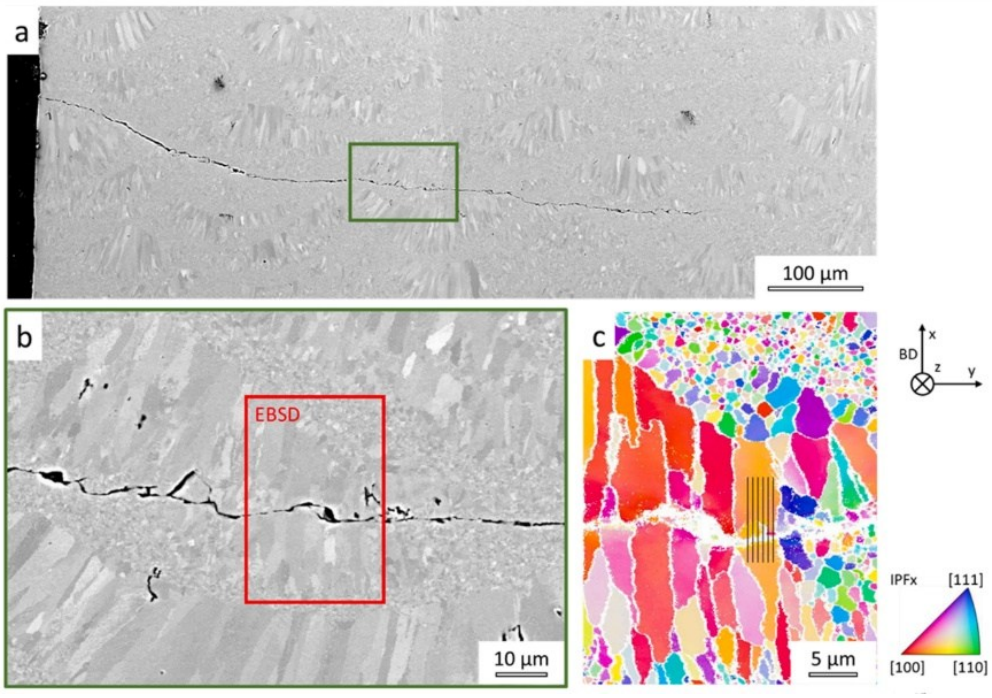

Figure 2.35. Crack path in a FCG tested sample of LPBF processed Scalmalloy: a, b) low and higher magnification SEM images and c) EBSD orientation map (102).

In the study conducted by Schimback et al. (102), the microstructure consists of fine grains, thus, the buildup of crack closure caused by roughness is greatly reduced. This results in a lower ΔK_{th} compared to materials with larger grains. However, coarse-grained areas play a big role in how cracks grow because they mainly contribute to roughness-induced crack closure. Interestingly, it has been noted that the crack path includes both coarse- and fine-grained regions without preference.

2.3.3 LPBF defects and the Kitagashi-Takahashi diagram

The fatigue behaviour was determined to be independent of the sample size but influenced by the size of fracture-inducing defects. The fractographic analysis presented in (100) revealed that AB and AH samples failed due to defects present on the rough, as-built, untreated surface. These defects included notches in roughness valleys situated near particles and irregularities in the melt surface (Fig. 2.36(a)). In comparison, CM samples primarily failed at semicircular etch pits, whereas MM samples experienced failure due to small surface defects, such as lack-of-fusion (LOF) defects, oxide inclusions, and inconsistencies in the material and microstructure (Fig. 2.36(b)). It has been widely reported that if defects are present in the surface and sub-surface regions, these defects affect fatigue strength considerably more than those presented away from the surface (42), (111).

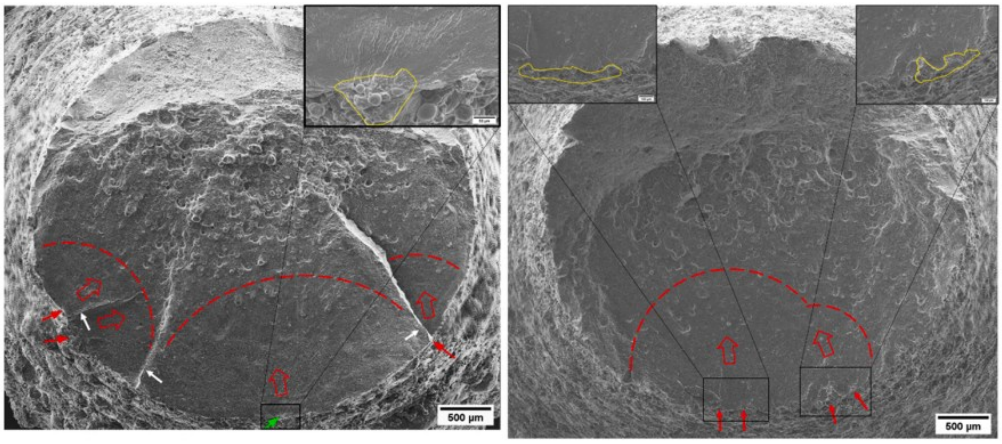

a)

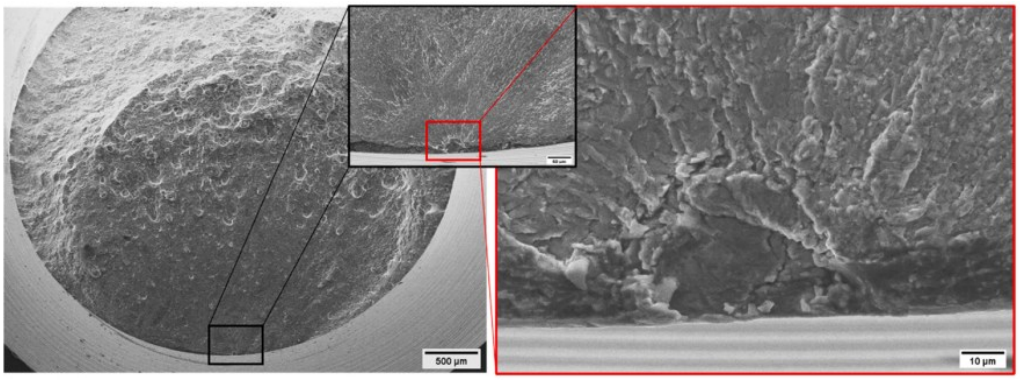

b)

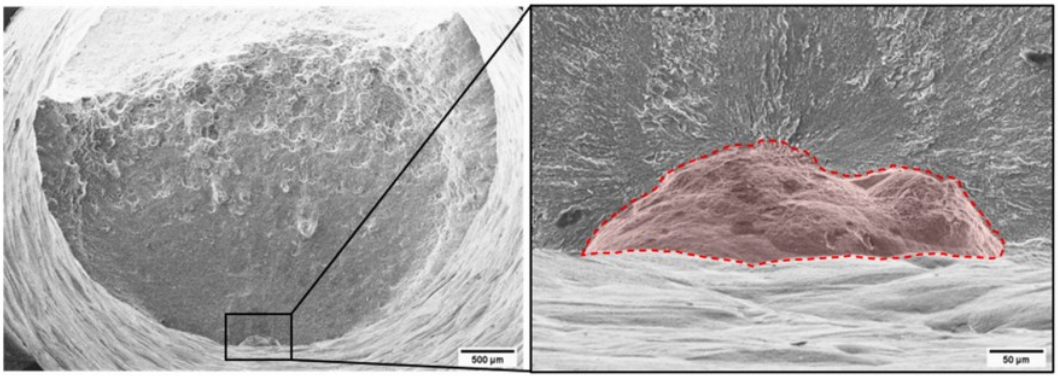

c)

Figure 2.36. SEM images showing crack initiation sites for conditions: a) AB (left) and AH (right), b) MM, c) CM (100).

Fractographic analysis from (100) shows that AB and AH samples tend to have multiple fracture initiation sites, while CM and MM samples typically fail due to a single defect initiating the fracture. Among CM and MM samples, the size of these defects plays an important role in determining fatigue performance. To describe the influence of defect size, the El-Haddad parameter is used through Murakami's √area (square root of defect size) parameter.

$$\sqrt{area_0} = \frac{1}{\pi}\left(\frac{\Delta K_{th}}{Y\,\Delta\sigma_{w0}}\right)^2, \qquad \text{Equation 8}$$

where $\Delta\sigma_{w0}$ is the fatigue strength of defect-free and machined samples. Thus, the following approximation relating fatigue strength to defect size was derived in (100):

$$\Delta\sigma_w = \frac{1.42(H_V+120)}{(\sqrt{area})^{1/6}} \quad \text{Equation 9}$$

The El-Haddad model describes the fatigue strengths (run-outs) of all four surface states presented in the study (Fig. 2.37). However, it should be noted that some data points are not close to the curve.

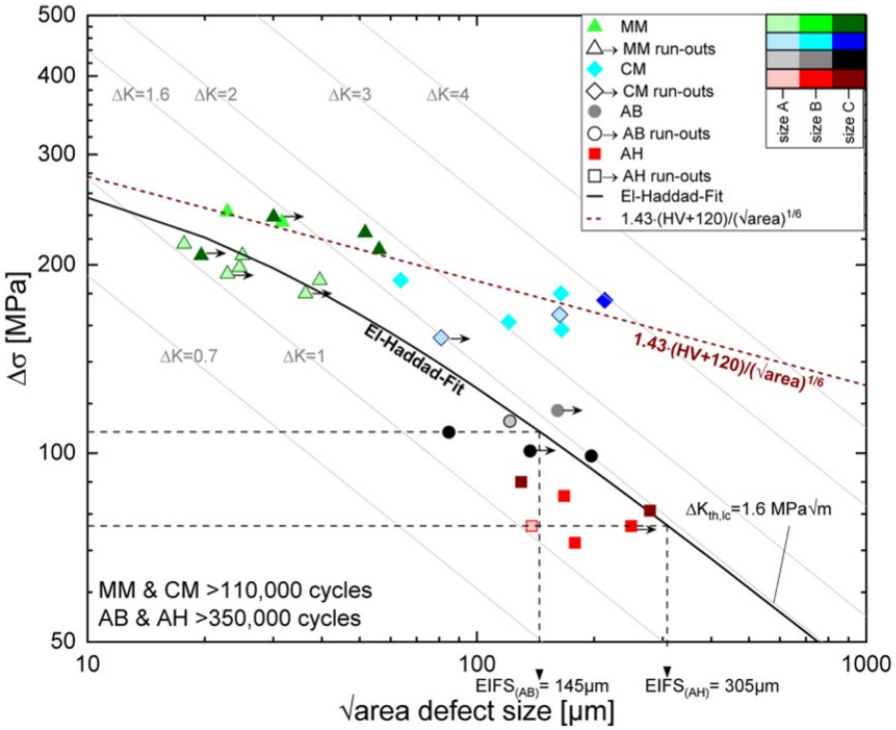

Figure 2.37. Kitagawa-Takahashi diagram for samples in AB, AH, CM and MM conditions investigated in (100).

In Qin et al. study (96), it has been shown that the fatigue properties of the Al-Mg-Sc-Zr alloy fabricated using LPBF exhibited anisotropy and it should be noted that nearly half of the CD//BD samples did not fit the relationship between defect size and fatigue limit (Fig. 2.38) as predicted by the traditional Kitagawa-Takahashi diagram that is:

$$\Delta K_{th} = \Delta\sigma F_w \sqrt{\pi\sqrt{area}}, \quad \text{Equation 10}$$

Where F_w is a geometric factor the value of which is dependent on the defect location (0.5 for internal, 0.65 for surface), σ is the stress amplitude, and √area is Murakami's parameter, whose value approximates the equivalent radius of defects (d/2) (112). This suggests that factors other than the presence of defects alone contribute to the observed anisotropic fatigue performance.

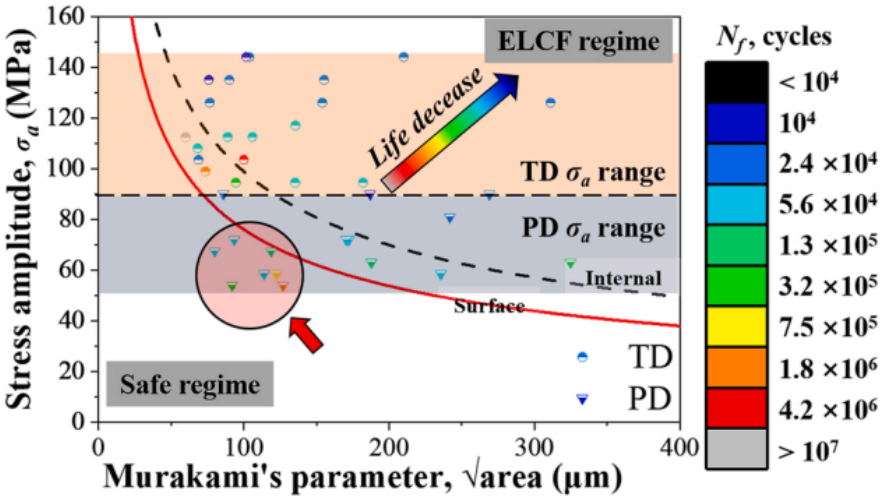

Figure 2.38. Stress amplitude as a function of Murakami's parameter for LPBF Scalmalloy (96).

Figure 2.39 (96) illustrates the typical fracture surfaces for samples after cyclic loading, the fractographs have been done for both PD (parallelly deposited, CD//BD) and TD (transversely deposited, CD⊥BD) samples. The fatigue fracture surfaces of these samples can be divided into three areas: crack initiation, crack propagation, and fast fracture. Cracks consistently originate from the surface, specifically at irregular defects that play a critical role in crack initiation. As shown in the analysis, these defects, highlighted in Figure 2.39b and 2.39d, are referred to as "LOFs" (lack of fusion defects) (96). It has been noted, the defects initiating the fracture in both TD and PD samples, experiencing similar numbers of cycles, have similar location, shape and size, however, a difference in fatigue strength σ_a for TD and PD samples is significant and equal to 36 MPa, σ_a for TD sample is 94.5 MPa, while σ_a for PD sample is 58.5 MPa.

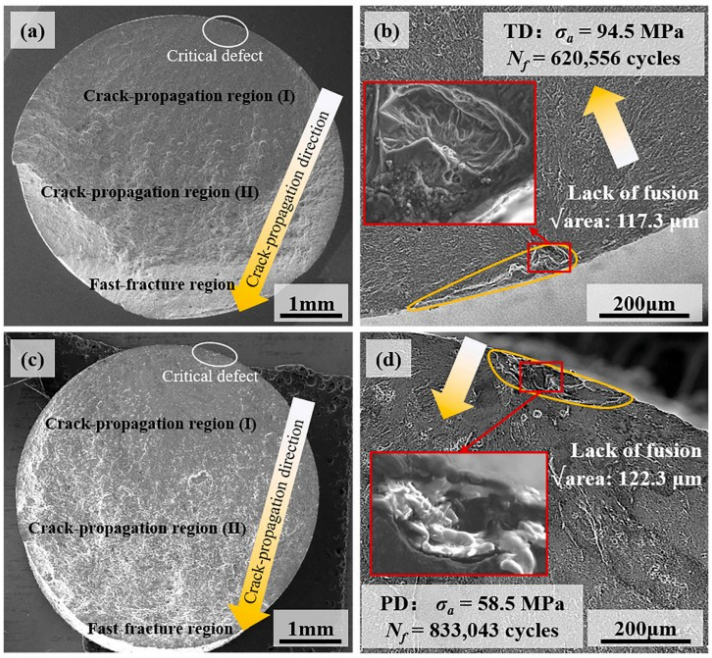

Figure 2.39. Fracture morphologies of failed TD (a,b) and PD (c,d) Al–Mg–Sc–Zr samples (96).

Qin et al. (96) have explained the anisotropy of their TD and PD samples as the following: the presence of LOF (lack of fusion) defects in the vertical samples resulted in irregular shapes, with the longest axis primarily aligned vertically to the building direction. This alignment has caused higher stress concentration and larger defect areas in the CD//BD samples compared to the CD⊥BD samples. Consequently, the fatigue resistance of the vertical samples has been significantly reduced. However, the author has not provided sufficient evidence on the shape and the size of defects, apart from fracture surfaces presented in Figure 2.39, which is contradictory to their suggestion as the size of defects for TD and PD samples there is comparable (√area = 117.3 µm for TD sample and √area = 122.3 µm for PD sample)

In Qin et al. work (99), the variation between defect size (d) and stress amplitude (σ_a) was demonstrated using Kitagawa-Takahashi diagram of LPBFed Al–Mg–Sc–Zr alloy in Direct-Aged and HIPed conditions (Fig. 2.40). Although ΔK_{th} values have not been reported, the K-T diagram remains helpful and demonstrates that the increased fatigue limit of the HIPed samples can be explained by a decrease in defect size for those samples.

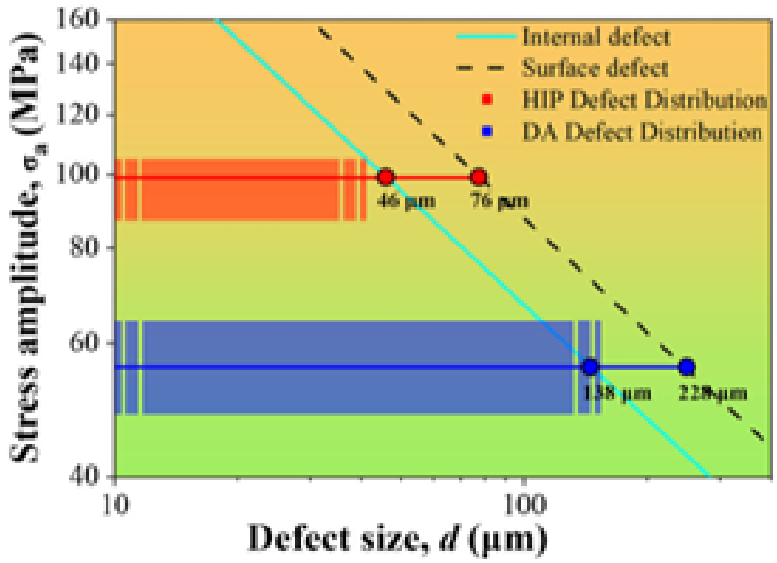

Figure 2.40. Kitagawa-Takahashi diagram of L-PBFed Al–Mg–Sc–Zralloy in DA and HIP conditions (99).

Schimbäck et al. (101) also investigated the fracture surface of samples after cyclic loading. In (101), the defect area was calculated using software and fractographs (Fig. 2.41). However, these calculations appear incorrect. Based on the scale bar in the micrographs, the actual area should be several orders of magnitude larger. This suggests either an error in the calculations or an incorrect scale bar. Also, a very limited number of fractographs has been presented, making it impossible to compare the defects for some samples that caused scatter of S-N curves, such as HC_F4 sample (HIP in the HC mode), that has failed at 2×10^5 cycles under 300 MPa, and HC_F5 or HC_F7 samples (also HIP in the HC mode), that have failed after approximately 2×10^5 cycles under lower stress levels. Thus, the work appears insufficient in accurately quantifying defect sizes and providing enough fractographic evidence, which limits the reliability of its conclusions regarding fatigue behaviour.

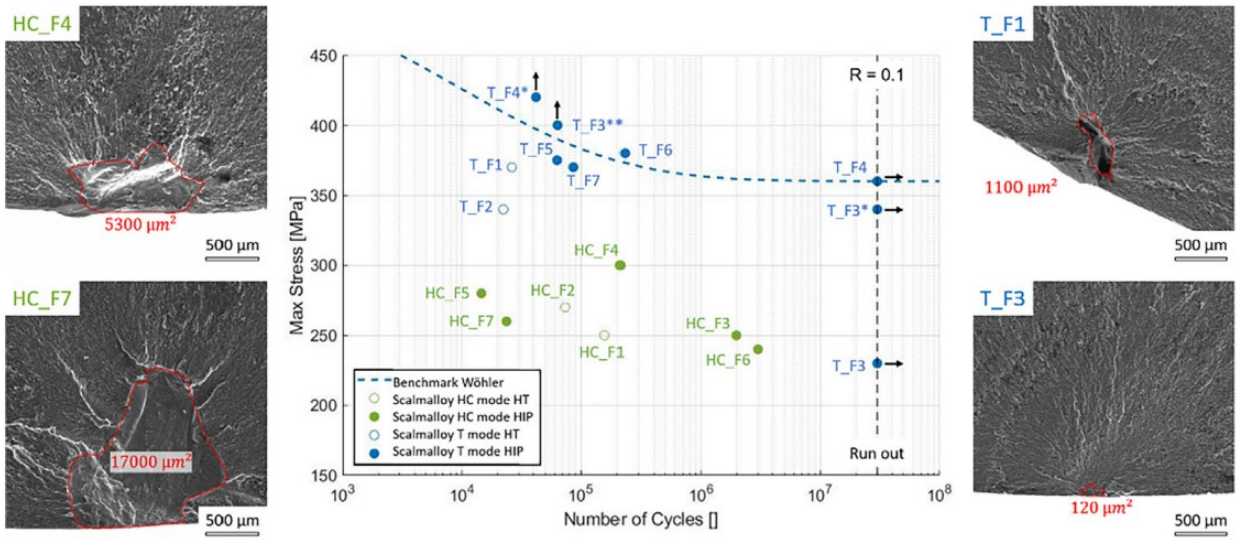

Figure 2.41. Fractographs for both T and HC mode samples after cyclic loading (101).

By using the area parameter for evaluation (Fig. 2.41), it was found that the CI defects in the HC specimens are larger than those in the T specimens. Every CI site can be categorized as either a LOF, which exhibits a characteristic visual appearance with an irregularly shaped, smooth oxide-covered surface, or a bulky oxide that is clearly visible due to charging effects in SEM. The correlation between fatigue limit and defect size can be seen in the Kitagawa-Takahashi diagram (Fig. 2.42). However, the scatter in the data, combined with the absence of cycle number (N) information, makes it challenging to draw firm conclusions from the Kitagawa–Takahashi diagram presented in the study.

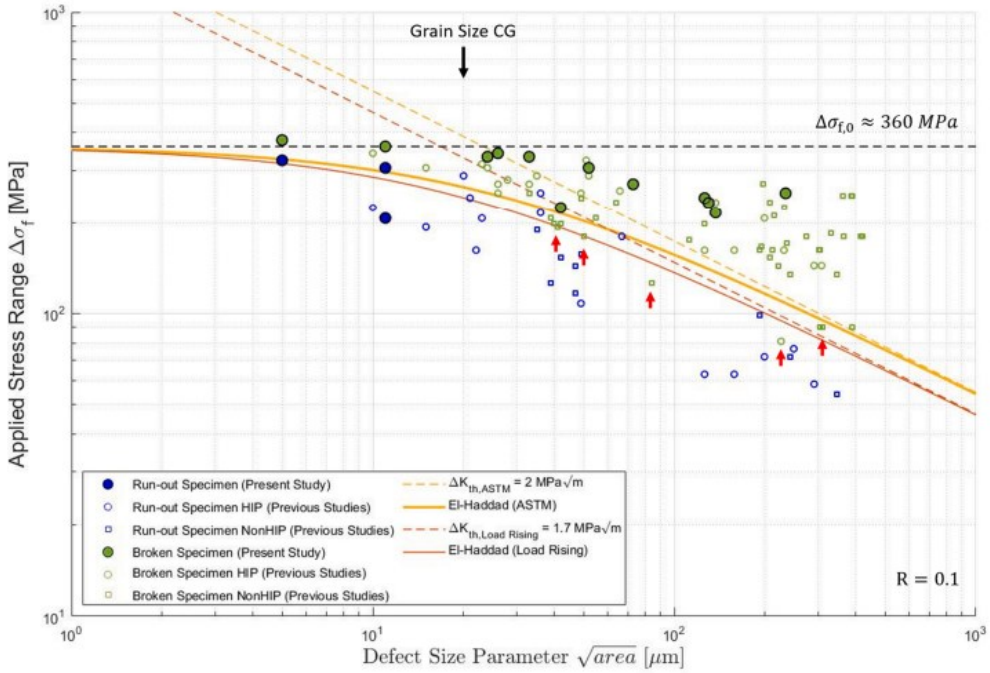

Figure 2.42. Kitagawa-Takahashi (K-T) plot of data from two studies (101), (102).

Based on the model, Schimbäck et al. have identified two distinct regimes (Fig. 2.42). For defect sizes below the area parameter (20µm), the fatigue strength no longer increases, as the largest microstructural feature becomes the limiting factor for fatigue strength. However, when the defect sizes surpass the area parameter, microstructural defects, such as LOF, pores and oxide inclusions become dominant as crack initiating sites. These defects significantly reduce the fatigue strength, consistent with the El-Haddad model.

Summary

The fatigue strength (σ_a) of LPBF-processed Scalmalloy in a stress ratio of R = 0.1 varies between 34 MPa and 162 MPa, which points out the significant role of sample surface quality with respect to fatigue performance. According to ASTM E466, fatigue testing of metallic materials requires longitudinal polishing to a surface roughness of 0.2µm or less. However, He et al. (2021) pointed out that a perfectly smooth surface cannot be reached in the case of a flat specimen; thus, the study has limited applicability in cases where a high-quality surface finish is essential.

Indeed, Qin et al. demonstrated a strong test direction influence with respect to build direction on the fatigue performance. The anisotropy in fatigue resistance correlated to the presence of LOF defects, which showed irregular shapes with the longest axis aligned predominantly in the direction perpendicular to the build direction. This alignment leads to higher values of stress concentrations and more detrimental effect in PD (CD//BD) built specimens, hence decreasing the fatigue limit. However, Qin et al. observed that the critical defect size (√area of defect) was almost the same for TD and PD specimens, respectively 117.3µm and 122.3µm (Fig. 2.39). This similarity suggests that their explanation of the build orientation effect is not fully clear, as critical defect size alone cannot explain the observed variations.

Consequently, Hot Isostatic Pressing has emerged as a very important post-treatment technique to enhance fatigue strength. Indeed, a great number of studies indicate marked enhancement in fatigue resistance after HIP treatment. For instance, samples treated with HIP in Qin et al. revealed considerable improvement in fatigue strength in comparison with the untreated and as-built ones. This can be explained by internal porosity reduction and partial elimination of material inhomogeneities. Schimbäck et al. (2022, 2023) reported very good fatigue strengths of up to 360 MPa after 3×10^7 cycles. This study underlines how optimization of the process parameters may improve the quality of parts. However, their study had significant limitations as calculations of defect area were apparently with error, which calls into question their Kitagawa-Takahashi (KT) diagrams and interpretations related to defects. Using the scale provided on micrographs (Fig. 2.41), it has been calculated that the actual size of the defect is much bigger compared to those presented in the study. Additionally, they provided fatigue strength data for HIP-treated samples only, while comparative results for as-built or heat-treated conditions are missing.

One of the important findings from the above studies is that yield strength is not directly proportional to fatigue strength. Whereas some post-treatments or some process adjustments could increase yield strength, the maximum yield strength may not correspond to the maximum fatigue strength. Again, this supports the idea of multiple factors contributing to fatigue performance, with defect size, surface quality, and microstructural properties playing a key role.

The following gaps have been found in the reviewed literature and the following aspects must be taken into account for further research:

- Building orientation effects should be further investigated with respect to the determination of whether anisotropic fatigue behaviour exists and why.
- Defect Analysis: Accurate defect size characterization and reporting are required for the plotting of a reliable KT diagram and accurate fatigue strength predictions.
- Surface Quality Improvements: All fatigue test samples should be prepared according to the relevant standards in order to avoid the influence of surface defects.

Research Questions

1. How do the various elements in the alloy behave during LPBF solidification in locations starting from the track boundary of each track that results in the equiaxed grain formation adjacent to the boundary and in columnar grain growth away from the boundary?

2. What should be the ΔK_{th} values for the LPBF alloy? How may the loading direction in combination with build orientation affect the crack path tortuosity through the bimodal grains and the resulting ΔK_{th} of the alloy in as-built and heat-treated states under tensile cyclic loading?

3. How do LPBF defects affect the cyclic number at failure and thus fatigues strength of the alloy under tensile cyclic loading? How may build orientation and heat treatment, in combination with LPBF defects, affect the fatigue strength of the alloy

Chapter 3 – Experimental procedure

This chapter describes the details of the research methodology applied and provides an overview of the equipment used in this study to address the research questions. It covers sample preparation procedure, experimental procedures, microstructure measurements and analytical techniques, following this sequence:

1. Firstly, it presents the Scalmalloy powder, LPBF machine and parameters used for LPBF.
2. Subsequently, the choice of LPBF parameters and heat treatment parameters for the main chapters of the current research has been explained based on preliminary experiments.
3. Following that, it describes the technique and procedure applied for the fatigue tests (S-N tests) and fatigue crack growth rate experiments (FCG tests).
4. Finally, the chapter discusses the microstructure, elemental distribution and failure analysis using SEM, EBSD and TEM.

The design of this study is presented in Figure 3.1

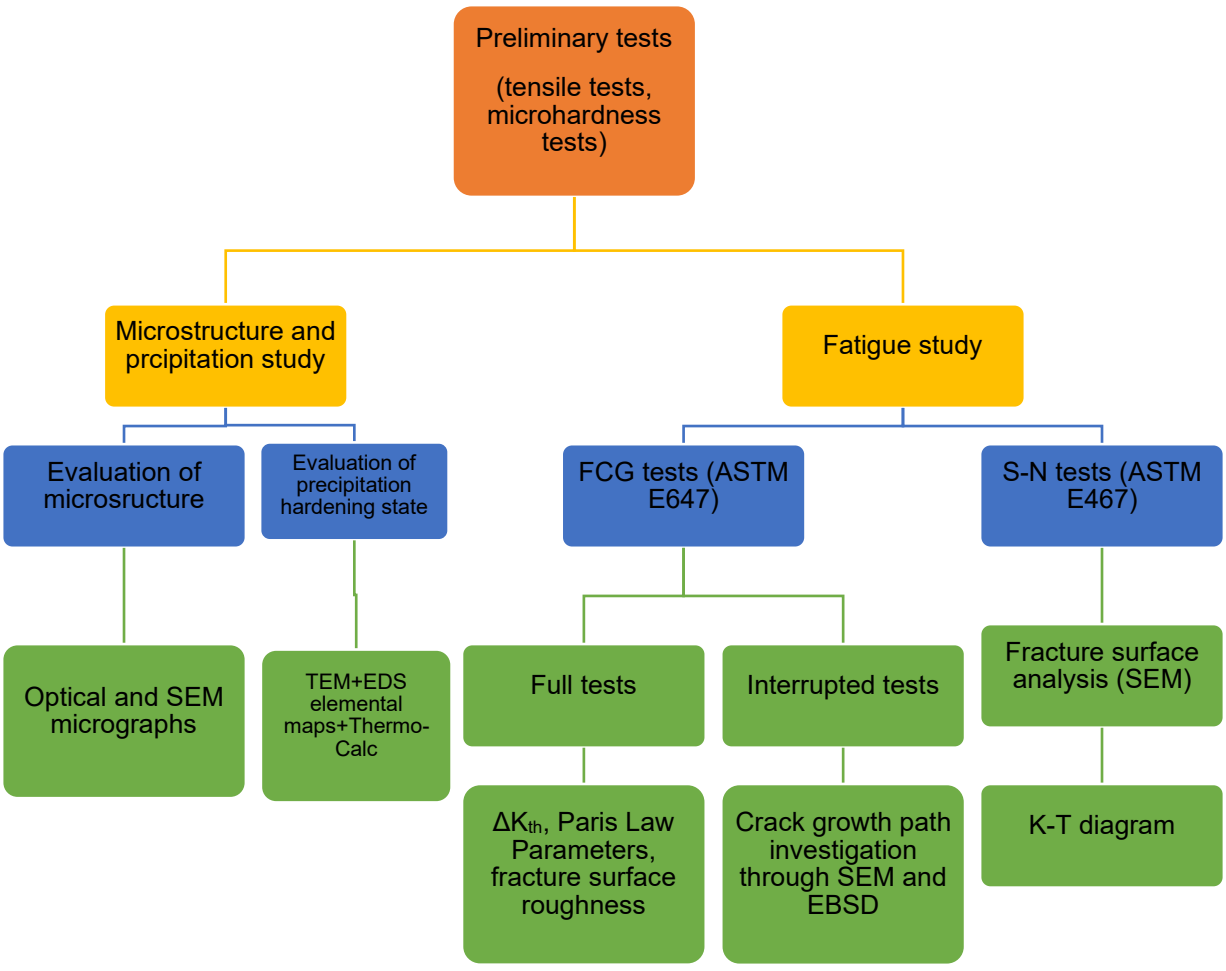

Figure 3.1. Flow chart showing the design of the current study.

3.1 Alloy powder, LPBF machine/parameters and heat treatment

Scalmalloy specimens were printed using a metal powder obtained from LPW Technology and, according to their specification (Appendix A), the particle size ranges from 20 μm to 63 μm. The composition for the batch of the powder sourced commercially and subsequently used in this study is listed in Table 3.1

Table 3.1. Composition of Scalmalloy powder.

Element		Units	Min	Max	Results
Al	Aluminium	Weight, %	-	Bal	Bal
Mg	Magnesium	Weight, %	4.00	4.90	4.55
Sc	Scandium	Weight, %	0.60	0.80	0.65
Zr	Zirconium	Weight, %	0.20	0.50	0.30
Mn	Manganese	Weight, %	0.30	0.80	0.51
Si	Silicon	Weight, %	-	0.40	0.16
Fe	Iron	Weight, %	-	0.40	0.14
Zn	Zinc	Weight, %	-	0.25	0.02
Cu	Copper	Weight, %	-	0.10	0.01
Ti	Titanium	Weight, %	-	0.15	<0.01
V	Vanadium	Weight, %	-	0.05	0.01
O	Oxygen	Weight, %	-	0.05	0.04

All samples were produced using a 3D printer supplied by Renishaw plc, headquartered in England, UK. The specific model used for this study is the Ren AM 400, as depicted in Figure 3.2. This printer is equipped with a pulsed laser, capable of delivering a maximum laser power of P_{max} = 400 W. The LPBF machine's build volume measures 248 mm x 248 mm x 285 mm along the Z-axis and typically employs a default laser spot size diameter of θ = 70 μm.

Figure 3.2. Renishaw AM400 LPBF machine (113).

In the Renishaw AM400 machine, there is an external powder hopper with valve interlocks and this is to allow for the additional material to be added whilst the process is running. There are also powder overflow containers outside the chamber and isolation valves. Unused materials are sieved and reintroduced to the process via the hopper while the system is running. As per system specification provided in the manufacturer's data sheet (Appendix B), the recommended range of metal powders compatible with this printer includes materials such as AlSi10Mg, CoCr, In625, In718, stainless steel 316L, Ti6Al4V. The printing process is presented in the photos below (Fig. 3.3):

Figure 3.3. LPBF process of samples used in the current study.

The printing parameters used for preliminary experiments are presented in Table 3.2. The samples for tensile tests had cylindrical shapes and were printed in three build directions (vertical, inclined at 45°C or horizontal) and with base plate at either room temperature (RT) or heated at 180 °C. The following parameters were applied to all samples: the layer thickness t = 50 µm, hatch spacing h = 50 µm and cross hatching strategy of 67° rotation.

Table 3.2. LPBF parameters, plate thermal conditions and sample build orientation.

Power, W	Scan Speed, mm/s	Energy Value, J/mm^3	Plate temperature	Build direction
250	1082	92.5	RT	Vertical
250	540	185	RT	Vertical
370	1600	92.5	RT	Vertical
370	800	185	RT	Vertical
250	1082	92.5	RT	Inclined
250	540	185	RT	Inclined
370	1600	92.5	RT	Inclined
370	800	185	RT	Inclined
250	1082	92.5	RT	Horizontal
250	540	185	RT	Horizontal
370	1600	92.5	RT	Horizontal
370	800	185	RT	Horizontal
250	1082	92.5	180 C°	Vertical
250	540	185	180 C°	Vertical
370	1600	92.5	180 C°	Vertical
370	800	185	180 C°	Vertical
250	1082	92.5	180 C°	Inclined
250	540	185	180 C°	Inclined
370	1600	92.5	180 C°	Inclined
370	800	185	180 C°	Inclined
250	1082	92.5	180 C°	Horizontal
250	540	185	180 C°	Horizontal
370	1600	92.5	180 C°	Horizontal
370	800	185	180 C°	Horizontal

3.2 Preliminary experiments

For the preliminary experiments, two levels of energy density (E=92.5 J/mm^3 and E=185 J/mm^3) were selected based on the findings from the literature review. Tensile testing and microhardness measurements were then performed to identify the optimal LPBF parameter window for Scalmalloy, processed using a Renishaw AM 400 system equipped with a pulsed laser for the main study. Following this, II step heat treatment (T6) or I step heat treatment (T5) was carried out at different time/temperature regimes to find out the heat treatment parameters that allow to achieve the maximum precipitation strengthening for LPBFed Scalmalloy.

3.2.1 Tensile testing

As LPBF machines used in the previous studies were equipped with a mainly continuous laser, it was examined how Power and Scan Speed influence defect formation in samples produced using a pulsed laser system. Tensile tests were conducted to assess which parameter combinations result in minimal defects, such as LOF and porosity, which affect UTS, MPa and ε, %. Tensile samples were machined from the built long samples to gauge length section 17.9 mm and diameter 5.05 mm (Fig. 3.4) and tensile testing was conducted using a Tinius Olsen H50KS tester. The illustration of the sample for tensile tests is presented below:

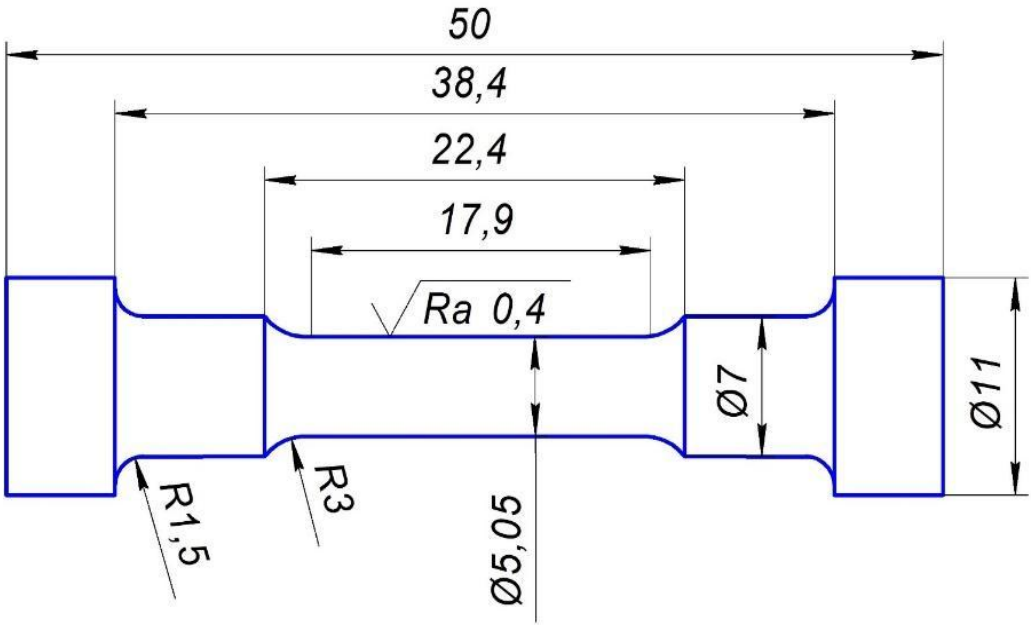

Figure 3.4. Illustration of a tensile sample with dimensions indicated.

Based on the tensile test results (Table 3.3 and Table 3.4), the samples produced with a heated plate generally exhibit higher yield strength (YS) and ultimate tensile strength (UTS) compared to those produced with an RT plate, demonstrating improved strength. However, some reduction of ductility is observed for samples

produced on the heated plate. Among the results presented in Tables 3.3 and 3.4, highlighted values in green indicate the best balance between strength and ductility. Specifically, for the RT plate, the vertical build sample processed at 370 W, 1600 mm/s, and 92.5 J/mm^3 achieved YS of 247.5 MPa, UTS of 327.5 MPa, and 22% strain, representing a strong correlation between strength and ductility.

Table 3.3. Tensile test results for the build produced with RT plate.

Power, W	Scan Speed, mm/s	EnergyValue, J/mm^3	Build direction	YS, MPA	UTS, MPa	ε, %
250	1082	92.5	Vertical	235	287.5	4.8
250	540	185	Vertical	177	255	21.7
370	1600	92.5	Vertical	247.5	327.5	22
370	800	185	Vertical	230	292.5	22
250	1082	92.5	Inclined	257.5	342.5	18
250	540	185	Inclined	255	337.5	24.1
370	1600	92.5	Inclined	227	307.5	14.3
370	800	185	Inclined	265	345	20.6
250	1082	92.5	Horizontal	265	337.5	15.4
250	540	185	Horizontal	251	316	17.4
370	1600	92.5	Horizontal	261	327.5	20.6
370	800	185	Horizontal	247.5	310	28.6

For the heated plate, the best combination of strength and strain was observed at 370 W, 1600 mm/s, and 92.5 J/mm^3, achieving YS of 271 MPa, UTS of 322 MPa, and 20.5% strain for horizontal build, YS of 297 MPa, UTS of 329 MPa, and 7% strain for inclined build and YS of 284 MPa, UTS of 313 MPa, and 7.5% for vertically built sample. It can be noticed that the average strain is lower for the samples produced with a heated plate. The difference between builds produced on RT plate and 180°C is from 35% to 75% depending on the build direction, however, YS and UTS are both higher for the samples built on the heated plate.

Table 3.4. Tensile test results for build produced with heated plate.

Power, W	Scan Speed, mm/s	Energy Value, J/mm^3	Build direction	YS, MPA	UTS, MPa	ε, %
250	1082	92.5	Vertical	262	290	5.2
250	540	185	Vertical	329	335	2.8
370	1600	92.5	Vertical	284	313	7.5
370	800	185	Vertical	314	338	9.5
250	1082	92.5	Inclined	259	289	2.4
250	540	185	Inclined	310	324	2.6
370	1600	92.5	Inclined	297	329	7
370	800	185	Inclined	298	332	7.1
250	1082	92.5	Horizontal	292	315	12.2
250	540	185	Horizontal	320	340	10.3
370	1600	92.5	Horizontal	271	322	20.5
370	800	185	Horizontal	300	323	10.5

To investigate the reason for low values of elongation to failure for samples produced on the heated plate, fracture surface analysis has been done for all the samples after tensile testing. A great amount of LOF can be observed on the fracture surface for the build produced with the temperature of 180°C that caused extremely low strain values for this build. To illustrate the correlation of strain values and the amount of unmelted powder on the surface, three stress-strain curves for the RT plate and heated plate builds (with lowest, medium and highest ε, %) are shown together with the corresponding fracture surface SEM images.

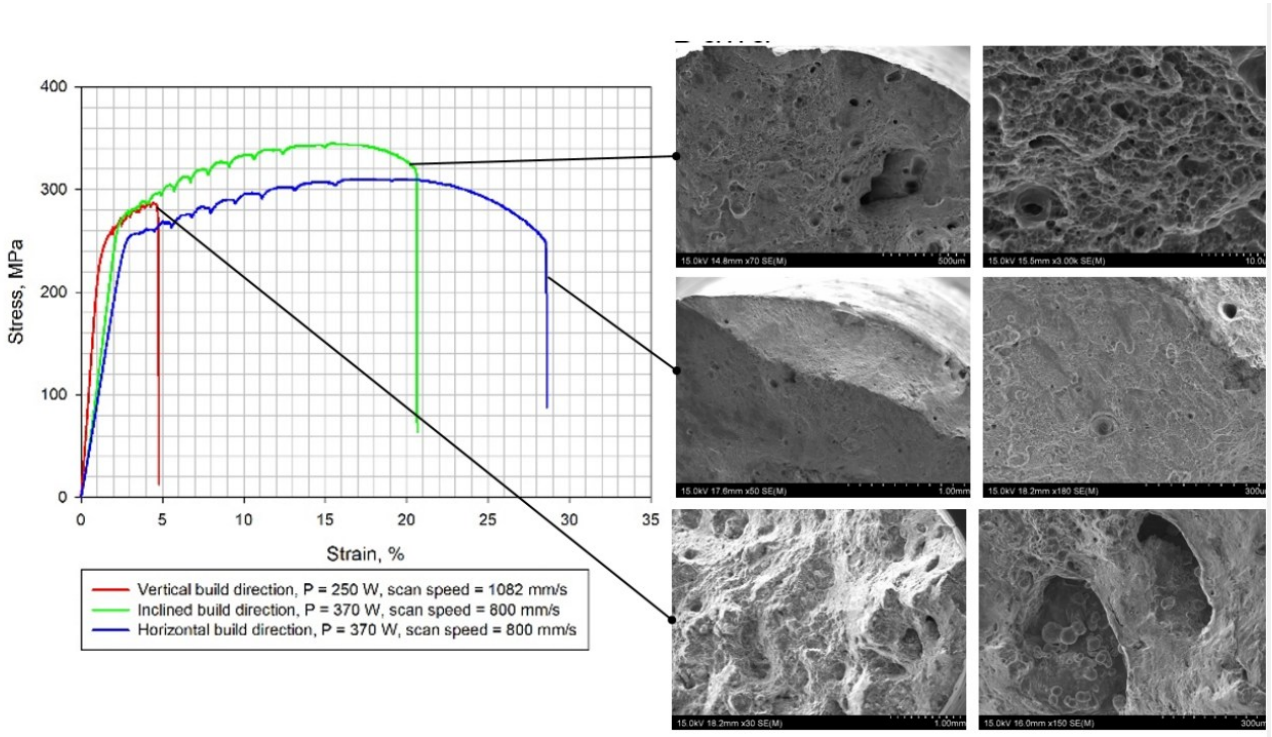

Figure 3.5. Stress-strain curves for samples produced with RT plate.

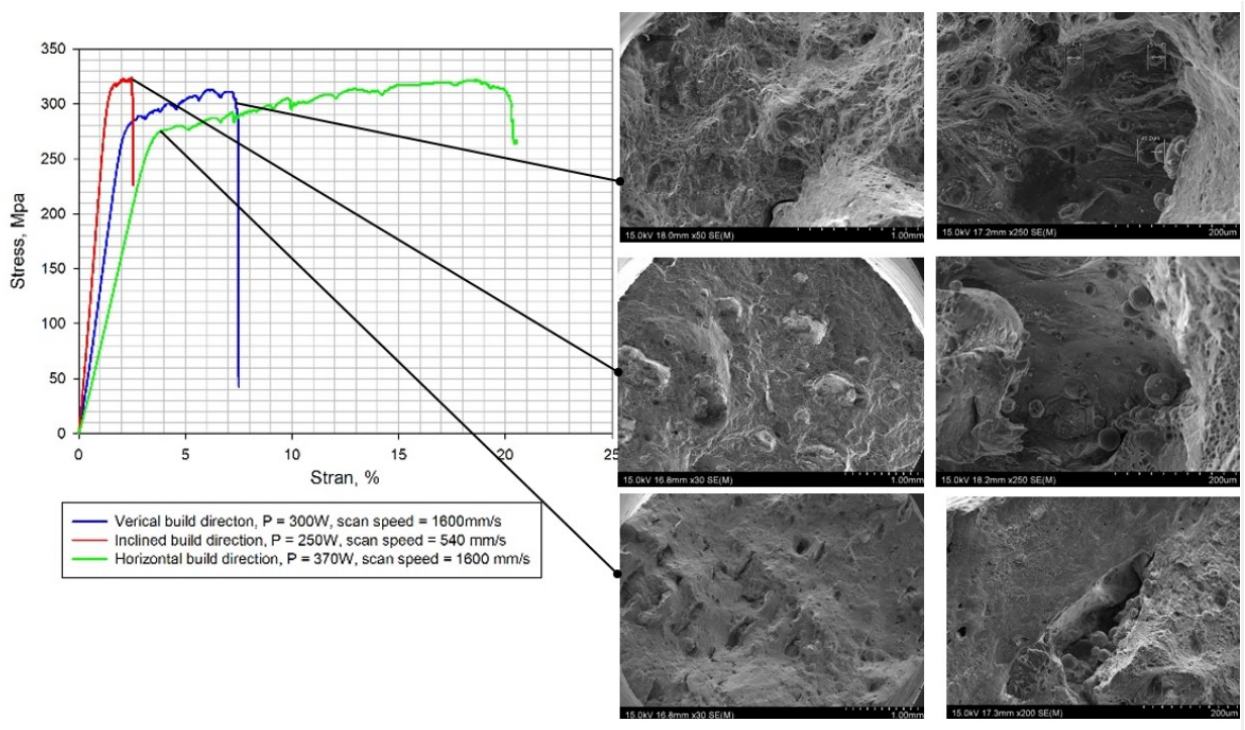

Figure 3.6. Stress-strain curves for samples produced with heated plate.

As evident from Figures 3.5, 3.6, low strain values correspond to the fractographs with a large amount of LOF. This trend suggests that incomplete melting and bonding between powder particles may have contributed to reduced ductility in these samples. However, for samples produced with the heated plate, the unmelted powder can be observed even in the sample with the highest strain equal to 20%. This indicates that some regions

within the material of samples produced with heated plate may experience inadequate melting, leading to the formation of LOF defects. Thus, after tensile tests, the best scanning strategy has been identified as: Laser Power (P) = 370 W, scan speed (v) = 1600 mm/s and these correspond to energy level (E) = 92.5 J/mm^3. These parameters were identified as the parameters leading to the minimum number of microstructural defects and subsequently leading to good mechanical properties. Moreover, optical images of the scan tracks (Fig. 4.1) revealed that sufficient track overlapping was achieved, confirming that the parameters chosen are optimal. However, the formation of certain defects was observed to occur in an uncontrolled manner.

3.2.2 Heat treatment and microhardness measurements

The aim of this section was to evaluate whether a two-step (T6) heat treatment is required or whether one-step (T5) heat treatment is sufficient for precipitation hardening, as the current literature has not provided reasonable evidence that it is unnecessary to conduct the solutionizing step of heat treatment for precipitation hardening. The selected heat treatment processes involved both one-step (T5) and two-step (T6) heat treatments, each performed at different temperatures and durations. The one-step heat treatment, referred to as T5 in this study, involves directly aging the LPBFed samples— at temperatures from 325°C to 360°C during from 1 hour to 8 hours—without performing any prior solution treatment. The two-step heat treatment, referred to T6 in this study, includes an initial solution treatment at 540°C, followed by water quenching, and then a secondary aging step at a lower temperature. The difference between T5 and T6 is that T6 involves solution treatment before aging, while T5 skips this first step and applies aging directly to the as-built material. The detailed parameters of heat treatment regimes for preliminary study of this research are provided below:

1) I step heat treatment (T5) - 325°C, 1 hour
2) I step heat treatment (T5) - 325°C, 2 hours
3) I step heat treatment (T5) - 325°C, 4 hours
4) I step heat treatment (T5) - 325°C, 8 hours
5) I step heat treatment (T5) - 360°C, 1 hour
6) I step heat treatment (T5) - 360°C, 2 hours
7) I step heat treatment (T5) - 360°C, 4 hours
8) II step heat treatment (T6) - 540°C, 1 hour + 325°C, 1 hour
9) II step heat treatment (T6) - 540°C, 1 hour + 325°C, 2 hours
10) II step heat treatment (T6) - 540°C, 1 hour + 325°C, 4 hours
11) II step heat treatment (T6) - 540°C, 1 hour + 325°C, 8 hours
12) II step heat treatment (T6) - 540°C, 1 hour + 360°C, 1 hour
13) II step heat treatment (T6) - 540°C, 1 hour + 360°C, 2 hours
14) II step heat treatment (T6) - 540°C, 1 hour + 360°C, 4 hours

The furnace being used is the McGregor laboratory muffle furnace, which is presented in the photo below (Figure 3.7.a). For precise temperature control, the k-type thermocouple has been used (Fig. 3.7.b)

a) b)

Figure 3.7. a) McGregor Furnace used for heat treatment of samples in the current study and b) k-type thermocouple.

For precise temperature control, PicoLog 6 data logging software was used. An example of temperature recording is provided below (Fig. 3.8). The furnace was heated up to 540°C first. After the sample insertion, some temperature fall was observed and then increased back to 540°C. After one hour holding time at 540°C, sample has been removed (Fig. 3.8.a). Similar data recording for aging treatment at 325°C is presented as well (Fig.3.8.b)

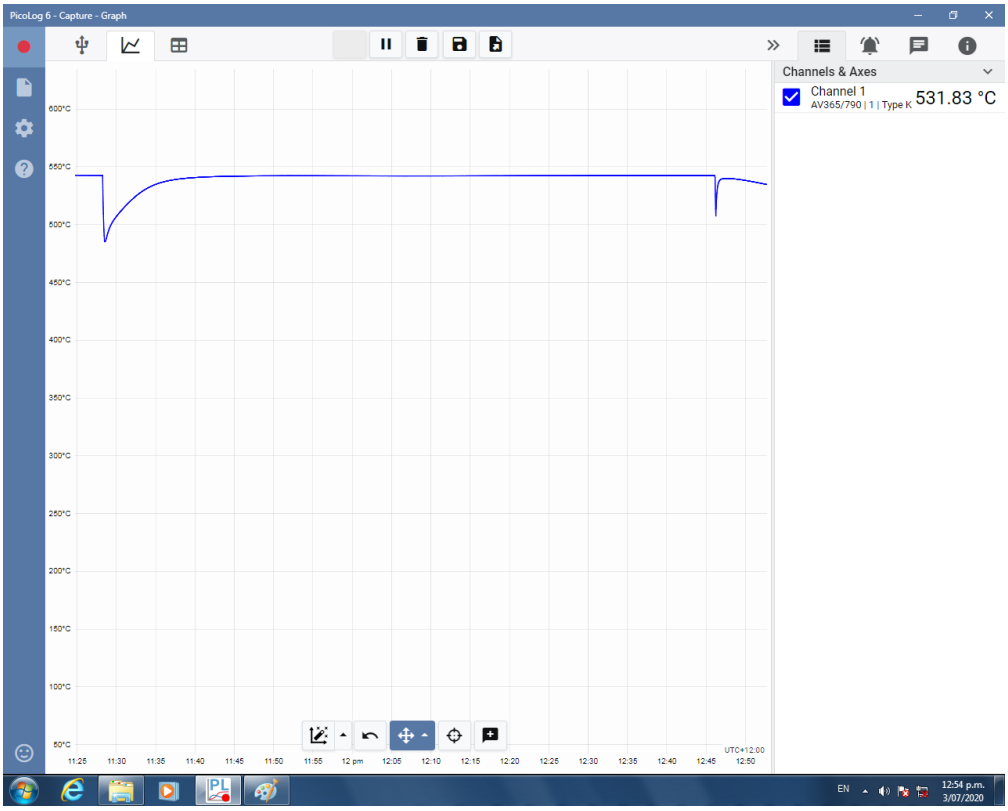

a)

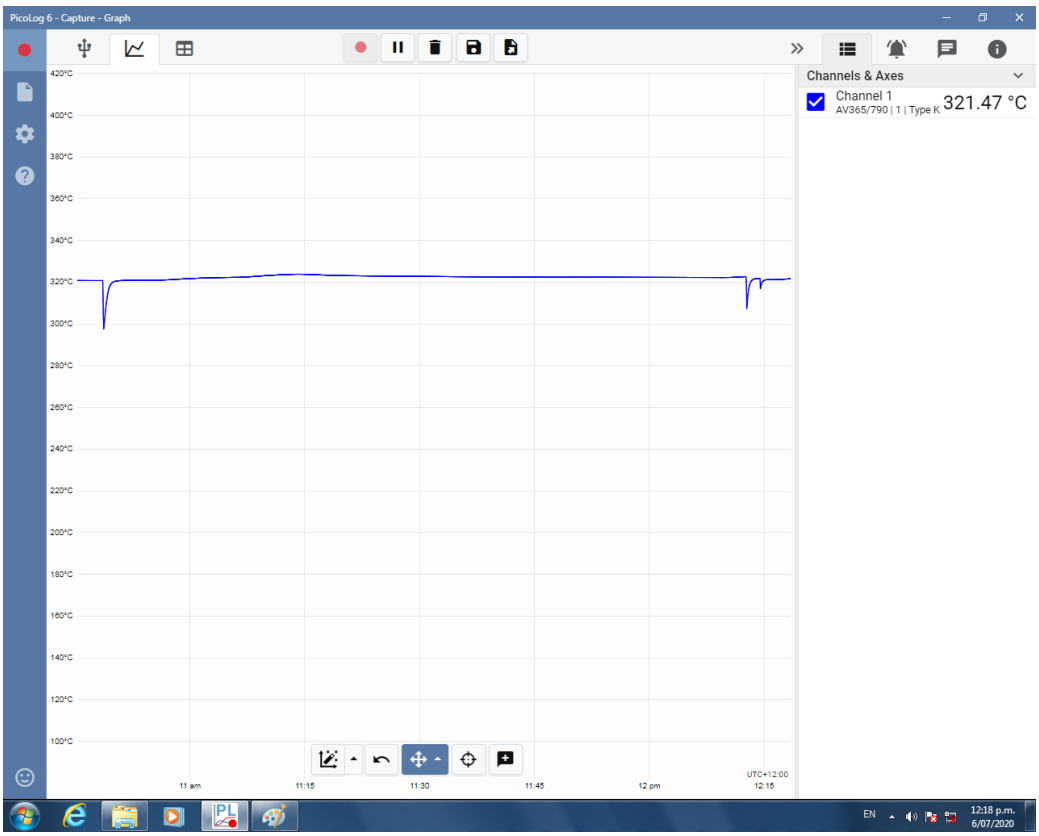

b)

Figure 3.8. Data logging during heat treatment using PicoLog software for a) solutionizing at 540°C for 1 b) aging at 325°C for 4h.

Microhardness tests were used to compare microhardness among the samples subjected to different heat treatments, either one-step (T5) or two-step (T6). The measurements were conducted using a Leco Microhardness Tester (LM800AT) with a 300g loading for 10s, for each sample, 5 measurements were made and the average of them was used as the result. The results of microhardness measurements plotted as a function of aging time are presented below in Figure 3.9.

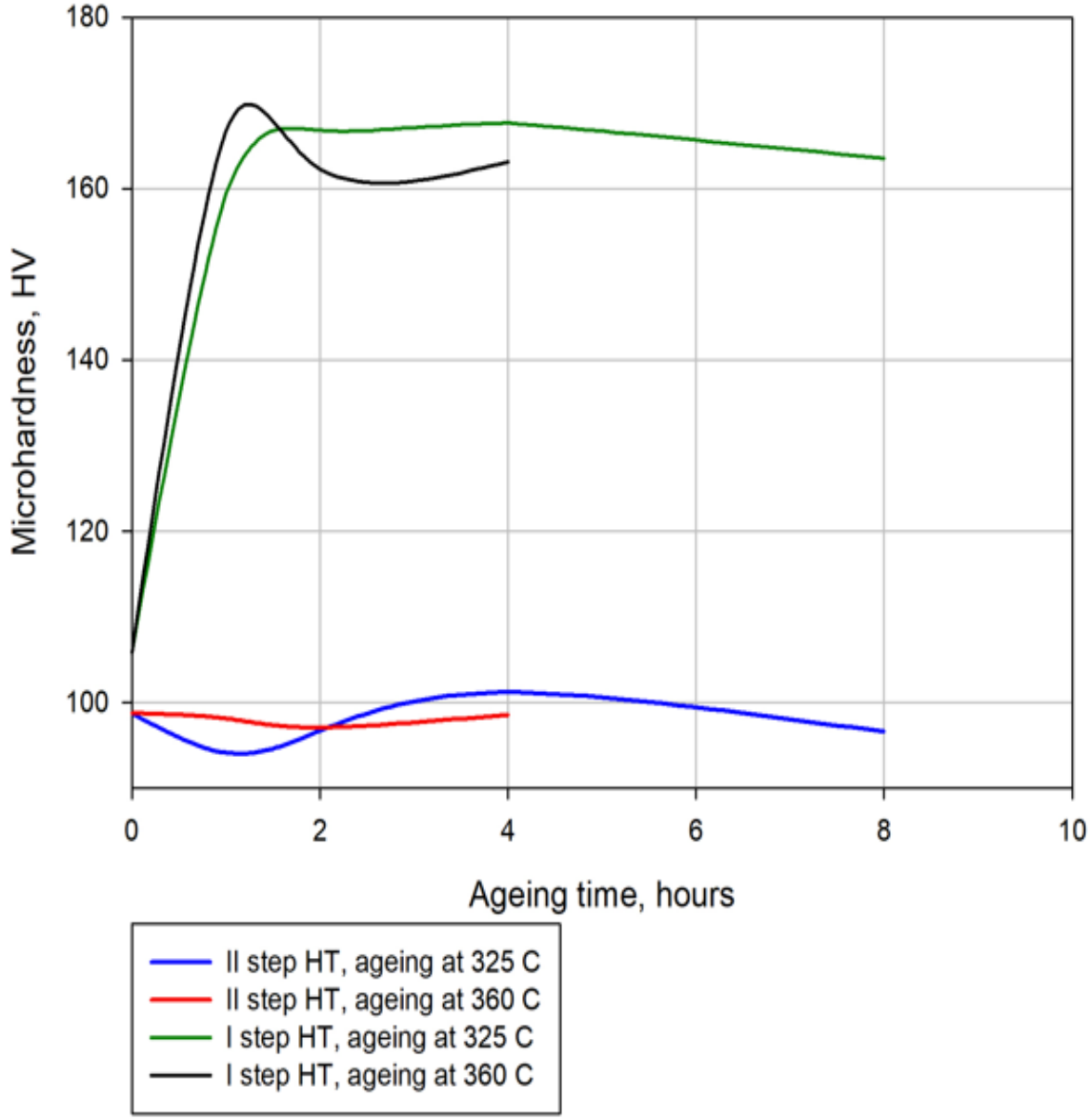

Figure 3.9. Microhardness test results of heat-treated samples plotted as a function of aging time for as-built samples and samples after high temperature holding.

The microhardness test results showed that samples after T6 with aging at 325°C or 360°C, both result in significantly lower microhardness values, with no clear indication of peak hardening. T5 treatment at 325°C demonstrates the highest microhardness values, peaking after 4 hours of aging, making it the most effective in achieving maximum hardening compared to other treatments. As for T5 treatment at 360°C, it can be noticed that, while this treatment shows initial hardening, the microhardness values are slightly lower and stabilize earlier, suggesting high chances of overaging compared to the 325°C regime. Thus, the one-step heat treatment (T5) at 325°C for 4 hours is the optimal heat treatment regime, achieving the highest microhardness and peak hardening. It can be suggested that the fast cooling during LPBF has resulted in Sc/Zr likely remaining in the solution, thereby enabling subsequent precipitation hardening during T5 heat treatment.

3.2.3 Results and selected samples parameters for the current research

Based on the analysis of the provided data, the most appropriate printing regime is achieved with a power of 370 W and a scan speed of 1600 mm/s, as this combination delivers an optimal balance between yield strength (YS), Ultimate Tensile Strength (UTS) and elongation (E). Specifically, this regime results in YS of 247.5 MPa and elongation of 22%, which represents one of the highest combinations of these properties. In contrast, other parameter combinations generally show a trade-off, with either a drop in elongation or yield strength. Notably, elongation and UTS are highly sensitive to defects in the printed samples. The superior UTS and elongation values under the optimal regime suggest that these samples have fewer defects compared to those printed with other parameter combinations, indicating better material quality and process consistency. These specific printing parameters result in pulsing laser, $P/v < 0.23$ J mm, which was previously low but is nowadays common, and is a suitable LPBF condition for minimal LOF keyhole pore formation. Thus, these printing parameters are utilized for all samples used in the current study. For heat treatment, the most appropriate regime to be found is one-step heat treatment (T5) at 325°C for 4h. Thus, in this study, all fatigue samples, both FCG and S-N, subjected to heat treatment underwent one-step aging at these parameters, and are marked as heat-treated (HT). As-built and T5 samples were used for the microstructural and precipitation study. Table 3.5 below provides detailed information on printing and heat treatment parameters for samples investigated in Chapter 4.

Table 3.5. Printing and heat treatment parameters for samples for microstructural and precipitation study.

Power, W	Scan Speed, mm/s	EnergyValue, J/mm^3	Build direction	Building plate temperature	Heat treatment condition
370	1600	92.5	Vertical	RT	As-built
370	1600	92.5	Vertical	RT	T5 - Aging at 325°C for 4h

For fatigue crack growth tests in Chapter 5 (Table 3.6) as per ASTM E647, there are four sample conditions depending on whether the base plate was heated and whether the sample was heat treated and they are: as-built using room temperature (RT) plate (AS_{RT}), as-built using heated plate (AS_H), built using RT plate and heat-treated (HT_{RT}), and built using heated plate and heat-treated (HT_H). Heat treatment was conducted using one-stage aging at 325 °C for 4hrs. Additionally, three build directions were tested: crack direction normal to build direction (CD⊥BD), crack direction parallel to build direction (CD//BD) and crack direction at 45° to build direction (∠CD,BD=45°).

Table 3.6. Parameters for LPBF and treatment conditions of FCG test samples.

Power, W	Scan Speed, mm/s	EnergyValue, J/mm^3	Build direction	Building plate temperature	Heat treatment condition	Sample identification
370	1600	92.5	CD//BD	RT	AB	$(CD\text{-}BD)_P+AS_{RT}$
370	1600	92.5	CD⊥BD	RT	AB	$(CD\text{-}BD)_N+AS_{RT}$
370	1600	92.5	∠CD,BD=45°	RT	AB	$(CD\text{-}BD)_{45}+AS_{RT}$
370	1600	92.5	CD//BD	180	AB	$(CD\text{-}BD)_P+AS_H$
370	1600	92.5	CD⊥BD	180	AB	$(CD\text{-}BD)_N+AS_H$
370	1600	92.5	∠CD,BD=45°	180	AB	$(CD\text{-}BD)_{45}+AS_H$
370	1600	92.5	CD//BD	RT	HT	$(CD\text{-}BD)_P+HT_{RT}$
370	1600	92.5	∠CD,BD=45°	RT	HT	$(CD\text{-}BD)_{45}+HT_{RT}$
370	1600	92.5	CD//BD	180	HT	$(CD\text{-}BD)_P+HT_H$
370	1600	92.5	∠CD,BD=45°	180	HT	$(CD\text{-}BD)_{45}+HT_H$

For S-N fatigue tests in Chapter 5 (Table 3.7), to investigate orientational effect on fatigue properties, samples were printed in two build directions, with a crack direction normal to the build direction (CD⊥BD) and a crack direction parallel to the build direction (CD//BD). Also, to study the effect of heat treatment, T5 (325°C, 4h) has been performed for comparison with non-heat treated (as-built samples). Thus, 4 groups of samples were tested: (CD⊥BD)-AB, (CD⊥BD)-HT, (CD//BD)-AB, (CD//BD)-HT.

Table 3.7. Parameters for LPBF and treatment conditions of fatigue test samples.

Power, W	Scan Speed, mm/s	EnergyValue, J/mm^3	Build direction	Building plate temperature	Heat treatment condition
370	1600	92.5	CD//BD	RT	AB
370	1600	92.5	CD⊥BD	RT	AB
370	1600	92.5	CD//BD	RT	HT
370	1600	92.5	CD⊥BD	RT	HT

3.3 Fatigue life and crack growth testing procedures

3.3.1 MTS Fatigue machine

Fatigue crack growth tests (ASTM E647) and constant amplitude axial fatigue tests (ASTM E467) were conducted using MTS Landmark Servohydraulic system (Fig. 3.10). MTS Multipurpose Elite software and an Epsilon COD gage were employed for fatigue crack size monitoring (FCG tests), cycle number (S-N tests) and recording the test results. Additionally, the software is equipped with the templates for the corresponding tests.

Figure 3.10. Landmark® Servohydraulic Test Systems.

3.3.2 Fatigue tests according to ASTM E466

For S-N tests, cylindrical samples were printed using the Renishaw AM400 machine and the parameters listed in Table 3.7. After the printing process, half of the samples were heat-treated at 325°C for 4h, then all samples were machined to the dimensions indicated on the drawing from Figure 3.11. To achieve the required surface roughness of the samples, after machining, at the test section of the sample, 0.1 mm of gauge diameter was removed by manual cylindrical grinding. After grinding, the final 0.025 mm of gauge diameter by manual longitudinal polishing was removed to impart a maximum surface roughness of 0.2-µm Ra in the longitudinal direction (refer to X1.2.3 in ASTM E466-15).

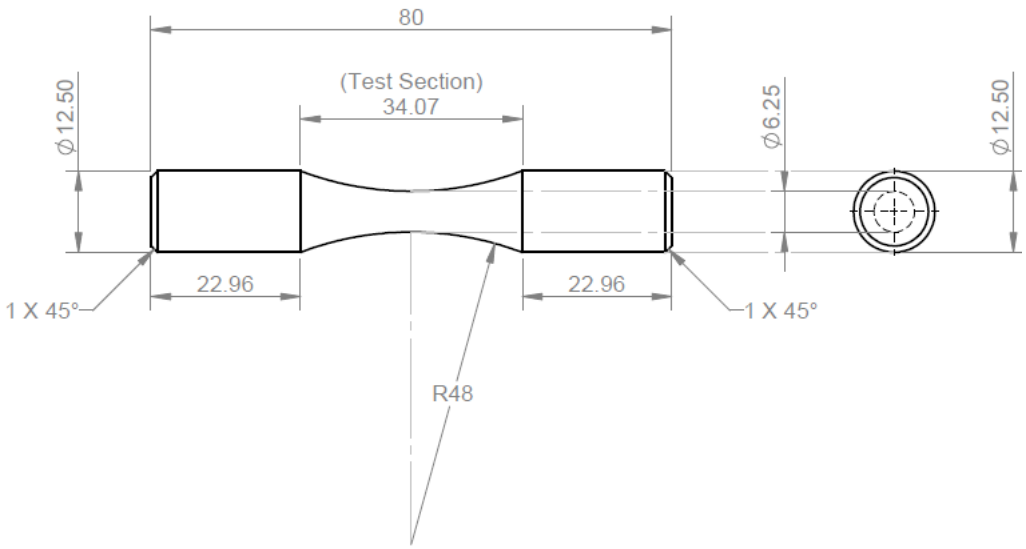

Figure 3.11. Fatigue samples dimensions after machining.

Fatigue tests were conducted using the following parameters: R (stress ratio) = 0.1, f (frequency) = 20 Hz, the maximum stress σ_{max} varied between 90 MPa and 320 MPa. The number of cycles to failure (N) was recorded for each sample with the corresponding σ_{max}, together generating the points on S-N curve. Post-failure analysis was conducted using scanning electron microscope (SEM) to characterize the fracture surfaces and identify dominant defects affecting fatigue life. Defect analysis was performed on all tested samples, to evaluate their impact on fatigue life. The following parameters were recorded during the fatigue testing: defect size ($\sqrt{a}$), measured using ImageJ software; defect location, categorized as either surface or subsurface relative to the fracture initiation sites; applied stress (σ_{max}, MPa), corresponding to the stress level at which fatigue failure occurred; and the number of cycles to failure (N), as captured during the fatigue tests. An example of defect area measurement is provided below in Figure 3.12.

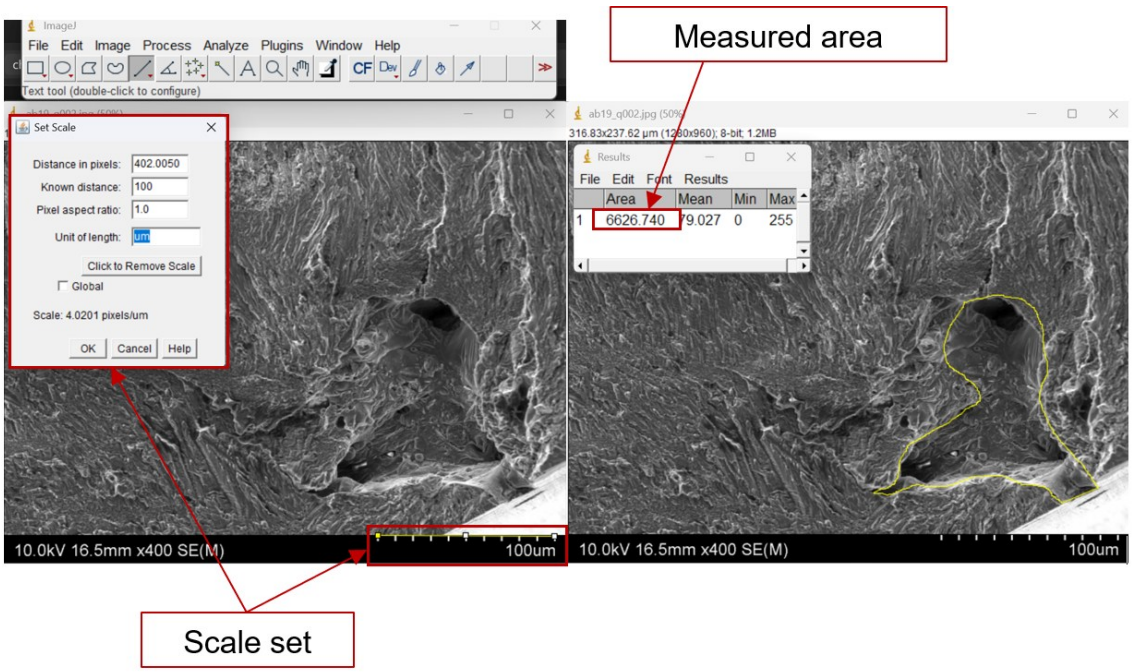

Figure 3.12. The defect measurement procedure on the fracture surface of sample CD//BD-AB-4 using ImageJ software.

3.3.3 Fatigue tests according to ASTM E647

For FCG tests, plate samples 39 mm x 37 mm x 6 mm in dimension were printed using a Renishaw AM400 machine (Fig. 3.13(a)). The printing parameters are described in Table 3.6. The plate samples were then machined into FCG compact tension (CT) samples. The CT sample size is slightly smaller than the originally built sample size and the dimension of a sample is shown in Fig. 3.13(b), in accordance with ASTM standard E647. As illustrated in Fig. 3.13(b), the orientation of the notch (same as crack direction, CD) can be parallel to build direction (BD), thus $(CD\text{-}BD)_P$, or normal to BD, thus $(CD\text{-}BD)_N$. Additionally, samples were also built with the plate at 45° to BD, $(CD\text{-}BD)_{45}$, as is also shown in Fig. 3.13(b).

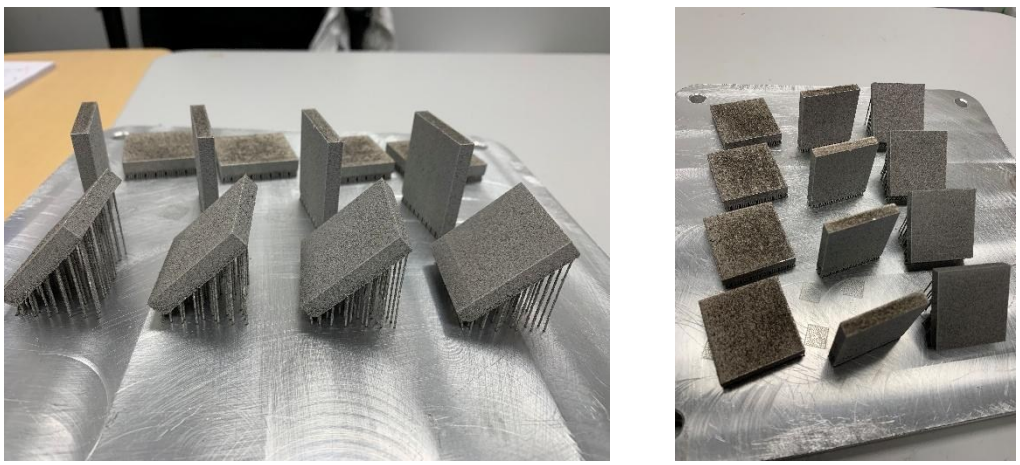

a)

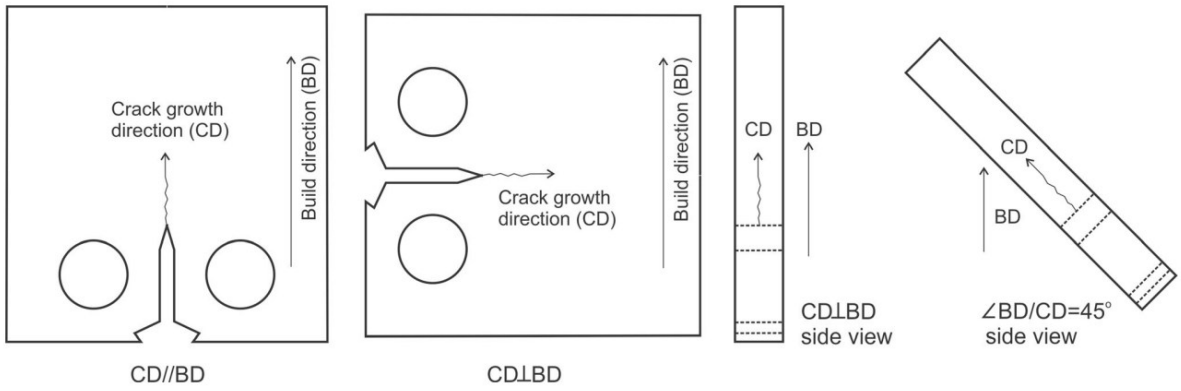

b)

Figure 3.13. a) Samples printed for FCG tests in as-built state (before machining), b) FCG samples after machining with crack growth direction and build direction indicated. Sample dimensions: 31.3 mm x 30.0 mm x 6.0 mm.

An MTS Landmark Servo hydraulic system was used for conducting the FCG tests with load frequency set at 20Hz and R = 0.1. MTS Multipurpose Elite software and an Epsilon Crack Opening Displacement (COD) gage (Fig. 3.14) were used for crack size monitoring using the compliance method. A clevis and pin assembly were used to hold the CT specimen onto the FCG grip. A clip gage was placed at the mouth-end of CT sample and used to measure vertical mouth opening displacement of CT sample. The clip gage was produced by Epsilon Tech. Corp. and satisfies all requirements of ASTM E647 standard.

Figure 3.14. Epsilon COD gage used for FCG tests.

The ΔK value was calculated during testing by the MTS software based on the ΔK=f (ΔF,B,W,a) equation for CT samples specified in ASTM E647, where F, B, W, a is the applied load, sample thickness, sample width, and crack size, respectively. A 1mm pre-crack was initiated following the ASTM standard before the beginning of FCG test. K-decreasing started at 3.1MPa $m^{1/2}$ with the normalized K-gradient C=-0.12mm^{-1} and K-increasing also beginning at 3.1MPa $m^{1/2}$. Figure 3.15 illustrates an example of maximum and minimum load

values and crack size values recorded in a test. In the K-decreasing stage, as the test proceeded and ΔK decreased to a low-value region, the load value signals tended to be noisier. The load value noise is reflected in the ΔK values calculated and recorded by the software. In the K-increasing state, when the crack size increased to just under 18mm, the crack propagated increasingly fast and pre-set load values could no longer be maintained, leading R to start increasing rapidly. The ΔK and da/dN values for average R ≥ 0.12 are not used.

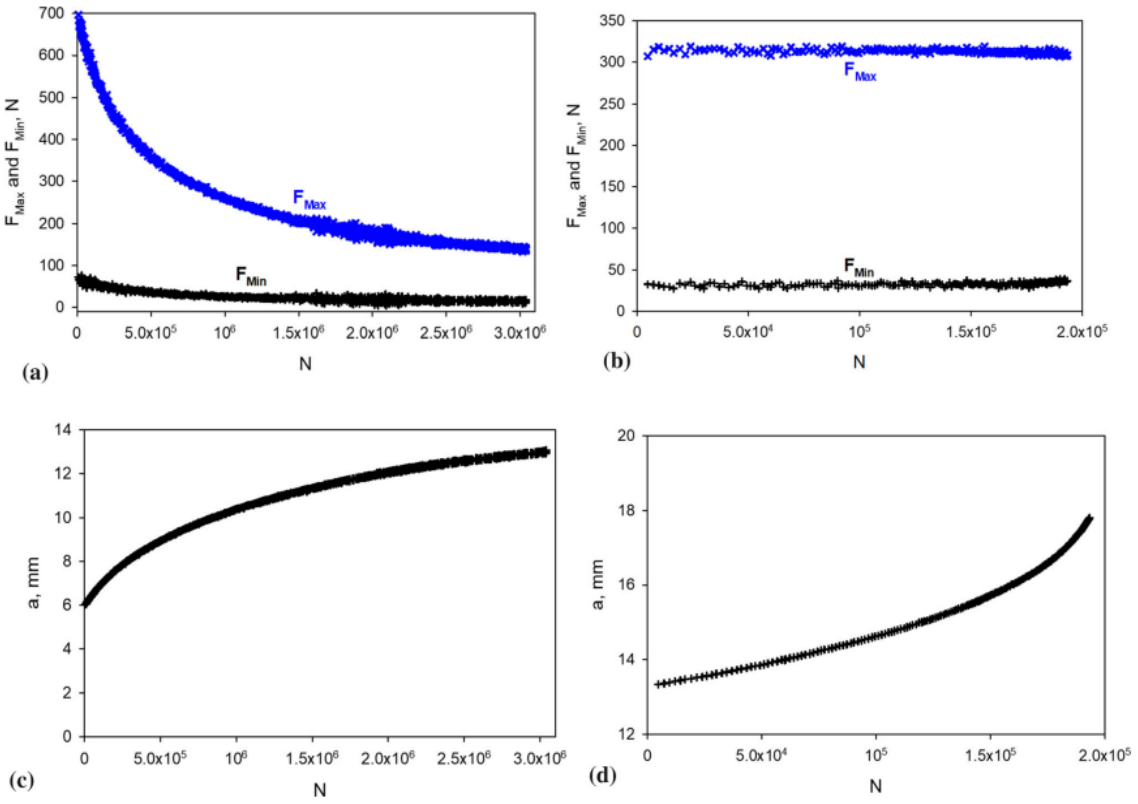

Figure 3.15. An example (for a (CD//BD) sample) of force and crack length data recorded during an FCG test: (a) and (b) maximum and minimum load, (c) and (d) crack length recorded for K-decreasing and K-increasing stage, respectively.

To compare the fatigue crack growth behaviour and resistance of different samples under similar conditions, the data from each test were averaged and smoothed to generate a curve. The smoothing process is depicted in Figure 3.16, where averaged points (indicated by circles) are used to draw a smooth curve that traces these points. This smoothed curve represents the FCG curve for the test. As illustrated in Figure 5.1, such a curve effectively reflects the original da/dN versus ΔK data.

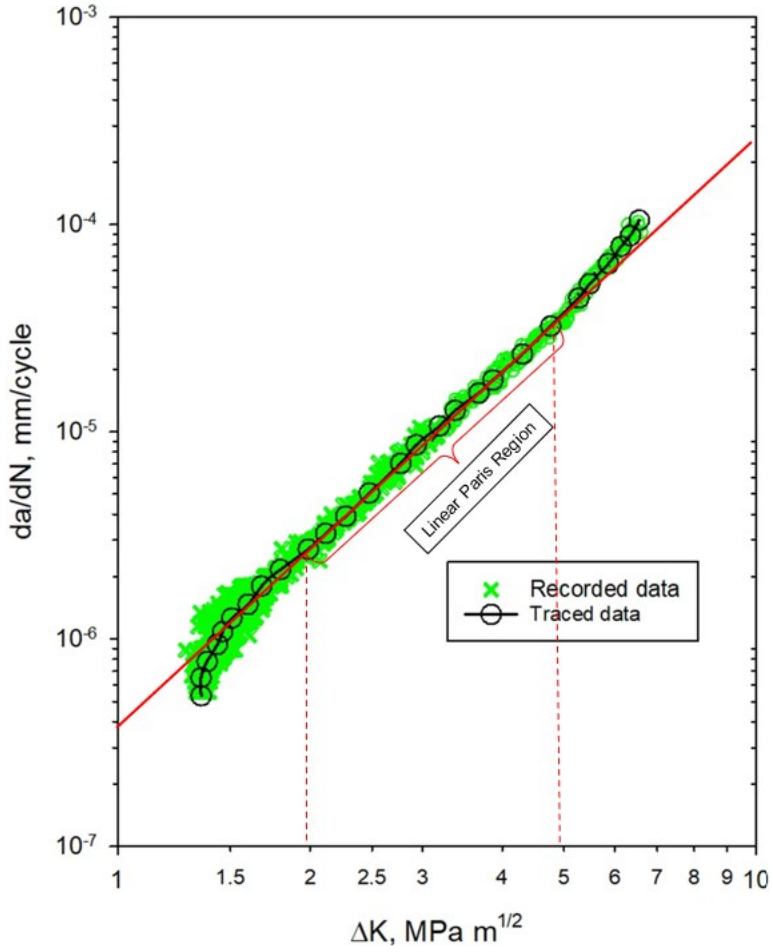

Figure 3.16. Recorded crack growth rate values versus recorded stress intensity factor values plotted together with the traced/smoothed data and smoothed curve (FCG curve) based on the recorded data for a $(CD\text{-}BD)_P+AS_{RT}$ sample.

To characterize the fatigue crack growth behaviour, the Paris law was used (Equation 6). The first step in identifying the Paris law parameters was the determination of the linear region of the da/dN versus ΔK curve, which is known to represent the Paris regime. The linear region was found according to the experimental data to be consistently within the range between ΔK=2 MPa√m and ΔK=5 MPa√m for all tested specimens (dashed lines in Figure 3.16). To determine the Paris parameters C and m, two data points of the smoothed curve were selected from Excel file (Figure 3.17) within the identified linear region. For each of these points, the corresponding values of da/dN and ΔK were extracted from the Excel file. Using the values from two selected points in the Paris equation resulted in a system of two equations with two unknowns. This system was then solved to obtain the values of the Paris law parameters. The example of Paris parameters determination for sample $(CD\text{-}BD)_P+AS_{RT}$ is provided below (Figure 3.17).

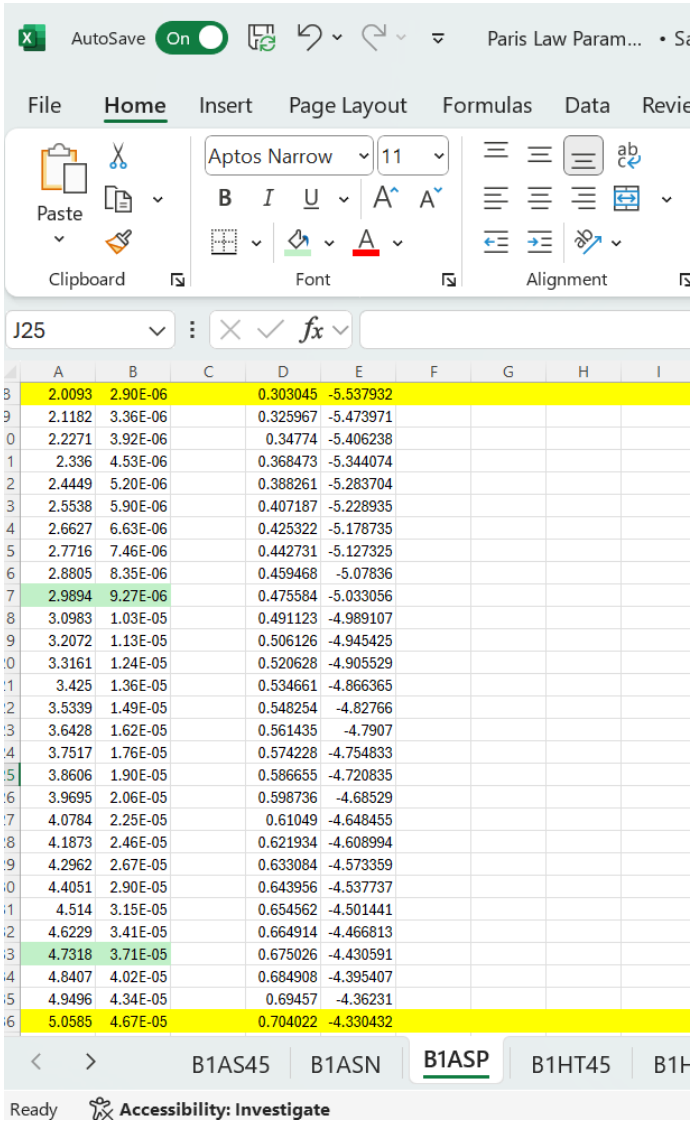

Figure 3.17. Excel data for smoothed da/dN versus ΔK curve for sample $(CD\text{-}BD)_P{+}AS_{RT}$.

From the Excel file of the smoothed curve (Figure 3.17), the border lines were identified for the linear region of the curve, which are ΔK=2MPa√m and ΔK=5MPa√m (marked in yellow). Data points selected are marked in green. Data point 1: ΔK= 2.9894 MPa√m and da/dN=9.27×10^{-6} mm/cycle. Data point 2: ΔK= 4,7318 MPa√m and da/dN=3.71×10^{-5} mm/cycle. Using the Paris Law, the following system of two equations with two unknowns was obtained:

$$9.27 \times 10^{-6} = c \times 2.9894^{m}$$

$$3.71 \times 10^{-5} = c \times 4.7318^{m}$$

$$\downarrow$$

$$0.2499 = 0.631768^{m}$$

$$ln0.2499 = m \times ln0.631768$$

The Parameter m was found as: $m = \frac{ln0.2499}{ln0.631768} = \frac{-1.3867}{-0.4592} = 3.02$. Then, the equation for the first data point was solved for c: $c = \frac{9.27\times10^{-6}}{2.9894^{3.02}} = \frac{9.27\times10^{-6}}{27.3} = 3.4 \times 10^{-7}$

3.3.4 Interrupted tests

The FCG interrupted tests were carried out using the K-decreasing test technique under constant load fatigue loading control mode. After completing the pre-crack process, crack growth was initiated at a specific ΔK value and stopped at another specific ΔK value - well below the fracture toughness (Kc) threshold - to ensure the CT specimen remained intact. Figure 3.18 shows a schematic representation of the CT sample after interrupted FCG test, with the corresponding da/dN vs ΔK curve. The test was set up to interrupt at a crack length of 10.5 mm. The primary purpose of this interrupted test was to analyze and study the crack growth pathway. Detailed examination of crack propagation through the material's microstructure was performed using SEM and EBSD analysis.

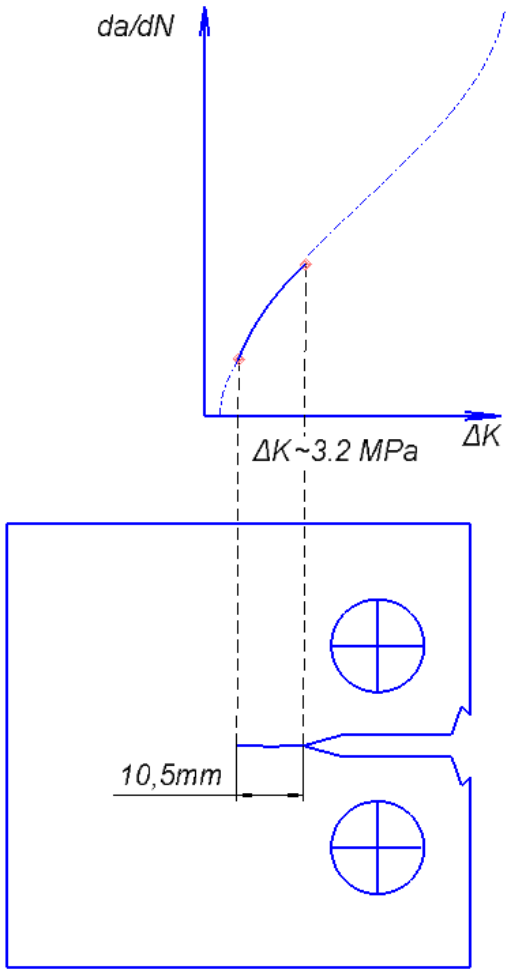

Figure 3.18. Schematic representation of CT sample after interrupted FCG test with the corresponding da/dN vs ΔK curve.

3.4 Microstructure, elemental distribution and failure analysis

3.4.1 Sample preparation

For microstructural examination and microhardness testing, samples were first prepared following the normal metallographic procedure. First, a Stuers Labotom-3 cutter was used to section the samples. After, the specimens were hot mounted with PolyFast in a Struers Labo-Press 3 at 150°C under a pressure of 25 kN. Each sample was then ground using Struers silicon carbide grinding papers with mesh sizes of 180, 500, 1200 and 2400 µm on a Buehler MetaServ rotary grinding machine. Following grinding, the samples were polished with Struers diamond paste on 6 µm MD-Dac fabric. Final polishing included 2 steps and was performed on a Struers TegraPol-25 automatic polisher. The first step was performed using a 3 µm diamond suspension on MD-ol fabric for 3 minutes. The second step was performed using a 0.04 µm colloidal silica suspension on MD-Chem fabric for 1 minute. Cleaning was done between each polishing step using ethanol. For etching, the Keller's solution, containing 2.5% HNO_3, 1.5% HCl, 1% HF, with the balance being distilled water, was used.

3.4.2 Optical microscope

Olympus BX51M was used to observe the microstructure of the samples. Images were captured and ScopePhoto system was then used to record the micrographs. Micrographs were taken at magnifications of x5, x10, x20 and x50. The optical microscope and optical micrographs are presented in Figure 3.19.

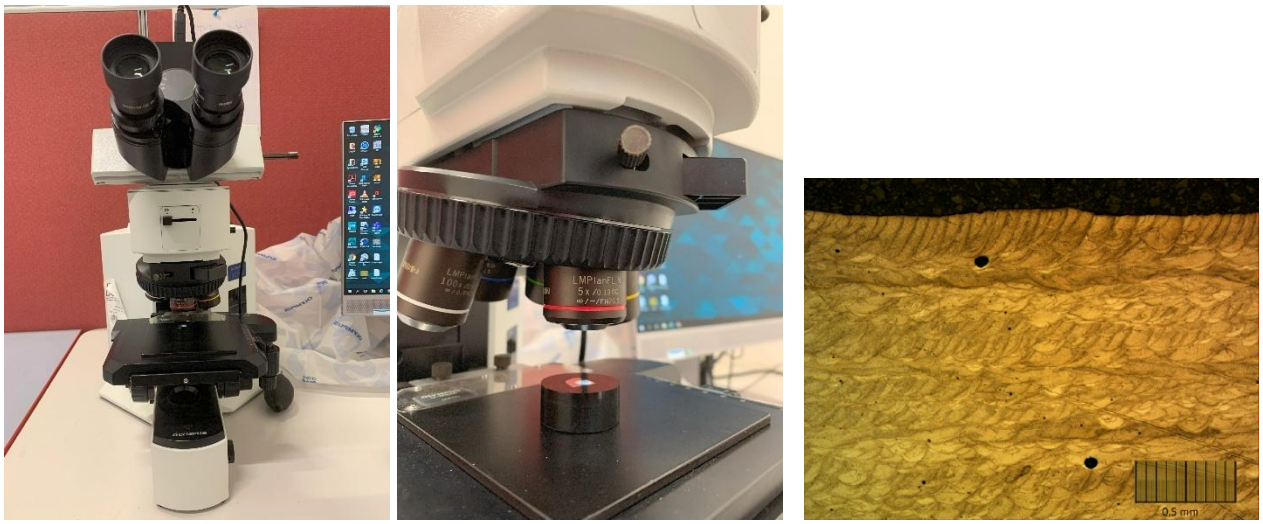

a) b) c)

Figure 3.19. a), b) Optical microscope Olympus BX51M, c) optical micrograph of LPBFed Scalmalloy, ×5.

3.4.3 SEM and EBSD

Hitachi SU-70 field emission scanning electron microscope (SEM) has been used in the current study. An SEM is an electron microscope that creates an image of a sample by emitting a beam of high-energy electrons. The electrons collide with the atoms in the sample to generate signals encoding information about the surface topography, composition, as well as other properties of the sample including electrical conductivity. The ultra-high-resolution imaging (1.0nm/15kV; 1.6nm/1kV) and up to 800,000-fold magnification of such a SEM is offered in the Hitachi SU-70 field emission scanning electron microscope. It is equipped with Energy-Dispersive X-ray (EDX) and Electron Backscatter Diffraction (EBSD) detectors from Thermo Scientific™ (Fig. 3.20).

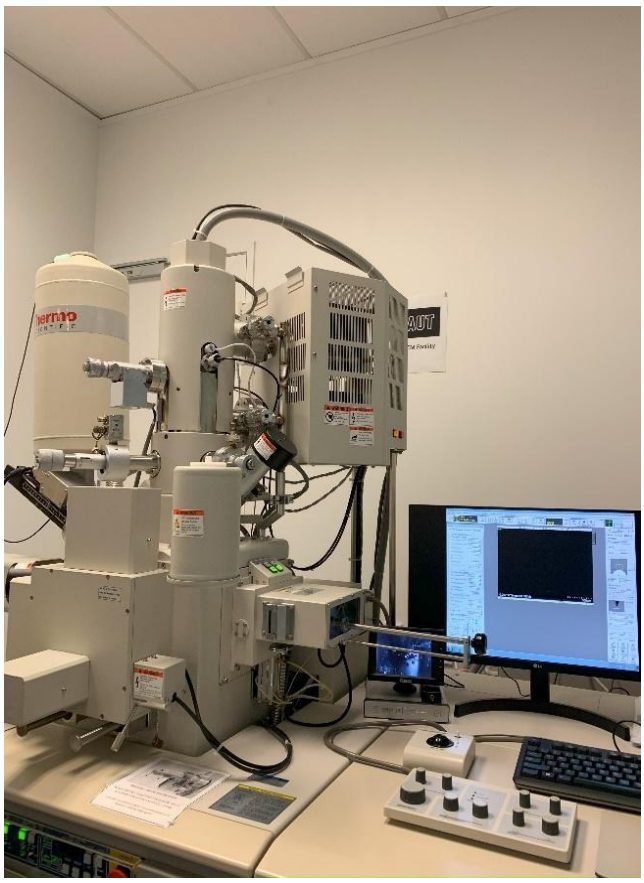

Figure 3.20. JEOL JSM FEG-SEM.

A 15-kV accelerated voltage setting is used in the current study to observe the microstructure and capture images of cross sections of Scalmalloy samples and the fractured FCG and S-N samples. An example of an SEM image for as-built cross section of Scalmalloy samples taken using SEM is presented below (Fig. 3.21).

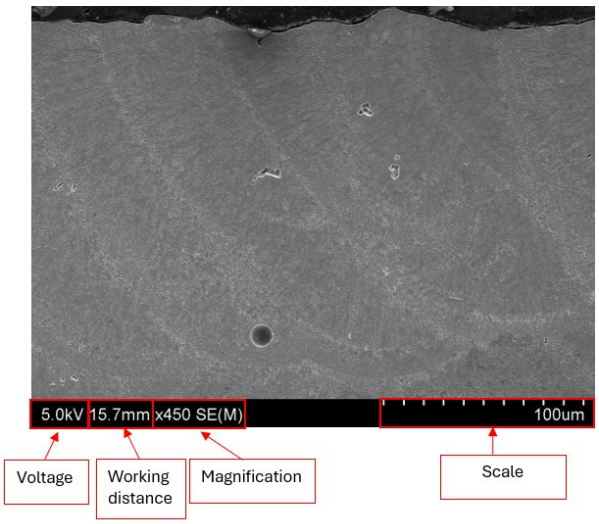

Figure 3.21. An example of an SEM image for as-built cross section of Scalmalloy obtained on Hitachi SU-70 SEM.

After FCG tests, metallographic examinations were conducted on the samples using a Hitachi SU-70 SEM equipped with electron backscatter diffraction (EBSD) capability. EBSD is utilized to collect the sample's crystallographic information while it is inside the SEM machine. The phosphor screen placed in an EBSD detector records a pattern produced by incident electrons from the electron-beam that collide and backscatter elastically from atomic planes of a crystal grain. The pattern (referred to as EBSD pattern) includes Kikuchi bands, through which crystal orientation is identified. The crystal orientation data is automatically detected and acquired through utilizing Thermo Scientific's NSS Spectral Imaging Software. An example of an EBSD crystal orientation map for sample $(CD\text{-}BD)_{45}+AB_{RT}$ after FCG interrupted test provided by the EBSD system is shown in Figure 3.22.

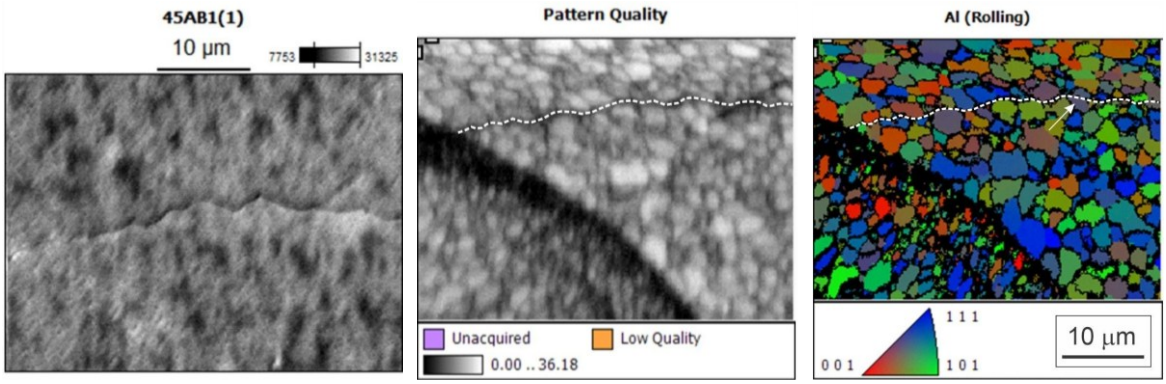

Figure 3.22. EBSD crystal orientation map (right) for $(CD\text{-}BD)_{45}+AB_{RT}$ sample after FCG interrupted test. Note: the color keys "Unacquired" and "Low Quality" appear as part of the EBSD software default scale but are not relevant here.

Additional SEM micrographs in this thesis were provided courtesy of Professor Teresa Guraya, Department of Mining and Metallurgical Engineering and Material Science, University of the Basque Country, Bilbao, Spain. The samples were examined using a JEOL JSM 7000F field-emission-gun scanning electron

microscope with an accelerating voltage of 5 kV, providing high-resolution observation of the microstructures. An example of SEM micrographs obtained through JEOL JSM 7000F is provided below (Fig. 3.23).

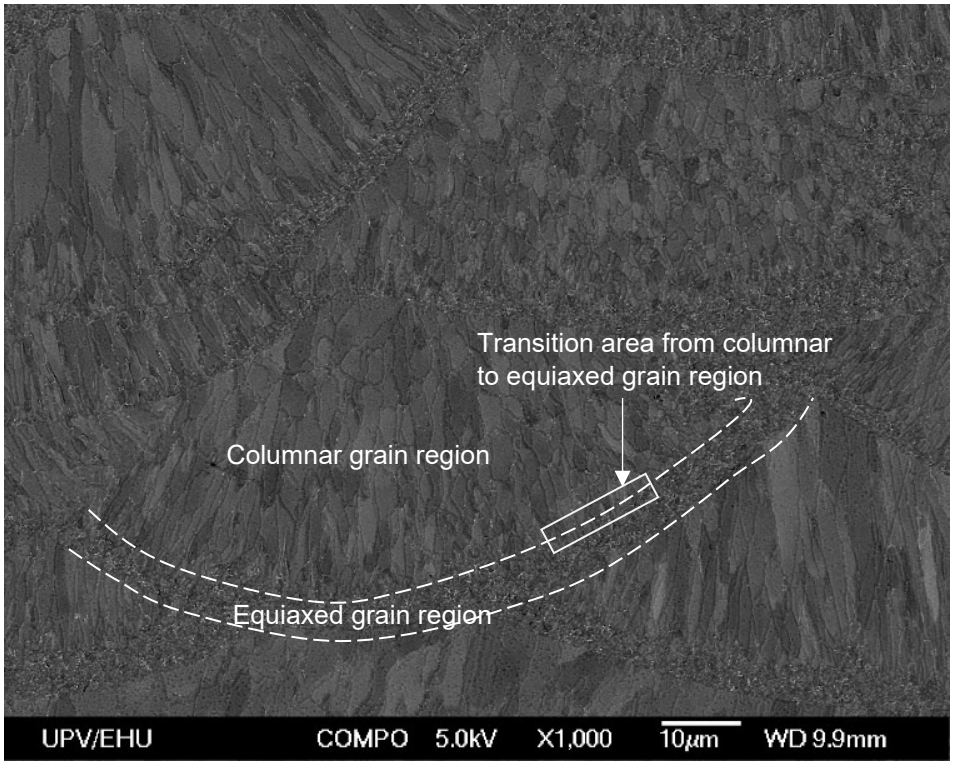

Figure 3.23. An example of an SEM image for heat-treated cross section of Scalmalloy obtained on JEOL JSM 7000F SEM.

3.4.4 TEM (EDS and diffraction)

TEM (Transmission Electron Microscopy) analysis was conducted by the courtesy of Professor Teresa Guraya from the Department of Mining and Metallurgical Engineering and Material Science in the University of the Basque Country, Bilbao, Spain. Lamellae 50-70nm in thickness were prepared in selected locations via standard lift-out protocol, using a Dual beam Helios 650 model, which consists of a 30kV field-emission scanning electron column with 0.9nm resolution and a 30kV Ga Focused Ion Beam (FIB). The location of a lamella can be taken in equiaxed and columnar grain regions or in an equiaxed-columnar boundary region. Figure 3.24 is an example showing a lamella being taken out from a columnar grain region. The lamellae were analysed using Talos F200i field emission gun transmission electron microscope (FEG-TEM) equipped with a Bruker X-Flash100 XEDS spectrometer.

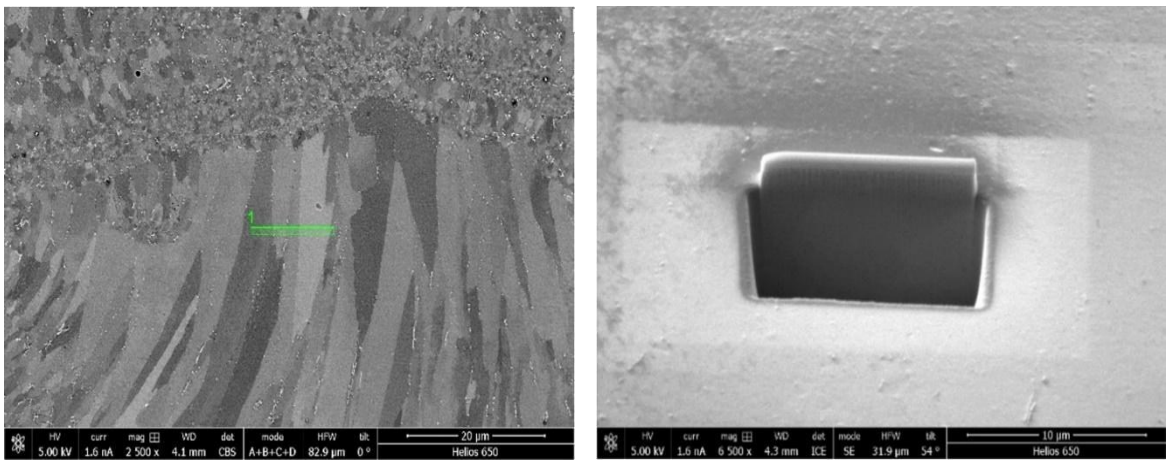

(a) (b)

Figure 3.24. Illustration of a TEM lamellae being taken: (a) FEG-SEM micrograph showing an equiaxed grain region on top of a columnar grain region with the lamella to be taken in the columnar grain region indicated by the green rectangular, and (b) the material in the front part having been taken out by FIB with material behind to be further taken out to form a lamella.

An example of TEM images of the equiaxed region in as-built sample is provided below in Figure 3.25. All TEM images of as-built, T6, T5 and samples after solutionizing only for three regions – columnar, equiaxed and transition (indicated in white in Figure 3.23) – are presented in Appendix C.

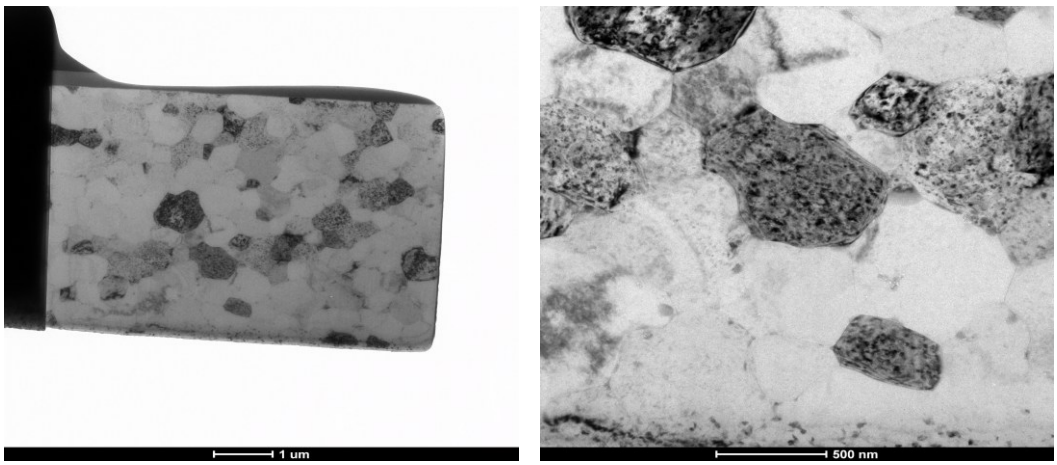

Figure 3.25. TEM image for equiaxed grain region of LPBFed Scalmalloy.

Elemental maps were performed by X-ray energy-dispersive spectroscopy (XEDS) in the STEM mode under high annular dark field (HAADF) detector for Z contrast imaging in STEM conditions, with a camera length of 200mm using a pixel size of 2nm, a dwell time of 900s and an image size of 512x512 pixels. Moreover, EDX microanalyses were carried out using a probe current of 800pA and a semi-convergence angle of 6 mrad. Velox software was used for the compositional map acquisition and processing. In elemental mapping using XEDS, an electron beam is two-dimensionally scanned over a specimen area and the characteristic X-ray spectra generated by the electron beam are acquired pixel by pixel. From those spectra, the X-ray intensities

or the calculated concentrations of the target elements are displayed pixel by pixel, to create an elemental map. An example of TEM and corresponding elemental maps of equiaxed grain region for T6 sample with the analysis is provided below in Figure 3.26.

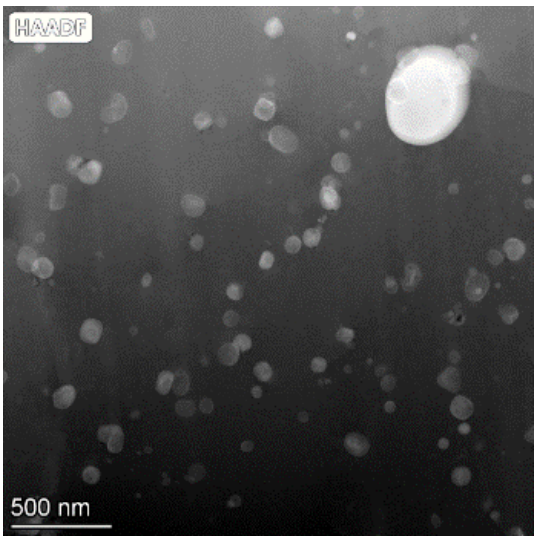

TEM

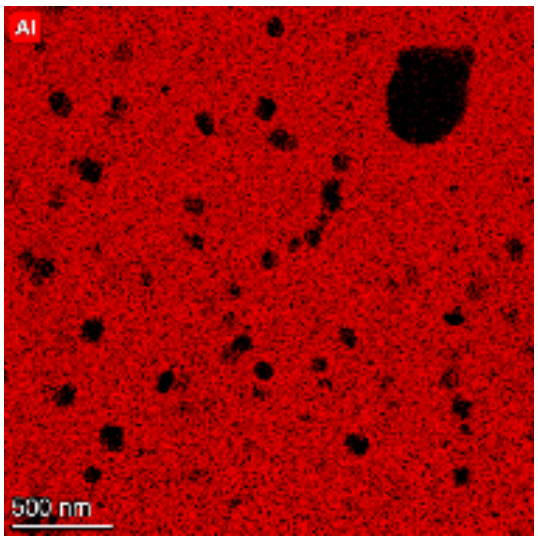

Al

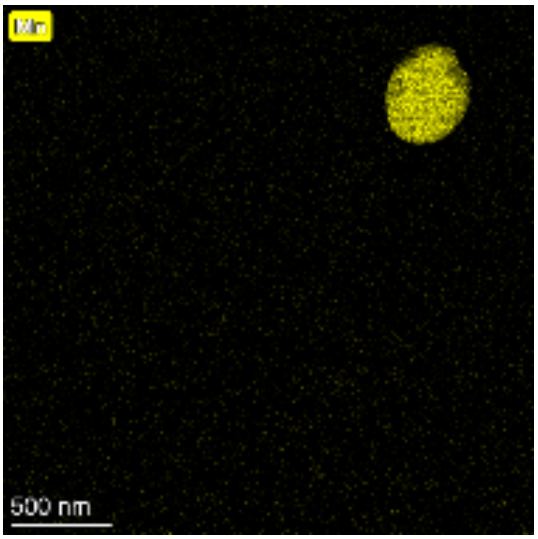

Mn

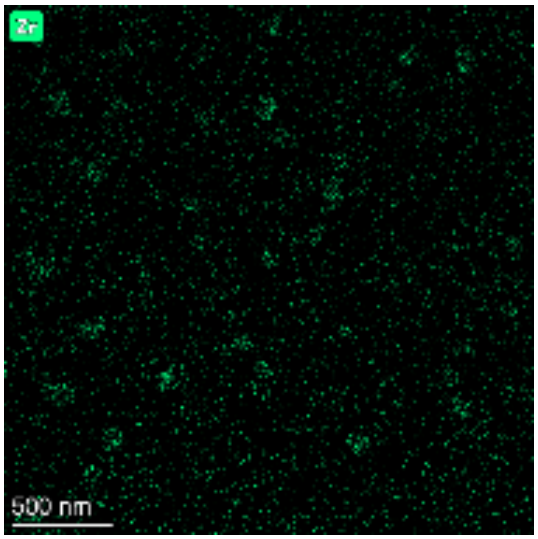

Zr

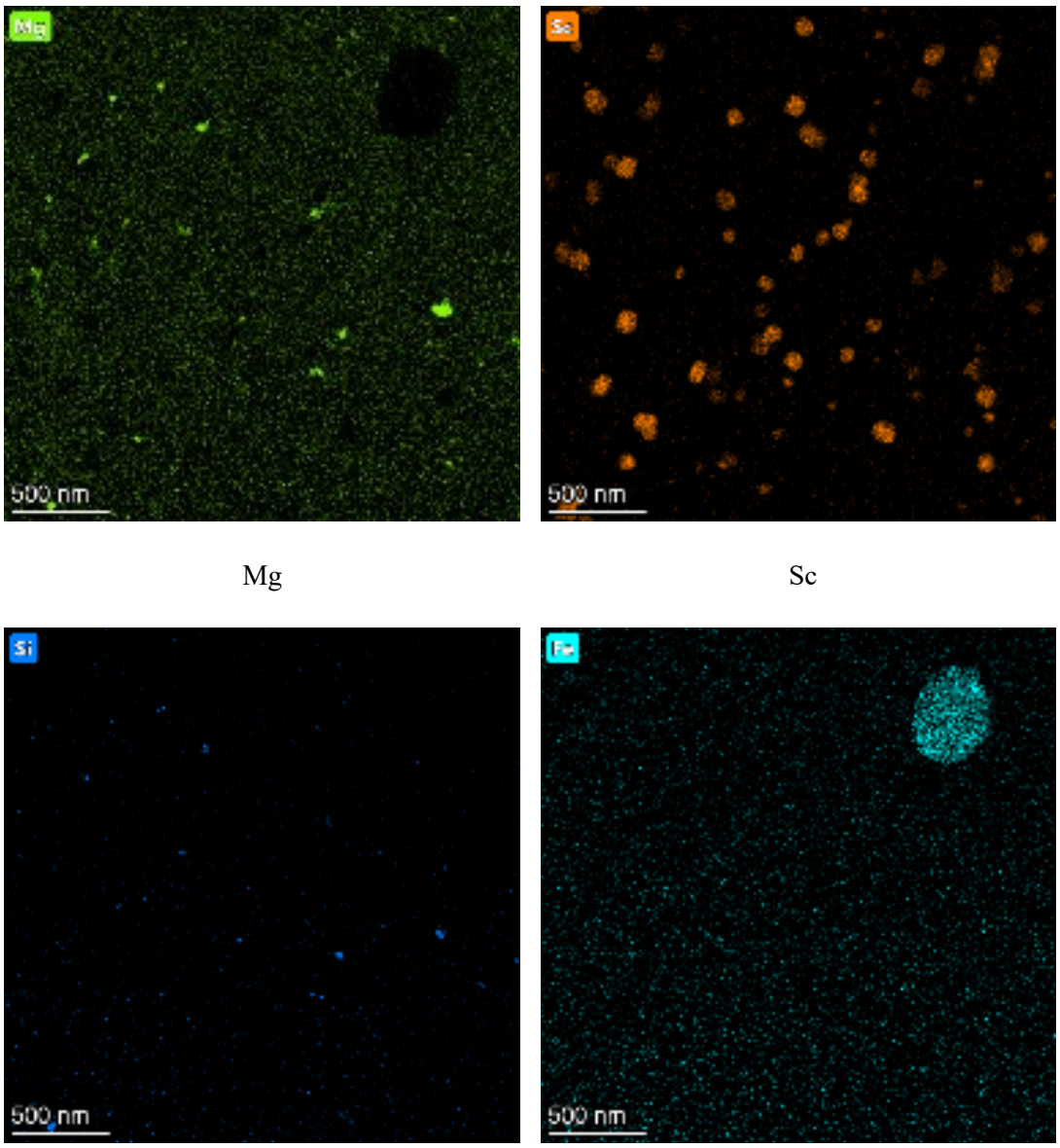

Figure 3.26. TEM and elemental maps of equiaxed grain region for T6 sample.

The Al-depleted region observed in the Al map corresponds to bright particles in the TEM image that is rich in Mn and Fe, as indicated in the respective elemental maps, suggesting the formation of a Mn-Fe-rich particle. The Sc and Zr maps reveal the presence of relatively large particles, approximately 100 nm in size, that are enriched with these elements, likely corresponding to primary Sc- and Zr-containing precipitates. The Mg map shows that magnesium is mainly distributed uniformly in the solid solution, however, some areas enriched with magnesium and correlating with the spots on the Si map are observed, suggesting the presence of Mg2Si particles.

Selected area diffraction patterns (SADP), a crystallographic experimental technique that is performed by using a transmission electron microscope, were obtained for as-built samples and samples after T5 and T6 to identify the superlattice structure that confirms the presence of Al_3(Sc,Zr) particles. In the current study, the superlattice structure was captured in T6 sample only (after II-step heat treatment). In the SAED pattern, each

obtained spot corresponds to a satisfied diffraction condition. An example of SADP for samples after T6 is presented below in Figure 3.27.

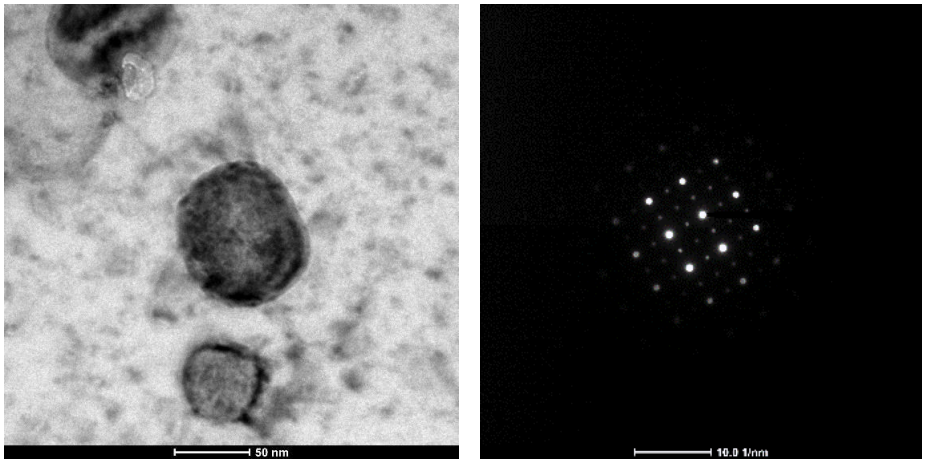

Figure 3.27. TEM image (a) and SADP (b) of the particle observed in the equiaxed region of sample after T6.

To determine the Miller indices (h, k, l) for the diffraction spots in the diffraction pattern, the following steps were completed:

1. Identifying the Zone Axis. The diffraction pattern represents a projection of reciprocal lattice points along a specific zone axis. The centre of the pattern corresponds to the transmitted beam (direct beam), which is a 000 reflection. The symmetry of the pattern helps determine the zone axis. Common zone axes for FCC materials include [110], [101], [011].

2. Measurements of the Interplanar Spacings. The reciprocal space distance of each spot from the centre is proportional to $\frac{1}{d_{hkl}}$, where d_{hkl} is the interplanar spacing for a given Miller index. Using the scale bar provided on SADP, the distances of the spots from the center were measured. After, Bragg's Law has been used:

$$d_{hkl} = \frac{\lambda L}{R}$$

Where λ is the electron wavelength, L is the camera length, R is the measured radius from the centre spot to a diffraction peak.

3. Identifying the Lattice Type. If the material is FCC (as in aluminum-based alloys), only reflections where h, k, l are all even or all odd are allowed. If additional weaker reflections appear at forbidden positions (e.g. (100), (110)), they indicate a superlattice structure, such as $Al_3(Sc,Zr)$, with an $L1_2$ ordering).

4. Indices identification based on their relative spacing. The smallest radius spots correspond to (100) or (110) for an ordered phase. The second set typically corresponds to (200) or (220). Higher order reflections (e.g., (300), (310), (222)) appear at larger distances. An example of SADP from Figure 3.27 with indices assigned is provided below in Figure 3.28.

.

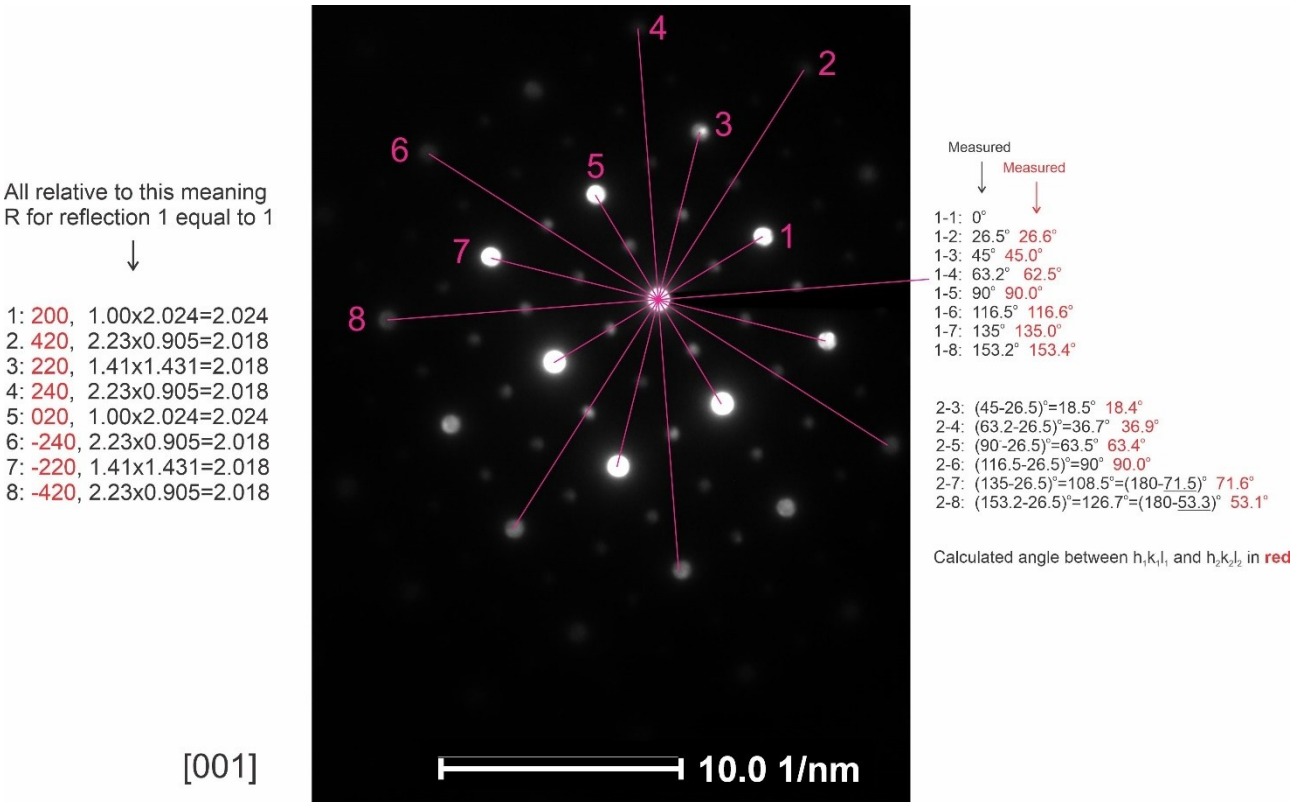

Figure 3.28. An example of SADP from Figure 3.27 with indices assigned.

Chapter 4 - Mechanism of bimodal grain formation

This chapter begins by presenting the generally known track appearance and the bimodal grain structure of the alloy in as-built state. Our observations on intermetallic particles that distribute differently in equiaxed grains and in columnar grains in as-built state will then be detailed. This is followed by presenting the determined elemental distributions that also differ in the different grain regions. Solidification path, segregation and whether particles may form in a region of the track are then considered, based on the equilibrium phase diagram and non-equilibrium phase diagrams and on location specific LPBF thermal conditions. These thus explain why bimodal grain structure forms during LPBF of the alloy. Analysis of aged samples will be shown to support the reasons for segregation patterns and particle distributions found in the as-built state. Finally, the identified mechanism of bimodal grain formation will be summarised.

4.1 Microstructures in as-built state

4.1.1 Track appearance, equiaxed grains and columnar grains

The optical microscopy images of the cross-sections of the melt pools are presented in Fig. 4.1. This clearly shows a pattern of stacked "weld" tracks, caused by the printing pattern (Fig. 1.3) that was followed during the LPBF process. As seen on the micrograph, the average hatch spacing is 70 µm, slightly higher than the hatch spacing used in LPBF experimental setup as it depends on the cross-sectioning angle—cutting at an angle other than 90° to the build direction can artificially increase the measured hatch spacing. The last layer, n layer, which includes the top surface, is approximately 112 µm. The previous layer, $n-1$ layer, has thickness of 35 µm, which is close to the layer thickness used in LPPBF experimental setup. However, tracks are not consistent in depth and height due to the use of pulsed laser and 67° rotation during the LPBF and thus, layer thickness cannot be read directly from the micrographs because of the combined effects of pulsed energy input and rotated scan vectors lead to extensive remelting and overlapping of melt pools across layers.

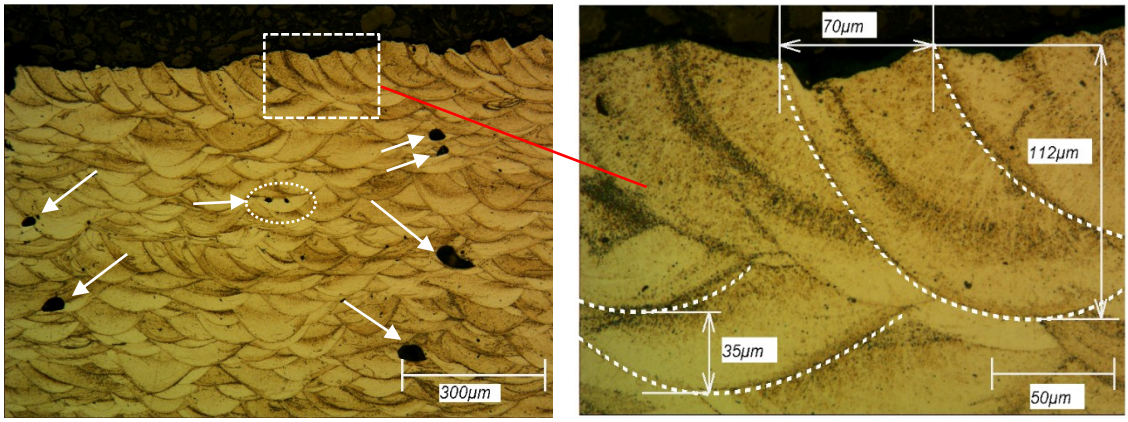

a) b)

Figure 4.1. Optical micrographs of an as-built sample with various features indicated a) x10, b) x50.

Examination of sample cross sections has revealed that LPBFed Scalmalloy samples have microstructure defects of pores up to 50 µm in diameter between the layers, these pores are marked with arrows in Figure 4.1 (a). Despite the tracks being well overlapped, these defects are identified as LOF. The presence of small LOF pores, in size of around 10- 15 µm, can hardly be detected (marked in dash oval in Figure 4.1 (a)), although the large LOF in size of around 50-100 µm are more common. It must be noted that, due to the nature of LPBF process (layer-by-layer melting), LOF is a very common type of defects and has been widely observed in the literature (102), (114) and it has not been reported LOF-free microstructure in samples produced by LPBF.

Grains can be shown clearly in higher magnification micrographs taken using SEM, shown in Fig. 4.2. SEM analysis showed that equiaxed grain region is around 10 µm wide with the grain size from 0,5µm to 1µm. Columnar grain size varies much more and is from 3 to 15µm. These observations have been later confirmed through TEM analysis, as presented in Figure 4.4, which provides a more detailed resolution of grain boundaries that is not clearly visible in the SEM images. (Fig. 4.2). Additional SEM micrographs for Scalmalloy samples in as-built, T5, T6 and after solutionizing only are presented in Appendix B.

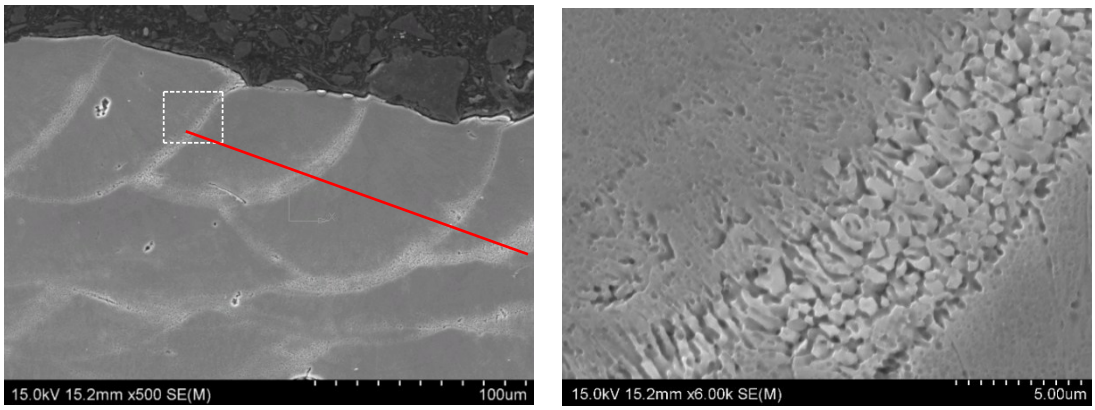

a)

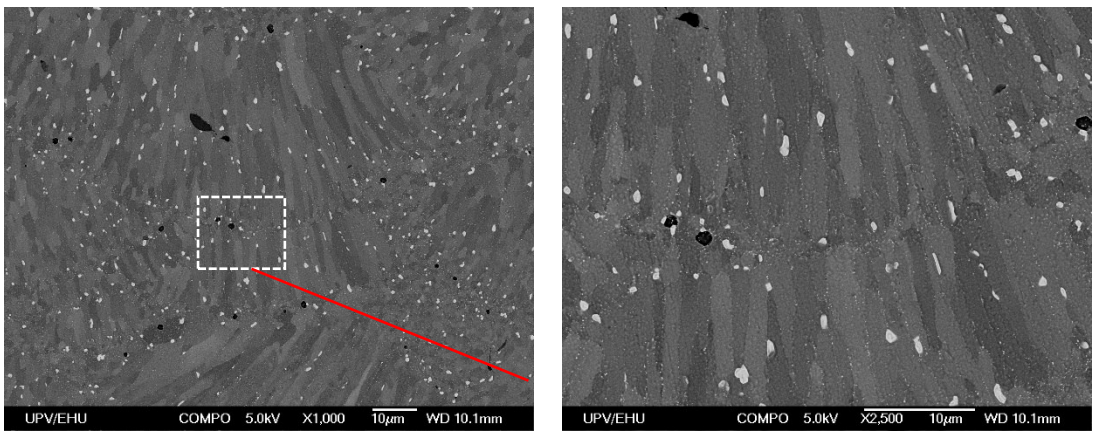

b)

Figure 4.2. SEM image of XZ-plane obtained from as-built sample obtained on a) Hitachi SU-70 SEM, b) JEOL JSM 7000F SEM.

The experimental observations presented align with the literature review on Scalmalloy and its processing characteristics. The literature review demonstrates that Scalmalloy has a bimodal microstructure consisting of fine equiaxed grains and coarse columnar grains. This aligns with the experimental findings in the present study that confirm a similar bimodal microstructure in the as-built samples. Also, the literature review describes the expected microstructural features: fine, equiaxed grains at the base of melt pools and coarse, columnar grains growing in the direction of heat flow. The experimental results demonstrate this, as the optical and SEM images show a clear difference between the fine grain region (0.5 to 1 µm) and the coarse columnar grains (3 to 15 µm). Thus, the experimental results confirm the representation of Scalmalloy's microstructure observed in the literature.

4.1.2 Distribution of intermetallic particles

In this study, three different regions in the Scalmalloy microstructure have been investigated: the equiaxed grain region (zone 1), the transition area from equiaxed grain region to columnar grain region (zone 2) and the columnar grain region (zone 3), as illustrated in Figure 4.3. These zones have been investigated using Transmission Electron Microscopy (TEM), and TEM images are presented in Figure 4.4. The lamellae have been extracted at 90 degrees to the LPBF building direction (xy plane), as indicated by the red marking in Figure 4.3. with the view direction indicated by the red arrows, which aligns with the positions and orientations in Figure 3.23.

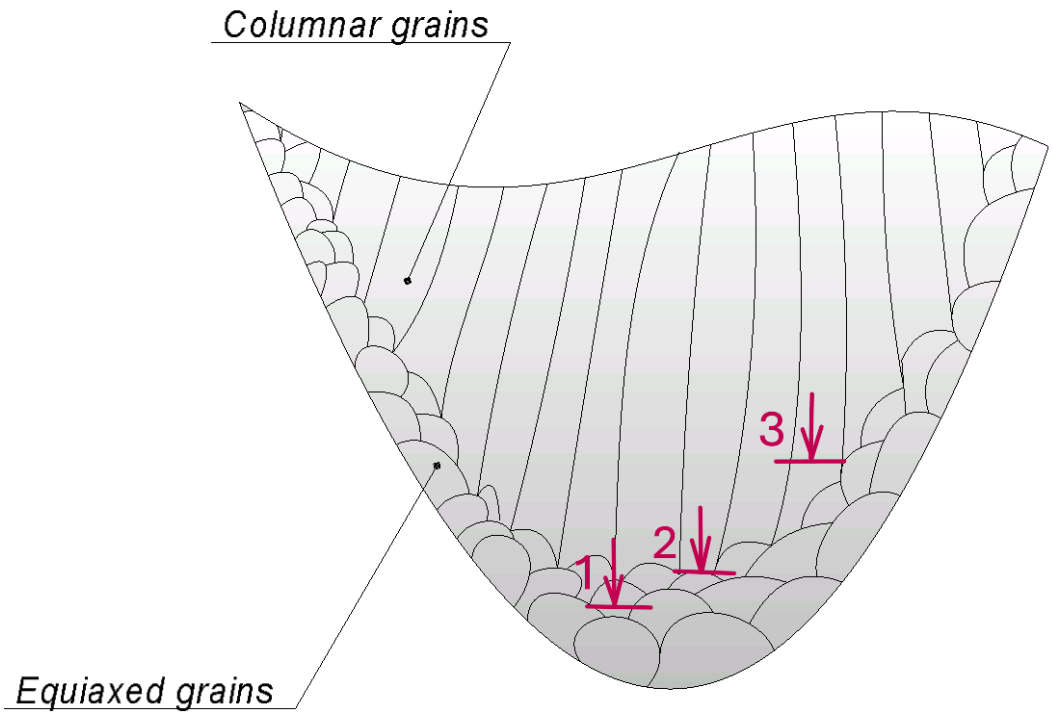

Figure 4.3. Schematic representation of areas chosen for investigation.

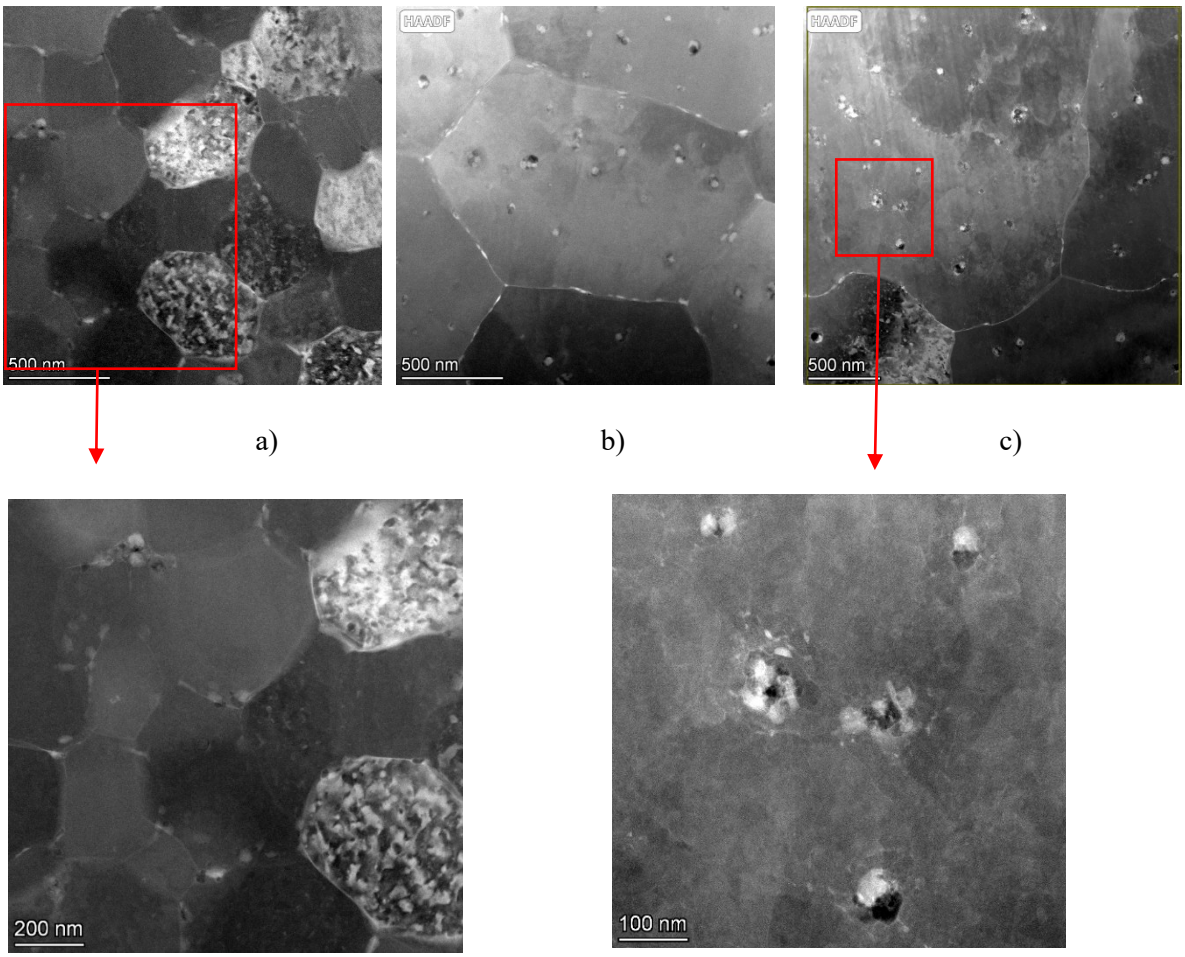

Figure 4.4. TEM images of as-built state in a) equiaxed grains region (zone 1), b) transition area (zone 2), c) columnar grains region (zone 3).

In Figure 4.4, different distributions of particles across these microstructural regions have been observed. The equiaxed-grain region is characterized by a lack of particles within the grains (no intragranular particles), as shown in Figure 4.4.a. However, some chains of particles, located between grains (transgranular) are observed. In contrast, in the transition region (zone 2) and columnar grain region (zone 3), particles are evident within the grains as well as between the grains – both intragranular and transgranular (Fig. 4.4.b and Fig. 4.4.c.). TEM imaging revealed the presence of particles with different sizes and contrasts:

- In the equiaxed-grain region (zone 1), Figure 4.4.a, bright, white particles predominantly located along the grain boundaries with sizes ranging from 20 to 30 nm are observed. Smaller dark particles with dimensions between 10 and 20 nm are found along the grain boundary.
- In the columnar grain region (zone 3) and transition area (zone 2), Figure 4.4.c, the analysis uncovered large, bright particles with an approximate size of 75 nm, alongside smaller, darker particles ranging from 35 to 50 nm.

In the equiaxed-grain region, the absence of intragranular particles and the predominant presence of particles along the grain boundaries suggest that this region allows sufficient elemental diffusion to grain boundaries during LPBF solidification, providing sufficient time for particles to precipitate. In contrast, the transition and

columnar grain regions exhibit both intragranular and transgranular particles, which may indicate a different diffusion behaviour, influenced by high cooling rates. This observation demonstrates the difference in particle formation and distribution across the track; thus, in the subsequent section, the elemental distribution in the equiaxed, transition and columnar regions will be further examined.

4.2 Elemental distribution in as-built state

4.2.1 Distribution in equiaxed grain region

Transmission Electron Microscopy (TEM) coupled with Energy Dispersive X-ray Spectroscopy (EDS) provides information about the microstructure and composition of materials at the nanoscale. The following observations, obtained through TEM images and EDS elemental maps, show the distribution of key elements in the equiaxed-grained region of the Scalmalloy sample. TEM image and elemental maps taken from the equiaxed-grained region are presented in Fig. 4.5.

- From TEM and Mg map: in the equiaxed grain region, Mg particles are segregated along the grain boundaries.
- From TEM and Fe map: bright particles correspond to Fe-rich intergranular particles.
- From Sc, Zr maps: no evidence of Sc/Zr-rich particles in the equiaxed grain region has been found.

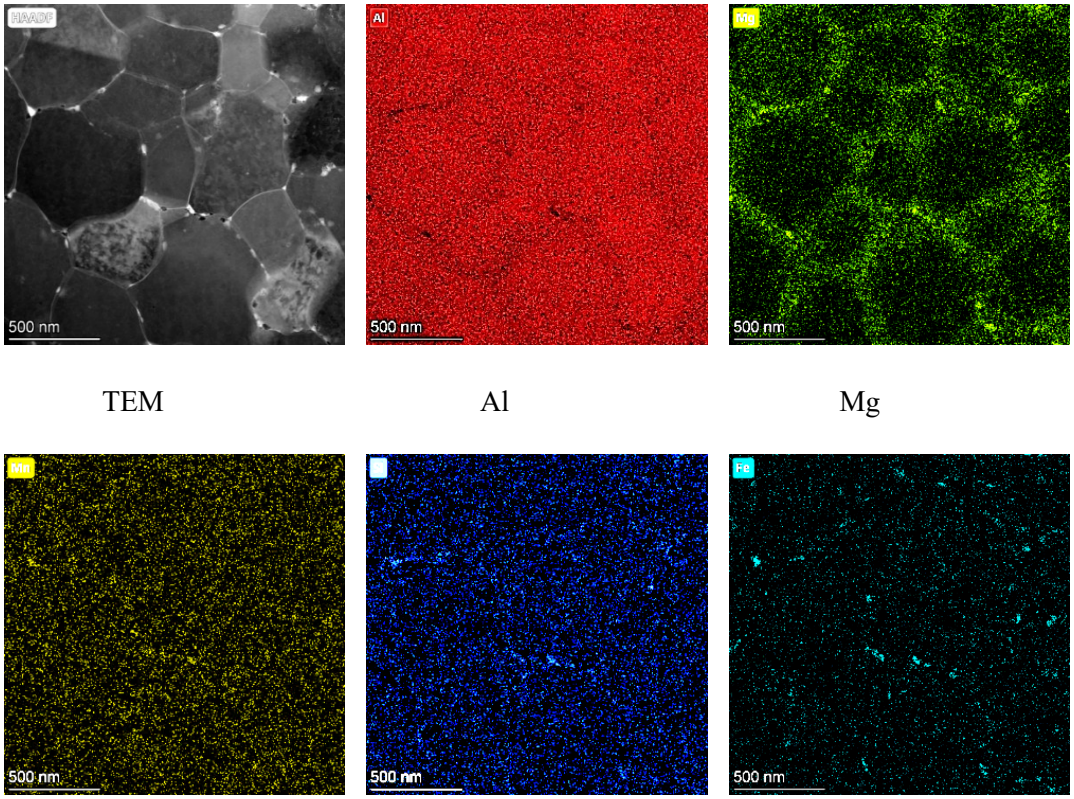

TEM Al Mg

Mn Si Fe

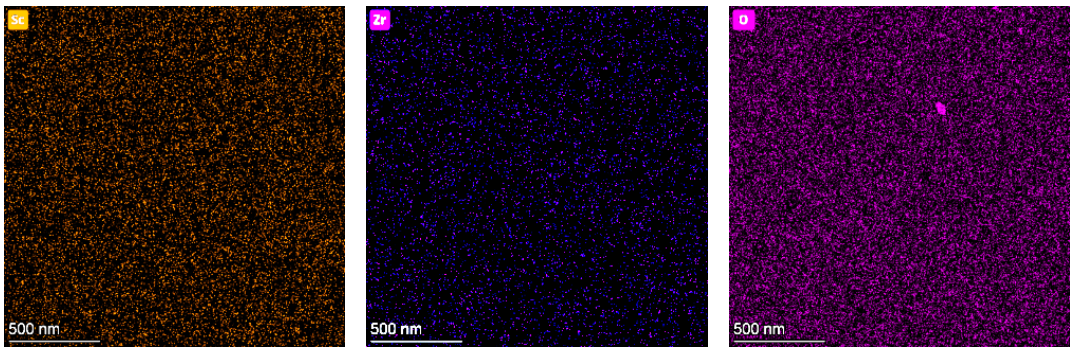

Sc Zr O

Figure 4.5. TEM-EDS elemental maps of the area shown by the TEM image taken in the equiaxed grain region.

From the TEM image above together with the corresponding EDS elemental (Al, Mg, Sc, Mn, Si, Zr, Fe, and O) maps in Figure 4.5, two major features of the equiaxed grain region can be observed. The first is that no Sc/Zr-rich particles can be detected. The second feature of the equiaxed region is the segregation of Mg along the grain boundaries, not just the very rich Mg particles, as is clear in the Mg map. Particles can be observed along the grain boundaries and these particles are rich in Mg and Si or in Fe possibly containing Mn, however these particles are not Sc or Zr-rich. Sc and Zr in as-built state do not segregate in the equiaxed grains region but are homogeneously distributed in the material in solid solution that enables post-process age hardening. The absence of Sc/Zr particles in the equiaxed grain region suggests that the fine equiaxed grains formed during the early stage of solidification next to and along the track boundary did not result from having the 50-100 nm (large) size Sc/Zr particles, as there are none. Inside the grains, there are no particles (of a few to a few tens of nanometres in size), as has already been pointed out. As is shown in Table 3.1, Scalmalloy contains Fe and Si. Thus, Mg_2Si- and Fe-containing intermetallic particles form in the later stages of solidification and are present in the grain boundary regions, as is commonly known in cast Al-alloy solidification.

4.2.2 Distribution in equiaxed-columnar transition grain region

From EDS analysis of transition area (from columnar to equiaxed grains, zone 2, as referred to in Fig. 4.3 and Fig. 4.4), it can be seen (Fig. 4.6):

- From Sc, Zr maps: no evidence of Sc and Zr segregations and no Sc/Zr-rich particles have been found.
- From Mg map: Mg segregations are still observed along the grain boundaries but also some Mg-rich particles are found inside the grains as spots.
- From Si map: Si-rich particles formed inside the grains as spots.
- From TEM image, Mg, Si maps: TEM image is consistent with the EDS maps suggesting Mg_2Si particles in size 70-90 nm formed.

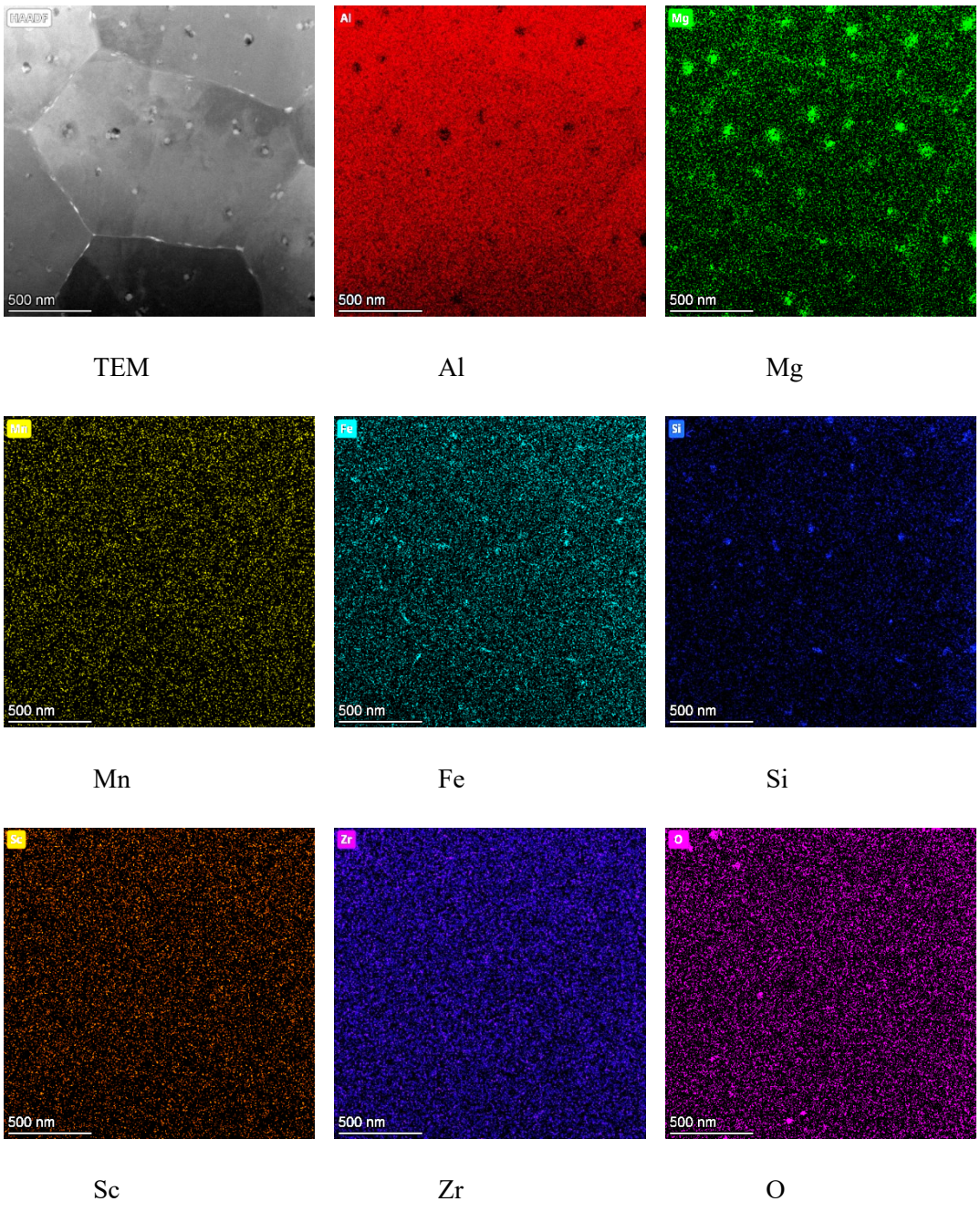

Figure 4.6. TEM-EDS elemental maps of the area shown by the TEM image taken in the transition grain region.

Moving slightly away from the track boundary, in the transition region between equiaxed and columnar grains, as shown in Fig. 4.6, distinct microstructural and compositional features have been revealed. The TEM image, coupled with EDS elemental maps, indicates that Mg continues to segregate along grain boundaries, similar to the equiaxed grain region, however in the transition area, additional Mg-rich particles are also observed inside the grains. These intragranular Mg concentrations, along with the Si distribution map, which similarly shows Si-rich particles within the grains, suggest the presence of second-phase particles. The overlapping presence of Mg and Si within the same regions in the TEM and corresponding EDS maps suggests the formation of Mg-Si intergranular particles, potentially Mg_2Si, with an approximate size of 70–90 nm. Importantly, similar to the equiaxed grains region, no segregation or clustering of Sc and Zr is detected in the transition region, and no

Sc/Zr-rich particles are present, as confirmed by their elemental maps coupled with TEM image. Thus, it can be concluded that Sc and Zr remain in solid solution within the transition zone, and do not contribute to particle formation at this stage.

4.2.3 Distribution in columnar grain region

Fig. 4.7 shows the TEM-EDS elemental maps of the area shown by the micrograph (top left) taken from a columnar region of the as-built sample as shown in Fig. 4.4. These maps indicate:

- From TEM image, Al, Mg and Si maps: Most Al-depleted particles shown in the Al maps are Mg- and Si-rich in Mg and Si maps, respectively, suggesting these are Mg_2Si. Compared to the equiaxed grains region, Mg segregation is considerably less visible along the grain boundaries (Fig. 4.5).
- From TEM image, Al, Mn, Fe maps: Bright particles on TEM are presented on Mn and Fe maps, they are likely to be $Al_6(Mn,Fe)$.
- From TEM image, Al and Sc map: there appears to be no Al_3Sc particles detectable and Sc appears to be evenly distributed.

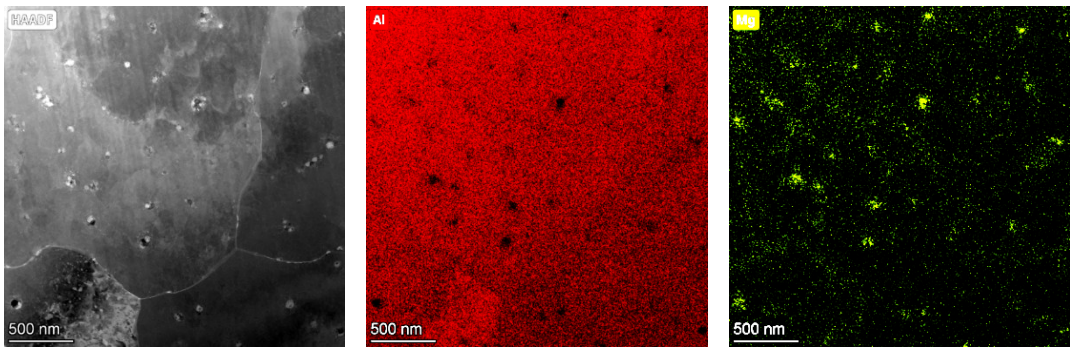

TEM Al Mg

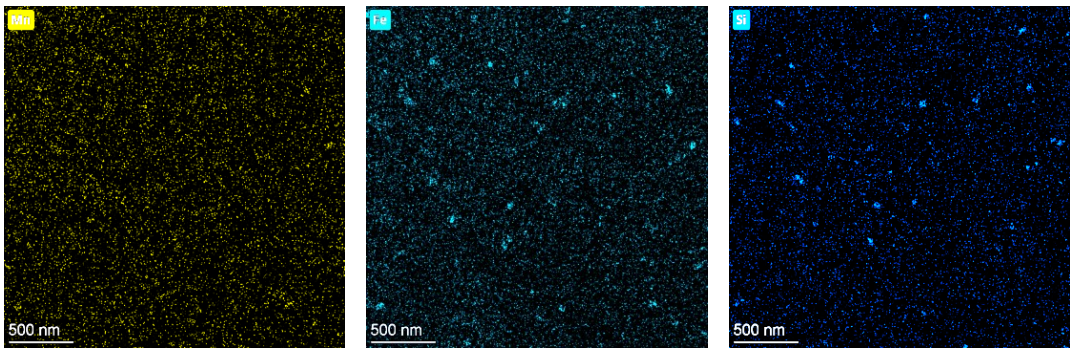

Mn Fe Si

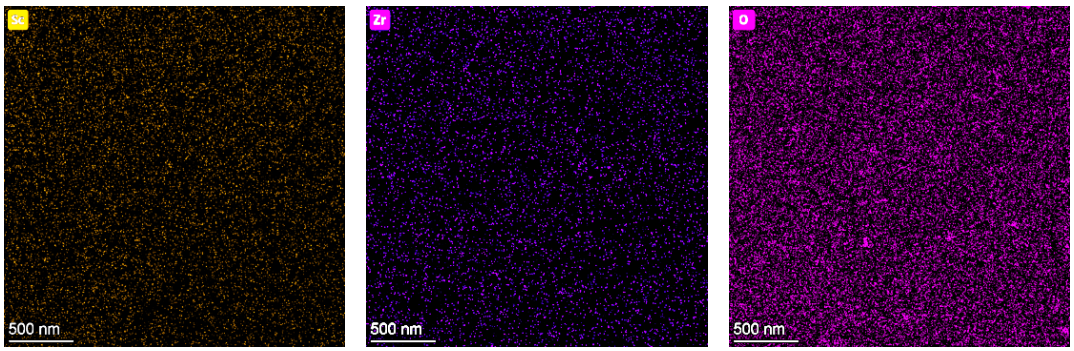

Sc Zr O

Figure 4.7. TEM-EDS elemental maps of the area shown by the TEM image taken in the columnar grain region.

The brief description above has shown, that away from the equiaxed-grain region, the features shown in the TEM image and EDS elemental maps in Figure 4.7 are very different for the columnar grain region and almost opposite to those observed in the equiaxed-grain region. First, particles that appear to be Mg–Si rich and Fe rich are mostly observed inside the grains as against being frequently at the grain boundaries in the equiaxed-grain region. As has been pointed out, referring to Figure 4.6, in the coarser grain side of the equiaxed-grain region bridging to columnar grain region (transition zone), particles are also present inside the grains. Again, as indicated by the Sc and Zr maps in Figure 4.7, there is no detectable presence of Sc- or Zr-rich particles. Second, the Mg map in Figure 4.7 suggests only a weak enrichment of Mg in the grain-boundary areas of the columnar grain region, very different from the strong grain-boundary Mg enrichment in equiaxed-grain region shown in the Mg map in Figure 4.5.

The columnar grain region has been further examined at higher magnification (Figure 4.8) to precisely investigate the composition and the size of the particles observed:

- From TEM image, Al, Mg, Si and Al, Mn, Fe maps: Al-depleted particles shown in the Al maps are Mg-Si rich and Mn-Fe rich, suggesting they are likely to be Mg_2Si and $Al_6(Mn,Fe)$ particles.
- From TEM image, Al and Sc map: there appears to be no Al_3Sc particle detectable and Sc appears to be evenly distributed.

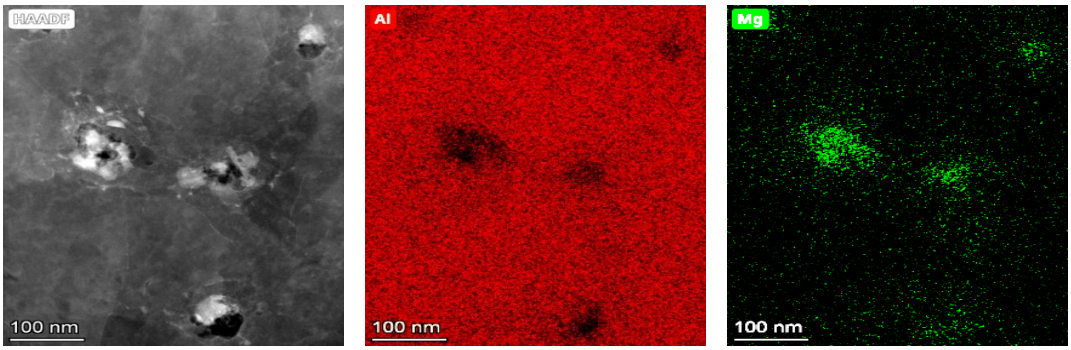

TEM Al Mg

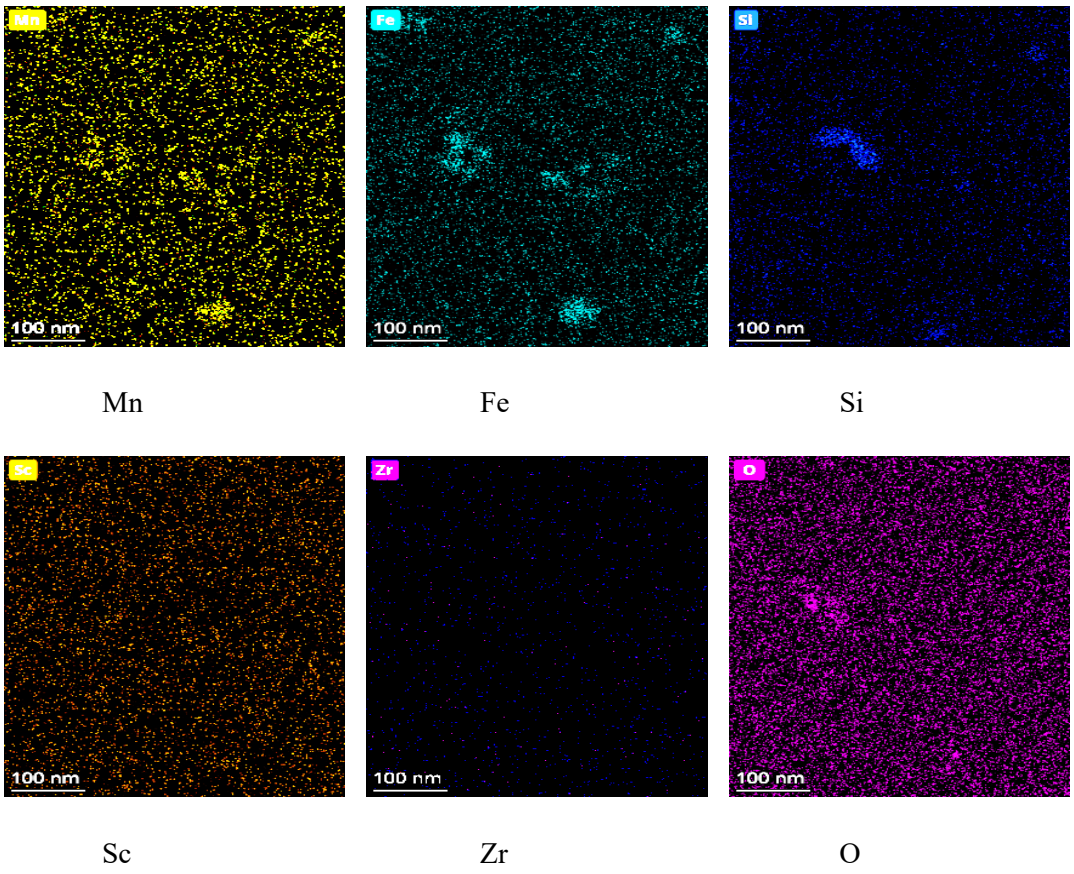

Figure 4.8. EDS mapping of columnar-grain region in as-built state at high magnification.

The Al elemental map shows the presence of Al-depleted regions, which correspond to bright particles in the TEM image. The composition of these particles suggests the formation of Mg_2Si and $Al_6(Mn,Fe)$ intermetallic phases. Specifically, bright particles observed in the TEM image correlate well with Mg and Si-rich zones, indicative of Mg_2Si particles in size of 50-100 nm. Additionally, the presence of bright, roughly 50-100 nm Mn-Fe-rich particles can be observed. Importantly, no evidence of $Al_3(Sc,Zr)$ particles is found at higher magnification, as confirmed by the uniform distribution of Sc in the corresponding map and the absence of localized Sc,Zr-rich zones. This indicates that both Sc and Zr remain in solid solution in this region.

4.3 LPBF and solidification path

4.3.1 Solidification based on equilibrium phase diagram

The LPBF-induced elemental distributions have been found to be different in the solidification of equiaxed to columnar grain regions, thus, the solidification path of Al-Mg-Sc-Zr was investigated using ThermoCalc software. The modelling has shown what phases occur at certain temperatures along the entire solidification path. According to the diagram presented in Figure 4.9, the Al_3Zr phase is solidified before FCC (688°C-639°C), facilitating heterogeneous nucleation sites for the main phase FCC (637°C) and modifying the as-cast grain structure. The Al_3Sc phase solidifies at 604°C, when 75% of FCC phase is solidified and consequently, its modifying effect is minor compared to Al_3Zr.

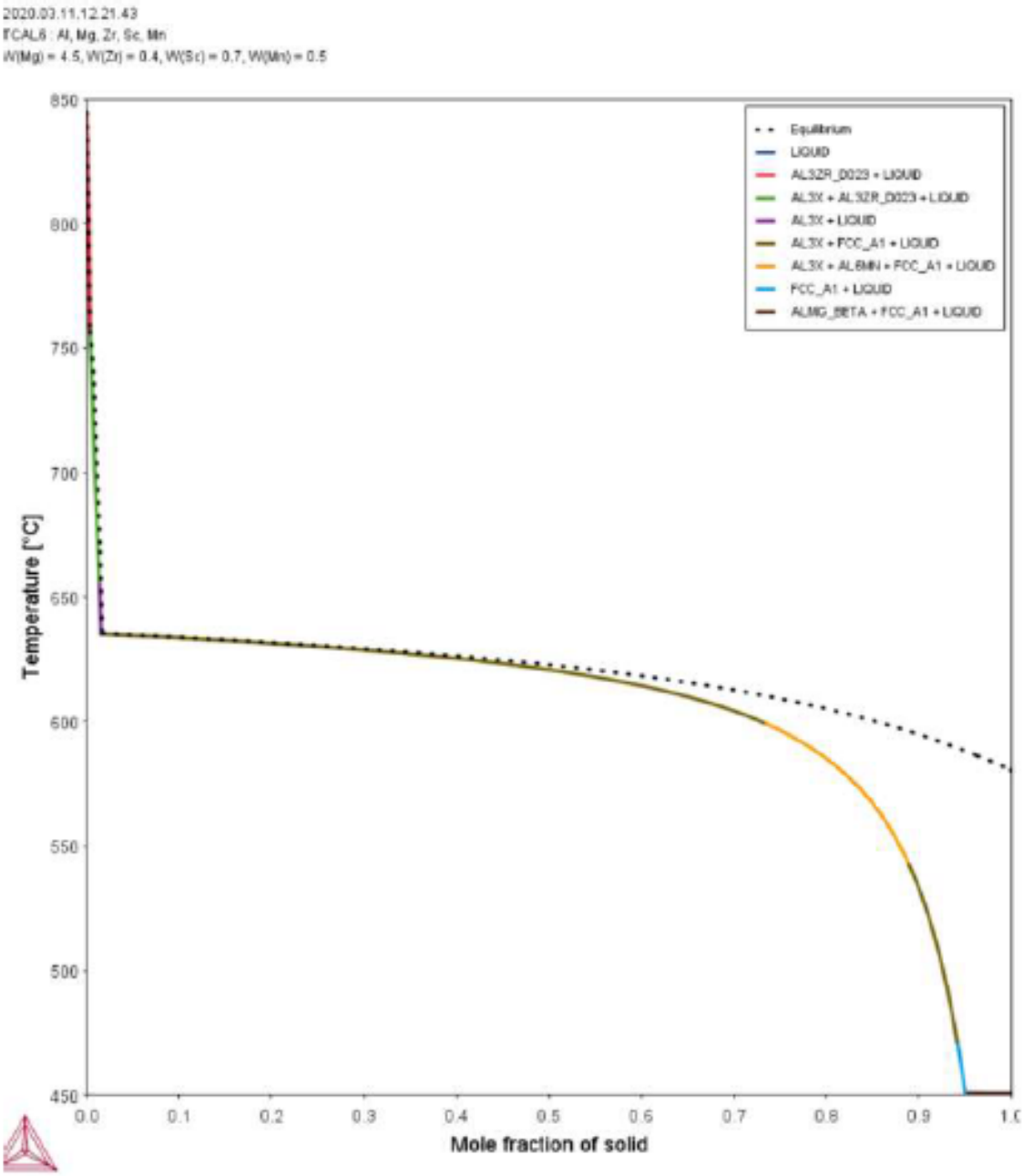

Figure 4.9. Phases formed during solidification according to Thermo-Calc.

However, these simulations assume complete liquid-state diffusion and no solid-state diffusion, thus representing equilibrium conditions based on the equilibrium phase diagram. In contrast, in the case of the LPBF process, extremely high cooling rates, up to approximately 10^6 K/s, occur. This leads to non-equilibrium solidification conditions. Under such rapid cooling, the phase formation and distribution may differ significantly from those predicted by equilibrium phase diagrams, indicating that conventional phase diagrams are not fully applicable to LPBF conditions.

4.3.2 Solidification considering non-equilibrium phase diagram

Non-equilibrium solidification is defined as the solidification of materials under conditions that are sufficiently different from those of their equilibrium phase diagrams, generally involving high cooling rates. As a result, the formed phase compositions and structures do not normally correspond to the predictions in their equilibrium phase diagrams.

Eskin has reviewed the extensive Russian research in the 1970s-1990s on Sc applications in Al-alloys (115). This work covers the development of metastable phase diagrams of the Al-Sc systems at different solidification rates, mechanisms of grain refinement, precipitation hardening through Al_3Sc particles, and recrystallization control. According to Eskin (115), the solubility of Sc in aluminium decreases rapidly with increasing temperature under equilibrium conditions. However, when cooling rates increase, as in non-equilibrium solidification processes, this solubility can expand. This can be explained as the fact that higher cooling rates "trap" more of the solute in the solid phase before equilibrium can be re-established. Besides that, the temperature of the eutectic reaction, so-called eutectic temperature, also decreases with increased cooling rates. This causes a shift in the phase formation compared to what is predicted by the equilibrium phase diagrams.

The non-equilibrium phase diagram (Fig. 4.10) demonstrates how phase boundaries and solubilities shift with increasing cooling rates. It must be noted, while existing literature reports solidification rates up to 10^5 K/s, the LPBF process achieves cooling rates around 10^6 K/s (116). Under such an extreme cooling rate, the conditions related to solidification are far from being equilibrium. Hence, conventional equilibrium phase diagrams, assuming much lower cooling rates, cannot predict either the phase components of the alloy or its behaviour in LPBF process. Thus, it can be concluded, the high cooling rates associated with LPBF lead to non-equilibrium solidification conditions that change phase formation and solubility compared to equilibrium predictions.

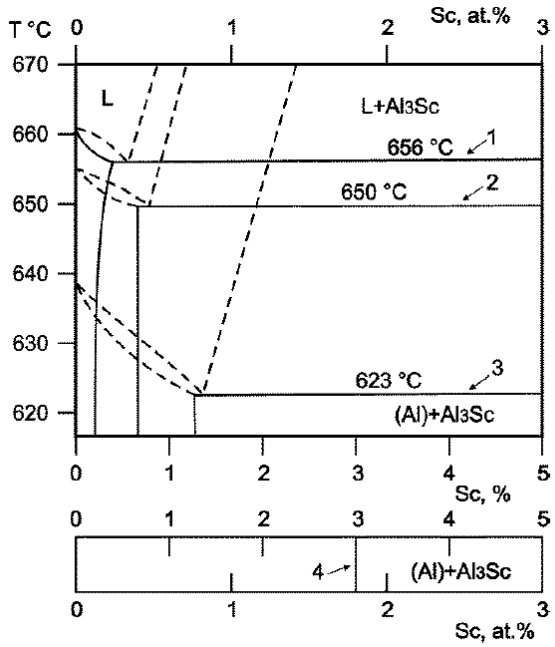

Figure 4.10. Metastable phase diagrams of the Al–Sc system as 5 K/s (1); 10^2 K/s (2); 10^3 K/s (3) and 10^5 K/s (4) (115).

4.3.3 LPBF thermal condition

The thermal conditions during LPBF are important as they directly influence the phase formation, microstructure and mechanical properties of the final printed parts. The cooling rate can be expressed as $dT/dt = R \times G$, where R is the local value of the solidification velocity and G is the temperature gradient at the solid-liquid (S/L) interface. Numerical simulations suggest that this gradient is between 5×10^6-10^7 with the highest values at the track boundary (117). The primary factor affecting variations in the cooling rate along the S/L interface is the variation in solidification velocity, R. The solidification velocity can be expressed as $R = Vcos\theta$, where V is the laser scan velocity vector and θ is the angle between the normal to the S/L interface and the direction of the laser scan.

Kurz et al. (118) have characterized the solidification conditions during laser surface treatment, which is comparable to LPBF (Figure 4.11). It has been demonstrated that R=0 at the track boundary as the track boundary is normal to the weld directions and increases rapidly with z. Temperature gradient G is the highest at the track boundary and decreases toward the inner part of the track. Cooling rate T, that is equal to $R \times G$, also increases strongly with z.

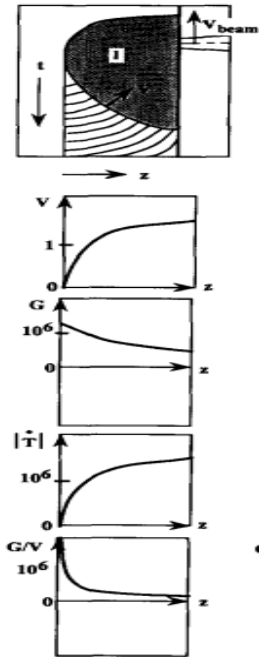

Figure 4.11. Characteristic solidification conditions during LPBF (118).

Schematic representation of the melt-pool shape and geometry during LPBF is presented in Figure 4.12. During the LPBF process, solidification starts at the boundary of the melt track, where θ, the angle between the direction of the solidification front and the scan direction, is 90°. As the solidification front is perpendicular to the laser scanning direction ($R_{S/L-1}$), the solidification front starts with a $R = 0$. Next to the track boundary, R increases very rapidly as θ decreases. Segregation in the region next to the track boundary is thus expected due to the very low R values. The presence of Mg–Si- and Fe-containing particles only in grain-boundary areas in the fine-equiaxed-grain region can also be expected to be the result of segregation of these elements during solidification due to the very low R. Further away from the track boundary, the angle θ decreases, thus, R increases rapidly ($R_{S/L-2}$).

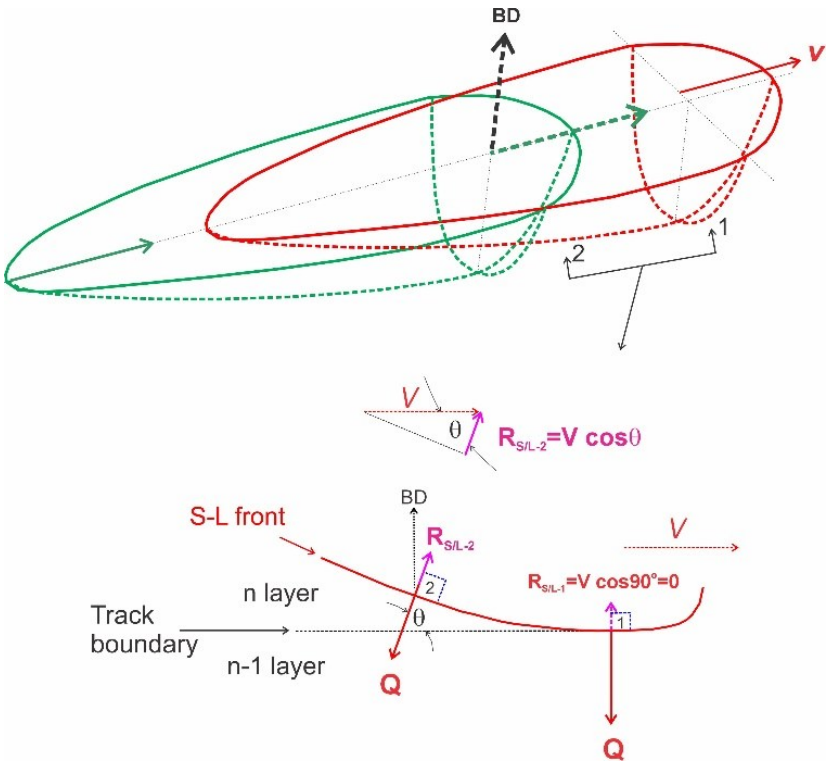

Figure 4.12. Schematic representation of the melt-pool shape and geometry during LPBF.

The precise shape of the melt pool in LPBF is still not fully understood. Del Guercio et al. (119), in their study of diffusion and segregation during the LPBF of an aluminium alloy, utilized an angle θ of 45° to characterize the melt pool. For this particular angle and a laser scan velocity $v = 1600\ mm/s$, the solidification rate R is:

$$R = V \cdot cos\theta = \frac{1600mm}{s} \cdot cos45° = \frac{1600mm}{s} \cdot 0.707 = 1.1m/s$$

At this solidification rate R, solute trapping during the solidification process is observed, as has been explained by Kurz and Trivedi (118), when R is 0.8 m/s or higher, solute trapping occurs during rapid solidification. However, θ=45° means a relatively short melt pool where the length of the melt pool is comparable to its depth. In contrast, if different values of θ are considered, that reflect a melt pool with a length-to-depth ratio of 2 and 3, the corresponding angles are calculated as 63.4° and 71.6° (Fig. 4.13).

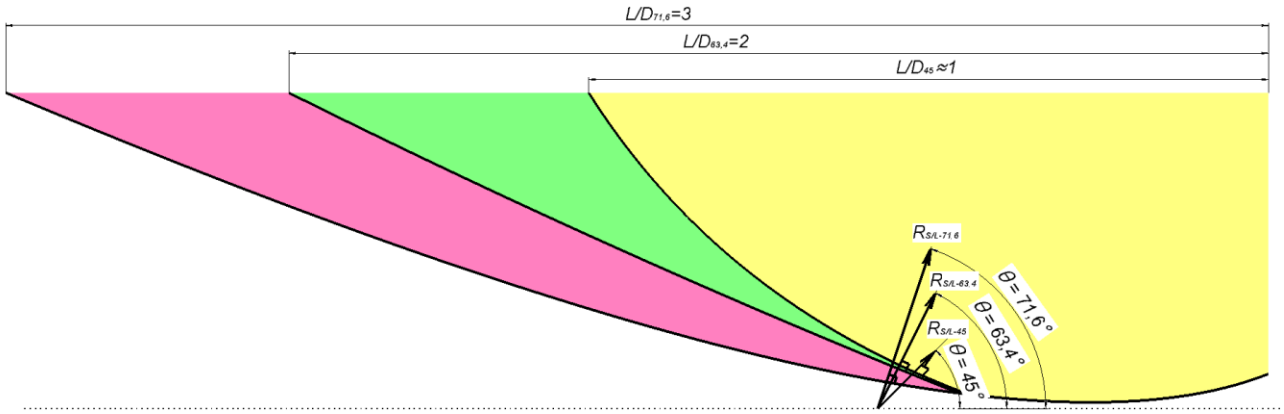

Figure 4.13. Schematic representation of the melt-pool shape and geometry depending on the angle θ.

These angles lead to the following solidification rates:

- For θ=63.4°, the solidification rate R is: $R = \frac{1600\ mm}{s} \times cos63.4 \approx 1600 \frac{mm}{s} \times 0.447 \approx 0.7\ m/s$
- For θ=71.6°, the solidification rate R is: $R = \frac{1600\ mm}{s} \times cos71.6 \approx 1600 \frac{mm}{s} \times 0.316 \approx 0.5\ m/s$

According to Kurz et al. (118), these calculated R values are within the range where diffusion is localized, approaching the critical value when solute trapping occurs (Fig. 4.14). Thus, only very low Mg segregation to grain boundary that has been observed in columnar grain region is reasonable. This is also consistent with theMg_2Si- and Fe-containing particles observed mainly in grain interiors in the coarser equiaxed-grains and in the whole columnar grain region, as the high R values also prevent Si and Fe from diffusing to grain boundaries to form particles there during solidification.

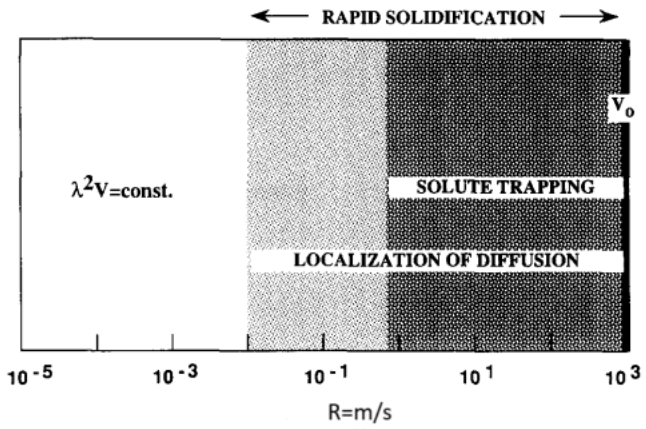

Figure 4.14. Various solidification rates in normal and rapid solidification processing (RSP) and characteristic phenomena appearing in metals under conditions of RSP (118).

4.3.4 Solidification and segregation during LPBF

Mg segregations

In equiaxed grains region, it has been noticed that Mg segregations exist around the grains (Fig. 4.5). As shown in Table 3.1, Scalmalloy contains Fe and Si, thus, Mg_2Si and Fe containing intermetallic particles form in the late stages during solidification and are present in grain boundary region, as is commonly known in cast Al alloy solidification.

It can be explained using the equilibrium Al-Mg phase diagram and Scheil equation. Referring to the Al-Mg-phase diagram (Fig. 4.13), the slopes of the liquidus and solidus are negative, meaning that, as Mg content increases, liquidus and solidus temperatures decrease (till≈18 wt%). Thus, for a 4.5 wt%Mg–Al alloy, Mg rejection during solidification and enrichment in the final solidification location means segregation to grain boundaries is expected, if solid–liquid front growth velocity (R) is sufficiently low to allow sufficient diffusion.

Point 1 on Al-Mg phase diagram (Fig. 4.15) shows when the first solid phase forms and concentration (C_S) of Mg is low following:

$$\frac{C_S}{C_L} = k$$

where C_L is the liquid composition and k is the partition ratio. Scheil was one of the first to suggest a method for predicting microsegregation, based on composition variation ahead of a solidification front. His method was based on the assumption that: a) no diffusion within the solid, b) complete mixing of solute in the liquid and c) the liquid and solid are in equilibrium at the L/S interface. With these assumptions, he obtained the following equation (120):

$$C_S = C_0 k(1 - f_s)^{k-1}$$

where C_0 is the initial composition of the alloy and f_S is the solid fraction. When experimental techniques made it possible to reliably measure the composition distributions within alloys, it became clear that the Scheil equation cannot predict well the actual solidification process. However, it helps to explain why segregations occur.

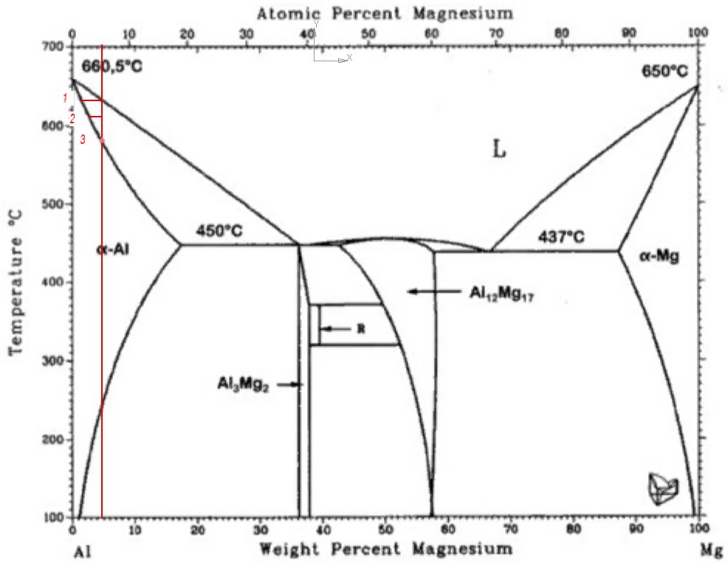

Figure 4.15. Al-Mg phase diagram (121).

Scalmalloy contains 4,5% of Mg, which is represented by the red line on the phase diagram. Point 1 shows when the first solid phase occurs and the minimum concentration of Mg is there. According to (120), it can be calculated as following: $C_S = C_0 k$,

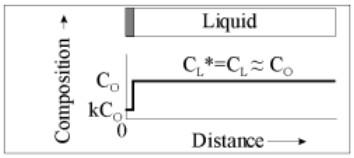

where k for Al-Mg phase diagram is equal to 0,53. Thus, Mg concentration in Scalmalloy at the initial point of solidification is 2,4%. After that, at Point 2 (T=610°C), Mg concentration is getting higher and is equal to

$$C_S^* = kC_L = kC_0(f_L)^{k-1}$$

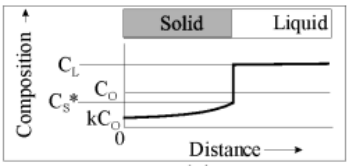

At the final stage, when the last liquid phase solidifies, solid composition with C_{SM} = 17,4% and eutectic phase with C_E = 33% are observed.

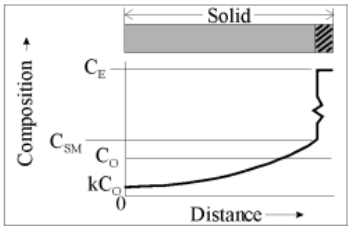

The amount of eutectic can be calculated as following:

$C_E = C_0 f_E^{k-1}$, where C_E = 33, C_0 = 4,5 and k = 0,53. Thus, 1,5% of eutectic containing 33% of Mg can be found in the solidified microstructure of Scalmalloy. Due to the high cooling rates, diffusion does not occur and solidified phases remain at the initial composition. Schematic representation of composition of solid is presented in Figure 4.16. However, it must be taken into account that LPBF, where high cooling rates exist, is non-equilibrium process and concentration values are different.

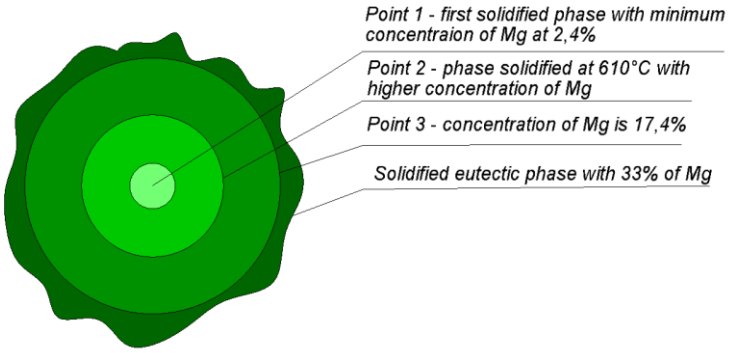

Figure 4.16. Schematic illustration of Mg redistribution after solidification.

To further understand, area compositions inside the grains and in a number of other areas each including a section of a grain boundary have been evaluated. An EDS spectrum can include a small Cu and a small Ga peak as a Cu grid was used and the sample can be slightly contaminated by Ga during lamellae preparation. They have thus been excluded from ZAF calculation. For the present purpose of examining elemental distributions, only Al, Mg, and Sc are selected for ZAF calculation, since these are the primary important elements of the alloys. Thus, the composition is viewed as normalized. Note that, from Table 3.1, atom percentage of Zr is low and the content at 0.3 wt% (<0.1 at%) is difficult for EDS to accurately determine. Sc is the major element to form Al_3(Sc,Zr). Table 4.1 lists the normalized compositions, corresponding to the areas marked in the Mg map in Figure 4.17.

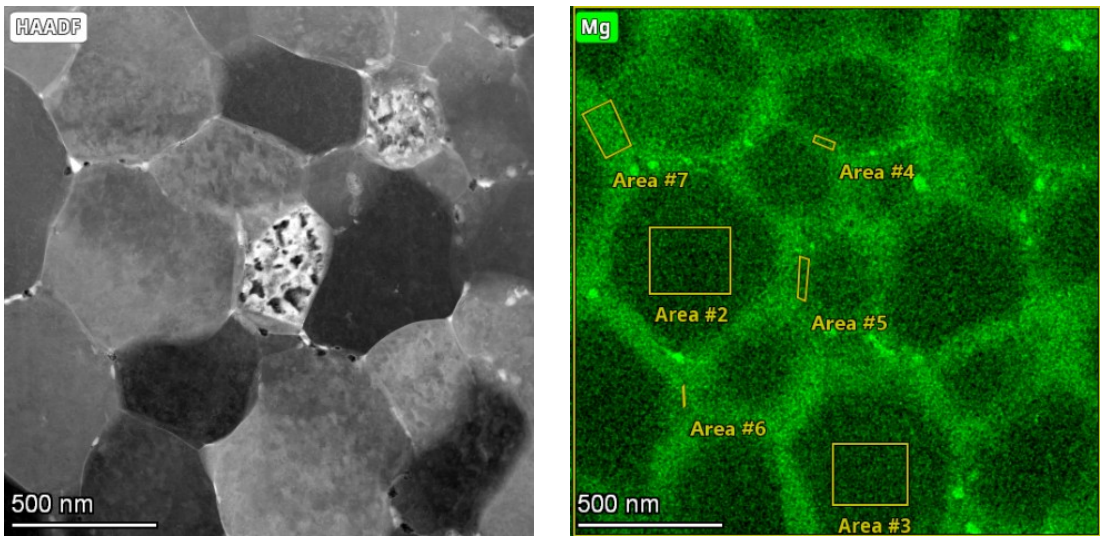

Figure 4.17. EDS map and normalised at% of Al, Mg and Sc of equiaxed grain region in as-built sample.

Table 4.1. Normalized wt% of Al, Mg, and Sc determined by STEM–EDS in areas shown in Figure 4.15.

	Area 1 (whole)	Area 2	Area 3	Area 4	Area 5	Area 6	Area 7
Al	94.21	95.89	95.77	92.78	94.35	86.32	91.85
Mg	5.45	3.80	3.89	6.70	5.29	7.02	7.78
Sc	0.34	0.31	0.34	0.52	0.36	0.54	0.37

The overall Mg content is 5.5at% for Area 1, which is the whole area of the TEM image including many grains, as is clearly shown in the TEM image and Mg map. Areas 2 and 3 are entirely areas inside the grains and at%Mg≈3.8 is significantly less (31%) than at%=5.5. Areas 4, 6 and 7 are primarily grain boundary areas and at%Mg ranges from 6.7 to 7.8, significantly higher (22% to 42%) than at%=5.5. Thus, these EDS analytical data clearly demonstrate the Mg enrichment in grain boundary areas, as is readily suggested in the Mg map EDS analysis on Area 5 shows at%Mg=5.3. The area may be viewed as a mixed area of grain boundary and grain interior, thus at%Mg (=5.3) is close to the overall content at 5.5at% with the difference being 4%.

Similar to providing the normalized compositions for equiaxed grains as explained before, Table 4.2 lists the compositions corresponding to the areas marked in the TEM micrograph (Fig. 4.18) for columnar grain region. The overall composition (Area 1) in Table 4.2 is very close to the alloy composition listed in Table 3.1.

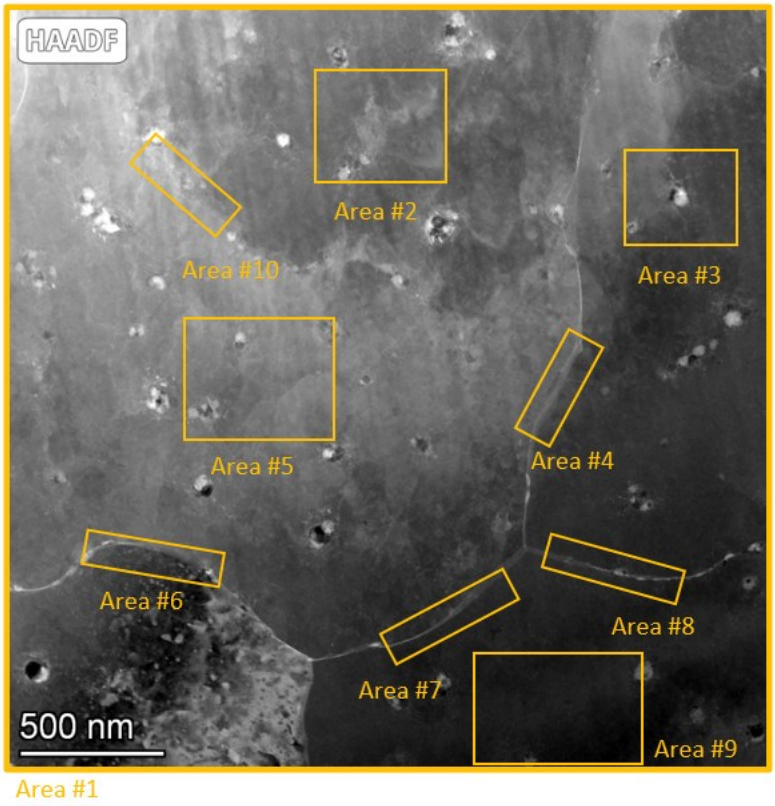

Figure 4.18. TEM–HAADF micrograph in columnar grain region ≈50 µm from track boundary in anas-built sample.

Table 4.2. Normalised wt% of Al, Mg, and Sc determined by TEM–EDS in areas shown in Figure 4.16.

	Area 1 Whole	Area 2 Inside	Area 3 Inside	Area 4 GB	Area 5 Inside	Area 6 GB	Area 7 GB	Area 8 GB	Area 9 Inside	Area 10 GB	Inside mean	GB mean
Al	94.78	94.98	95.04	94.89	94.94	93.75	95.27	94.07	95.49	93.33	95.11 ±0.25	94.50 ±0.71
Mg	4.53	4.25	4.25	4.44	4.42	5.54	4.10	5.16	3.69	5.85	4.15 ±0.32	4.81 ±0.66
Sc	0.69	0.77	0.71	0.67	0.66	0.71	0.63	0.78	0.83	0.82	0.74 ±0.07	0.70 ±0.06

About 10%Mg, = (4.55–4.12)/4.55, has been depleted inside the grains and segregated at the grain boundaries of the columnar grains. This is a weak segregation, in comparison to 24%Mg, = (4.55–3.47)/4.55, that has segregated in the grain-boundary areas in the equiaxed-grain region.

Sc segregations

The slight segregation of Sc to grain boundaries in the equiaxed-grain region but not in columnar grain region, however, may need to be considered further. Sc contents listed in Table 4.1 may suggest possibly a slight segregation of the element at grain boundaries, although there is no indication of Sc enrichment in Sc map (Fig. 4.25). The overall Sc content determined is at 0.34at% (area 1), although Sc in the original powder is higher (Table 3.1). Area 2 and area 3 (Fig. 4.15) are grain interior and their Sc contents at 0.31-0.34at% may be viewed slightly lower (0-9%) than the overall Sc content. Areas 4, 6 and 7 of Figure 4.15 are primarily grain boundary areas and their Sc contents are 0.52, 0.58 and 0.37at%, respectively. Thus, on average, Sc content in grain boundary area in equiaxed grain zone detected can generally be viewed from slightly higher (9%) to significantly higher (71%) than that of the overall Sc content (0.34at%), although accuracy for low concentration detection may be high. As for columnar grain region (Table 4.2), there appears no segregation of Sc that can be detected according to the data of Sc content values. Al–Sc-phase diagram (Fig. 4.19) suggests that, for the alloy containing 0.34 at% Sc, eutectic should form after the formation of proeutectic Al_3Sc during cooling. The proeutectic Al_3Sc or $Al_3(Sc,Zr)$ should act as nuclei whether they can be detected or not.

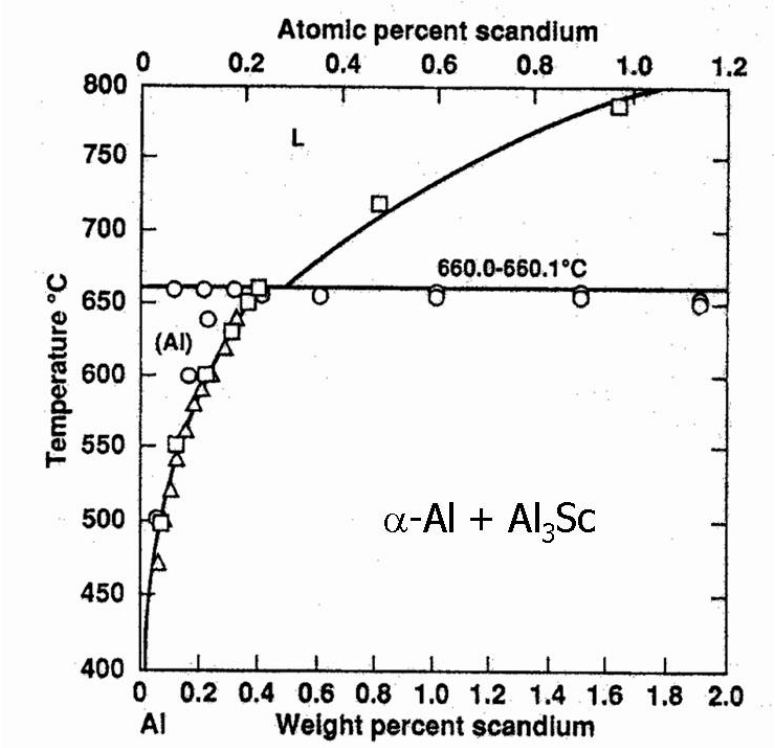

Figure 4.19. Al-Sc phase diagram (122).

In Figure 4.17, the STEM image does not show the usual coupled eutectic growth pattern. Instead, it exhibits a divorced eutectic solidification. Norman et al. (123) demonstrated that, when using an Al–0.7(wt%) Sc alloy with a cooling rate of up to 1000 K/s, they found no evidence of coupled eutectic growth under TEM analysis. Instead, they observed that only α(Al) phases grew outward from the Al_3Sc nuclei, which is characteristic of divorced eutectic solidification. In divorced eutectic growth, as the α(Al) phase grows, it tends to push out some of the Sc content. This process leads to the Sc being rejected and segregated to areas near the grain

boundaries. Since the growth rate is slower in the fine, equiaxed grain-boundary regions, there is more time for diffusion to occur. This results in a higher concentration of Sc at the grain boundaries.

Moving away from the track boundary, R and cooling rate (dT/dt) increase very rapidly and reaches extremely high values (118). Hooper (27) conducted direct measurements of $\frac{dT}{dt}$ on the surface of the melt track during the LPBF process of Ti6Al4V and reported that $\frac{dT}{dt}$ ranged from 10^6 to 40×10^6 K/s. This range is highly dependent on the LPBF parameters used, such as laser power, scan speed and layer thickness. In a separate study, Hyer et al. (124) estimated the rate of temperature change for AlSi10Mg during LPBF. They based their estimation on the relationship between $\frac{dT}{dt}$ and the secondary arm spacing of the solidified structure. Rosenthal equation, which is used to describe thermal conditions in welding and similar processes, was also applied. Their results showed that $\frac{dT}{dt}$ values for AlSi10Mg could range from 10^5 to 10^7 K/s. Considering these findings, it is reasonable to suggest that the cooling rate, $\frac{dT}{dt}$, can reach at least 10^5 K/s just a short distance away from the boundary of the melt track. An increase in dT/dt may have a strong effect on the effectiveness of Sc to form and thus to grain refine. To illustrate this with the Al–Sc binary system: the equilibrium composition for the Al–Al_3Sc eutectic is 0.56 wt% Sc (125), (126). In a Scalmalloy with 0.65 wt% Sc, the formation of proeutectic Al_3Sc is efficient under near-equilibrium conditions, such as in areas with low solidification rates (R). However, moving further from the track boundary where solidification occurs more rapidly, the system moves away from equilibrium. In these conditions, the effectiveness of Sc in forming Al_3Sc and thus in refining the grain structure decreases. It has been demonstrated (115) that the values of eutectic composition are ≈0.6, ≈0.8, ≈1.3, and ≈3.0 wt% for dT/dt equal to 5, 10^2, 10^3, and 10^5 K/s, respectively. Data on nonequilibrium eutectic compositions indicate that in an Al–0.65 wt% Sc alloy, scandium (Sc) becomes ineffective for grain refining if the cooling rate $\frac{dT}{dt}$ exceeds 10^2 K/s. Therefore, in this alloy, which also contains 0.3 wt% Zr (0.09 at% Zr), the formation of proeutectic Al_3Sc, which is crucial for grain refinement, is unlikely to occur throughout most of the melt due to the high cooling rates. This connection between cooling rate and the effectiveness of grain refining helps explain why increasing the baseplate temperature (TB) in Laser Powder Bed Fusion (LPBF) can lead to a larger region of equiaxed grains, as observed by Yang et al. (75). Raising TB reduces the heat transfer rate from the melt track, which in turn lowers $\frac{dT}{dt}$. This reduction in the cooling rate enhances the likelihood of proeutectic Al_3Sc formation, thereby expanding the region where equiaxed grains form.

4.4 Elemental distribution after aging treatment

Further illustration of distribution of elements after aging treatment is not for the study of how Sc has played the role on precipitation strengthening. Rather, how aging treatment has affected the elemental distributions in the LPBF samples of the alloy presented here is for the further support of the understanding of the distributions

in the as-built state. Thus, the suggested mechanism of how Sc affects the bimodal microstructure formed can be better understood.

Fig. 4.20 shows the TEM-EDS elemental maps of the area shown by the micrograph (top left) taken from an equiaxed grain region of T5 as shown.

- From TEM and Mg map: in the equiaxed grain region, Mg particles are segregated along the grain boundaries.
- From TEM and Sc map: evidence of Sc-rich particles in the equiaxed grain region have been found.

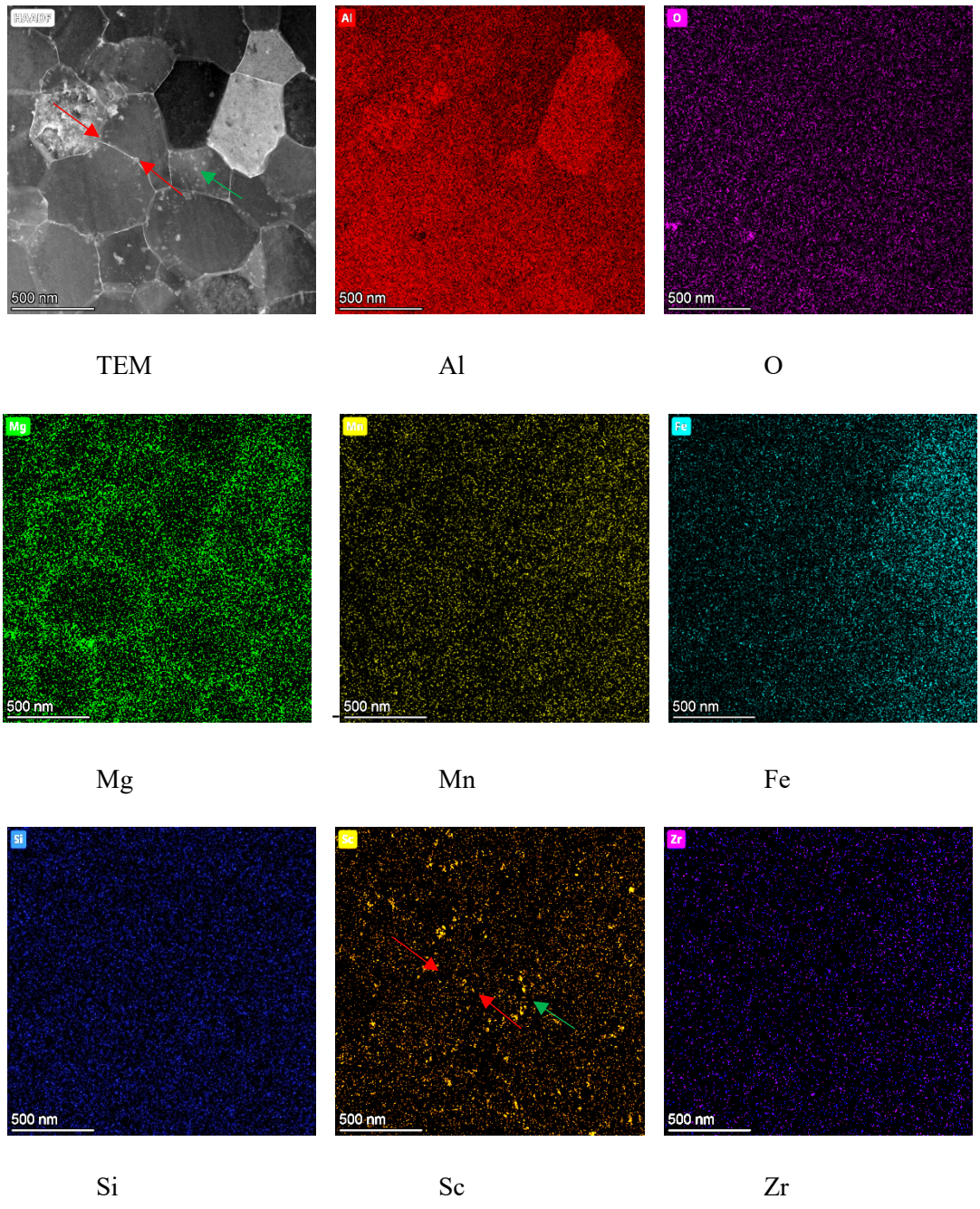

Figure 4.20. TEM (HAADF) micrograph, top left, and EDS elemental maps taken and analysed in equiaxed grain region in T5 sample.

Mg map in Figure 4.20 shows that Mg content should be still higher in grain-boundary areas than the content in grain interiors. Mg appears to be significantly less enriched in gran-boundary areas in Figure 4.20, in comparison to the high degree of enrichment in the areas shown in the Mg map in Figure 4.5. This is because a portion of Mg from the Mg-rich grain-boundary areas has diffused to grain interiors when the sample was held at the aging temperature. The Si maps shown in Figure 4.20 display an even distribution of Si, meaning that Mg–Si (likely Mg_2Si) particles that can be detected in the as-built state in Figure 4.5 have dissolved during aging treatment. The Fe map in Figure 4.20, compared to that in Figure 4.5, also suggests that the Fe-rich particles in the as-built state have largely dissolved during aging treatment.

However, the Sc map shown in Figure 4.20 suggests the presence of Sc-rich particles after aging treatment, as opposed to the as-built state showing no Sc-rich particles in Figure 4.5. As has been explained, according to the literature (60), the strengthening Al_3Sc precipitates after aging treatment can be 1–2 nm or less in size. These small-size precipitates are not distinguishable in the Sc map of Figure 4.20. The Sc map in Figure 4.20 suggests that there are Sc-rich particles larger than a few nanometers. Observing closely, the TEM micrograph and the Sc map in Figure 4.20 suggest that more Sc-rich particles are present along the grain boundaries. An example of such particles is pointed to by the two red arrows in Figure 4.20 in the TEM image and in the Sc map. Forming Sc-rich particles in grain-boundary areas during aging treatment is reasonable, as there is a slight Sc segregation to the areas during solidification in the equiaxed-grain region, as has already been shown and explained. Note also that Sc-rich particles are also observed in grain interiors and an example is indicated by a green arrow in both the TEM image and the map in Figure 4.20. Sc-rich particles larger than a few nanometers in size ingrain interiors suggest that Sc supersaturation during solidification may not be homogeneous.

The elemental distributions in the columnar grain region of the aged sample are shown in Figure 4.21. These maps indicate:

a. From TEM image, Al, Mg and Si maps: Most Al depleted particles shown in the Al maps are Mg and Si rich in Mg and Si map, respectively. Also, similar to as-built state, Mg segregations are identified along the grain boundaries.

b. From TEM image, Al, Mn, Fe and Si maps: Large bright particles (up to 0,4μm) located along the grain boundaries on TEM are presented on Mn, Fe, Si maps.

c. From TEM image, Al and Sc map: Tiny Sc particles discontinuously distributed along the grain boundaries are presented on Sc map. To evaluate the size of these particles, TEM-EDS elemental maps at higher magnification are presented (Fig. 4.22 and Fig. 4.23).

d. From Fe and Zr maps: Zr appeared on the map repeating the pattern from Fe map.

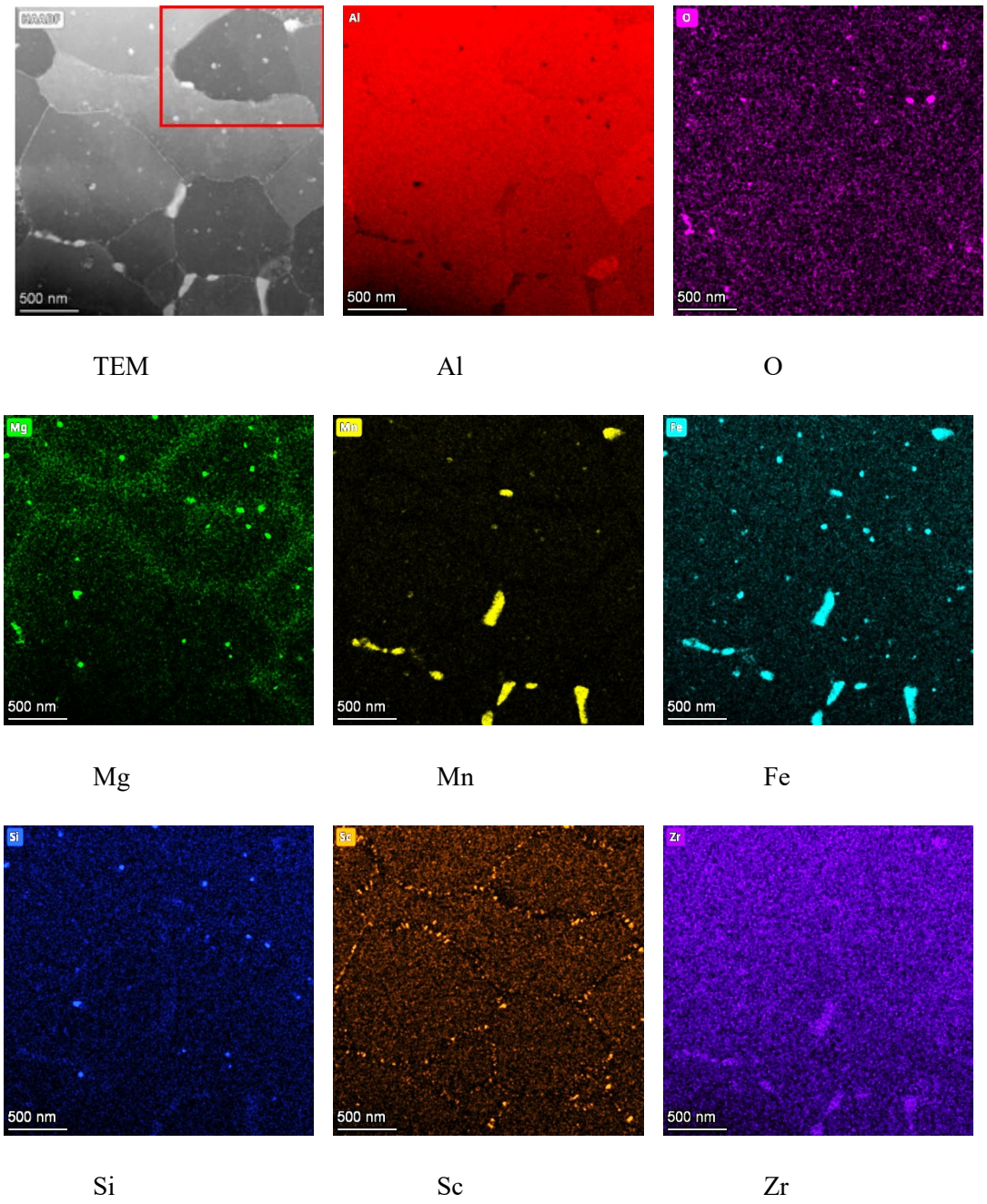

Figure 4.21. TEM (HAADF) micrograph, top left, and EDS elemental maps taken and analysed in columnar grain region next adjacent to equiaxed grain region in T5 sample.

Al-depleted regions observed in the Al map correspond to bright particles in TEM image that are rich in Mg and Si, as indicated in the respective elemental maps, suggesting the formation of Mg_2Si particles. Similar to the as-built condition, Mg segregations along the grain boundaries are observed. Additionally, large elongated particles in size up to 0.4 µm in size are identified in the TEM image and are mirrored in the Mn and Fe maps, suggesting the presence of intermetallic phases such as $Al_6(Mn,Fe)$, particularly along the grain boundaries. Importantly, the Sc map shows the presence of fine, discontinuously distributed particles along grain boundaries, which are absent in the equiaxed region. These are suggested to be Al_3Sc precipitates. To gain more information on size of these precipitates, TEM images of transition area at higher magnification together

with elemental maps are presented in Figure 4.22 and Figure 4.23. Lastly, the Zr map follows a similar pattern to that of Fe, demonstrating either co-location or minor Zr incorporation into Fe-rich phases.

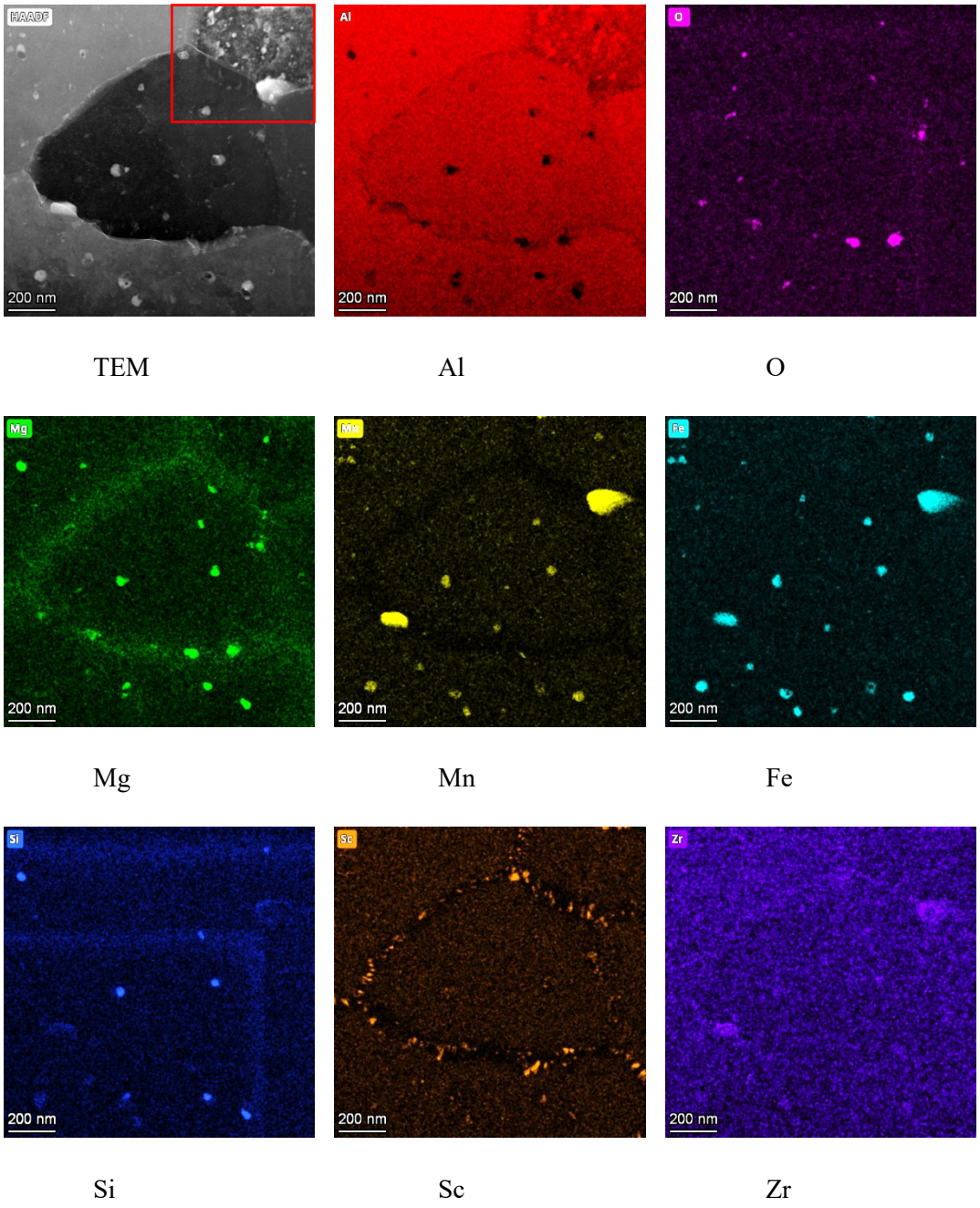

Figure 4.22. TEM (HAADF) micrograph, top left, and EDS elemental maps taken and analysed in columnar grain region next adjacent to equiaxed grain region in T5 sample (higher magnification).

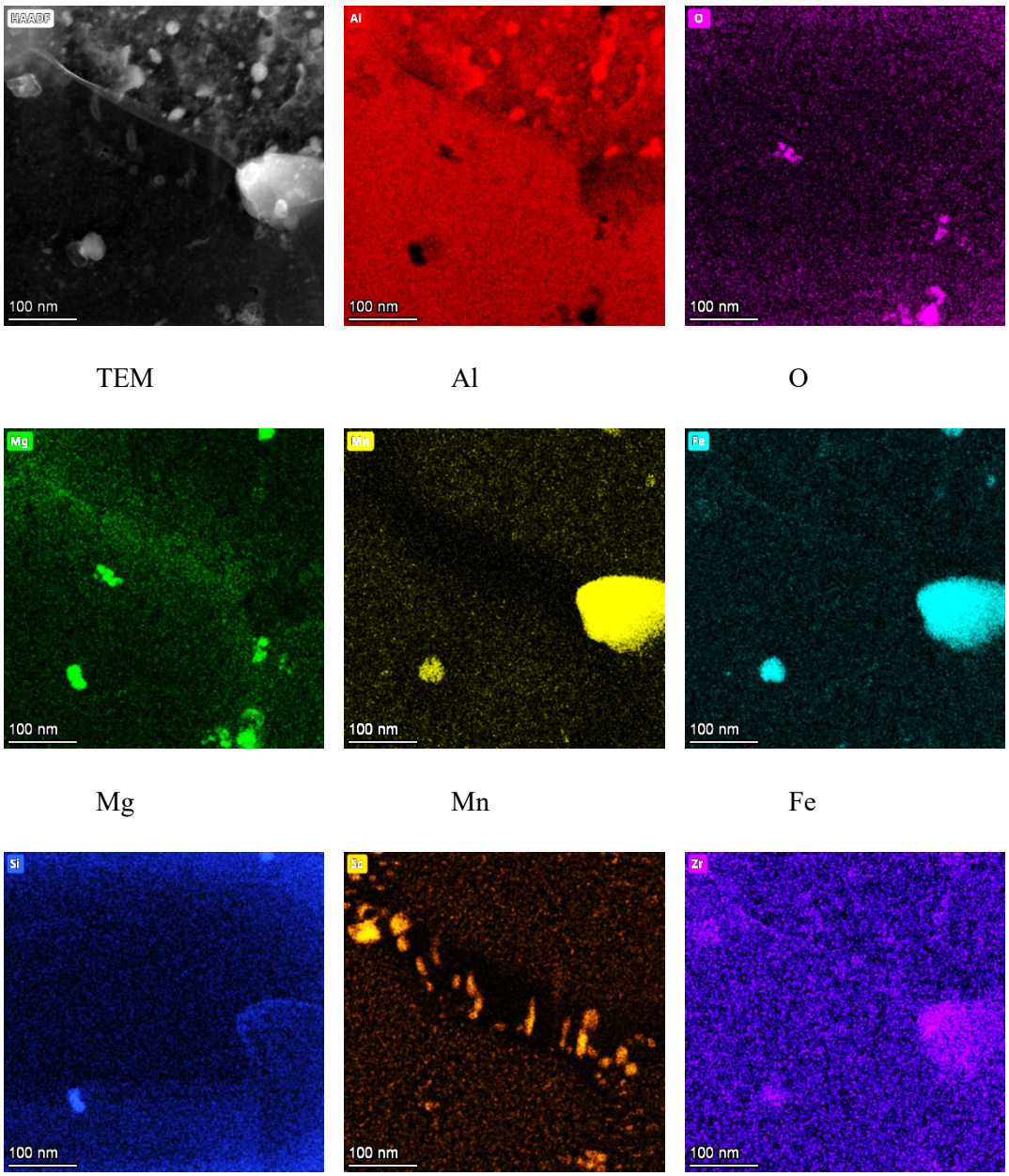

Figure 4.23. TEM (HAADF) micrograph, top left, and EDS elemental maps taken and analysed in columnar grain region next adjacent to equiaxed grain region in T5 sample (higher magnification).

Figures 4.22 and 4.23 present high-magnification TEM and EDS elemental maps from the columnar grain region near the equiaxed boundary in the T5-treated Scalmalloy sample, providing detailed information into the precipitation behaviour of Sc. The Sc elemental map shows a discontinuous distribution of fine Sc-rich particles aligned predominantly along grain boundaries. These particles appear as spots in the Sc map and correlate with regions of Al depletion in the Al map, which confirms the formation of Al_3Sc precipitates. These particles are in the size range of 20-80 nm and are elongated at ~90° to the grain boundary.

Fig. 4.24 shows the TEM-EDS elemental maps of the area shown by the micrograph (top left) taken from a columnar region of T5 as shown. These maps indicate:

a. From TEM image, Al, Mg and Si maps: Most Al depleted particles shown in the Al maps are Mg and Si rich in Mg and Si map, respectively, suggesting these are Mg_2Si.

b. From TEM image, Al, Mn and Fe maps: Bright particles on TEM are presented on Mn, Fe maps. They are likely to be $Al_6(Mn,Fe)$

c. From TEM image, Al and Sc map: Tiny Sc particles are presented on Sc map, suggesting these are Al_3Sc particles.

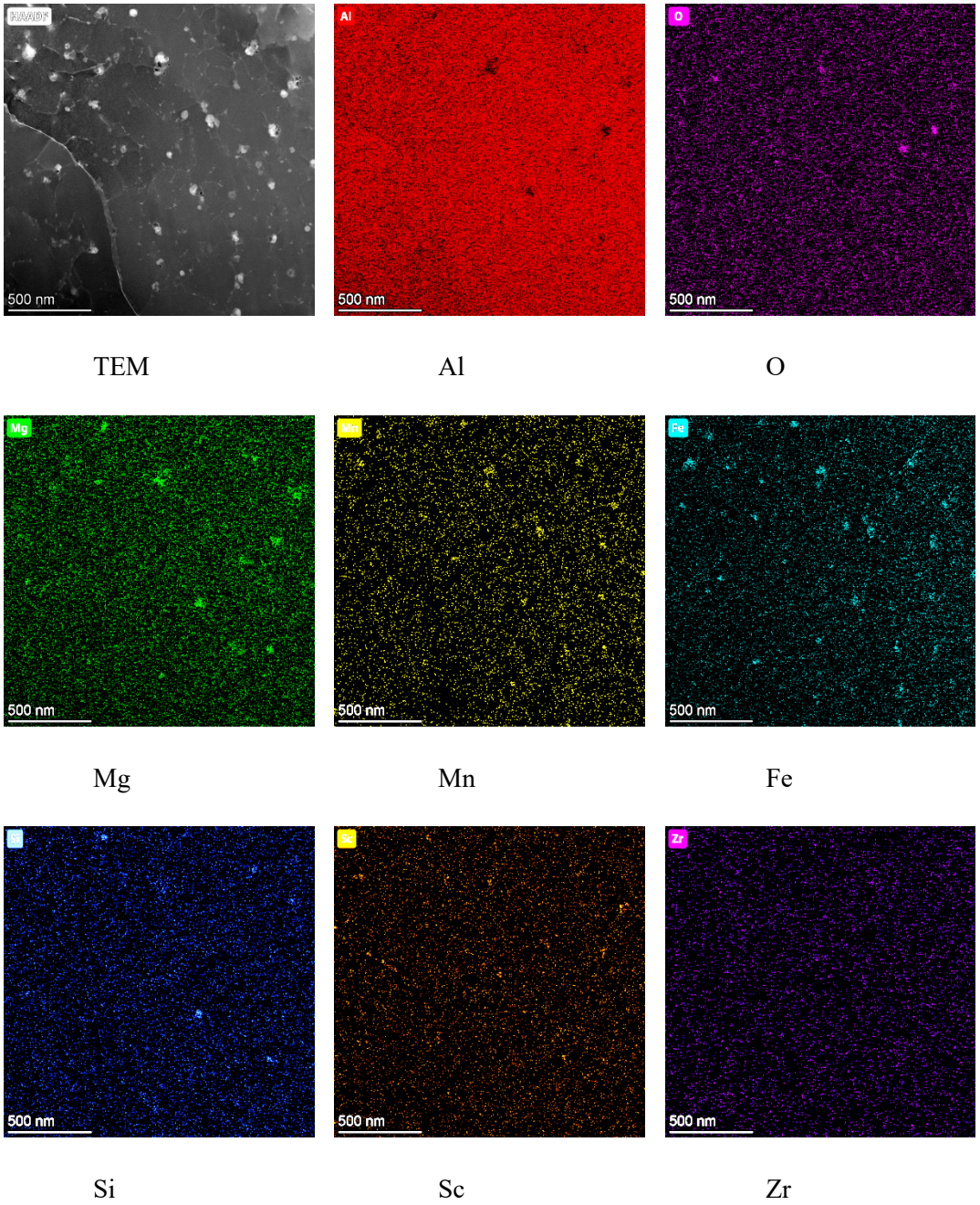

Figure 4.24. TEM (HAADF) micrograph, top left, and EDS elemental maps taken and analysed in columnar grain region in T5 sample.

Little Mg enrichment in the grain-boundary areas is shown in the Mg map. This is because of the ready homogenization of Mg during aging treatment from the low Mg segregation in grain-boundary areas in the

columnar grain region in the as-built state (as shown in Figure 4.7). Many Mg_2Si- and Fe-rich particles inside the grains in the as-built state have remained, as is indicated by the Mg, Si, and Fe maps in Figure 4.24. This is very different from the dissolution of the Mg–Si- and Fe-rich particles in grain boundaries in the as-built state during aging treatment and may be the result of rapid diffusion in the fine-equiaxed-grain region. Grain-boundary diffusion rate may be much higher than lattice diffusion rate and grain-boundary areas are large in the fine-equiaxed-grain region. Furthermore, in the fine-grain region, elemental diffusion only needs a short distance for elemental homogenization in grain interiors. In contrast, the dissolution of particles mostly in grain interiors in the coarser and columnar grain region requiring lattice diffusion could be a much slower process. This may explain the insignificant amount of dissolution in the coarse and columnar grain region during the time at aging temperature. As for Sc, the Sc map in Figure 4.24 shows some Sc-rich particles throughout in the aged sample. This is consistent with the lack of Sc segregation to grain-boundary areas in columnar grain region in as-built state.

4.5 Proposed mechanism of bimodal grain formation

Based on the measurements, observations and analysis above, the proposed mechanism of bimodal grain formation is:

Equiaxed grain region located near the track boundary:

- **Mechanism of equiaxed grain formation:** An equilibrium phase diagram can be applied in the area close to the melt track boundary as the growth and cooling rates are very low (Fig. 4.25). These conditions are favourable for forming Al_3Sc phases, which act as nucleation sites for the fine equiaxed grains, typically around 0.5 μm in size.
- **Segregations of elements:** During solidification, a considerable diffusion of elements outward is also facilitated by a low growth rate, which leads to the segregation of elements and intermetallic particles forming along the grain boundaries in the equiaxed grain region.

Transition area from equiaxed to columnar grain region - a few microns away from the track boundary

- **Increase in Grain Size:** Moving slightly away from the track boundary, the growth rate R increases sharply (Fig. 4.25). This spike in growth rate shifts the composition of the divorced eutectic toward higher values, surpassing the Sc content of the alloy. Thus, the grain size in the equiaxed region increases to approximately 1.5 μm due to the decreased grain-refining effect caused by the reduced effectiveness of Sc.

Columnar grain region – further away from the track boundary:

- **Columnar grains region:** Due to the high growth rates, the grain refining effect of Sc is completely lost, resulting in columnar grains growth (Fig. 4.25). In this region, a non-equilibrium phase diagram is applied to describe the solidification process.

- **Localized Diffusion:** In the columnar grain region, due to the high growth rate during solidification, highly localized diffusion is observed. This localized diffusion prevents the segregation of elements during solidification.

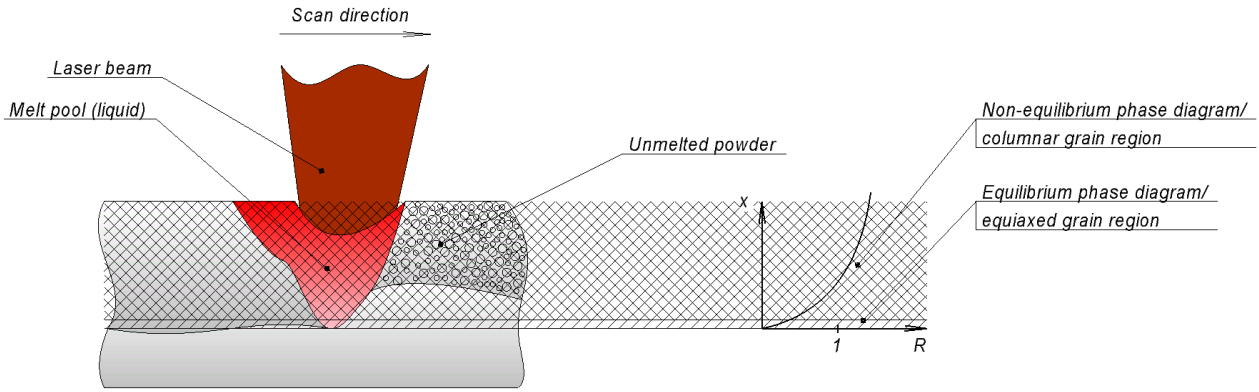

Figure 4.25. Schematic representation of LPBF conditions allowing formation of bimodal microstructure in Scalmalloy.

Chapter 5 – Fatigue behaviour of bimodal grain structure

Following on from the understanding of the forming mechanism of the bimodal grain structure, in this chapter, how cyclic loading with different loading directions on this grain structure in combination with LPBF defects affect fatigue behaviour and properties will be presented. The first part of the chapter is to present the data from FCG testing, both from growth rates in region II and ΔK_{th} values in region I. Also in this part, crack paths in both as-built and T6 samples tested will be illustrated, and how the bimodal grain structure in response to cyclic loading is not significantly affected by loading direction will be explained. The second part of the chapter is to present the data on fatigue life and strength of the LPBF bimodal grain structure samples. How LPBF defects dominantly affect strength under cyclic loading and why increasing quasi-static strength after T6 treatment does not affect high-cycle fatigue strength will be described. Finally, a further discussion will be had to provide a clearer understanding of why load direction insufficiently affects the high cycle fatigue strength of the bimodal grain structure.

5.1 Fatigue crack growth (FCG) under various loading directions

5.1.1 Fatigue crack growth of as-built and T6 samples

The da/dN versus ΔK data are presented across four figures, each demonstrating different experimental conditions and sample orientations. Figure 5.1 shows three curves for as-built samples, which were printed on a room temperature (RT) plate. These samples are oriented in three distinct directions relative to the build direction: crack direction parallel to the build direction, normal to the build direction, and at 45° to the build direction. Figure 5.2 shows four curves: three for as-built samples printed on a heated plate in the same three orientations (normal, parallel, and 45 degrees to the build direction) as those in Figure 5.1, and one additional curve for an as-built sample with crack direction parallel to the build direction, but printed on an RT plate, provided for comparison. Figure 5.3 presents three curves for heat-treated samples printed on an RT plate, with crack directions either parallel to the build direction or at a 45-degree angle to it. Additionally, this figure includes a curve for an as-built sample with a crack direction parallel to the build direction and printed on an RT plate for comparative purposes. Figure 5.4 shows three curves for heat-treated samples printed on a heated plate, with crack directions parallel to the build direction and at a 45-degree angle to it. It also includes a comparative curve for an as-built sample with a crack direction parallel to the build direction, printed on an RT plate.

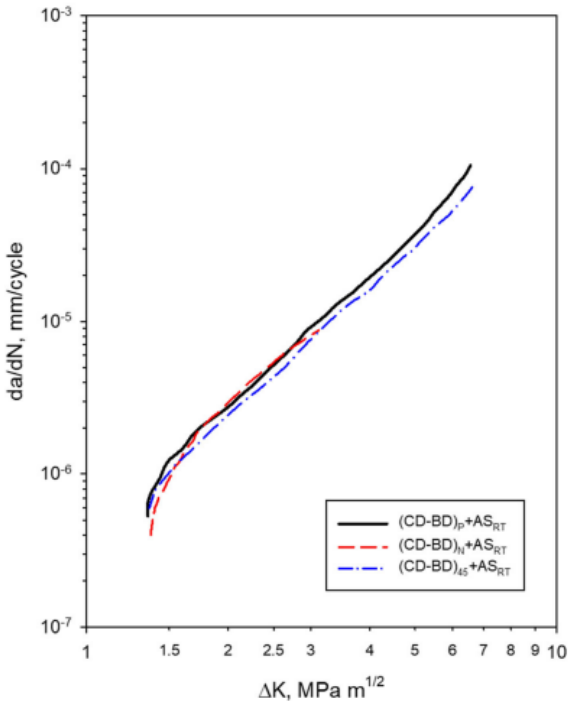

Figure 5.1. Fatigue crack growth curves for as-built samples made using room temperature plate.

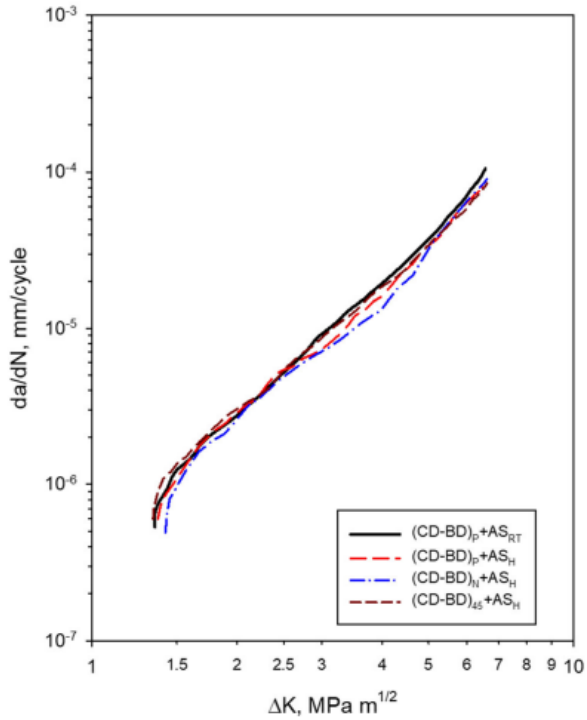

Figure 5.2. Fatigue crack growth curves for as-built samples made using heated plate.

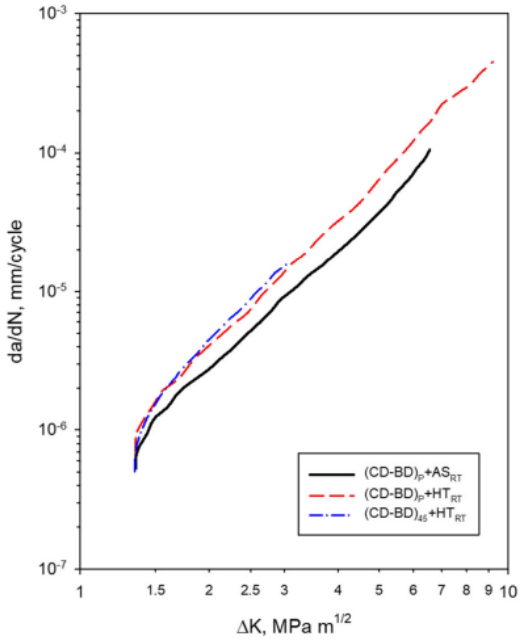

Figure 5.3. Fatigue crack growth curves for heat-treated samples made using room temperature plate.

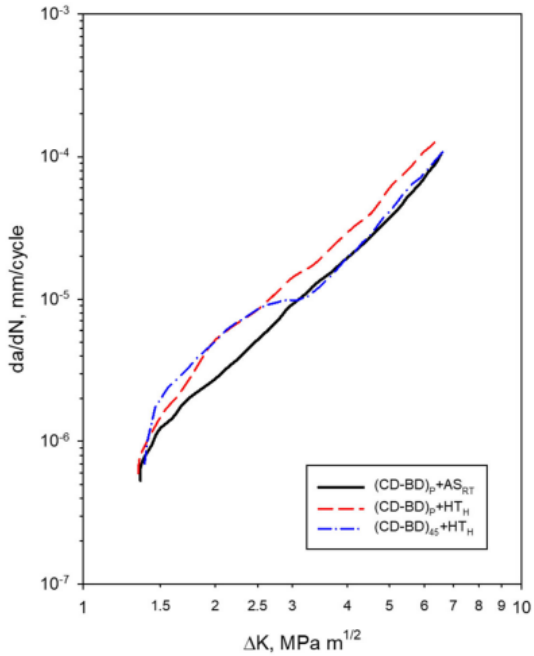

Figure 5.4. Fatigue crack growth curves for heat-treated samples made using heated plate.

These figures together illustrate the effects of print direction, plate temperature and heat treatment on the fatigue crack growth behaviour of the samples. The similarity of curves and ΔK_{th} across various conditions demonstrates the limited influence of build orientation, plate temperature and heat treatment on crack growth behaviour under cyclic loading. A detailed analysis of fatigue crack growth curves is presented below focusing on fatigue crack growth rate and threshold intensity factor ΔK_{th}.

5.1.1.1 Fatigue crack growth rate

In Figures 5.1 and 5.2, FCG curves for different CD-BD orientations for as-built samples under both room temperature and heated base plate conditions are presented. The FCG curves show consistent behaviour across the three orientations for both conditions. The Paris Law Parameters C and m have been identified for each sample tested, the results are summarised in the table (Table 5.1) and presented below:

Table 5.1. Paris Law Parameters for as-built samples.

Sample	Paris Law Parameters	
	C, (mm/cycle)/(MPa√m)^m	m
$(CD\text{-}BD)_P+AS_{RT}$	3.4×10^{-7}	3.02
$\underline{(CD\text{-}BD)_N+AS_{RT}}$	$\underline{5.47 \times 10^{-7}}$	$\underline{2.49}$
$(CD\text{-}BD)_{45}+AS_{RT}$	2.97×10^{-7}	2.95
$\underline{(CD\text{-}BD)_P+AS_H}$	$\underline{3.32 \times 10^{-7}}$	$\underline{2.87}$
$\underline{(CD\text{-}BD)_N+AS_H}$	$\underline{4.26 \times 10^{-7}}$	$\underline{2.68}$
$(CD\text{-}BD)_{45}+AS_H$	3.82×10^{-7}	2.86

These parameters were found to be similar across all CD-BD orientations and conditions, indicating that the fatigue crack growth rate (da/dN) is not significantly affected by CD orientation in relation to BD. The Paris law parameters (C and m) are thus largely independent of orientation and base plate temperature. However, it should be noted that Paris Law Parameters for samples $(CD\text{-}BD)_N+AS_{RT}$, $(CD\text{-}BD)_P+AS_H$, $(CD\text{-}BD)_N+AS_H$ cannot be calculated accurately (highlighted in Table 5.1) as Paris Law region for $(CD\text{-}BD)_P+AS_H$ and $(CD\text{-}BD)_N+AS_H$ is not linear due to some test error, and $(CD\text{-}BD)_N+AS_{RT}$ sample was used for the interrupted test for crack growth path investigation.

Figures 5.3 and 5.4 show FCG curves for heat-treated samples and built at either RT plate (Fig. 5.3) or heated plate (Fig. 5.4). Similar to as-built samples, Paris Law parameters C and m have been found using the technique described above for $(CD\text{-}BD)_P+AS_{RT}$ sample. The parameters for the heat-treated samples are (Table 5.2):

Table 5.2. Paris Law Parameters for heat-treated samples.

Sample	Paris Law Parameters	
	C, (mm/cycle)/(MPa√m)^m	m
$(CD\text{-}BD)_P+HT_{RT}$	3.7×10^{-7}	3.37
$\underline{(CD\text{-}BD)_{45}+HT_{RT}}$	$\underline{7.3 \times 10^{-7}}$	$\underline{2.76}$
$(CD\text{-}BD)_P+HT_H$	6.51×10^{-7}	2.76
$\underline{(CD\text{-}BD)_{45}+HT_H}$	$\underline{1.74 \times 10^{-7}}$	$\underline{3.41}$

Across all conditions and orientations, the Paris law parameters C and m are relatively stable, indicating minimal orientational effect or sensitivity to heat treatment. This observation aligns with previous studies, which consistently show that the Paris law parameters are robust to variations in microstructure (109). However, for some curves that represent heat-treated samples, similar to as-built samples, Paris Law Parameters cannot be accurately found due to interrupted test ($(CD\text{-}BD)_{45}+HT_{RT}$) or test error ($(CD\text{-}BD)_{45}+HT_{H}$) that leads to non-linear Paris Law region.

The Paris Law parameters *C* and *m* are primarily material-dependent, which means their values are mainly influenced by the properties of the alloy rather than the samples conditions, such as heat treatment or sample orientation. This explains why no significant differences in *C* and *m* values have been observed across various LPBFed Scalmalloy samples, as they all have been printed from the same alloy composition. To further confirm this material dependence, comparisons have been made using other alloys, including Al5083 (127), Al6005 (128), belonging to Al alloys and Ti Grade 2 (129). Titanium Grade 2 has been specifically included as a representative of a different material class from aluminium alloys. The resulting differences in Paris Law parameters across these materials reinforce the conclusion that *C* and *m* are predominantly dictated by the material's inherent characteristics.

Brahami et al. in (127) investigated and compared fatigue crack growth rate of diverse range of Aluminium alloy, including 5083-H22 alloy, which, as well as Scalmalloy, belongs to 5xxx Al alloy series. All samples in the research work have been tested at a stress ratio of R = 0.1, making it possible to compare the results obtained by Brahami et al. with the results of the present study. The results from (127) summarised in Table 5.3, present the Paris law equations for each alloy of their study.

Table 5.3. Paris Law Equations for Aluminum Alloys (127).

Material	Paris Law	ΔK region	C, (mm/cycle)/(MPa√m)^m	m
7075-T3	$da/dN=1.7E^{-7}\Delta K^{2.55}$	11-38 MPa√m	1.7×10^{-7}	2.55
2024-T3	$da/dN=5.35E^{-8}\Delta K^{3.23}$	7-18 MPa√m	5.35×10^{-8}	3.23
6082-T6	$da/dN=1.9E^{-6}\Delta K^{2.44}$	5-12MPa√m	1.9×10^{-6}	2.44
5083 H22	$da/dN=1.29E^{-6}\Delta K^{2.53}$	3.5-8 MPa√m	1.29×10^{-6}	2.53

The results demonstrated that there is no significant variation in m Parameter, with values ranging narrowly from 2.44 to 3.23. However, C parameter shows more variation, ranging from 5.35×10^{-8} for 2024-T3 to 1.9×10^{-6} for 6082-T6 alloy.

To further illustrate the lack of influence of material condition on fatigue crack growth (FCG) behaviour, it is useful to consider an example from the literature where a single alloy has been tested in multiple heat-treated states. Liu et al. (128) examined FCG behaviour of 6005A aluminium alloy containing Sc in three heat-treated conditions (Fig.5.5, Table 5.4): under-aged (UA), peak-aged (PA), and over-aged (OA) samples (128). All

specimens have been tested at a load ratio of R=0.1, which again aligns with the conditions used in the current study and thus allows a comparison.

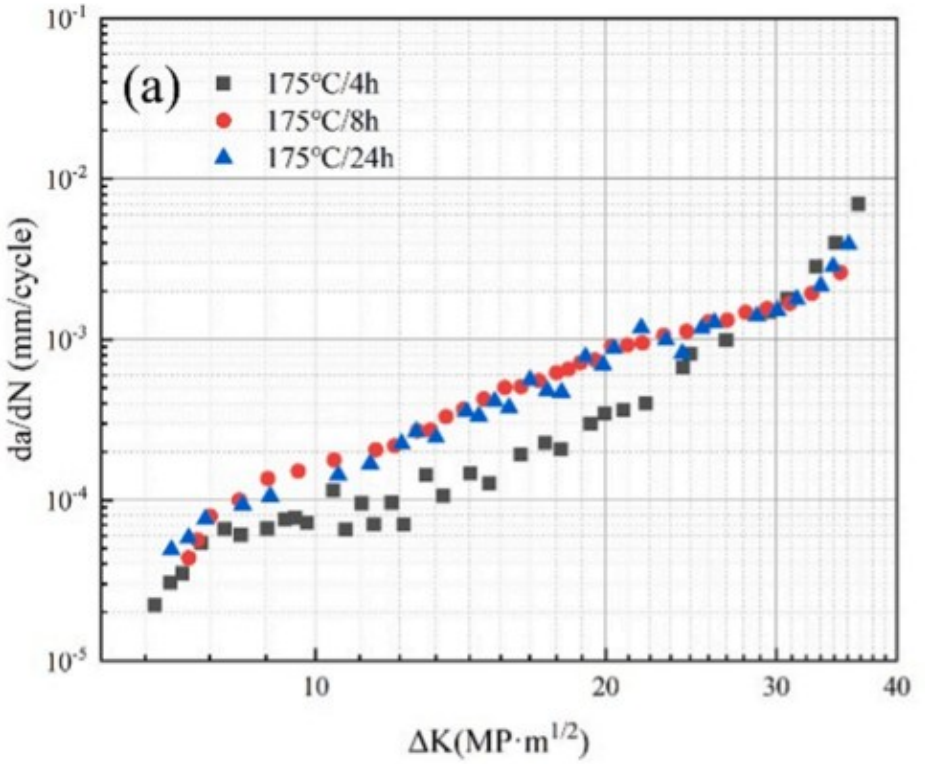

Figure 5.5. Curves showing the relationship between the FCGR and ΔK for various heat treatment conditions of Al6005 and Paris Law parameters for the corresponding curves (128)

Table 5.4. The values of the constants based on the fitting of the Paris Regions of the samples treated with different aging tempers from (128).

Sample	C, (mm/cycle)/(MPa√m)^m	m
UA	2.8093×10-8	3.2040
PA	6.7842×10-7	2.372
OA	1.0605×10-6	2.1542

When comparing the fatigue crack growth parameters of the UA, PA, and OA samples, it can be noted that the Paris Law parameters are relatively similar. However, the presence of a non-linear region in the Paris Law curves, as presented in the study, complicates the precise determination of these parameters.

In another study (129), the fatigue properties of additively manufactured Ti Grade 2 have been analysed in comparison with Al alloys. The fatigue crack growth behaviour, quantified by the Paris law, is determined as $C = 3.0 \times 10^{-9}$ (mm/cycle)/(MPa√m)^m and m = 4.2 while the aluminium alloys generally have C values in the range of 10^{-8} to 10^{-6} (mm/cycle)/(MPa√m)^m. Compared to various aluminium alloys, such as 7075-T6, 6082-

T6, 5083-H22, and 2024-T3 (with m values typically ranging from 2.5 to 4.0), Ti Grade 2 exhibits a higher m and a significantly lower C value.

Thus, the Paris law parameters *C* and *m*, which describe the relationship between fatigue crack growth rate (da/dN) and the stress intensity factor range (ΔK), are primarily material-dependent. Other factors such as heat treatment, build direction, or build plate temperature have minimal effect. This is clearly illustrated in Figure 5.6, where the FCG behaviour of AM Ti Grade 2 differs significantly from that of aluminium alloys, regardless of their processing or treatment conditions.

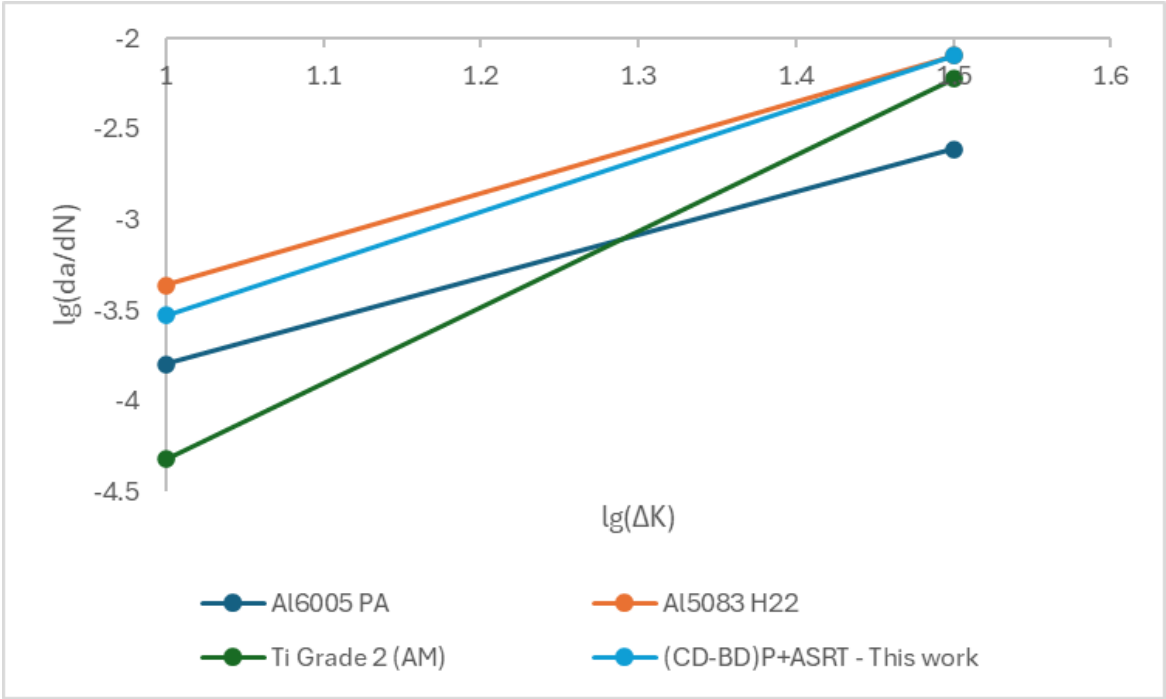

Figure 5.6. Logarithmic relationship between fatigue crack growth rate (FCGR) and the range of stress intensity factors.

To conclude, *C* and *m* parameters for both as-built and heat-treated samples vary minimally across different crack directions to build direction orientations, and base plate temperatures and are equal to $(3-5)\times10^{-7}$, (mm/cycle)/(MPa√m)^m and 2.9-3.0 correspondingly. The comparison of *C* and *m* parameters for other Al alloys in the previous studies demonstrated that these parameters obtained in the current study are similar and differ significantly from the parameters for Ti alloy. These findings suggest that the Paris law parameters are inherent to the material and largely unaffected by other processing conditions, meaning that *C* and *m* are primarily material-dependent.

5.1.1.2 Threshold intensity factor (ΔK_{th})

The threshold stress intensity factor (ΔK_{th}) is an important measure of the material's resistance to crack propagation and is defined as the minimum ΔK value below which the crack does not grow. From FCG curves provided in Figures 5.1-5.4, the ΔK_{th} has been determined as follows (Table 5.5):

Table 5.5. The threshold stress intensity factor (ΔK_{th}) for samples in the present study.

Sample	ΔK_{th}, MPa $m^{1/2}$
$(CD\text{-}BD)_P+AS_{RT}$	1.36
$(CD\text{-}BD)_N+AS_{RT}$	1.36
$(CD\text{-}BD)_{45}+AS_{RT}$	1.4
$(CD\text{-}BD)_P+AS_H$	1.42
$(CD\text{-}BD)_N+AS_H$	1.42
$(CD\text{-}BD)_{45}+AS_H$	1.34
$(CD\text{-}BD)_P+HT_{RT}$	1.34
$(CD\text{-}BD)_{45}+HT_{RT}$	1.27
$(CD\text{-}BD)_P+HT_H$	1.3
$(CD\text{-}BD)_{45}+HT_H$	1.46

For samples printed with the crack direction parallel, normal or at 45 degrees to the build direction - $(CD\text{-}BD)_P$, $(CD\text{-}BD)_N$, $(CD\text{-}BD)_{45}$ - the ΔK_{th} values, as the average for a particular orientation, range between 1.36 and 1.39 MPa $m^{1/2}$ demonstrating the minimal variation, suggesting that the crack orientation relative to build direction does not influence ΔK_{th}. Similarly, the base plate temperature (heated plate vs. room temperature) shows only a minor effect on ΔK_{th}. Samples built on a heated plate have values from 1.3 to 1.46 MPa $m^{1/2}$, while room temperature plate samples range from 1.27 to 1.4 MPa $m^{1/2}$. This close grouping further supports that base plate temperature has a limited impact on the ΔK_{th} values. Heat-treated samples exhibit ΔK_{th} values from 1.27 to 1.46, while for as-built samples, it varies from 1.34 to 1.42 demonstrating that heat treatment does not have any effect on ΔK_{th} values.

These values indicate that the ΔK_{th} is not significantly affected by the orientation, base plate temperature or heat treatment as all the curves are closely grouped around these ΔK_{th} values. However, the ΔK_{th} values observed in this study (≈1.36 MPa $m^{1/2}$) are lower than the value reported by Zerbst et al. (109) for Al5038-H321, which is 1.9 MPa $m^{1/2}$ at R = 0.1 (Fig. 5.7). It must be noted, the authors referred to the use of an Al5038 alloy, however, this is likely a typographical error, as there is no known Al5038 alloy, and it is assumed they intended to reference the Al5083 alloy instead. The Al5083 alloy with a similar composition to Scalmalloy, shows different ΔK_{th} values, which might be attributed to the differences in microstructure, in particular, it could be suggested that in normally wrought alloys such as Al5083, the grain size is relatively large, leading to a more pronounced crack closure effect and thus contributing to higher ΔK_{th} values.

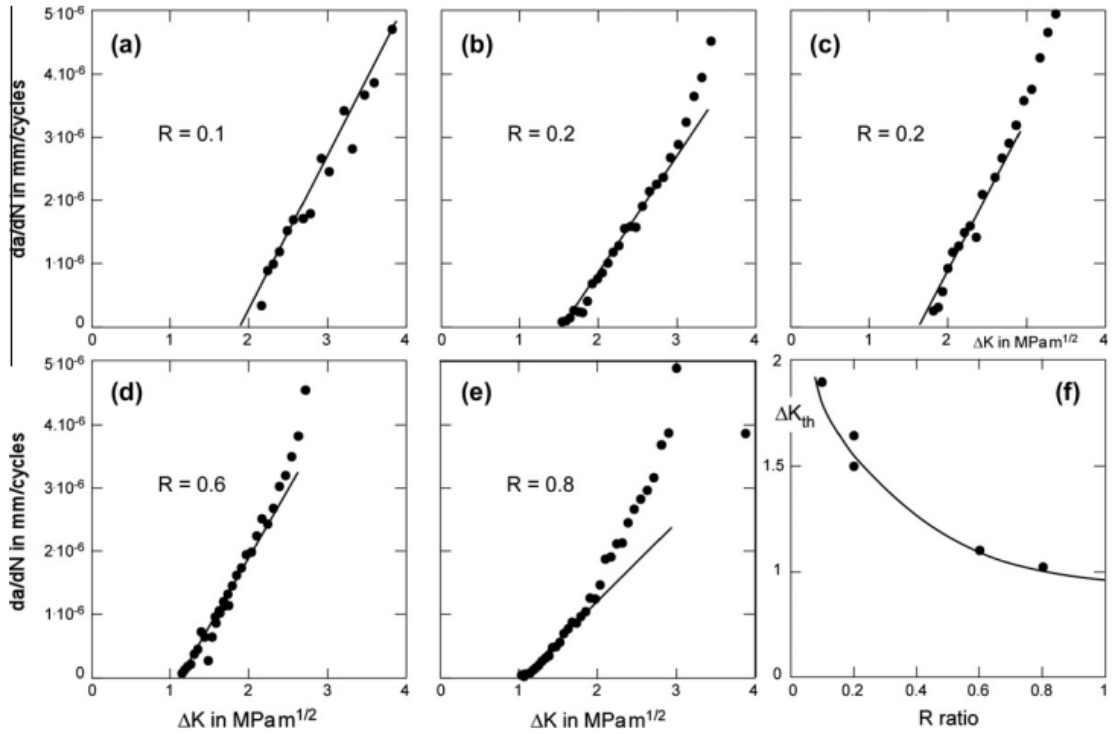

Figure 5.7. Determination of the intrinsic threshold value ΔK_{th} for the material Al5830 H321: (a)–(e) Determination of ΔK_{th} for R ratios of 0.1, 0.2, 0.6 and 0.8; (f) Determination of ΔK_{th} by extrapolating the ΔK_{th} values of (a)–(e) to R = 1 (130).

It has been widely demonstrated (109) (131) (132), that ΔK_{th} shows a significant increase with larger grain sizes, which is attributed to the roughness-induced crack closure effect. The roughness-induced crack closure effect is caused by the network of defects along the crack edges, which can prevent crack opening under cyclic loading. This effect is further increased by shear mode displacements, often leading to crack branching (Fig. 5.8).

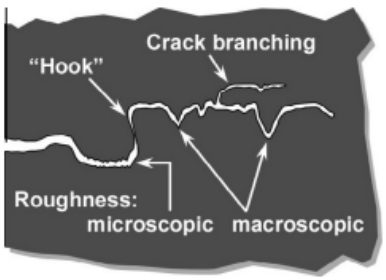

Figure 5.8. Crack tortuosity and branching as major contributors to roughness-induced crack closure (109).

These microstructural features cause variations in the crack path, which cause the increased contact between the crack surfaces and thus lower the effective stress intensity at the crack tip. This mechanism is particularly significant near the fatigue crack growth threshold, where it can contribute to a decrease in the crack propagation rate by increasing the resistance to crack opening and growth. Studies have also shown that larger grains cause a rougher crack surface that tends to enhance crack closure, thereby impacting the effective threshold for crack propagation (109) (Fig.5.9).

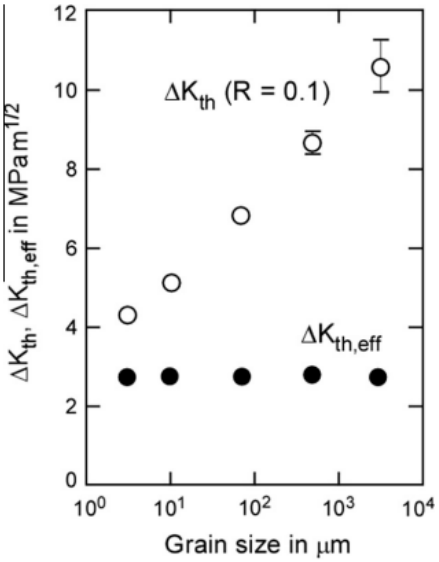

Figure 5.9. Effect of the grain size on the overall and intrinsic crack propagation thresholds, ΔK_{th} and ΔKth,eff, in ARMCO iron (109).

The effect of roughness of the fractured surface on the threshold stress intensity factor has also been demonstrated by Gray et al. (133). As illustrated in Figure 5.10, increasing the surface roughness leads to a higher ΔK_{th} value, which is in agreement with Zerbst et al. (109). It has also been shown that this effect is especially pronounced when stress ratio R = 0.1, compared to R = 0.7, where the crack closure effect is minimal. The high crack closure effect at R=0.1 with the elevated ΔK_{th} is due to a decrease in ΔK_{eff} caused by crack tip blockage, while increasing R allows the crack to remain open throughout the load cycle, reducing the crack closure effect.

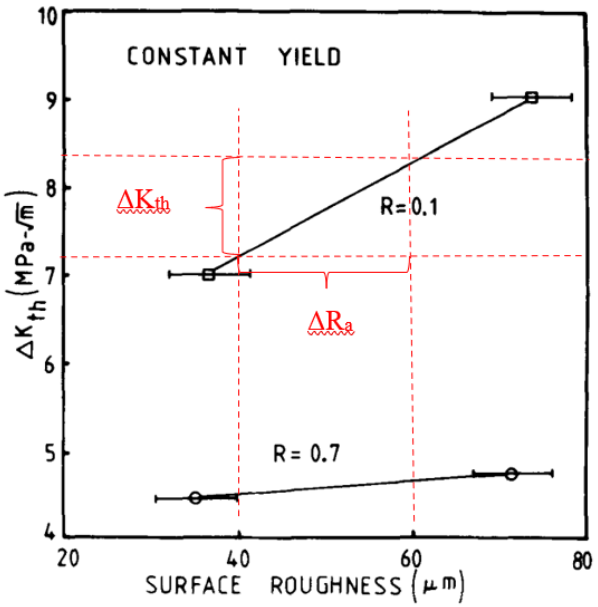

Figure 5.10. Relation between surface roughness and ΔKth, for roughness measurements near threshold (133).

The bar chart (Fig. 5.11) below displays the relation between surface roughness (R_a) and ΔK_{th} values for samples tested for fatigue crack growth in this study. It is observed that the fracture surface roughness values (represented by the yellow bars) and ΔK_{th} (represented by the green line) do not show significant differences across all sample conditions. Compared to data presented in (133), where ΔR_a = 20µm causes an increase of ΔK_{th} at ≈1 MPa√m, in this study, R_a does not vary significantly, from 2.39 µm to 3.46 µm. Although there are some variations, the overall trend suggests that the current study maintains consistent levels of $R_a \approx 2.9$ µm and $\Delta K_{th} \approx 1.36$ MPa√m.

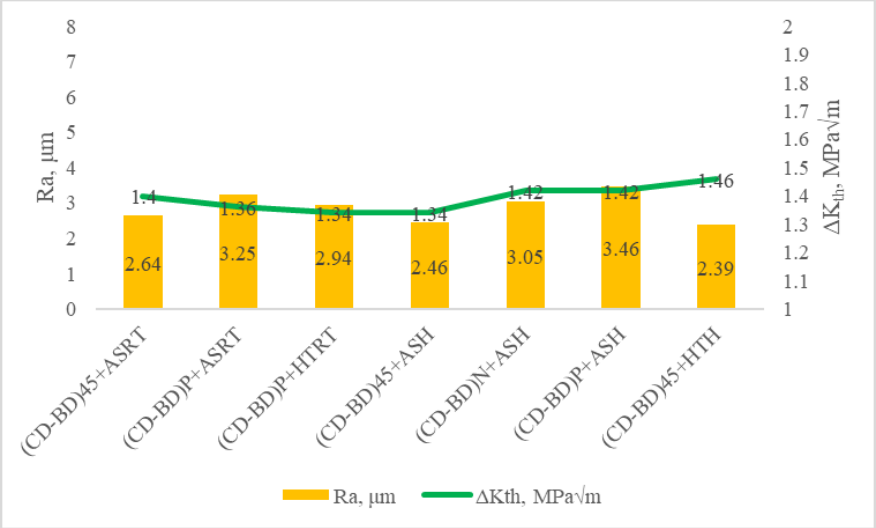

Figure 5.11. Fracture surface roughness (R_a) and ΔK_{th} for samples used in the current study.

Scalmalloy is characterized by its small grain size, thus, low fracture surface roughness, which significantly affects its fatigue crack propagation. The threshold stress intensity factor, ΔK_{th}, as discussed above, is affected by microstructural features, and in the case of Scalmalloy, the fine grains contribute to lower ΔK_{th} values. In this study, despite variations in orientation and heat treatment, the ΔK_{th} remained consistent, indicating that the bimodal microstructure does not significantly affect ΔK_{th}. This suggests that the microstructural characteristics of the alloy, such as those affected by orientation and heat treatment, do not substantially alter the crack path tortuosity or the threshold value. To validate this inference, the crack growth path was examined in both the as-built and T6 grain structures and the findings are presented in the following section.

5.1.2 Crack growth path in as-built and T6 bimodal grain structure

To analyse the crack tip region of a sample tested with a K-decreasing scenario, SEM has been used. Figure 5.13a presents SEM micrographs detailing the crack propagation through the bimodal microstructure. At lower magnifications (bottom left of Fig. 5.12a), the crack path appears relatively smooth overall. In the equiaxed grains region (bottom right of Fig. 5.12a), the crack path is notably smooth, reflecting the sub-micron grain sizes present in these regions. Due to the small grain sizes, it is difficult to verify the mode of fracture, whether it is transgranular or intergranular, directly from these images. However, regardless of fracture mode, the

roughness of the crack path is determined by the grain size at the particular region, indicating that the crack roughness (R_a) in equiaxed grain area is less than 1 μm.

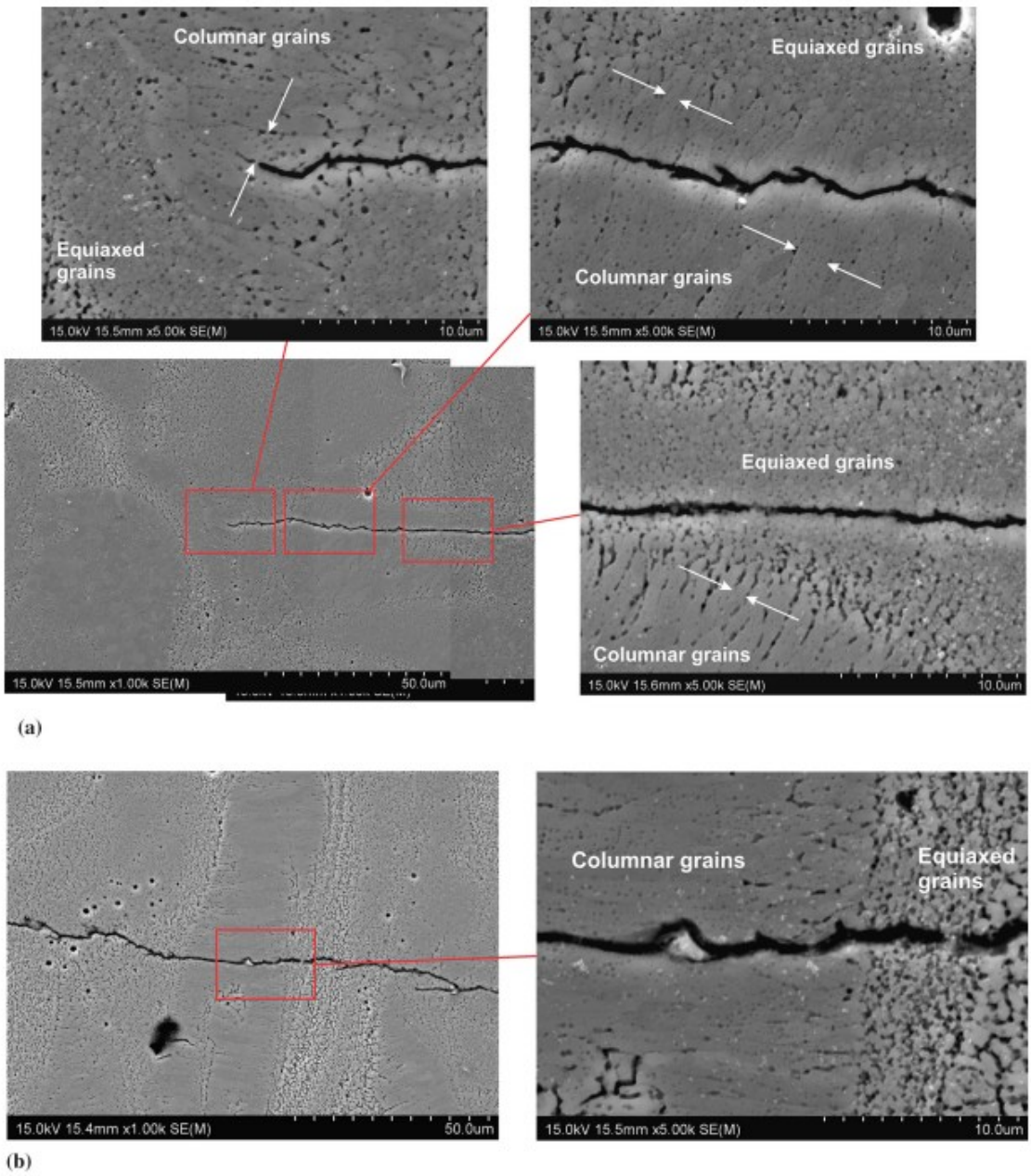

Figure 5.12. SEM micrographs taken in (a) the crack tip and thus in a near threshold region and (b) 5.2mm (ΔK=2.8MPa $m^{1/2}$) from crack tip of a $(CD\text{-}BD)_P+AS_{RT}$ sample (CD and BD to the left). In (a) each pair of arrows indicates the width of the columnar grain.

The SEM micrographs reveal that as the crack propagates into the columnar grain region (upper right of Fig. 5.12a), there is no significant increase in crack growth resistance compared to the equiaxed grains. The crack grows transgranularly and shows a slight deviation of a few degrees from the base direction (BD) before adjusting and continuing in the equiaxed region. Columnar grains, oriented at approximately 80° to the BD, provide minimal additional resistance for crack to grow. The width of the columnar grains, ranging from 1 to

2 μm (bottom right of Fig. 5.12a) and the crack's deviation suggest that the crack path remains mostly smooth on a micron scale, despite local tortuosity.

As the crack progresses into a new track (top left of Fig. 5.12a), the mode of fracture shifts as the crack moves through equiaxed grains and then into differently oriented columnar grains, where grain boundaries are inclined at angles 5-10° to the BD. The crack propagation along grain boundaries becomes evident in this region. This change in crack propagation mode highlights that the crack path remains generally smooth, with only minor deviations, in the Paris law region (Fig. 5.12b), which corresponds to $\Delta K = 2.8$ MPa $m^{1/2}$.

An SEM micrograph for $(CD\text{-}BD)_{45}$ sample, with an Electron Backscatter Diffraction (EBSD) orientation map shows the crack path through and along the columnar grain boundaries (Fig. 5.13). The EBSD map illustrates that the crack predominantly follows the grain boundaries, except for a few grains where the crack path propagates intergranularly. This observation confirms that, regardless of the sample orientation, columnar grains can be nearly parallel or at a significant angle to the BD and do not significantly influence the crack path. The features observed in the fracture surfaces of the as-built samples (Fig. 5.13) include smooth propagation through equiaxed grains regions and minor zigzag steps in the columnar grains regions due to the small grain widths (1-2 μm).

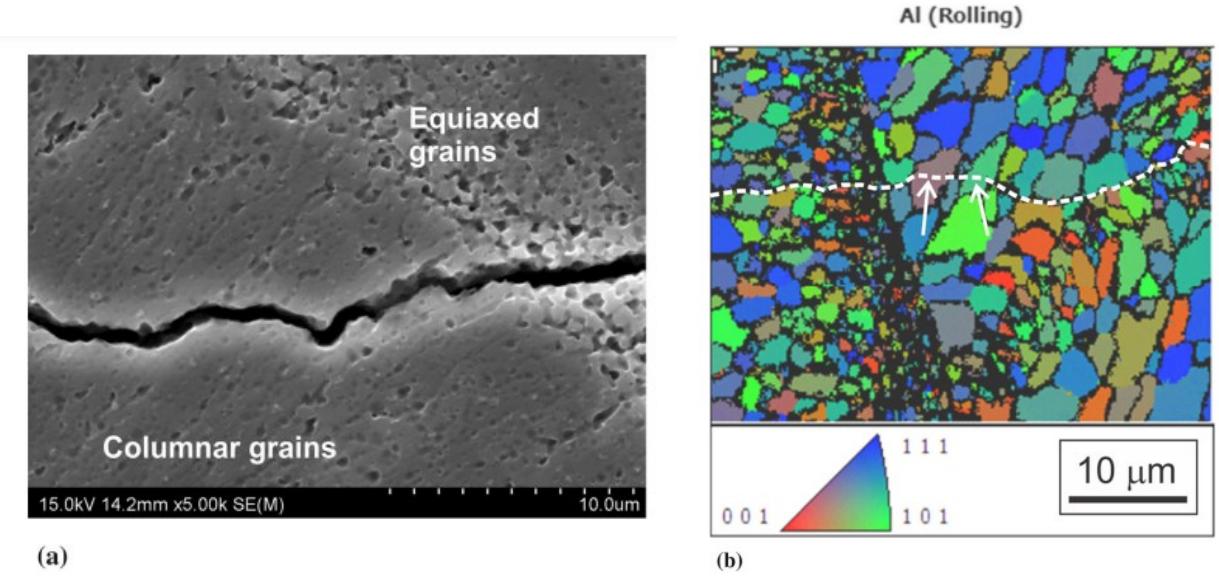

Figure 5.13. (a) SEM micrograph and (b) EBSD orientation map taken in locations near threshold region in K-decreasing $(CD\text{-}BD)_{45}$+AS_{RT} sample. In (b) the dotted line superimposed represents the crack traced in pattern quality map in which the crack is clear and the two arrows point to grains of transgranular crack growth.

An example of examining the fracture surface is shown in Fig. 5.14, for an as-built $(CD\text{-}BD)_{45}$ sample. This fractograph is highly representative of the fracture surfaces of all the samples in both the Paris law and near-threshold regions. Regions or bands of equiaxed and columnar grains that have been fractured through are clear in the fractograph. It also reveals that locally in equiaxed regions that the fracture surface is very smooth and the zigzag steps in the fracture surface of columnar regions are very small. The examination of the fracture surface represented in Figure 5.14 is thus consistent with the examination of the fracture path shown in Fig.

5.12 and 5.13. In general, all the examinations have suggested a very smooth fracture path in the equiaxed region and zigzag step height being generally less than a micron in the columnar grain region.

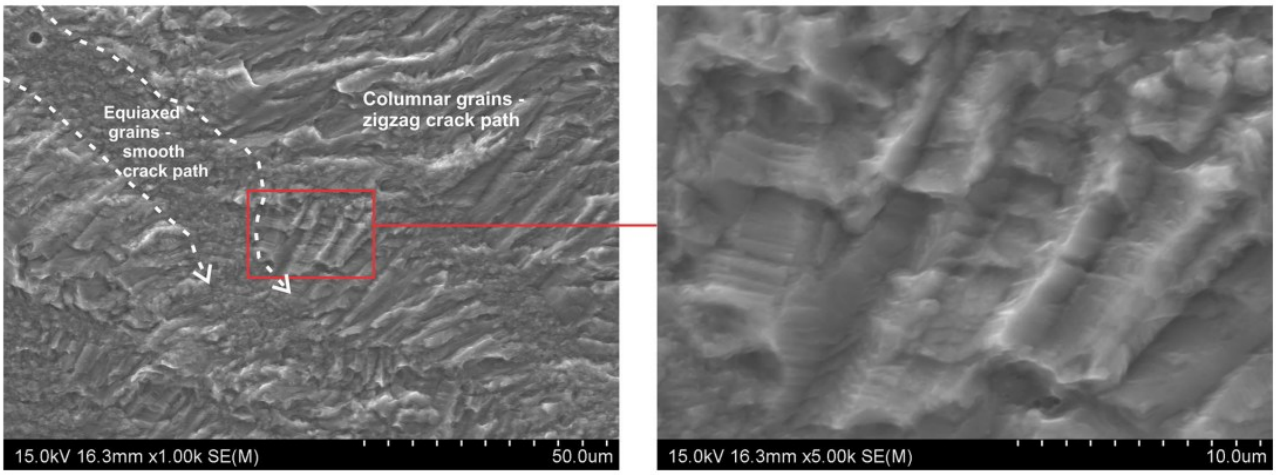

Figure 5.14. SEM fractographs taken in a near threshold region in K-decreasing $(CD\text{-}BD)_{45}$+AS_{RT} sample, with smooth crack path in equiaxed grain region and zigzag crack path with small steps in columnar grain region indicated.

To investigate the effect of heat treatment on fatigue crack growth, aging at 325°C for 4h has been performed. Figure 5.15 shows an SEM micrograph of a heat-treated $(CD\text{-}BD)_{45}$ sample. The heat treatment resulted in a slight homogenization of the microstructure, which made the grain boundaries less clear. Despite this, the crack growth behaviour observed in the aged sample remains consistent with those in the as-built samples. The crack path remains smooth in the equiaxed regions and exhibits small zigzag steps through the columnar grains.

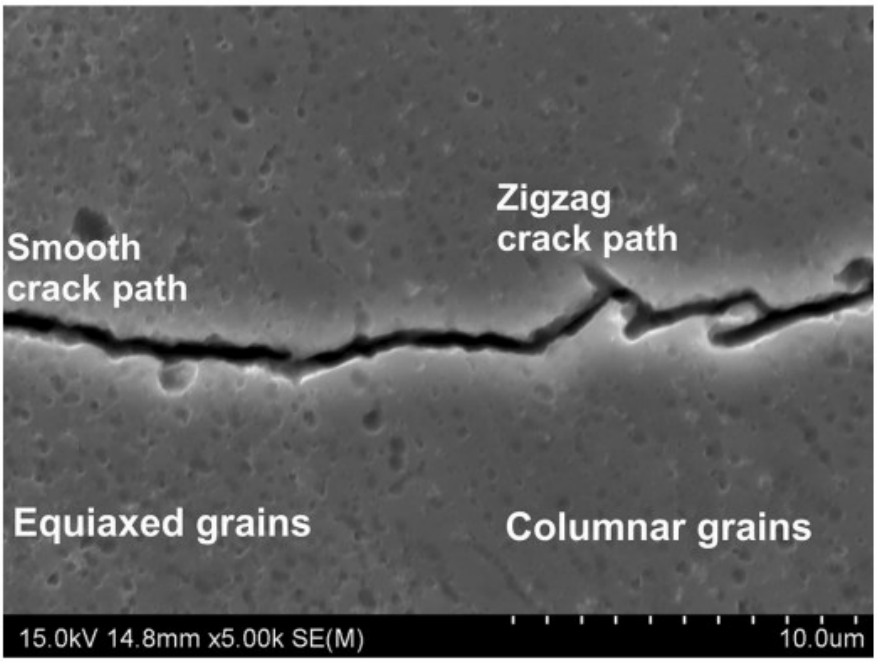

Figure 5.15. SEM micrographs taken in a near threshold region in K-decreasing $(CD\text{-}BD)_{45}HT_{RT}$ sample, with smooth crack path in equiaxed grain region and zigzag crack path with small steps in columnar grain region indicated.

The analysis of the crack path and fracture surfaces suggests that fine bimodal microstructure, characterized by small equiaxed and columnar grains, does not induce significant roughness in the crack path. This observation is in agreement with findings by Zerbst et al. (109), who noted that ΔK_{th} is closely related to Young's modulus and that large grain sizes can significantly increase roughness-induced crack closure effect. ΔK_{th} increase with grain size increase has been also reported by Pao et al. (134). However, for the LPBFed Scalmalloy samples in this study, the grain sizes are small, typically less than 1 μm for equiaxed grains and up to 2 μm for columnar grains. Thus, the roughness of the crack path remains low, leading to ΔK_{th} values for all samples regardless of their orientation, heat treatment and base plate temperature, of approximately 1.3-1.4 MPa $m^{1/2}$.

5.1.3 Discussion on how grain structure affects crack growth

The influence of microstructure on crack growth behaviour, the effect of heat treatment (homogenization), and how it correlates with ΔK_{th} have been investigated through a combination of FCG tests, SEM micrographs, and EBSD analysis. It has been demonstrated that in regions with equiaxed grains, which have sub-micron sizes, the crack path is remarkably smooth (Fig. 5.13). when the crack propagates into the columnar grain regions, the mode of crack growth is mainly transgranular, although a few columnar grains with a crack propagating through them have been observed (Fig. 5.13). The columnar grains, with widths ranging from 1 to 2 μm, similar to equiaxed grains, do not provide a significant increase in crack growth resistance due to the small grain widths (1-2 μm). Although there is some deviation from the base direction, the overall crack path remains smooth with small zigzag steps through columnar grains

Aging has induced slight homogenization in the microstructure of Scalmalloy, as demonstrated on the SEM micrograph (Fig. 5.15). Despite the grain boundaries being less clearly visible, the fracture behaviour remains identical to that observed in as-built samples. The crack propagates smoothly through equiaxed grains and in small zigzag steps through columnar grains. This observation suggests that heat treatment does not significantly change the impact of grain structure on crack growth behaviour and confirms that the bimodal grain structure maintains a low roughness-induced crack closure effect regardless of heat treatment conditions.

Fracture surface analysis (Fig.5.14) further confirms the observations from SEM micrographs of the crack path. The smooth fracture surfaces in equiaxed regions and the minimal zigzag steps in columnar regions indicate that the crack path remains largely unaffected by the grain structure. The small step sizes observed in columnar grain regions are due to the small grain widths (1-2 μm), supporting the conclusion that the crack path is generally smooth.

The consistent ΔK_{th} values of approximately 1.3-1.4 MPa $m^{1/2}$ across various conditions and orientations confirm the minimal effect of grain size (whether it is equiaxed or columnar grain region) and orientation on the threshold stress intensity factor. Low ΔK_{th} values are attributed to the fine microstructure in the Scalmalloy samples produced by LPBF, which causes low fracture surface roughness and minimal roughness-induced crack closure effect.

In conclusion, the analysis of crack growth path shows that the bimodal microstructure, which consists of equiaxed and columnar grains, does not significantly hinder crack propagation. Both grain types, columnar and equiaxed, promote a smooth crack path with minimum branching and zigzag steps in columnar regions. The consistency in crack path characteristics and ΔK_{th} across various conditions demonstrates the limited influence of grain type (either equiaxed or columnar), build orientation and heat treatment on crack growth behaviour under cyclic loading.

5.2 Fatigue life (S-N) and fatigue strength

5.2.1 S-N data for various loading conditions

This section presents the fatigue data obtained from testing the Scalmalloy samples under varying conditions:

- As-built group: crack direction parallel to build direction, CD//BD-AB, and crack direction normal to build direction, CD⊥BD-AB (Fig. 5.16).
- Heat-treated group: crack direction normal to build direction, CD⊥BD-HT, and crack direction parallel to build direction, CD//BD-HT (Fig. 5.17).

After the presentation of data comparing the fatigue strength values in terms of loading direction, the same fatigue data will then be plotted comparing values from as-built samples to heat-treated samples (Fig.5.18).

5.2.1.1 S-N curves for as-built samples

S-N curves for the as-built group of samples are presented in Figure 5.16. The fatigue data of CD⊥BD-AB are similar to the data of CD//BD-AB, up to about $N=2\times10^5$, where fatigue strength decreases in an almost linear way, as cycle number increases. From about $N=2\times10^5$, the fatigue strength values of CD//BD-AB appear to be lower than the values of CD⊥BD-AB samples. This S-N relationship is common for 5xxx series Al alloys. To determine whether the experimental results for Scalmalloy obtained in this study are reasonable and align with established material performance, a comparison has been conducted with literature data for Al 5056 (135).

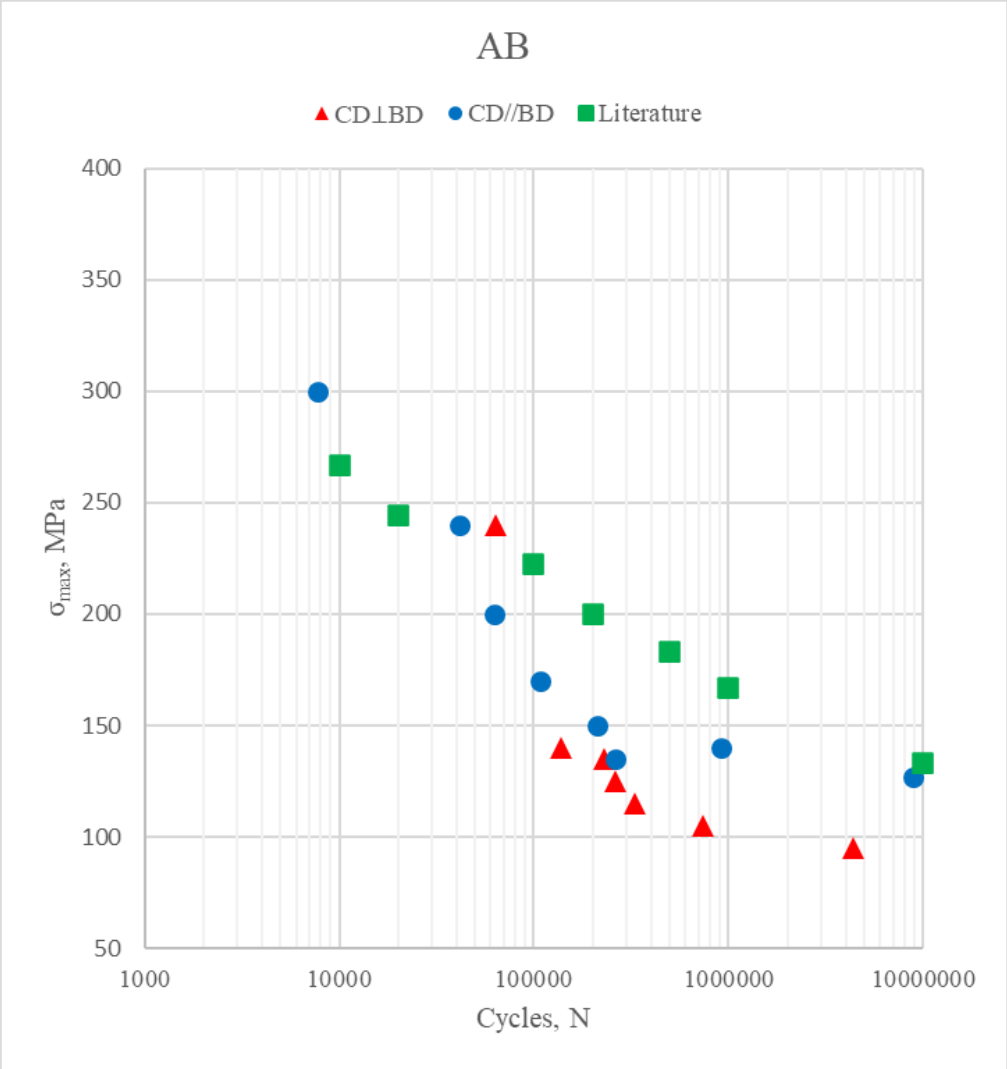

Figure 5.16. S-N curves for CD⊥BD and CD//BD as-built Scalmalloy samples along with S-N curve for 5056 Al alloy from (135).

The experimental results for both CD⊥BD and CD//BD builds of Scalmalloy exhibit a similar fatigue trend to the literature reference curve. The S-N curves for Scalmalloy produced via LPBF are shifted to the left after $N=4\times10^5$ when compared to conventional Al 5056. This shift means lower fatigue strength at the same number of cycles, which might be caused by the presence of defects of the type found in LPBFed samples. However, the overall trend is similar, which confirms that the S-N curves of Scalmalloy are reasonable.

Analysing S-N curves for the as-built state, it can be noted that beyond 4×10^5 cycles, the curve begins to flatten, as is characteristic of fatigue data. As the maximum stress decreases below 150 MPa, the fatigue life of CD⊥BD-AB and CD//BD-AB samples increases, transitioning into the high-cycle fatigue regime ($N > 10^6$ cycles). Across the stress ranges, there is no significant difference in the S-N behaviour of CD⊥BD and CD//BD orientations until the fatigue limit is approached, where significant distinctions are observed, thus, CD//BD build demonstrates slightly better fatigue resistance in the high-cycle regime. The S-N curve for CD⊥BD-AB samples shows scatter in the mid-cycle range (~1.5×10^5 cycles), which can be attributed to the LOF defects.

Thus, the S-N curves for the as-built samples of LPBFed Scalmalloy exhibit typical fatigue behaviour, consistent with established observations in literature (136), and CD//BD Scalmalloy samples demonstrate relatively better fatigue resistance than CD⊥BD samples, particularly in the mid- and high-cycle regimes. The reason for this difference will be explored later in this chapter.

5.2.1.2 S-N curves for T6 samples

S-N curves for heat-treated samples in both CD//BD and CD⊥BD are presented in Figure 5.17. At maximum stress greater than 200 MPa, CD⊥BD-HT and CD//BD-HT samples achieve mid-cycle fatigue life, with failures occurring in the range of 3×10^4 to 10^5 cycles. At maximum stress below 150 MPa, the samples transition into the high-cycle fatigue regime, with fatigue lives extending beyond 10^6 cycles. Similar to S-N curves of as-built samples, the trends observed in these curves remain typical for Al aluminium alloy and consistent with fatigue data presented in the study by Vinogradov et al. (135).

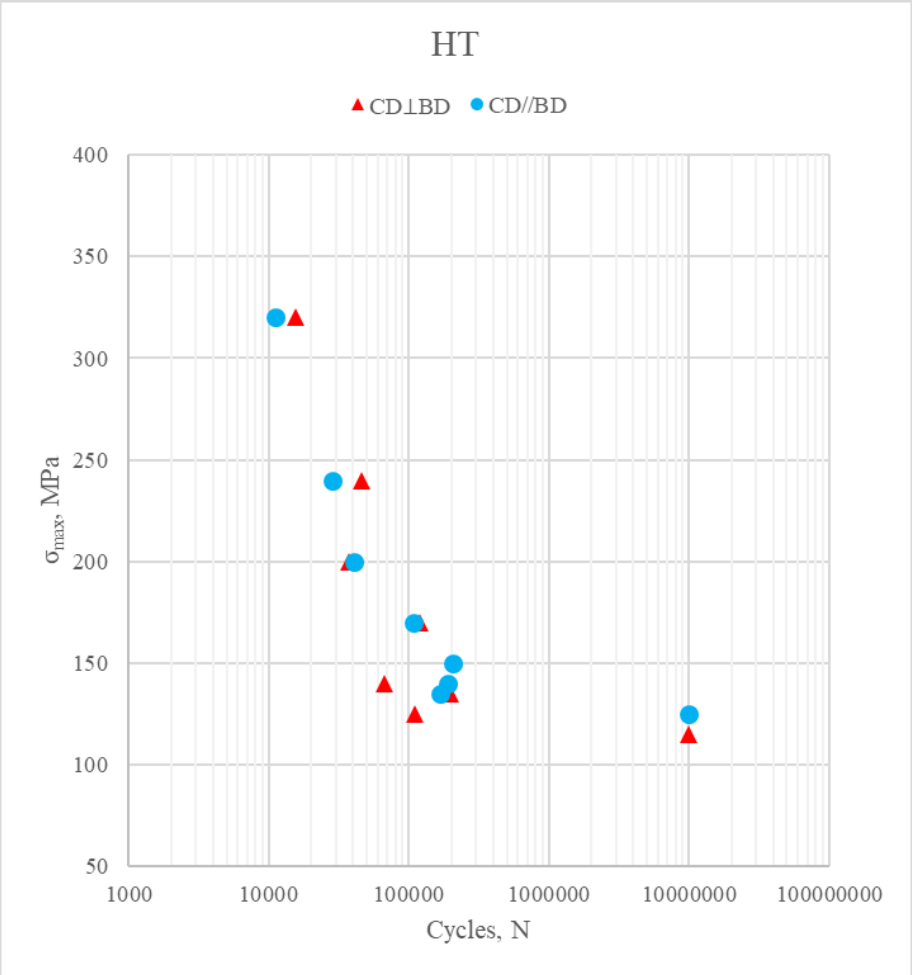

Figure 5.17. S-N curves for CD⊥BD and CD//BD samples after heat treatment.

Further to the data presented above for comparing the effect of build orientation, S-N curves for Scalmalloy in as-built (AB) and heat-treated (HT) conditions have been compared (Fig. 5.18). It has been shown that heat treatment does not significantly affect the fatigue properties of the material and both the CD⊥BD and CD//BD

orientations exhibit similar fatigue performance trends and fatigue limit, regardless of the heat treatment condition.

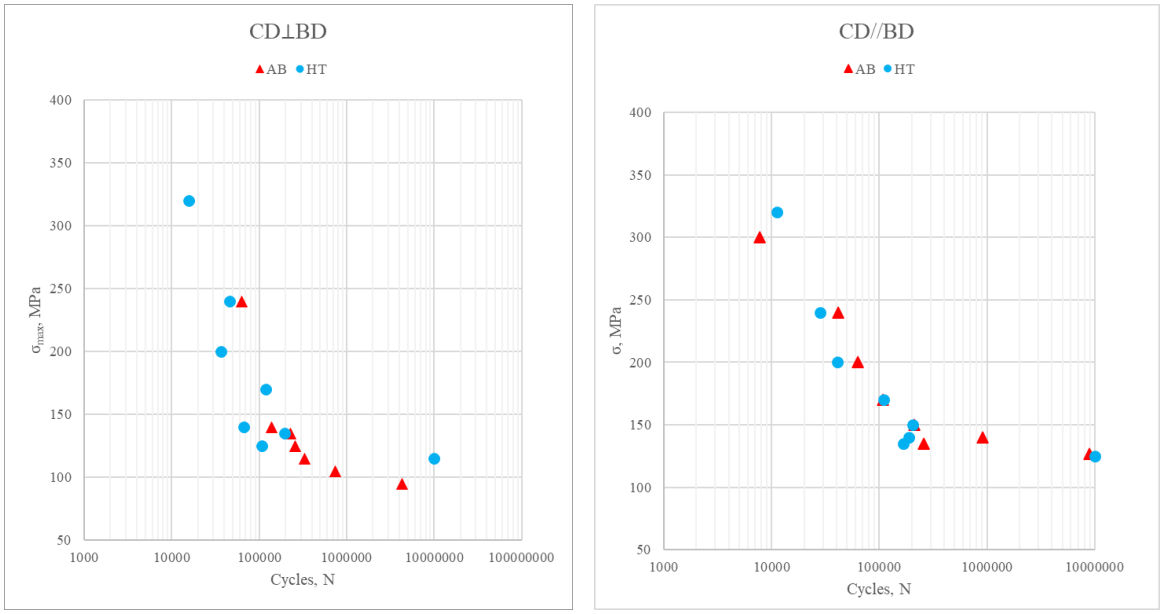

a) b)

Figure 5.18. S-N curves for CD⊥BD (a) and CD//BD (b) samples in as-built and heat-treated conditions.

The above data presentation points to:

- The data are typical following the general S-N trends but the present data largely located more to the left, meaning the fatigue strength values are lower than conventional Al 5056 (135).
- CD⊥BD samples appear to be at least slightly lower in fatigue strength than CD//BD samples in the high cycle range when $N>10^5$.
- Heat treatment has not been found to affect the fatigue strength.

As has been introduced and reviewed in Chapter 2.3.3, fatigue and particularly high cycle fatigue is highly defect sensitive. Thus, defect observation and analysis of the tested samples have been made to establish how LPBF defects may have affected the fatigue behaviour as presented, observed and stated above.

5.2.2 Observation and measurement of defects

As explained in Chapter 3, after fatigue testing, each sample has been examined and the size of defects presented in the fracture surfaces together with the locations of the defects have been measured. In this section, fracture surface defect sizes detected and measured in S-N tested samples will first be presented and explained. There are two types of defects detected, and they are LOF and spherical pores. Defects located on the surface of the sample are crucial, as they act as primary sites for crack initiation. The influence of subsurface defects

becomes less critical as their distance from the surface increases. The schematic illustration of critical sample surface defect leading to fracture is presented in Figure 5.19.

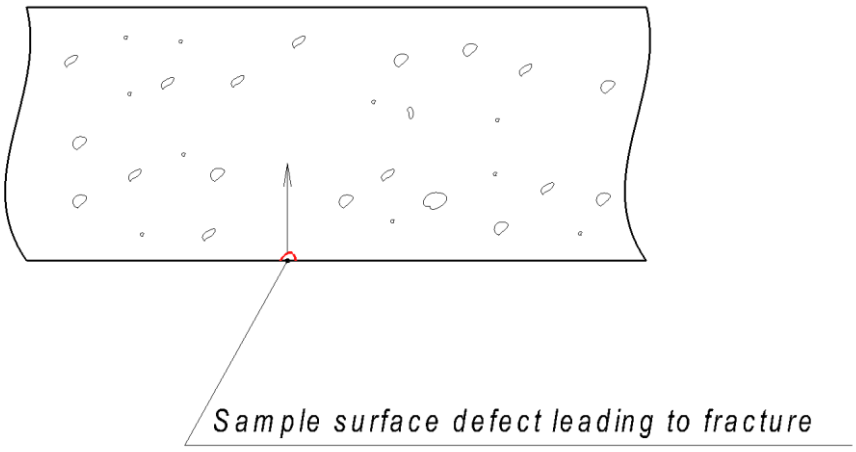

Figure 5.19. Schematic illustration of a sample surface defect leading to fracture.

Further to the description in Experimental Chapter 3, a typical example of LOF surface defect and the result of measurement on the defect area are shown in Fig. 5.20. The low magnification SEM image in Figure 5.20(a) clearly illustrates the crack propagation originating from this defect (Fig. 5.20(b)) and progressing towards the final fracture of the sample. In Fig. 5.20, an example of subsurface defects is shown. Gas or keyhole pores may not be high in number but they do occasionally appear, as shown in Figure 5.22. The complete set of fractographs showing the defects and their measured results of sizes is presented in Appendix D.

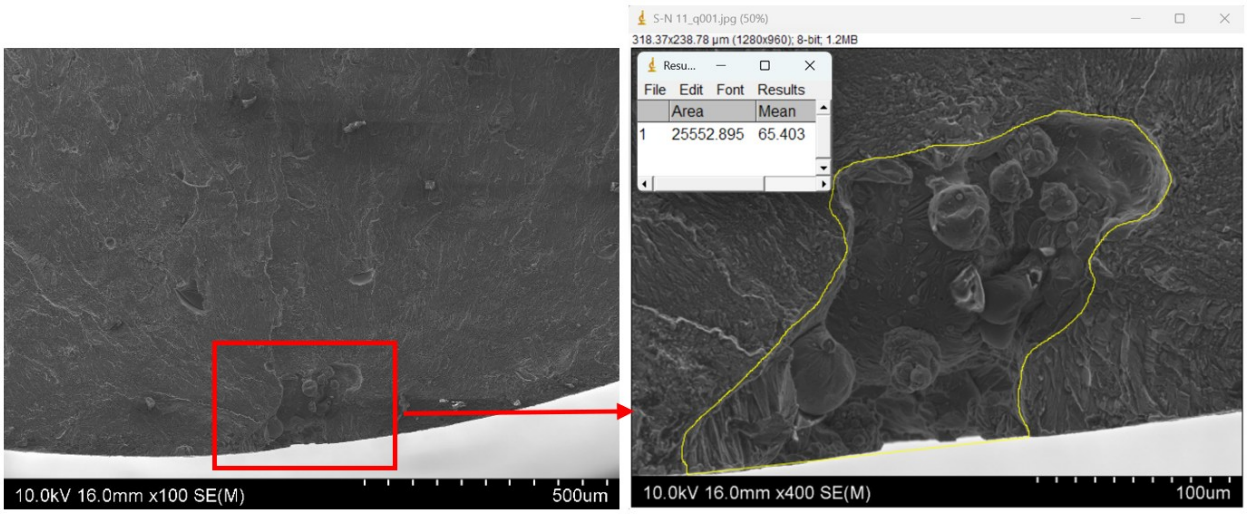

a) b)

Figure 5.20. Fracture surface of CD//BD-HT sample tested at 135 MPa a)x100, b)x400.

Surface defect of the sample before testing, where the fracture initiated, for CD//BD-HT sample is presented in Figure 5.20. This defect is classified as Lack of Fusion (LOF), which occurs due to incomplete bonding

between layers or material regions, typically from insufficient heat. This defect is located adjacent to the fracture edge and its area and, as indicated in the image analysis, is approximately 25,553 μm² (√a = 160 μm). The defect has an irregular and clustered appearance, with regions of voids and unmelted material.

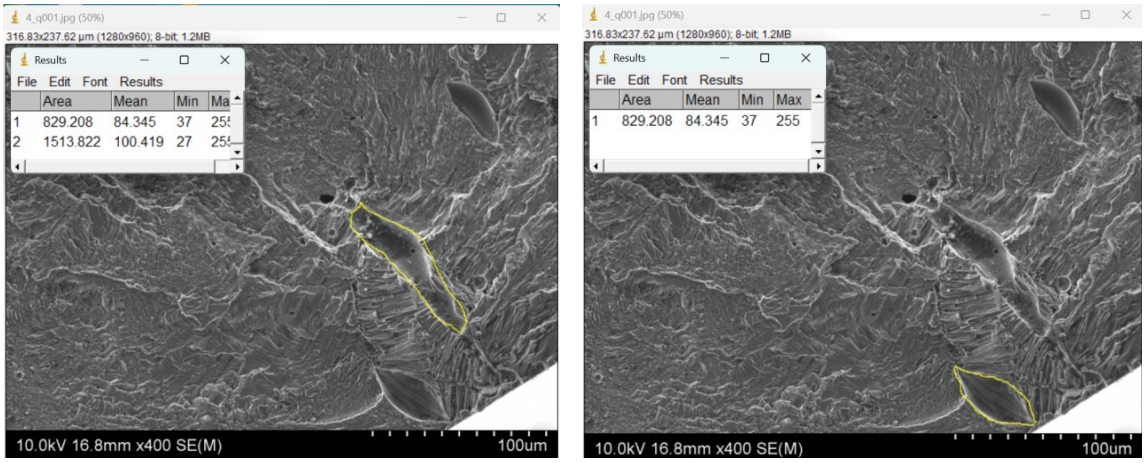

Figure 5.21. Defects initiated fracture for CD//BD-HT sample tested at 170 MPa.

The defect presented in Figure 5.21 is subsurface, as evident from its position ≈ 50 μm away from the material's surface edge. Similar to the defect in Figure 5.20, this defect is classified as LOF, with two voids with an area of ≈ 829 μm² (√a = 29 μm) and 1,514 μm² (√a = 39 μm). Another type of defects, which is rarely observed, is the gas or key hole pore (Fig. 5.22). For samples CD⊥BD-AB the pore observed is the subsurface defect located ≈ 100μm away from the edge and has area of 602μm² (√a = 25 μm).

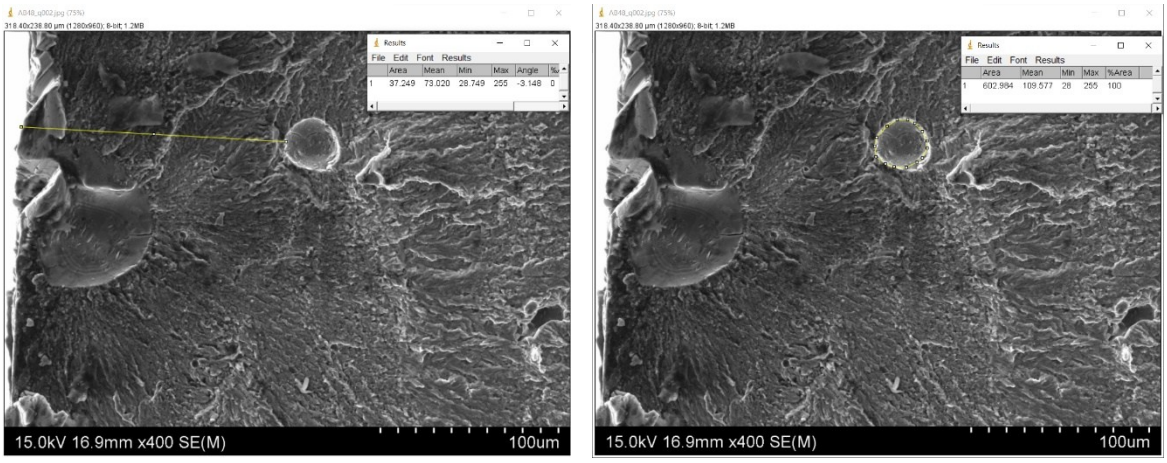

Figure 5.22. Gas or keyhole pore observed on fracture surface of CD⊥BD-AB sample tested at 240 MPa.

The table below (Table 5.6) lists the values of Murakami's √area parameters for various tested samples. As has been introduced in Chapter I, the parameter is the square root of defect size. In the table, information of the samples on build orientation, applied maximum stress (σ_{max}, MPa), and the number of cycles to failure (N(cycles)) is also given. The data will be used for the analysis of how defects affect fatigue strength in the next section.

Table 5.6. Murakami's √area parameters, σ_{max}, $\Delta\sigma$, and the corresponding number of cycles for samples in the current study.

Sample	√a, μm	σ_{max}, MPa	Δσ, MPa	N(cycles)
CD//BD, AB				
CD//BD-AB-1	71	200	180	63064
CD//BD-AB-2	160	170	153	108527
CD//BD-AB-3	53	150	135	210260
CD//BD-AB-4	81	140	126	915178
CD//BD, HT				
CD//BD-HT-1	63	200	180	40920
CD//BD-HT-2	35	240	216	28195
CD//BD-HT-3	68	170	153	108874
CD//BD-HT-4	54	140	126	188071
CD//BD-HT-5	106	150	135	205505
CD//BD-HT-6	30	320	288	11159
CD//BD-HT-7	160	135	121.5	165882
CD⊥BD, AB				
CD⊥BD-AB-1	71	240	216	63734
CD⊥BD-AB-2	190	140	126	137722
CD⊥BD-AB-3	151	135	121.5	229201
CD⊥BD-AB-4	155	125	112.5	260127
CD⊥BD-AB-5	117	115	103.5	332149
CD⊥BD-AB-6	143	105	94.5	741044
CD⊥BD -AB-7	126	95	85.5	4339675
CD⊥BD, HT				
CD⊥BD-HT-1	172	320	288	15676
CD⊥BD-HT-2	115	240	216	46274
CD⊥BD-HT-3	304	200	180	37182
CD⊥BD-HT-4	187	170	153	120828
CD⊥BD-HT-5	404	140	126	67064
CD⊥BD-HT-6	185	135	121.5	199230
CD⊥BD-HT-7	692	125	112.5	109343
CD⊥BD-HT-8	NA	115	103.5	10,000,000

5.2.3 Evaluating effect of defects using Kitagawa-Takahashi method

As has been explained in Chapter 1.3, the Kitagawa-Takahashi (K-T) method has been regarded as an effective method to evaluate how defects affect fatigue strength. As can be seen from the K-T diagram for as-built samples (Fig. 5.23), most data points are located outside the non-crack growth (safe) region. The defect areas in these samples can therefore be evaluated based on their distance from the safe region, using the predicted ΔK_{th} values. Generally, the dataset follows the expected relationship between stress range and defect size, with larger defects correlating with lower stress levels

Samples that failed before 100,000 cycles (marked in red) experienced short cycle life, as they appear in the high-stress region ($\Delta\sigma > 160$ MPa). The samples that experienced a high number of cycles (N > 500,000 cycles, marked in dark blue) and samples within the 400,000–500,000 range (marked in dark green) mainly fall within the range of $\Delta K = 1.2\text{-}1.4$ MPa$\sqrt{m}$, which is indicated by the dashed and dotted lines. This alignment suggests that the fatigue crack growth threshold is accurately captured in Chapter 5.1.1. Atzori et al. (137) have provided a summary of a_o for many aluminium alloys and based on their data, the critical size of defect leading to fracture is suggested to be 85µm. Thus, based on this assumption, ΔKth determined 1.37 MPa$\sqrt{m}$ and K-T diagram, fatigue limit for Scalmalloy is estimated to be 124 MPa.

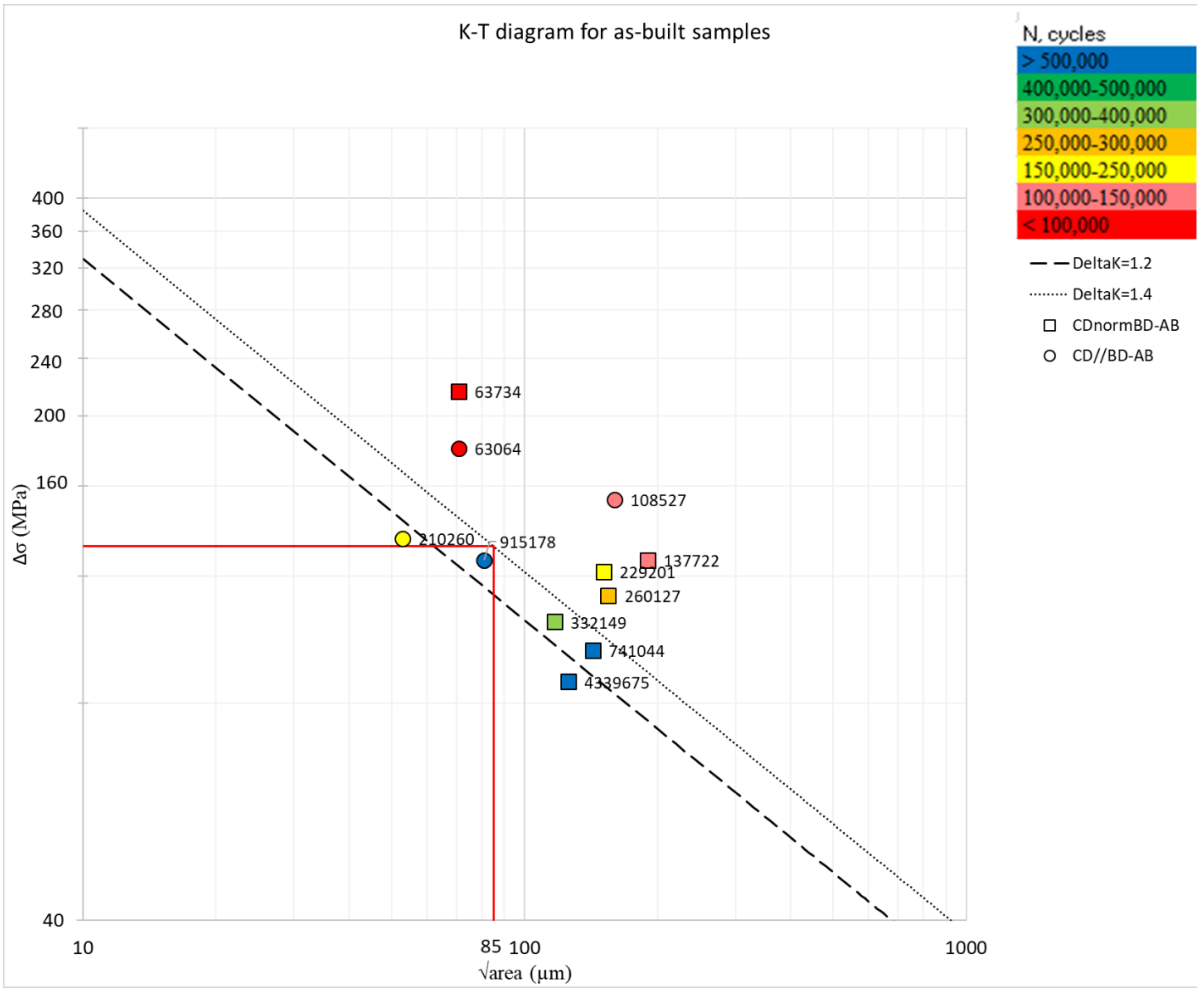

Figure 5.23. K-T diagram for as-built LPBFed Scalmalloy samples.

Unlike the as-built samples, in K-T diagram for heat-treated samples (Fig. 5.24), high-cycle fatigue samples (N > 500,000 cycles) are absent from the dataset, as the number of tested samples was not large. The highest observed fatigue life in the HT samples falls within N = 150,000–250,000 (yellow markers) and these samples generally fall close to the ΔK = 1.2-1.4 MPa√m range. Similar to K-T diagram for as-built samples, samples that failed before 100,000 cycles (marked in red) experienced short cycle life, as they appear in the high-stress region (Δσ > 160 MPa).

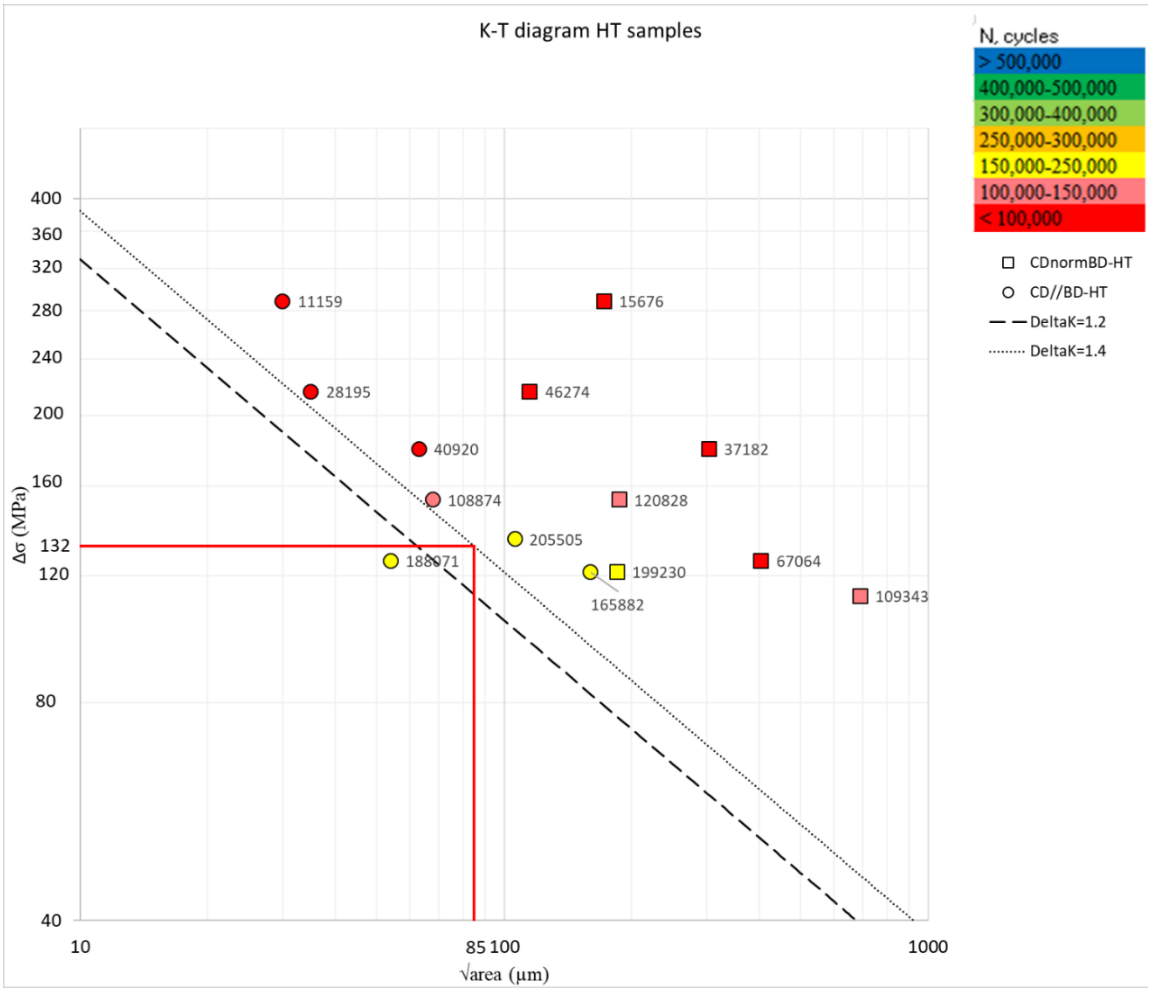

Figure 5.24. K-T diagram for heat-treated LPBFed Scalmalloy samples.

Samples with Δσ < 160 MPa and experiencing low number of cycles (< 100,000, marked in red) have defects with size √a > 300 μm. The example of one of these defects is presented in Figure 5.25, where a large defect in the LPBF-fabricated Scalmalloy, in size over 600 μm, is shown. These kinds of defects occasionally occur in the process and are normally caused by uncontrolled process variations, such as insufficient energy input, and can be formed due to incomplete fusion between powder layers. While these kinds of defects are rare, they may have a significant effect on the fatigue strength of the material.

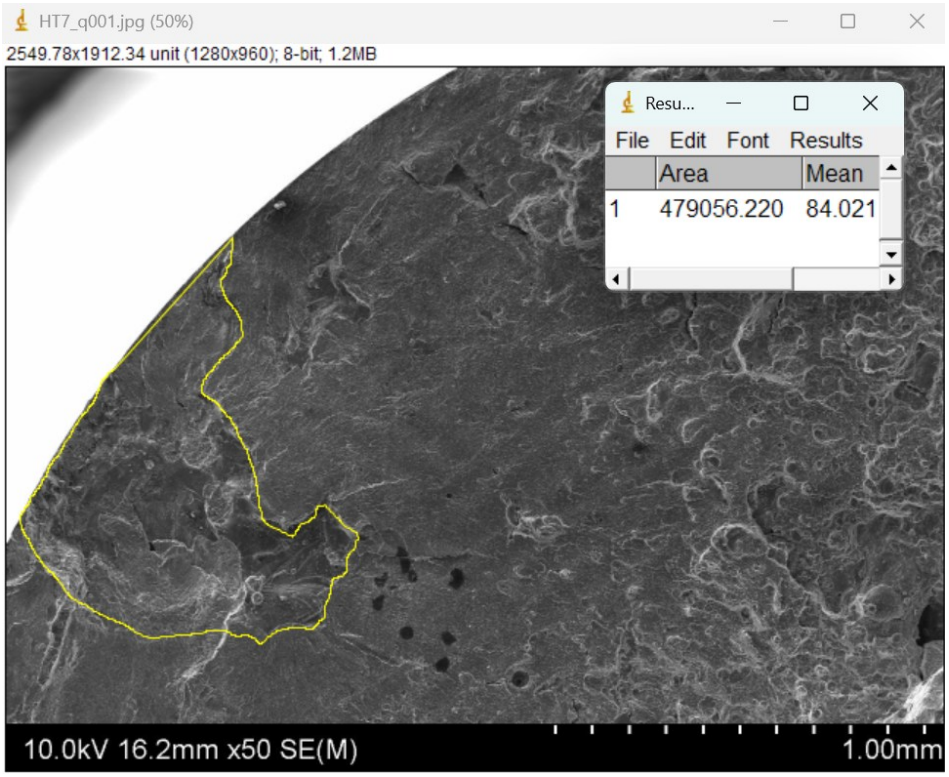

Figure 5.25. Defects initiated fracture for CD⊥BD-AB sample tested at 115 MPa.

The analysis of K-T diagrams reveals a clear and expected trend: high stress range and larger defect sizes consistently lead to lower fatigue life, while samples that experienced a high number of cycles tend to align with the ΔK = 1.2–1.4 MPa$\sqrt{m}$ range. Importantly, the high-cycle fatigue samples do not appear randomly distributed but are clustered near the ΔK values, defined as ΔK_{th} for LPBFed Scalmalloy in this study, confirming the validity of fatigue tests. This suggests that the data presented in this study follows well-established fatigue principles, where crack growth behaviour is predominantly determined by stress intensity factors and defect size.

5.3 Further discussion on how load direction affects fatigue properties

To provide a more comprehensive analysis of fatigue behaviour of LPBFed Scalmalloy, S-N curves from existing literature have been compiled into a single graph, along with the S-N curves obtained in this study (Fig. 5.26). This graphical summary allows a direct evaluation of how different surface treatments, heat treatments and crack direction orientation relative to build direction influence fatigue performance across a wide range of stress levels. By summarizing data from multiple sources, including prior studies and the present research, this graph highlights the gap in previous studies and shows the relative positioning of our results within the broader context of fatigue performance in LPBFed Scalmalloy.

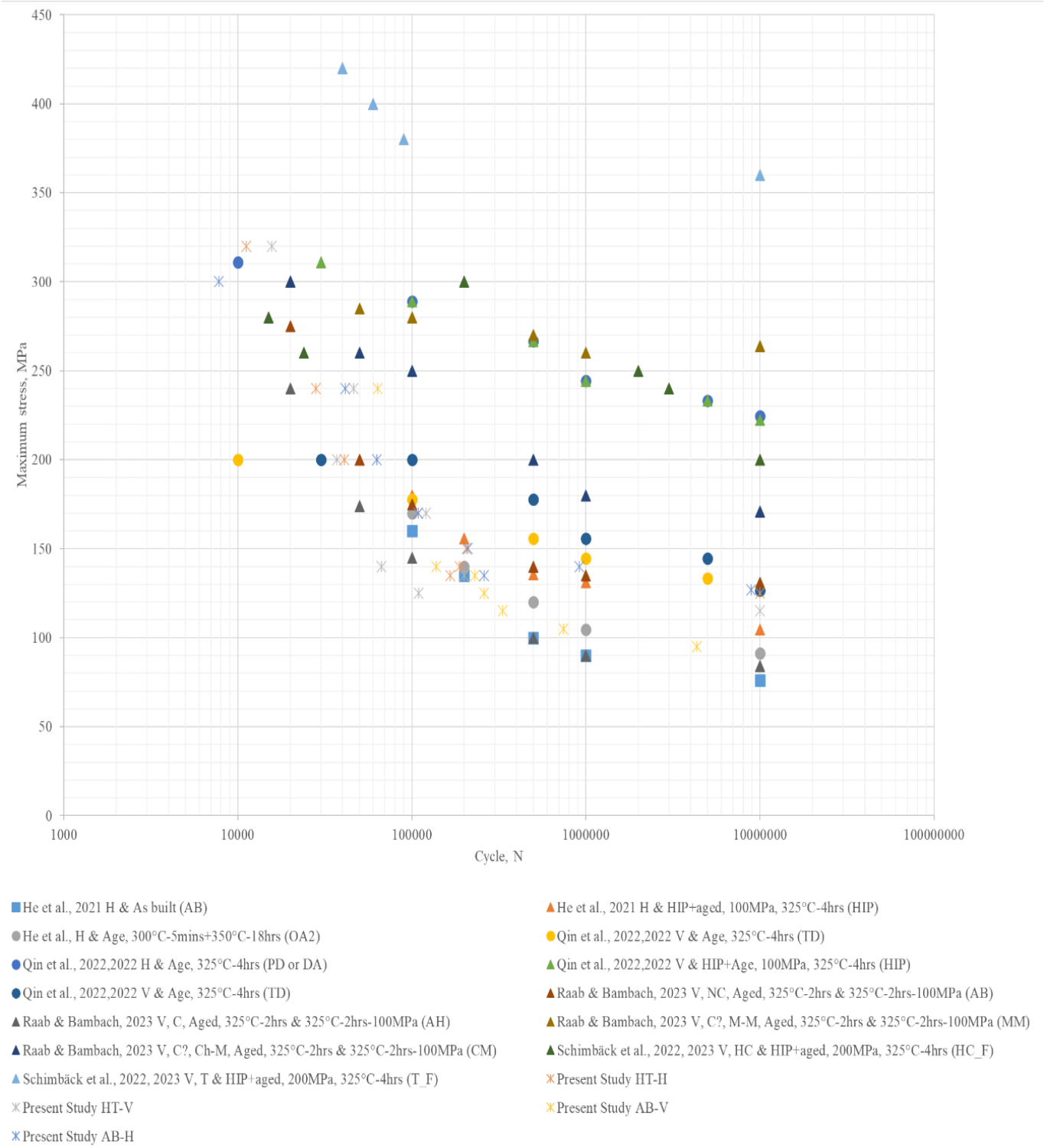

Figure 5.26. Comparison of S-N curves presented in literature with S-N curves obtained in the current study.

To highlight key findings on fatigue strength at $N \geq 10^7$ observed across these datasets, a detailed summary and comparative analysis are provided below:

1. **He et al.:** The data presented in this study for AB samples with CD//BD is lower compared to data obtained in this study. Additionally, data for AB samples with CD⊥BD has not been provided.

2. **Qin et al.:** The data for heat-treated samples with CD⊥BD (σ_{max}=126MPa) is very comparable to data presented in this study for the same orientation of heat-treated samples (σ_{max}=130MPa), however, data for heat-treated samples with CD//BD (σ_{max} =224MPa) is considerably higher than values presented in this study for heat-treated samples with CD//BD (σ_{max} =130MPa). Comparison of K-T diagrams is required to explain non-agreement of this study with the study by Qin et al.
3. **Raab and Bambach:** In this study, only heat-treated followed by HIP samples have been investigated, thus, AB means as-built surface, without any following treatment after the LPBF process (Non-surface HIP). The fatigue limit for AB (NSHIP) samples with CD⊥BD in this study (σ_{max}=131MPa) is very comparable to fatigue limit values for heat-treated samples with CD⊥BD in this study (σ_{max} =130MPa). Additionally, data for as-hatched (AH) samples with CD⊥BD (σ_{max}=84MPa) is also very comparable to the fatigue limit of heat-treated samples with CD⊥BD in this study (σ_{max}=130MPa). However, the work of Raab and Bambach, while valuable in its scope, is not directly relevant to our study. Their study is focused on the investigation of HIPed samples with different surface treatment methods, rather than as-built or heat-treated ones, as in the current study. After HIP, samples have significant microstructural changes that influence fatigue behaviour, thus, their findings are not fully comparable to data for the as-built or heat-treated samples obtained in this study. Additionally, their study does not include the effect of build direction on fatigue performance.
4. **Schimback et al.:** Similar to Raab and Bambach, Schimback et al. investigated HIPed Scalmalloy samples, thus their study is not completely relevant to the current study. Additionally, their work did not investigate the direction of the crack with regard to the build direction orientation effect. While their investigation contributes to the understanding of HIPed sample performance, it does not have the data necessary for comparisons with findings in this study.

Figure 5.26 with the following analysis above compares this study with previous research, highlighting key similarities and differences in fatigue performance of LPBFed Scalmalloy. The table below (Table 5.7) summarizes these data points of fatigue strength at $N \geq 10^7$, making it easier to compare relevant test results from previous studies with values obtained in the current study. The fatigue strength reported by previous studies is generally consistent and reasonable, however the fatigue strength of 224 MPa reported by Qin et al. (96) appears unusually high and is considered unreasonable. This value significantly exceeds those observed in other studies and the present work, suggesting a possible difference in testing conditions or evaluation methodology.

Table 5.7. Summary on fatigue strength data from previous and current studies.

Authors	Fatigue strength, MPa AB-CD//BD	Fatigue strength, MPa AB-CD⊥BD	Fatigue strength, MPa HT-CD//BD	Fatigue strength, MPa HT-CD⊥BD	Fatigue strength, MPa AB-CD⊥BD - NSHIP
He et al.:	76	-	-	-	-
Qin et al.:	-	-	224	126	-
Raab and Bambach:	-	-	-	-	131
Schimback et al.:	-	-	-	-	-
Present study	127	<95	125	115	

Comparison of K-T diagrams is required next to clearly illustrate and explain the reasons for both agreements and discrepancies between the fatigue strength results obtained in the current study and those reported in the literature. The K-T diagram below (Figure 5.27) provides a visual representation of fatigue performance in relation to defect size, summarising data from previous studies by Qin et al., Raab and Bambach, and Schimback et al. for non-HIPed samples. The dashed and dotted lines represent ΔK_{th} values of 1.2 MPa·m$^{1/2}$ and 1.4 MPa·m$^{1/2}$, respectively. The ΔK_{th} values of 1.2 and 1.4 MPa·m$^{1/2}$ were selected for threshold lines based on the experimental determination presented in Table 5.5, where ΔK_{th} values for Scalmalloy samples ranged between 1.27 and 1.46 MPa·m$^{1/2}$. The alignment or deviation of data points from the threshold lines indicates that the straight lines derived from the ΔK_{th} values determined in this work accurately distinguish between the non-crack growth (safe) and crack growth (unsafe) regions. As only data relevant to the current study (for non-HIPed samples) has been summarised, this comparison supports the discussion on why some values from earlier studies do not fully align with the results of the current research. For instance, Qin et al. (96) reported a fatigue strength of 224 MPa for heat-treated CD//BD samples, significantly higher than the 125 MPa obtained in the present study. Thus, the influence of defect evaluation methods, heat treatment and surface conditions on fatigue performance is considered.

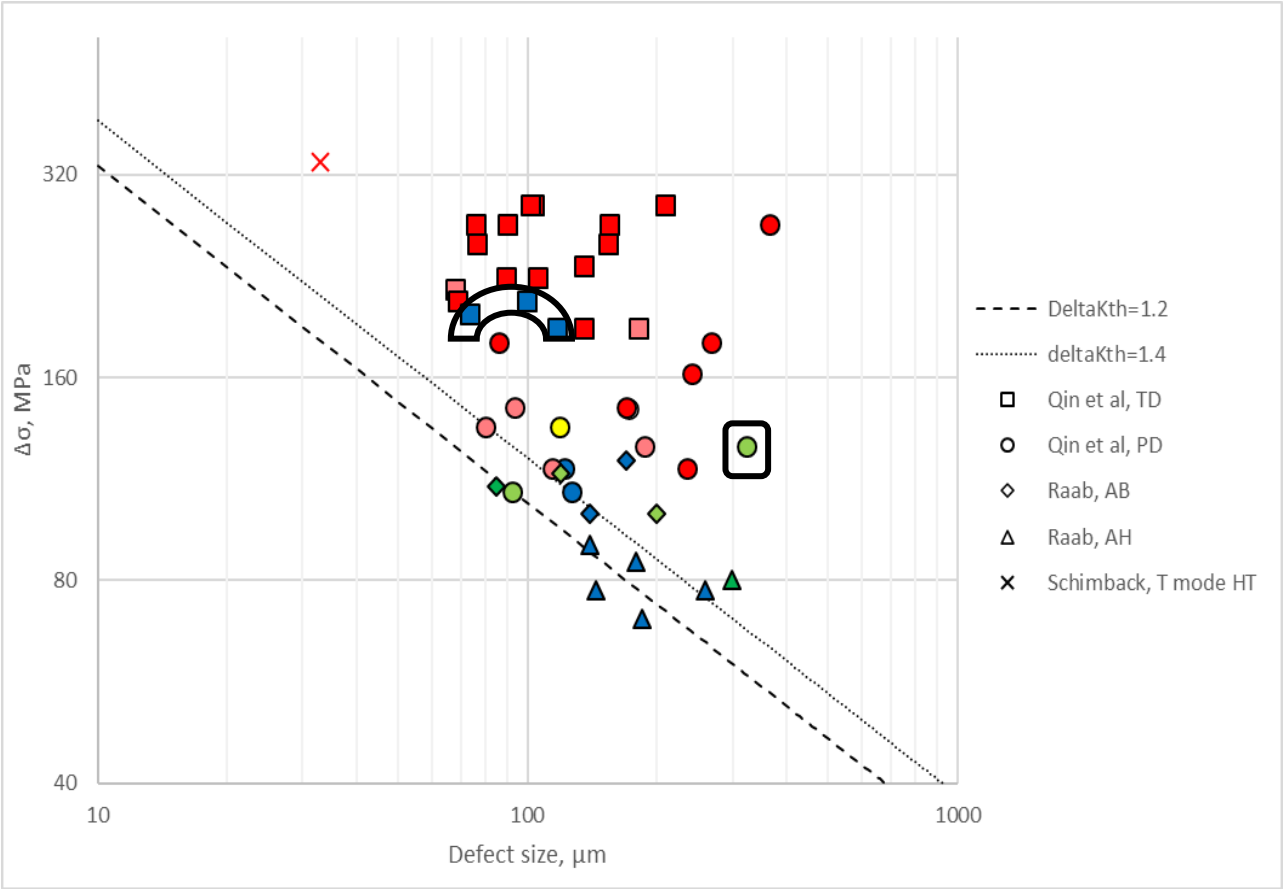

Figure 5.27. Data results for defect size and fatigue performance for as-built or heat-treated LPBFed Scalmalloy samples summarized from previous studies (96), (100), (102).

There are several important points to note in the data plotted in Fig. 5.27, particularly regarding values from previous studies that appear significantly deviated from the expected trend lines

1. Qin et al.'s data points for samples with CD//BD experiencing high number of cycles (three blue points) are plotted significantly above the ΔK_{th} trend lines, indicating unrealistically high fatigue strengths for high cycle number for the given defect sizes, therefore these values should be viewed as incorrect. Data points for samples with CD⊥BD align well with the current study and are in the region of ΔK_{th} = 1.2 – 1.4 MPa·m$^{1/2}$, except one highlighted green point.
2. Raab's data mostly align with or remain slightly above the ΔK_{th} limits, indicating better agreement with expected fatigue behaviour.
3. Schimback et al.'s result (red X): This outlier significantly exceeds the ΔK_{th} range, however, N is only 28,000 cycles, therefore, these values should be viewed as incorrect

As some previous studies have reported fatigue behaviour for HIPed samples, data for K-T diagram for these samples has been summarized separately (Fig. 5.28) to illustrate how it differs from non-HIPed samples. This approach helps to visualize how HIPed samples behave differently from non-HIPed ones, particularly in terms of defect sensitivity and fatigue thresholds. The alignment or deviation of data points from the threshold lines

(ΔK_{th} = 1.2 and ΔK_{th} = 1.4) further emphasizes the impact of different processing methods on fatigue performance.

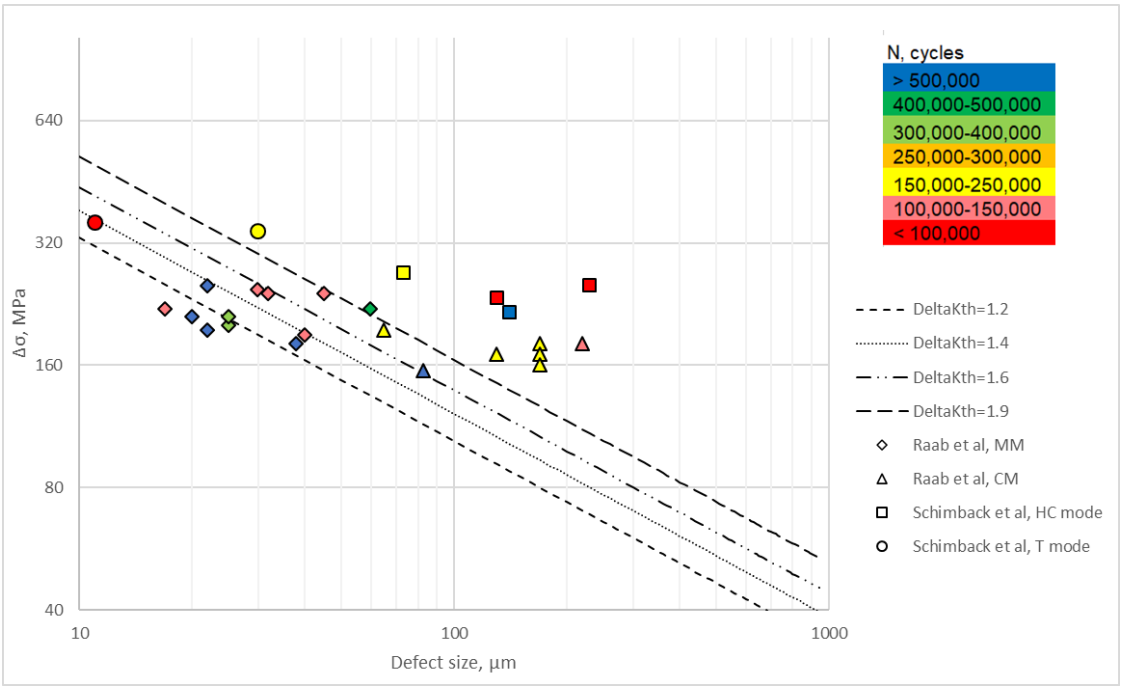

Figure 5.28. Data results for defect size and fatigue performance for HIPed LPBFed Scalmalloy samples summarized from previous studies (100), (101), (102).

Data for HIPed samples plotted in Fig. 5.28 are clearly outside of defect-dependent fatigue strength limits described and explained for non-HIPed samples. This could mean that HIP may have resulted in an increase in ΔK_{th} and thus in the samples being more tolerant the defects. However, if a_o=85µm, $\Delta\sigma_E$=180MPa for ΔK_{th}=1.9MPa·m$^{1/2}$. Although no microstructure analysis was conducted in the referenced studies to quantify the grain size change that may occur during high temperature HIP. If grain growth does occur during HIP, a larger grain structure could provide more crack closure effect, thus increasing ΔK_{th}. But as shown in the figure, most $\Delta\sigma$ data are above $\Delta\sigma_E$=180MPa for a_o<85µm. This is unexplainable.

To summarize all the above, it can be stated that: several studies reviewed and analysed, including those by Schimback et al., presented Kitagawa-Takahashi diagrams with ΔK_{th} value 1.96 MPa·m$^{1/2}$ at R=0.1. Our results, with ΔK_{th} ranging from 1.27 to 1.46 MPa·m$^{1/2}$, are more reasonable as it more correctly divides the non-crack growth and crack growth regions for as-built and heat-treated samples from the previous and current studies. The fatigue behaviour of LPBF Scalmalloy was analysed, focusing on fatigue life and fatigue strength under varying conditions. The results have shown that build orientation slightly affects fatigue performance in the high-cycle regime, while heat treatment does not impact fatigue strength. Defects, mainly lack of fusion and pores, play a major role in limiting fatigue performance, as confirmed by defect analysis and Kitagawa-Takahashi diagrams. The analysis of S-N curves from the current study along with other studies, together with a reasonable assumption of a_o=85µm, and the ΔK_{th} =1.2-1.4 MPa$\sqrt{m}$ determined in this study, suggests that the fatigue strength/limit σ_{max}=140MPa. This fatigue strength is the same for as-built and aged samples, although for the limited run-out samples values the apparent fatigue strength (σ_{max}=115-125MPa at N=10^7) are

lower in the present series of tests. Thus, findings in the current research, confirmed by FCG test results with more reasonable ΔKth values, offer a much improved understanding of fatigue behaviour of LPBFed Scalmalloy.

Conclusions

In this thesis, the solidification behaviour during laser powder bed fusion (LPBF) of Scalmalloy leading to the formation of the bimodal grain structure and the crack growth behaviour of the alloy under cyclic loading have been studied. The key findings are as follows:

1. **Formation of bimodal grain structure**

- The LPBF-induced elemental distributions were found to be different in the solidification of equiaxed to columnar grain regions, suggestively due to the conditions of solidification in LPBF. The very low growth and cooling rates of grains in the region next to the track boundary allow for $Al_3(Sc,Zr)$ to form and act as a nucleus for the fine equiaxed-grain (~0.5 μm) growth next to and along the track boundary. The very low growth rate also allows for elements to diffuse outward during solidification, as observed with segregation of elements to grain boundaries in the fine-equiaxed-grain region.
- The equiaxed-grain size increases to ~1.5 μm over a few microns distance from track boundary as a result of the steep increase in the cooling rate away from track boundary. This has resulted from the shifting of the composition of the divorced eutectic to higher values than the Sc content of the alloy. Thus, grain refining effect diminishes and grain size increases.
- Further (only a few microns) away, grain-refining effect of Sc (with its content of the alloy) will be totally lost, resulting in a columnar grain growth. Away from track boundary, the high growth rate during solidification in the columnar grain region results in highly localized diffusion, preventing significant segregation influences in the microstructural transition and the eventual formation of columnar grains.

2. **Fatigue crack growth and threshold stress intensity factor**

- The stress intensity factor threshold value (ΔK_{th}) has been determined to be at 1.3-1.4 $MPa \cdot m^{1/2}$ and is not affected by the orientation of the crack growth direction (CD) in relation to build direction (BD) in both as-built state and heat-treated state of LPBF Scalmalloy.
- The reason for the lack of orientation and heat-treating effects, is that crack path needs to propagate similarly through the equiaxed grains and columnar grains regularly spaced in the bimodal microstructure in all orientations. The crack path propagating through the sub-micron size equiaxed grains and either intergranularly, with CD in a low angle to BD, or transgranularly, with a zigzag step height in typically 1-2 μm, has not provided a strong effect on roughness-induced crack closure. Heat treatment by one-step aging has changed the grain sizes and shapes little. Thus, the ΔK_{th} values for all samples are low.

- In Paris region, $C \approx 3.3 \times 10^{-10}$ (m/cycle)/(MPa$\sqrt{m}$)^m and $m \approx 2.9$ for as-built samples and heat treatment have only increased slightly the FCG that $C \approx 5\ 9 \times 10^{-10}$ (m/cycle)/(MPa$\sqrt{m}$)^m and $m \approx 3.0$. These values are in agreement with the values found in most aluminium alloys.

3. **LPBF defects and fatigue strength/life**

- As expected, fatigue strength is strongly and negatively affected by LPBF-induced defects, primarily by lack of fusion (LOF). The use of K-T approach has largely explained the effect of defects on fatigue strength of the current samples. The defect sizes detected on fracture surfaces of tested samples (at or near the edge location of samples) are consistent with the size range of LOF defects formed during PBF, with some up to or greater than 200μm.
- The analysis of the S-N data from this study and data from other studies, together with a reasonable assumption of $a_o \approx 85\mu m$ and the ΔK_{th} values of 1.3-1.4 MPa $m^{1/2}$ determined in this study, suggests the fatigue strength/limit for defect free ($a_o < 85\mu m$) samples being $\Delta\sigma \approx 124$MPa. This fatigue strength is the same for as-built and aged samples, although for the limited run-out samples in the present work, the apparent fatigue strength (σ_{max}=115-125MPa at $N=10^7$) is lower. This is likely due to the possibility of having LOF free samples being low.
- The orientation effect on fatigue strength has been found to be low and the slight reduction of fatigue strength in CD⊥BD should be the result of the average size of LOFs, which is generally larger in CD⊥BD than CD//BD. This is because the melting between layers should be more insufficient than the melting between tracks when a LOF defect forms during LPBF.
- Using the K-T approach to analyse the present data of fatigue strength/life to relate to defect sizes and the data from literature has suggested that ΔK_{th} equal to 1.34 MPa·$m^{1/2}$**,** determined in the present study to be correct.

List of References

1. *Microstructure evolution and mechanical property response of 3D-Printed Scalmalloy with different heat-treatment times at 325° C.* Kuo, C. N., Peng, P. C., Liu, D. H., & Chao, C. Y. 2021, Metals, pp. 11(4), 555.

2. *Medical applications of 3D printing.* Durfee, W. K., & Iaizzo, P. A. 2019, Engineering in medicine, pp. 527-543.

3. renishaw. *www.renishaw.com.* [Online] https://www.renishaw.com/resourcecentre/en/details/Renishaw-AM250-laser-melting-machine--38778?lang=Language%20Independent.

4. *Selective laser melting (SLM) and topology optimization for lighter aerospace componentes.* Seabra, M., Azevedo, J., Araújo, A., Reis, L., Pinto, E., Alves, N., & Mortágua, J. P. 2016, Procedia Structural Integrity, pp. 1, 289-296.

5. *High Power Selective Laser Melting (HP SLM) of Aluminum Parts.* Buchbinder, D., Schleifenbaum, H., Heidrich, S., Meiners, W., & Bültmann, J. J. P. P. 2011, Physics Procedia, pp. 12, 271-278.

6. Jacob, G., Jacob, G., Brown, C. U., Donmez, M. A., Watson, S. S., & Slotwinski, J. *Effects of powder recycling on stainless steel powder and built material properties in metal powder bed fusion processes.* Gaithersburg : MD: US Department of Commerce, National Institute of Standards and Technology, 2017.

7. *Comparison of density measurement techniques for additive manufactured metallic parts.* Spierings, A. B., Schneider, M. U., & Eggenberger, R. J. R. P. J. 2011, Rapid Prototyping Journal, pp. 17(5), 380-386.

8. *Low-Power Laser Powder Bed Fusion Processing of Scalmalloy®.* Martucci, A., Aversa, A., Manfredi, D., Bondioli, F., Biamino, S., Ugues, D., & Fino, P. 2022, Materials, pp. 15(9), 3123.

9. *Single track formation in selective laser melting of metal powders.* Yadroitsev, I., Gusarov, A., Yadroitsava, I., & Smurov, I. 2010, Journal of Materials Processing Technology, Vol. 210(12), pp. 210(12), 1624-1631.

10. *Density of Additively-Manufactured, 316L SS Parts Using Laser Powder-Bed Fusion at Powers Up to 400W.* Kamath, C., El-Dasher, B., Gallegos, G. F., King, W. E., & Sisto, A. 2014, The International Journal of Advanced Manufacturing Technology, Vol. 74, pp. 74, 65-78.

11. *Main defects observed in aluminum alloy parts produced by SLM: From causes to consequences.* Galy, C., Le Guen, E., Lacoste, E., & Arvieu, C. 2018, Additive manufacturing, Vol. 22, pp. 22, 165-175.

12. *Effect of energy input on formability, microstructure and mechanical properties of selective laser melted AZ91D magnesium alloy.* Wei, K., Gao, M., Wang, Z., & Zeng, X. 2014, Materials Science and Engineering, Vols. A, 611, pp. A, 611, 212-222.

13. *Reducing porosity in AlSi10Mg parts processed by selective laser melting.* Aboulkhair, N. T., Everitt, N. M., Ashcroft, I., & Tuck, C. 2014, Additive manufacturing, Vol. 1, pp. 1, 77-86.

14. *Critical review of LPBF metal print defects detection: roles of selective sensing technology.* Guillen, D., Wahlquist, S., & Ali, A. 2024, Applied Sciences, Vol. 14(15), pp. 14(15), 6718.

15. *A novel classification method for pores in laser powder bed fusion. .* Nudelis, N., & Mayr, P. 2021, Metals, pp. 11(12), 1912.

16. *Formation of keyhole and lack of fusion pores during the laser powder bed fusion process.* Shrestha, S., & Chou, K. 2022, Manufacturing Letters, pp. 32, 19-23.

17. *Formation of metastable cellular microstructures in selective laser melted alloys. .* Prashanth, K. G., & Eckert, J. 2017, Journal of Alloys and Compounds, pp. 707, 27-34.

18. *Microstructure and strength of selectively laser melted AlSi10Mg.* Wu, J., Wang, X. Q., Wang, W., Attallah, M. M., & Loretto, M. H. 2016, Acta Materialia, pp. 117, 311-320.

19. *Additive manufacturing of metallic components–process, structure and properties.* DebRoy, T., Wei, H. L., Zuback, J. S., Mukherjee, T., Elmer, J. W., Milewski, J. O., & Zhang, W. 2018, Progress in materials science, pp. 92, 112-224.

20. *Laser powder bed fusion of AA7075 alloy: Influence of process parameters on porosity and hot cracking.* Stopyra, W., Gruber, K., Smolina, I., Kurzynowski, T., & Kuźnicka, B. 2020, Additive Manufacturing, pp. 35, 101270.

21. *Prediction of solidification cracking in pulsed laser welding of 2024 aluminum alloy.* Sheikhi, M., Ghaini, F. M., & Assadi, H. 2015, Acta Materialia, pp. 82, 491-502.

22. *Review of high-strength aluminium alloys for additive manufacturing by laser powder bed fusion. .* Rometsch, P. A., Zhu, Y., Wu, X., & Huang, A. 2022, Materials & Design, pp. 219, 110779.

23. *Additive manufacturing of Scalmalloy® satellite parts.* Begoc, S., Montredon, F., Pommatau, G., Leger, G., Gas, M., & Eyrignoux, S. Madrid, Spain : s.n., 2019. Proceedings of the 8th European Conference for Aeronautics and Space Sciences (EUCASS). pp. pp. 1-4.

24. APWORKS. [Online] https://www.apworks.de/scalmalloy.

25. *Secondary ageing and formability of an Al-Cu-Mg alloy (2024) in W and under-aged tempers.* Österreicher, J. A., Nebeling, D., Grabner, F., Cerny, A., Zickler, G. A., Eriksson, J., & Schlögl, C. M. 2023, Materials & Design, pp. 226, 111634.

26. *Digitisation of metal AM for part microstructure and property control.* Dogu, M. N., McCarthy, E., McCann, R., Mahato, V., Caputo, A., Bambach, M., & Brabazon, D. 2022, International Journal of Material Forming, pp. 15(3), 30.

27. *Melt pool temperature and cooling rates in laser powder bed fusion.* Hooper, P. A. 2018, Additive Manufacturing, pp. 22, 548-559.

28. *3D printing of high-strength aluminium alloys.* Martin, J. H., Yahata, B. D., Hundley, J. M., Mayer, J. A., Schaedler, T. A., & Pollock, T. M. 2017, Nature, pp. 549(7672), 365-369.

29. *Composition-dependent solidification cracking of aluminum-silicon alloys during laser powder bed fusion.* Hyer, H., Zhou, L., Mehta, A., Park, S., Huynh, T., Song, S., & Sohn, Y. 2021, Acta Materialia, pp. 208, 116698.

30. *Residual stresses in additively manufactured AlSi10Mg: Raman spectroscopy and X-ray diffraction analysis.* Marola, S., Bosia, S., Veltro, A., Fiore, G., Manfredi, D., Lombardi, M., & Battezzati, L. 2021, Materials & Design, pp. 202, 109550.

31. *3D printing of high-strength aluminium alloys.* Martin, J. H., Yahata, B. D., Hundley, J. M., Mayer, J. A., Schaedler, T. A., & Pollock, T. M. 2017, Nature, pp. 549(7672), 365-369.

32. *Scalmalloy®= A Unique High Strength AlMgSc Type Material Concept Processed by Innovative Technologies for Aerospace Applications. .* Palm, F., Leuschner, R., Schubert, T., & Kieback, B. s.l. : The European Powder Metallurgy Association, 2010. European Congress and Exhibition on Powder Metallurgy. p. p. 1.

33. *Effect of laser rescanning on the grain microstructure of a selective laser melted Al-Mg-Zr alloy.* Griffiths, S., Rossell, M. D., Croteau, J., Vo, N. Q., Dunand, D. C., & Leinenbach, C. 2018, Materials Characterization, pp. 143, 34-42.

34. *Effect of platform temperature on the porosity, microstructure and mechanical properties of an Al–Mg–Sc–Zr alloy fabricated by selective laser melting.* Shi, Y., Yang, K., Kairy, S. K., Palm, F., Wu, X., & Rometsch, P. A. 2018, Materials Science and Engineering, pp. A, 732, 41-52.

35. *SLM-processed Sc-and Zr-modified Al-Mg alloy: Mechanical properties and microstructural effects of heat treatment.* Spierings, A. B., Dawson, K., Kern, K., Palm, F., & Wegener, K. 2017, Materials Science and Engineering, pp. A, 701, 264-273.

36. *Influence of SLM scan-speed on microstructure, precipitation of Al3Sc particles and mechanical properties in Sc-and Zr-modified Al-Mg alloys.* Spierings, A. B., Dawson, K., Uggowitzer, P. J., & Wegener, K. 2018, Materials & Design, pp. 140, 134-143.

37. *Grain growth during selective laser melting of a Co–Cr–Mo alloy.* Chen, Z. W., Phan, M. A. L., & Darvish, K. 2017, Journal of Materials Science, pp. 52(12), 7415-7427.

38. Davoli, P. Principles of current methodologies in high-cycle fatigue design of metallic structures. [book auth.] K., & Papadopoulos, I. V. Dang Van. *High-Cycle Metal Fatigue: From Theory to Applications.* Vienna : Springer Vienna, 1999, pp. 1-56.

39. Campbell, F. C. (Ed.). *Fatigue and fracture: understanding the basics.* Novelty, Ohio : ASM international, 2012.

40. Materials, American Society for Testing and. *Standard test method for measurement of fatigue crack growth rates: designation: E 647-08.* s.l. : ASTM international, 2008.

41. ASTM. ASTM E647-13a: Standard Test Method for Measurement of Fatigue Crack Growth Rates. 2014.

42. *A comparison of fatigue strength sensitivity to defects for materials manufactured by AM or traditional processes.* Beretta, S., & Romano, S. 2017, International Journal of Fatigue, pp. 94, 178-191.

43. Everaerts, J. *Fatigue Crack Initiation and Facet Formation in Ti-6Al-4V Wires.* 2017.

44. *Prediction of non propagating cracks.* El Haddad, M. H., Topper, T. H., & Smith, K. N. 1979, Engineering fracture mechanics, pp. 11(3), 573-584.

45. *Mechanical properties of SLM-printed aluminium alloys: a review.* Ponnusamy, P., Rahman Rashid, R. A., Masood, S. H., Ruan, D., & Palanisamy, S. 2020, Materials, pp. 13(19), 4301.

46. *Fine-structured aluminium products with controllable texture by selective laser melting of pre-alloyed AlSi10Mg powder.* Thijs, L., Kempen, K., Kruth, J. P., & Van Humbeeck, J. 2013, Acta Materialia, pp. 61(5), 1809-1819.

47. *Selective laser melting of aluminum die-cast alloy—Correlations between process parameters, solidification conditions, and resulting mechanical properties.* Buchbinder, D., Meiners, W., Wissenbach, K., & Poprawe, R. 2015, Journal of Laser Applications, p. 27(S2).

48. *Mechanical properties of AlSi12 alloy manufactured by laser powder bed fusion technique.* Kimura, M., Hirayama, A., Yoshioka, J., Maekawa, H., Kusaka, M., Kaizu, K., & Takahashi, T. 2020, Journal of Failure Analysis and Prevention, pp. 20, 1884-1895.

49. *Inoculation treatment of an additively manufactured 2024 aluminium alloy with titanium nanoparticles.* Tan, Q., Zhang, J., Sun, Q., Fan, Z., Li, G., Yin, Y., & Zhang, M. X. 2020, Acta Materialia, pp. 196, 1-16.

50. *Selective laser melting additive manufacturing of 7xxx series Al-Zn-Mg-Cu alloy: Cracking elimination by co-incorporation of Si and TiB2. .* Zhou, S. Y., Su, Y., Wang, H., Enz, J., Ebel, T., & Yan, M. 2020, Additive Manufacturing, pp. 36, 101458.

51. *Selective laser melting of high strength Al–Cu–Mg alloys: Processing, microstructure and mechanical properties.* Zhang, H., Zhu, H., Qi, T., Hu, Z., & Zeng, X. 2016, Materials Science and Engineering, pp. A, 656, 47-54.

52. *An understanding of duplex microstructures encountered during high strength aluminium alloy laser beam melting processing.* Opprecht, M., Garandet, J. P., Roux, G., & Flament, C. 2021, Acta Materialia, pp. 215, 117024.

53. *A review of Laser Powder Bed Fusion Additive Manufacturing of aluminium alloys: Microstructure and properties.* Kotadia, H. R., Gibbons, G., Das, A., & Howes, P. D. 2021, Additive Manufacturing, pp. 46, 102155.

54. *Design approaches for printability-performance synergy in Al alloys for laser-powder bed additive manufacturing.* Mishra, R. S., & Thapliyal, S. 2021, Materials & Design, pp. 204, 109640.

55. *Developing a high-strength Al-Mg-Si-Sc-Zr alloy for selective laser melting: Crack-inhibiting and multiple strengthening mechanisms.* Li, R., Wang, M., Li, Z., Cao, P., Yuan, T., & Zhu, H. 2020, Acta Materialia, pp. 193, 83-98.

56. *Recent advances in hot tearing during casting of aluminium alloys.* Li, Y., Li, H., Katgerman, L., Du, Q., Zhang, J., & Zhuang, L. 2021, Progress in Materials Science, pp. 117, 100741.

57. *Process and mechanical properties: applicability of a scandium modified Al-alloy for laser additive manufacturing.* Schmidtke, K., Palm, F., Hawkins, A., & Emmelmann, C. 2011, Physics Procedia, pp. 12, 369-374.

58. *Microstructural features of Sc-and Zr-modified Al-Mg alloys processed by selective laser melting. .* Spierings, A. B., Dawson, K., Heeling, T., Uggowitzer, P. J., Schäublin, R., Palm, F., & Wegener, K. 2017, Materials & Design, pp. 115, 52-63.

59. *Microstructure and mechanical properties of as-processed scandium-modified aluminium using selective laser melting.* Spierings, A. B., Dawson, K., Voegtlin, M., Palm, F., & Uggowitzer, P. J. 2016, Cirp Annals, pp. 65(1), 213-216.

60. *Microstructure characterization of SLM-processed Al-Mg-Sc-Zr alloy in the heat treated and HIPed condition.* Spierings, A. B., Dawson, K., Dumitraschkewitz, P., Pogatscher, S., & Wegener, K. 2018, Additive Manufacturing, pp. 20, 173-181.

61. *Strain rate and temperature effects on dynamic properties of high-strength weldable aluminum-scandium alloy.* Lee, W. S., & Chen, T. H. 2009, Journal of Materials Research, pp. 24(1), 198-211.

62. *The Al-Sc (aluminum-scandium) system.* Murray, J. L. 1998, Journal of Phase Equilibria and Diffusion, pp. 19(4), 380.

63. *Thermodynamic measurements and assessment of the Al–Sc system.* Cacciamani, G., Riani, P., Borzone, G., Parodi, N., Saccone, A., Ferro, R., & Schmid-Fetzer, R. 1999, Intermetallics, pp. 7(1), 101-108.

64. *Non-equilibrium solidification of hyperperitetic Al-Zr alloys.* Nes, E., & Billdal, H. 1977, Acta Metallurgica, pp. 25(9), 1031-1037.

65. *Alloy designing and characterization of rapidly solidified Al-Zr (-V) base alloys.* Park, W. W. 1996, Materials & Design, pp. 17(2), 85-88.

66. *Structure and Phase Decomposition of a Rapidly Solidified Supersaturated Al-Zr Solid Solution.* Hori, S., Kitagawa, H., Masutani, T., & Takehara, A. 1977, Journal of Japan Institute of Light Metals, pp. 27(3), 129-137.

67. *The solidification behaviour of dilute aluminium–scandium alloys.* Norman, A. F., Prangnell, P. B., & McEwen, R. S. 1998, Acta materialia, pp. 46(16), 5715-5732.

68. *On the occurrence of a eutectic-type structure in solidification of Al-Zr alloys.* Wang, F., Eskin, D. G., Khvan, A. V., Starodub, K. F., Lim, J. J. H., Burke, M. G., & Mi, J. 2017, Scripta Materialia, pp. 133, 75-78.

69. *Scandium in aluminium alloys: physical metallurgy, properties and applications.* Royset, J. 2007, Metallurgical Science and Tecnology, p. 25(2).

70. *Simulation of microsegregation during solidification and homogenization of new Al–Mg alloys with Sc and Zr additions.* Samaras, S. N., Katsamas, A., & Heidemenopoulos, G. N. Chalkidiki, Greece : s.n., 2008, October. Proceedings of the 3rd International Conference on Manufacturing Engineering (ICMEN). pp. (pp. 1-3).

71. *Thermodynamics-based computational design of Al-Mg-Sc-Zr alloys.* Haidemenopoulos, G. N., Katsamas, A. I., & Kamoutsi, H. 2010, Metallurgical and Materials Transactions , pp. A, 41, 888-899.

72. *Selective laser melting of a novel Sc and Zr modified Al-6.2 Mg alloy: Processing, microstructure, and properties.* Li, R., Wang, M., Yuan, T., Song, B., Chen, C., Zhou, K., & Cao, P. 2017, Powder Technology, pp. 319, 117-128.

73. *Overview: Application of heterogeneous nucleation in grain-refining of metals.* Greer, A. L. 2016, The Journal of chemical physics, p. 145(21).

74. *The effect of cooling rate on the morphology of primary Al3Sc intermetallic particles in Al–Sc alloys.* Hyde, K. B., Norman, A. F., & Prangnell, P. B. 2001, Acta Materialia, pp. 49(8), 1327-1337.

75. *Columnar to equiaxed transition in Al-Mg (-Sc)-Zr alloys produced by selective laser melting.* Yang, K. V., Shi, Y., Palm, F., Wu, X., & Rometsch, P. 2018, Scripta Materialia, pp. 145, 113-117.

76. *The latest development of Sc-strengthened aluminum alloys by laser powder bed fusion.* Bayoumy, D., Kan, W., Wu, X., Zhu, Y., & Huang, A. 2023, Journal of Materials Science & Technology, pp. 149, 1-17.

77. *Excellent strength–ductility balance of Sc-Zr-modified Al–Mg alloy by tuning bimodal microstructure via hatch spacing in laser powder bed fusion.* Ekubaru, Y., Gokcekaya, O., Ishimoto, T., Sato, K., Manabe, K., Wang, P., & Nakano, T. 2022, Materials & Design, pp. 221, 110976.

78. *Selective laser melting of rare earth element Sc modified aluminum alloy: Thermodynamics of precipitation behavior and its influence on mechanical properties.* Zhang, H., Gu, D., Yang, J., Dai, D., Zhao, T., Hong, C., & Poprawe, R. 2018, Additive Manufacturing, pp. 23, 1-12.

79. *Effect of bimodal microstructure on the tensile properties of selective laser melt Al-Mg-Sc-Zr alloy.* Ma, R., Peng, C., Cai, Z., Wang, R., Zhou, Z., Li, X., & Cao, X. 2020, Journal of alloys and compounds, pp. 815, 152422.

80. *Microstructure and mechanical properties of a novel selective laser melted Al–Mg alloy with low Sc content.* Churyumov, A. Y., Pozdniakov, A. V., Prosviryakov, A. S., Loginova, I. S., Daubarayte, D. K., Ryabov, D. K., & Valchuk, S. V. 2019, Materials Research Express, pp. 6(12), 126595.

81. *Laser powder bed fusion of high-strength Sc/Zr-modified Al–Mg alloy: phase selection, microstructural/mechanical heterogeneity, and tensile deformation behavior.* Wang, Z., Lin, X., Kang, N., Chen, J., Tan, H., Feng, Z., & Huang, W. 2021, Journal of Materials Science & Technology, pp. 95, 40-56.

82. *Strength-ductility synergy of selective laser melted Al-Mg-Sc-Zr alloy with a heterogeneous grain structure.* Wang, Z., Lin, X., Kang, N., Hu, Y., Chen, J., & Huang, W. 2020, Additive Manufacturing, pp. 34, 101260.

83. *Grain refinement and performance enhancement of laser powder bed fusion in-situ processed Al-Mg alloy modified by ScH3 and ZrH2.* Li, X., Liu, Y., & Zhou, Z. 2022, Materials Characterization, pp. 190, 112068.

84. *A study on Sc-and Zr-modified Al–Mg alloys processed by selective laser melting. .* Zhu, Y., Zhao, Y., & Chen, B. 2022, Materials Science and Engineering, pp. A, 833, 142516.

85. *Processing of Al-Sc aluminum alloy using SLM technology.* Koutny, D., Skulina, D., Pantělejev, L., Paloušek, D., Lenczowski, B., Palm, F., & Nick, A. 2018, Procedia Cirp, pp. 74, 44-48.

86. *Exceptional grain refinement in directly built up Sc-modified AlMg-alloys is promising a quantum leap in ultimate light weight design.* Palm, F., & Schmidtke, K. . Novelty : ASM International, 2013, March, ASM International, p. 108.

87. *Effect of aging treatment on the microstructure and mechanical properties of Al-3.02 Mg-0.2 Sc-0.1 Zr alloy printed by selective laser melting.* Li, R., Chen, H., Zhu, H., Wang, M., Chen, C., & Yuan, T. 2019, Materials & Design, pp. 168, 107668.

88. *Microstructure and mechanical properties of Al-Mg-Zr alloys processed by selective laser melting.* Croteau, J. R., Griffiths, S., Rossell, M. D., Leinenbach, C., Kenel, C., Jansen, V., & Vo, N. Q. 2018, Acta Materialia, pp. 153, 35-44.

89. *Selective laser melting Al-3.4 Mg-0.5 Mn-0.8 Sc-0.4 Zr alloys: From melting pool to the microstructure and mechanical properties.* Zhao, J., Xue, X., Wang, B., Liu, T., Luo, L., Luo, L., & Fu, H. 2021, Materials Science and Engineering, pp. A, 825, 141889.

90. *Enhanced strength of the selective laser melted Al-Mg-Sc-Zr alloy by cold rolling.* Ma, R., Peng, C., Cai, Z., Wang, R., Zhou, Z., Li, X., & Cao, X. 2020, Materials Science and Engineering, pp. A, 775, 13897.

91. *Comparison of microstructure and mechanical properties of Scalmalloy® produced by selective laser melting and laser metal deposition.* Awd, M., Tenkamp, J., Hirtler, M., Siddique, S., Bambach, M., & Walther, F. 2017, Materials, pp. 11(1), 17.

92. *Fatigue and dynamic aging behavior of a high strength Al-5024 alloy fabricated by laser powder bed fusion additive manufacturing.* He, P., Webster, R. F., Yakubov, V., Kong, H., Yang, Q., Huang, S., & Li, X. 2021, Acta Materialia, pp. 220, 117312.

93. *Relations between fatigue strength and other mechanical properties of metallic materials.* Pang, J. C., Li, S. X., Wang, Z. G., & Zhang, Z. F. 2014, Fatigue & Fracture of Engineering Materials & Structures, pp. 37(9), 958-976.

94. *Effects of defects, inclusions and inhomogeneities on fatigue strength.* Murakami, Y., & Endo, M. 1994, International journal of fatigue, pp. 16(3), 163-182.

95. *Hot isostatic pressing (HIP) technology and its applications to metals and ceramics.* Bocanegra-Bernal, M. H. 2004, Journal of materials science, pp. 39(21), 6399-6420.

96. *Anisotropic high cycle fatigue property of Sc and Zr-modified Al-Mg alloy fabricated by laser powder bed fusion.* Qin, Z., Kang, N., El Mansori, M., Wang, Z., Wang, H., Lin, X., & Huang, W. 2022, Additive Manufacturing, pp. 49, 102514.

97. Smith, J. O. *The effect of range of stress on the fatigue strength of metals.* s.l. : University of Illinois at Urbana Champaign, College of Engineering, 1942.

98. *The influential factors on very high cycle fatigue testing results.* Wen-jie, P., & Huan, X. s.l. : EDP Sciences, 2018, MATEC Web of Conferences, pp. Vol. 165, p. 20002.

99. *Improved fatigue properties of laser powder bed fusion of Al–4.74 Mg–0.70 Sc–0.32 Zr alloy via hot isostatic pressing.* Qin, Z., Kang, N., Zong, H., Zhan, C., Fang, Y., Wang, Z., Huang, W. 2022, Materials Research Letters, pp. 10(11), 720-727.

100. *Fatigue properties of Scalmalloy® processed by laser powder bed fusion in as-built, chemically and conventionally machined surface condition.* Raab, M., & Bambach, M. 2023, Journal of Materials Processing Technology, pp. 311, 117811.

101. *An improved process scan strategy to obtain high-performance fatigue properties for Scalmalloy®.* Schimbäck, D., Mair, P., Kaserer, L., Perfler, L., Palm, F., Leichtfried, G., & Pogatscher, S. 2022, Materials & Design, pp. 224, 111410.

102. *Deformation and fatigue behaviour of additively manufactured Scalmalloy® with bimodal microstructure.* Schimbäck, D., Kaserer, L., Mair, P., Palm, F., Leichtfried, G., Pogatscher, S., & Hohenwarter, A. 2023, International Journal of Fatigue, pp. 172, 107592.

103. *Transition of tensile deformation behaviors in ultrafine-grained aluminum.* Yu, C. Y., Kao, P. W., & Chang, C. P. 2005, Acta Materialia, pp. 53(15), 4019-4028.

104. *Dislocation Density Changes in Ultrafine-grain Aluminum during Tensile Deformation.* Adachi, H., Miyajima, Y., Shibata, A., Terada, D., & Tsuji, N. Pittsburgh : Springer International Publishing, 2016. In ICAA13 Pittsburgh: Proceedings of the 13th International Conference on Aluminum Alloys. pp. pp. 61-66.

105. *Fatigue of 2024-T351 aluminium alloy at different load ratios up to 1010 cycles.* Mayer, H., Schuller, R., & Fitzka, M. 2013, International Journal of Fatigue, pp. 57, 113-119.

106. *A comparative investigation on the microstructure and mechanical properties of additively manufactured aluminum alloys.* Muhammad, M., Nezhadfar, P. D., Thompson, S., Saharan, A., Phan, N., & Shamsaei, N. 2021, International Journal of Fatigue, pp. 146, 106165.

107. *Structural integrity of additively manufactured aluminum alloys: Effects of build orientation on microstructure, porosity, and fatigue behavior.* Nezhadfar, P. D., Thompson, S., Saharan, A., Phan, N., & Shamsaei, N. 2021, Additive Manufacturing, pp. 47, 102292.

108. *Fatigue strength estimation methodology of additively manufactured metallic bulk material.* Schneller, W., Leitner, M., Leuders, S., Sprauel, J. M., Grün, F., Pfeifer, T., & Jantschner, O. 2021, Additive Manufacturing, pp. 39, 101688.

109. *About the fatigue crack propagation threshold of metals as a design criterion–a review.* Zerbst, U., Vormwald, M., Pippan, R., Gänser, H. P., Sarrazin-Baudoux, C., & Madia, M. 2016, Engineering Fracture Mechanics, pp. 153, 190-243.

110. *An investigation of the effects of stress ratio and crack closure on the micromechanisms of fatigue crack growth in Ti-6Al-4V.* Dubey, S., Soboyejo, A. B. O., & Soboyejo, W. O. 1997, Acta Materialia, pp. 45(7), 2777-2787.

111. *Effects of defects in laser additive manufactured Ti-6Al-4V on fatigue properties.* Wycisk, E., Solbach, A., Siddique, S., Herzog, D., Walther, F., & Emmelmann, C. 2014, Physics Procedia, pp. 56, 371-378.

112. *Material defects as the basis of fatigue design.* Murakami, Yukitaka. 2012, International Journal of Fatigue, pp. 41, 2-10.

113. AM400. *TECH-LABS.* [Online] https://tech-labs.com/products/am400.

114. *Role of particle size distribution on microstructure, defects, and mechanical properties in laser-based powder bed fusion of Scalmalloy®.* Singh, J., Rovisco, A., Taylor, H., Mireles, J., Rivas, J., Oliveira, J. P., & Wicker, R. 2025, Journal of Manufacturing Science and Engineering, pp. 1-30.

115. *Sc applications in aluminum alloys: Overview of Russian research in the 20th century.* Eskin, D. G. 2018, Light Metals 2018, pp. 1565-1572.

116. *Rapid solidification and non-equilibrium phase constitution in laser powder bed fusion (LPBF) of AlSi10Mg alloy: analysis of nano-precipitates, eutectic phases, and hardness evolution.* Qin, H., Dong, Q., Fallah, V., & Daymond, M. R. 2020, Metallurgical and Materials Transactions , pp. A, 51, 448-466.

117. *Temporal evolution of temperature gradient and solidification rate in laser powder bed fusion additive manufacturing.* Yoshioka, J., & Eshraghi, M. 2023, Heat and Mass Transfer, pp. 59(7), 1155-1166.

118. *Rapid solidification processing and microstructure formation. .* Kurz, W., & Trivedi, R. 1994, Materials Science and Engineering, pp. A, 179, 46-51.

119. *Cracking behaviour of high-strength AA2024 aluminium alloy produced by Laser Powder Bed Fusion.* Del Guercio, G., McCartney, D. G., Aboulkhair, N. T., Robertson, S., Maclachlan, R., Tuck, C., & Simonelli, M. 2022, Additive Manufacturing, pp. 54, 102776.

120. *Processing parameters in laser powder bed fusion metal additive manufacturing.* Oliveira, J. P., LaLonde, A. D., & Ma, J. 2020, Materials & Design, pp. 193, 108762.

121. *Friction Stir Welding of Dissimilar Metal: A Review.* Akshansh, M. 2018, International Journal for Research in Applied Science & Engineering Technology.

122. *Homogeneous nucleation kinetics of Al 3 Sc in a dilute Al-Sc alloy.* Hyland, R. W. 1992, Metallurgical Transactions A, pp. 23, 1947-1955.

123. *The solidification behaviour of dilute aluminium–scandium alloys.* Norman, A. F., Prangnell, P. B., & McEwen, R. S. 1998, Acta materialia, pp. 46(16), 5715-5732.

124. *Understanding the laser powder bed fusion of AlSi10Mg alloy.* Hyer, H., Zhou, L., Park, S., Gottsfritz, G., Benson, G., Tolentino, B., & Sohn, Y. 2020, Metallography, Microstructure, and Analysis, pp. 9, 484-502.

125. *The effect of scandium, transition metals and in purities on hardening of aluminium alloys upon decomposition of solid solutions; Vliyanie skandiya, perekhodnykh metallov i primesej na uprochnenie alyuminievykh splavov pri raspade tverdogo rastvora.* Zakharov, V. V., & Rostova, T. D. 2007, Metallovedenie i Termicheskaya Obrabotka Metallov.

126. *Coarsening-and creep resistance of precipitation-strengthened Al–Mg–Zr alloys processed by selective laser melting.* Griffiths, S., Croteau, J. R., Rossell, M. D., Erni, R., De Luca, A., Vo, N. Q., & Leinenbach, C. 2020, Acta Materialia, pp. 188, 192-202.

127. *Fatigue crack growth rate, microstructure and mechanical properties of diverse range of aluminum alloy: a comparison.* Brahami, A., Bouchouicha, B., Zemri, M., & Fajoui, J. 2018, Mechanics and Mechanical Engineering, pp. 22(1), 329-339.

128. *Effect of aging treatments on fatigue properties of 6005A aluminum alloy containing Sc.* Liu, Y., Pan, Q., Liu, B., Yu, Q., Li, G., & Pan, D. 2022, International Journal of Fatigue, pp. 163, 107103.

129. *Tensile and fatigue crack growth behavior of commercially pure titanium produced by laser powder bed fusion additive manufacturing.* Hasib, M. T., Ostergaard, H. E., Liu, Q., Li, X., & Kruzic, J. J. 2021, Additive Manufacturing, pp. 45, 102027.

130. *An analytical fracture mechanics model for estimation of S–N curves of metallic alloys containing large second phase particles.* Zerbst, U., Madia, M., & Hellmann, D. 2012, Engineering Fracture Mechanics, pp. 82, 115-134.

131. *A theoretical model for roughness induced crack closure.* Ravichandran, K. S. 1990, International Journal of Fracture, pp. 44, 97-110.

132. *Some considerations on fatigue crack closure at near-threshold stress intensities due to fracture surface morphology.* Ritchie, R. O., & Suresh, S. 1982, Metallurgical Transactions A, pp. 13, 937-940.

133. *Roughness-induced crack closure: an explanation for microstructurally sensitive fatigue crack growth.* Gray, G. T., Williams, J. C., & Thompson, A. W. 1983, Metallurgical Transactions, pp. A, 14, 421-433.

134. *Fatigue crack propagation in ultrafine grained Al–Mg alloy.* Pao, P. S., Jones, H. N., Cheng, S. F., & Feng, C. R. 2005, International Journal of Fatigue, pp. 27(10-12), 1164-1169.

135. *Fatigue properties of 5056 Al-Mg alloy produced by equal-channel angular pressing.* Vinogradov, A., Nagasaki, S., Patlan, V., Kitagawa, K., & Kawazoe, M. 1999, Nanostructured Materials, pp. 11(7), 925-934.

136. Schijve, J. *Fatigue of Structures and Materials.* 2009.

137. *Material fatigue properties for assessing mechanical components weakened by notches and defects.* Atzori, B., Meneghetti, G., & Susmel, L. 2005, Fatigue & fracture of engineering materials & structures, pp. 28(1-2), 83-97.

138. *Effect of Aging Heat Treatment in an Al-4008 Produced by Liquid Metal Printing. U. .* Ladeiro, C., Nunes, F., Trindade, M., & Costa, J. 2024, Porto Journal of Engineering, pp. 10(1), 45-58.

139. *SLM-processed Sc-and Zr-modified Al-Mg alloy: Mechanical properties and microstructural effects of heat treatment.* Spierings, A. B., Dawson, K., Kern, K., Palm, F., & Wegener, K. 2017, Materials Science and Engineering, pp. A, 701, 264-273.

140. *Columnar to equiaxed transition in Al-Mg (-Sc)-Zr alloys produced by selective laser melting.* Yang, K. V., Shi, Y., Palm, F., Wu, X., & Rometsch, P. 2018, Scripta Materialia, pp. 145, 113-117.

141. *Study of the pore formation on CoCrMo alloys by selective laser melting manufacturing process.* Monroy, K., Delgado, J., & Ciurana, J. 2013, Procedia Engineering, pp. 63, 361-369.

142. Karnesky, R. A. *Mechanical properties and microstructure of Al–Sc with rareearth element or Al2O3 additions.* Evanston, IL : Northwestern University, 2007.

143. *New aluminum alloys specifically designed for laser powder bed fusion: a review.* Aversa, A., Marchese, G., Saboori, A., Bassini, E., Manfredi, D., Biamino, S., & Lombardi, M. 2019, Materials, pp. 12(7), 1007.

144. *Making selective-laser-melted high-strength Al–Mg–Sc–Zr alloy tough via ultrafine and heterogeneous microstructure.* Wang, Z., Lin, X., Kang, N., Wang, Y., Yu, X., Tan, H., & Huang, W. 2021, Scripta Materialia, pp. 203, 114052.

Appendix A. Scalmalloy composition data sheet provided by LPW Technologies

The specification of the alloy powder used for printing samples for the current study provides the information on the composition and particle size.

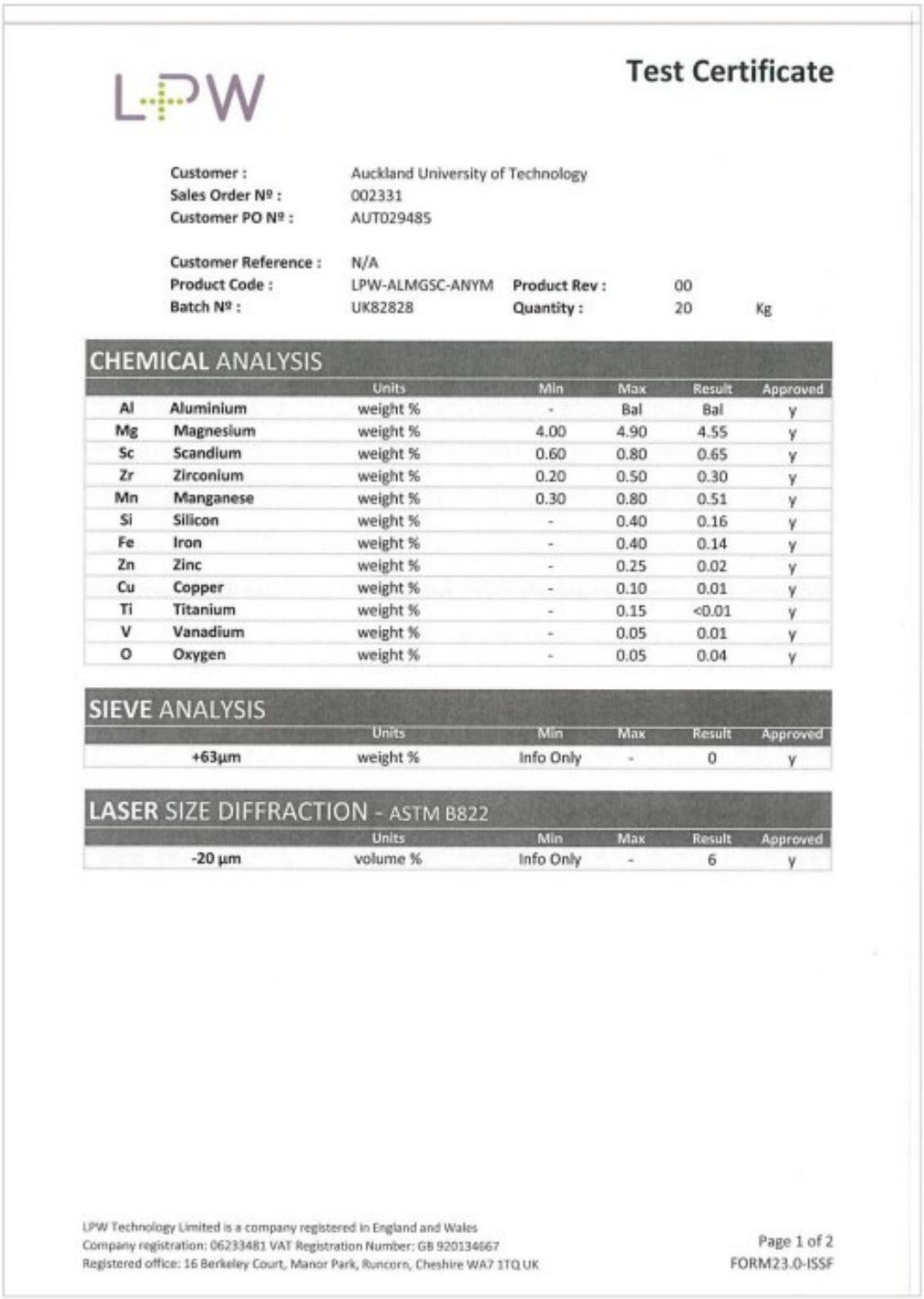

LPW

Test Certificate

Customer :	Auckland University of Technology			
Sales Order Nº :	002331			
Customer PO Nº :	AUT029485			
Customer Reference :	N/A			
Product Code :	LPW-ALMGSC-ANYM	**Product Rev :**	00	
Batch Nº :	UK82828	**Quantity :**	20	Kg

CHEMICAL ANALYSIS

		Units	Min	Max	Result	Approved
Al	Aluminium	weight %	-	Bal	Bal	y
Mg	Magnesium	weight %	4.00	4.90	4.55	y
Sc	Scandium	weight %	0.60	0.80	0.65	y
Zr	Zirconium	weight %	0.20	0.50	0.30	y
Mn	Manganese	weight %	0.30	0.80	0.51	y
Si	Silicon	weight %	-	0.40	0.16	y
Fe	Iron	weight %	-	0.40	0.14	y
Zn	Zinc	weight %	-	0.25	0.02	y
Cu	Copper	weight %	-	0.10	0.01	y
Ti	Titanium	weight %	-	0.15	<0.01	y
V	Vanadium	weight %	-	0.05	0.01	y
O	Oxygen	weight %	-	0.05	0.04	y

SIEVE ANALYSIS

	Units	Min	Max	Result	Approved
+63µm	weight %	Info Only	-	0	y

LASER SIZE DIFFRACTION - ASTM B822

	Units	Min	Max	Result	Approved
-20 µm	volume %	Info Only	-	6	y

Test Certificate

Customer :	Auckland University of Technology			
Sales Order Nº :	002331			
Customer PO Nº :	AUT029485			
Customer Reference :	N/A			
Product Code :	LPW-ALMGSC-ANYM	**Product Rev :**	00	
Batch Nº :	UK82828	**Quantity :**	20	Kg

NOTES

LPW Technology Certifies that the material on this document conforms to the specification above.

*This document is validated by suppliers authorised inspection representative in accordance with EN 10204 type 3.1 Inspection Document

Generated By	Validated By*
LPW 43	LPW
Date	Date
11/05/2018	11/05/2018

Appendix B. SEM images of Scalmlloy

Below are the SEM images illustrating the microstructure of Scalmalloy in the as-built condition, after T5 heat treatment, after T6 heat treatment, and following solutionizing only. The characteristic bimodal microstructure, consisting of both equiaxed and columnar grains, is clearly observed across all the conditions. An increase in particle size is evident after the heat treatments.

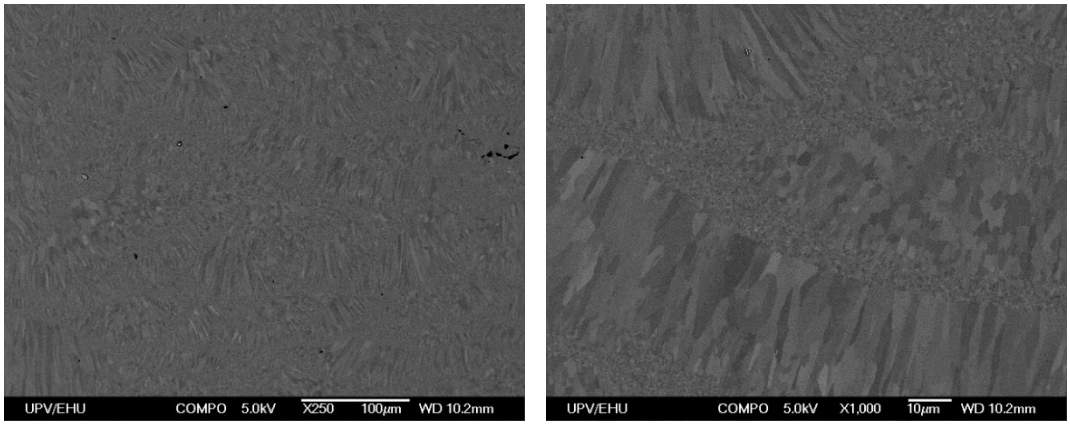

Figure B.1. SEM image of Scalmalloy sample in as-built state.

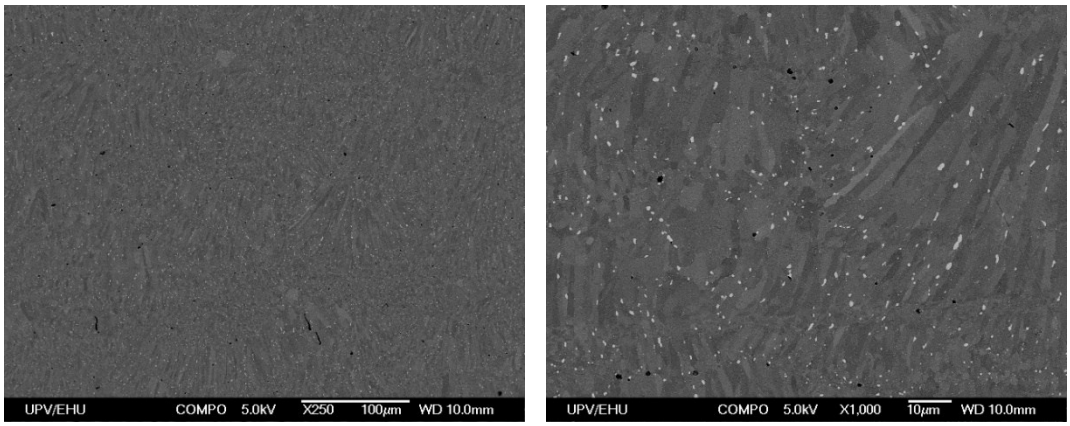

Figure B.2. SEM image of Scalmalloy sample after solutionizing.

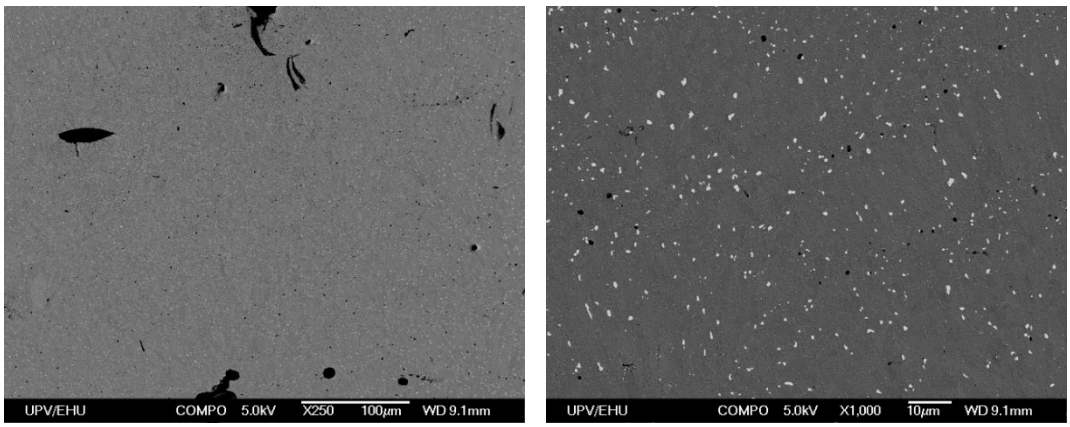

Figure B.3. SEM image of Scalmalloy sample after T6 heat treatment.

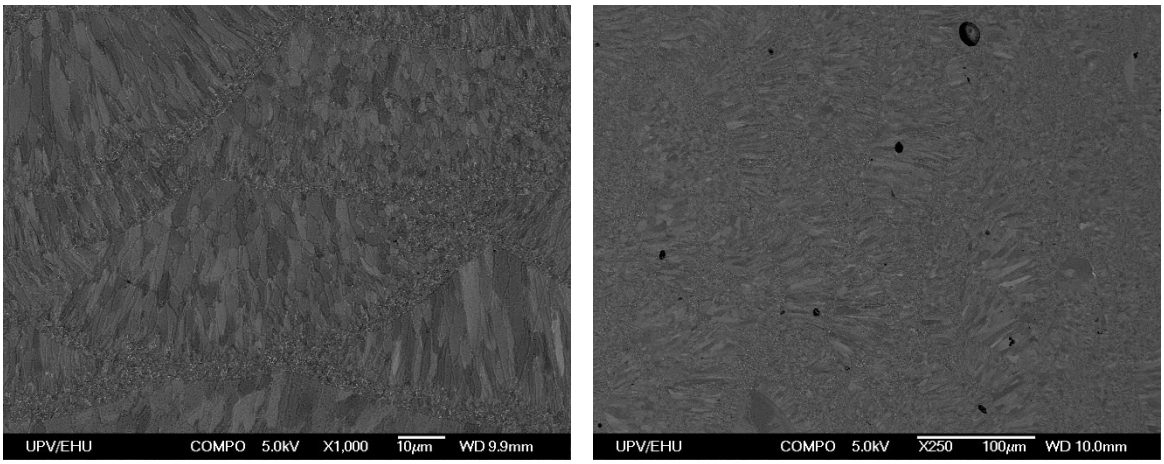

Figure B.4. SEM image of Scalmalloy sample after T5 heat treatment.

Appendix C. TEM images of Scalmlloy

Below are the TEM images of Scalmalloy in the as-built condition, after T5 heat treatment, after T6 heat treatment, and following solutionizing only. For each condition, TEM images were taken from three distinct regions of the samples: the equiaxed region, the transition region (from equiaxed to columnar), and the columnar region. These TEM images provide the information on grain size variations and particle distribution across different microstructural regions.

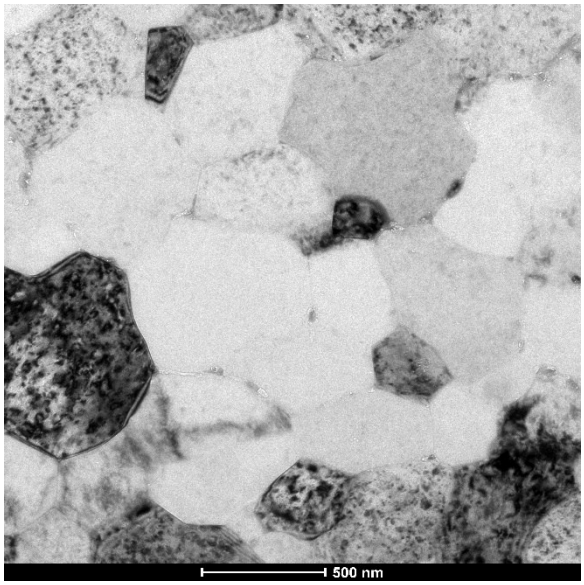

a)

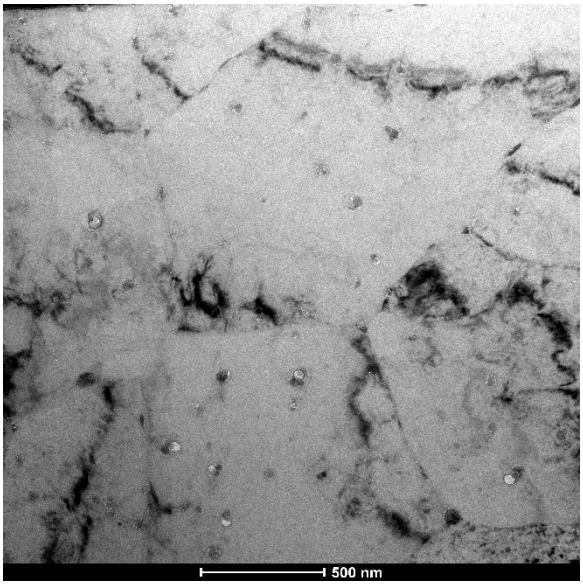

b)

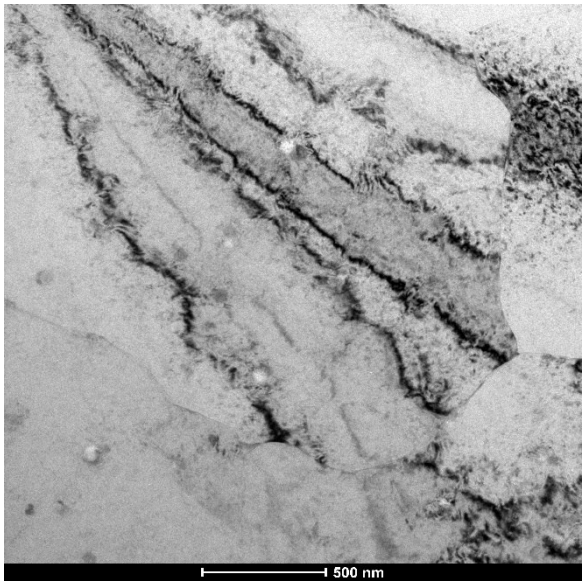

c)

Figure C.1. TEM image of Scalmalloy sample in as-built state a)equiaxed, b) transition, c) columnar grain region.

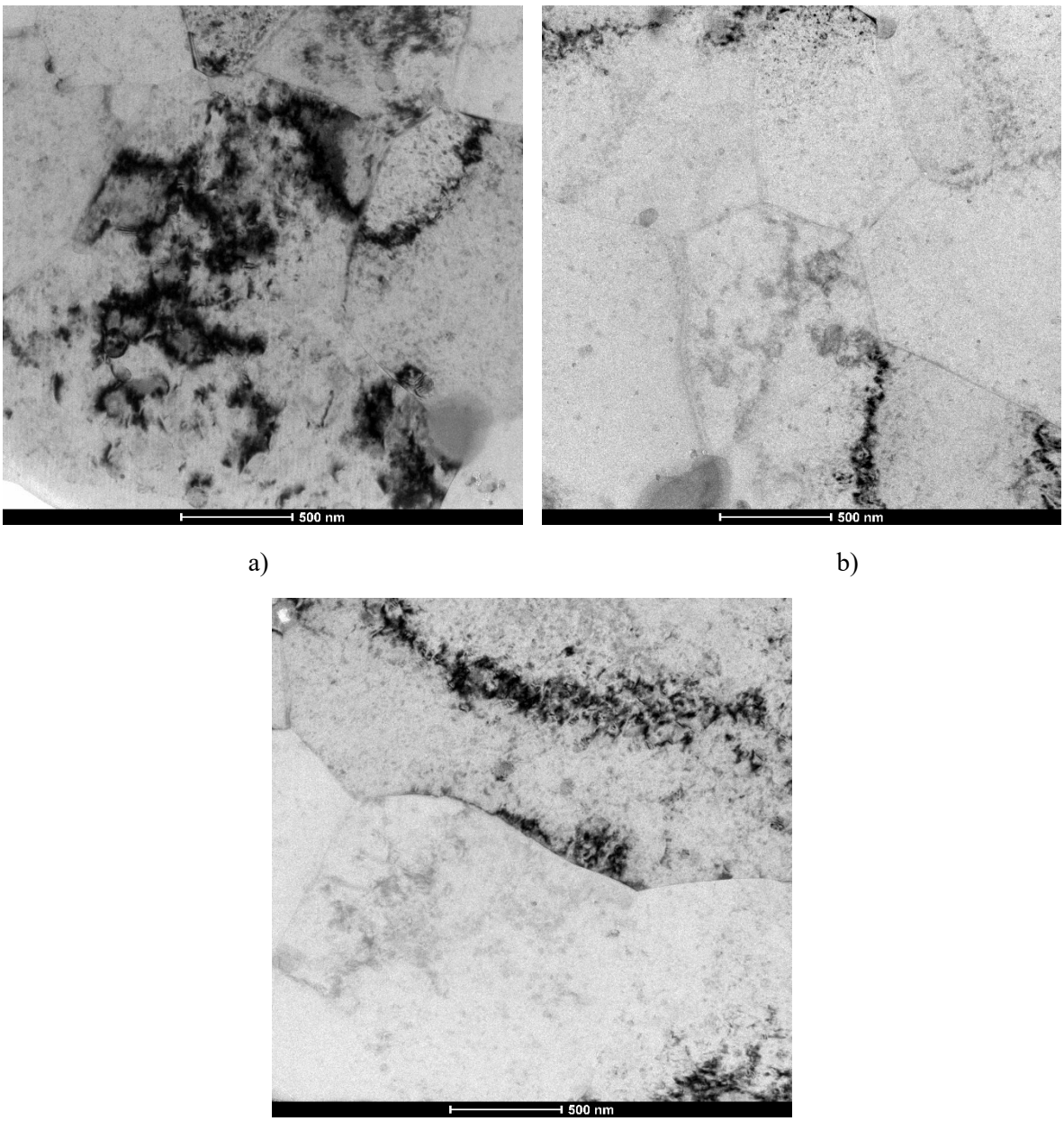

a) b)

c)

Figure C.2. TEM image of Scalmalloy sample after solutionizing a) equiaxed, b) transition, c) columnar grain region.

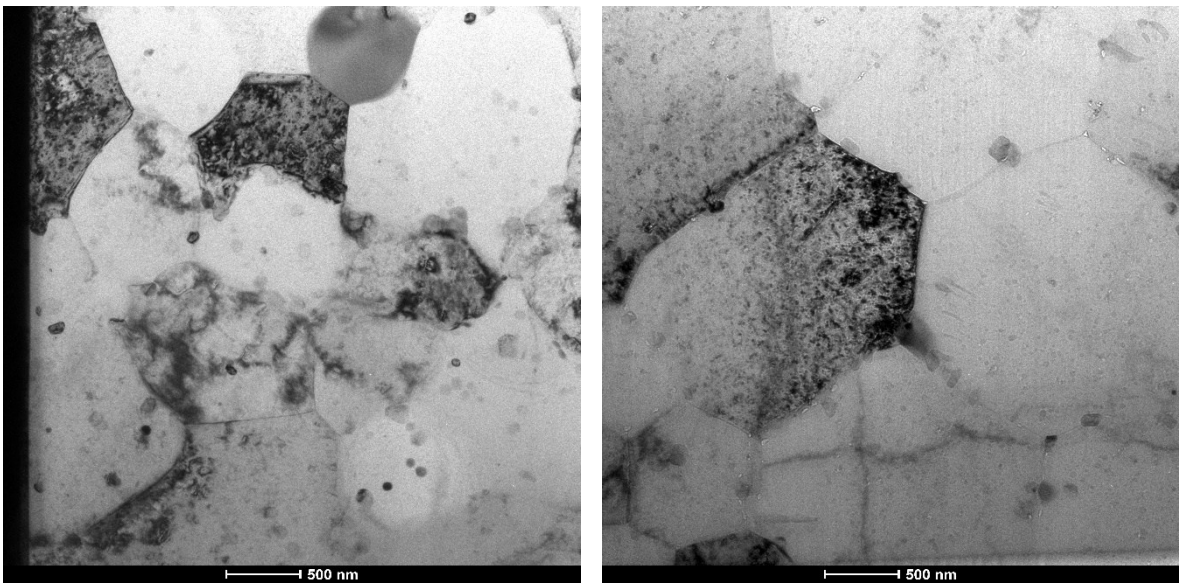

a) b)

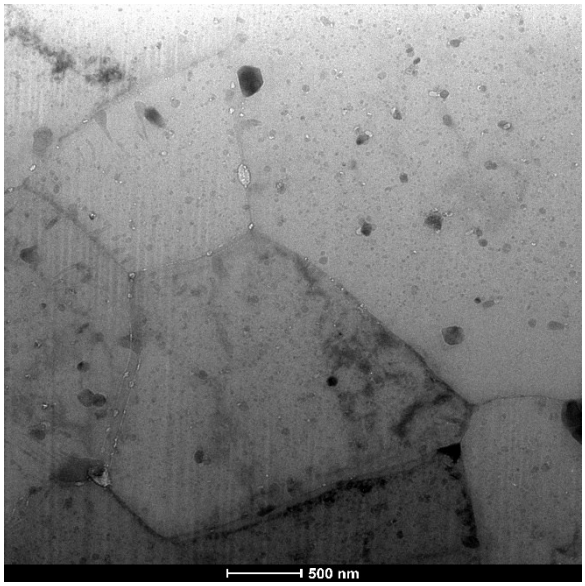

c)

Figure C.3. TEM image of Scalmalloy sample after T6 heat treatment a)equiaxed, b) transition, c) columnar grain region.

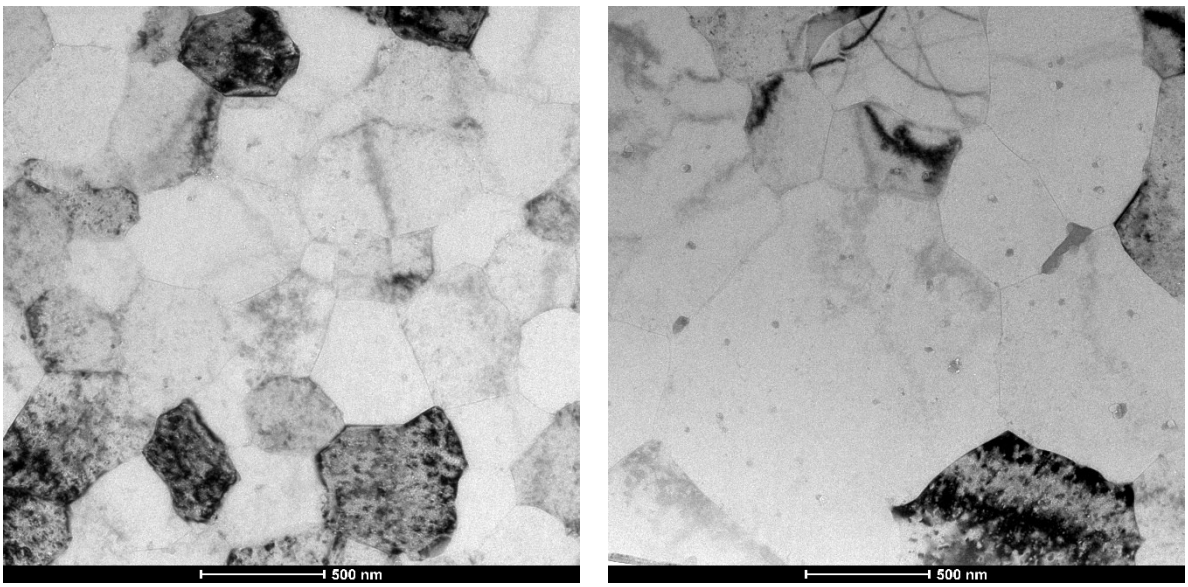

a) b)

Figure C.4. TEM image of Scalmalloy sample after T5 heat treatment a)equiaxed, b) transition grain region.

Appendix D. Fractographs of S-N samples showing the defects and their measured results of sizes

Below are fractographs of samples subjected to S-N fatigue testing. The low-magnification images clearly identify the fracture initiation sites, high-magnification images detail measurements of the specific defects responsible for initiating fractures.

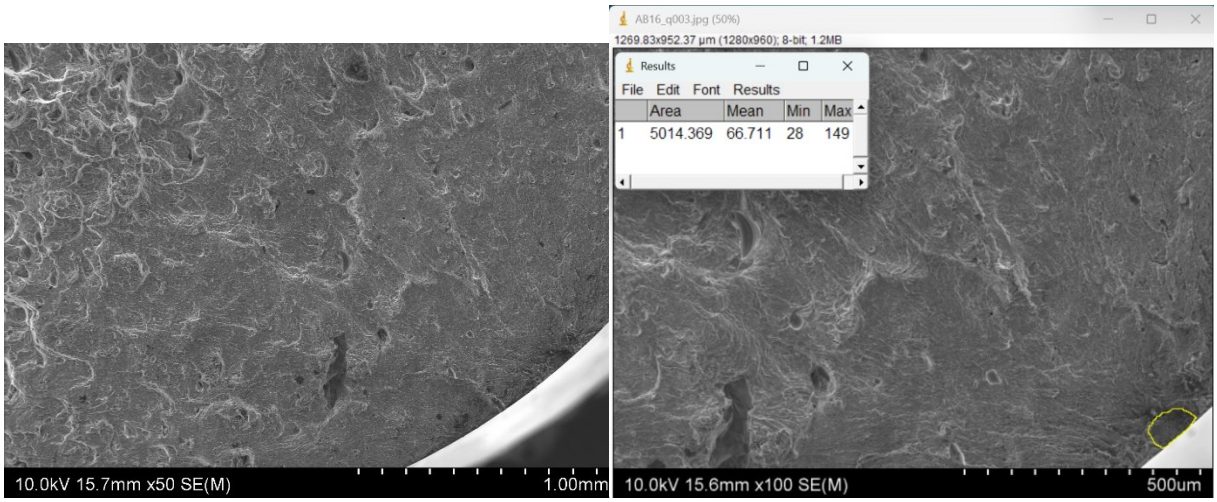

a) b)

Figure D.1. Fracture surface of sample CD//BD-AB-1 a) x50, b) x100.

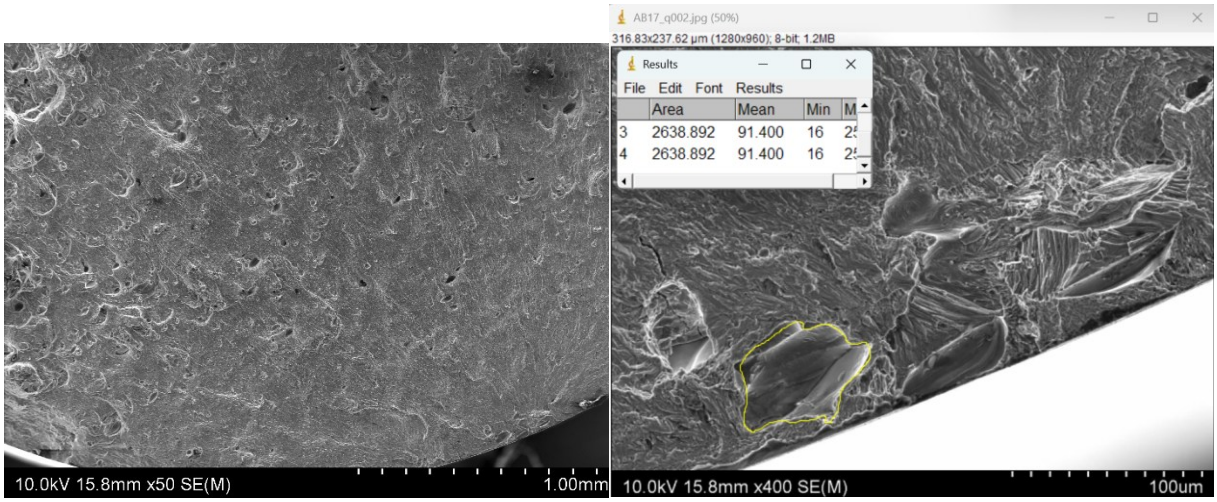

a) b)

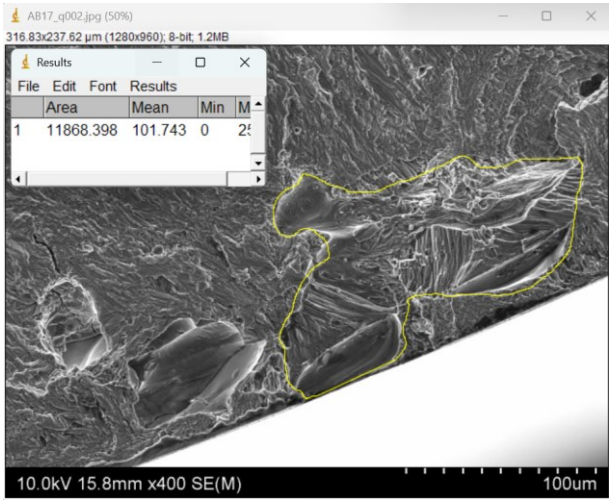

c)

Figure D.2. Fracture surface of sample CD//BD-AB-2 a) x100, b) x400, c) x400.

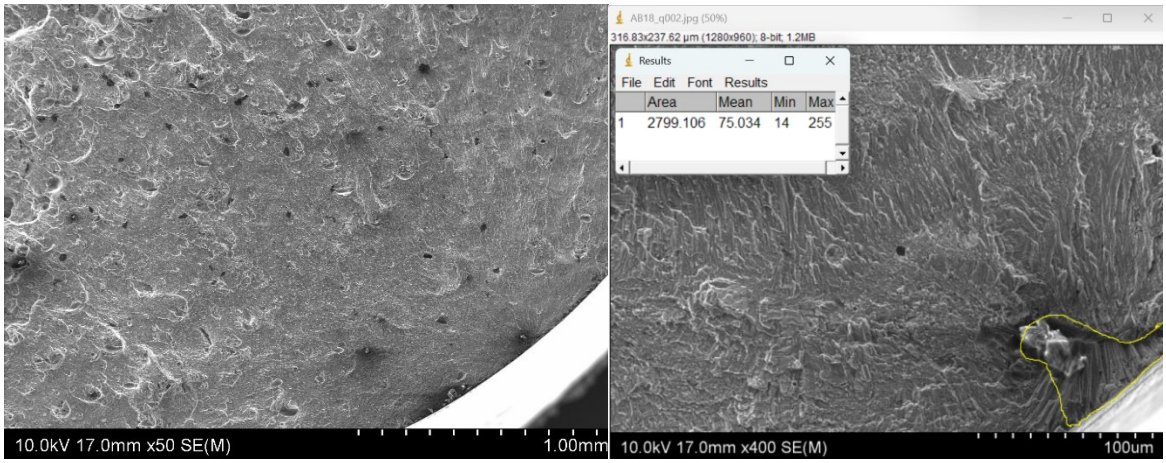

a) b)

Figure D.3. Fracture surface of sample CD//BD-AB-3 a) x50, b) x400.

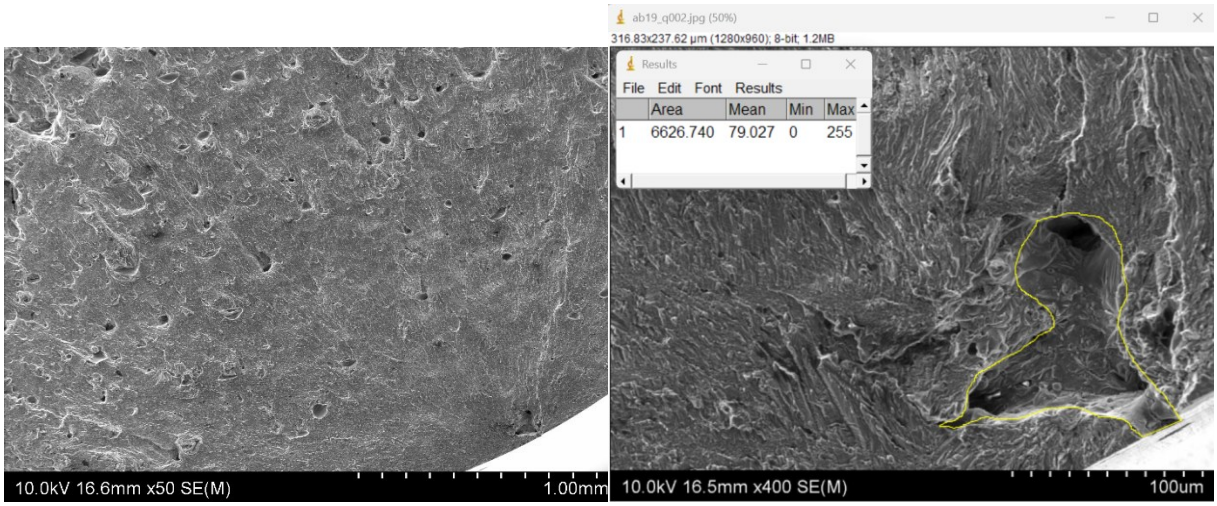

a) b)

Figure D.4. Fracture surface of sample CD//BD-AB-4 a) x50, b) x400.

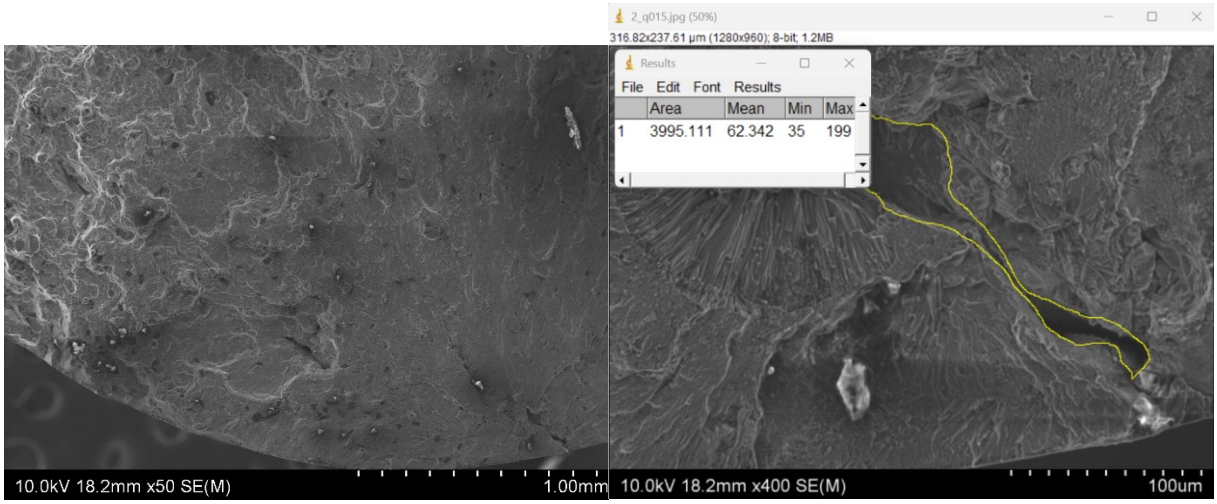

a) b)

Figure D.5. Fracture surface of sample CD//BD-HT-1 a) x50, b) x400.

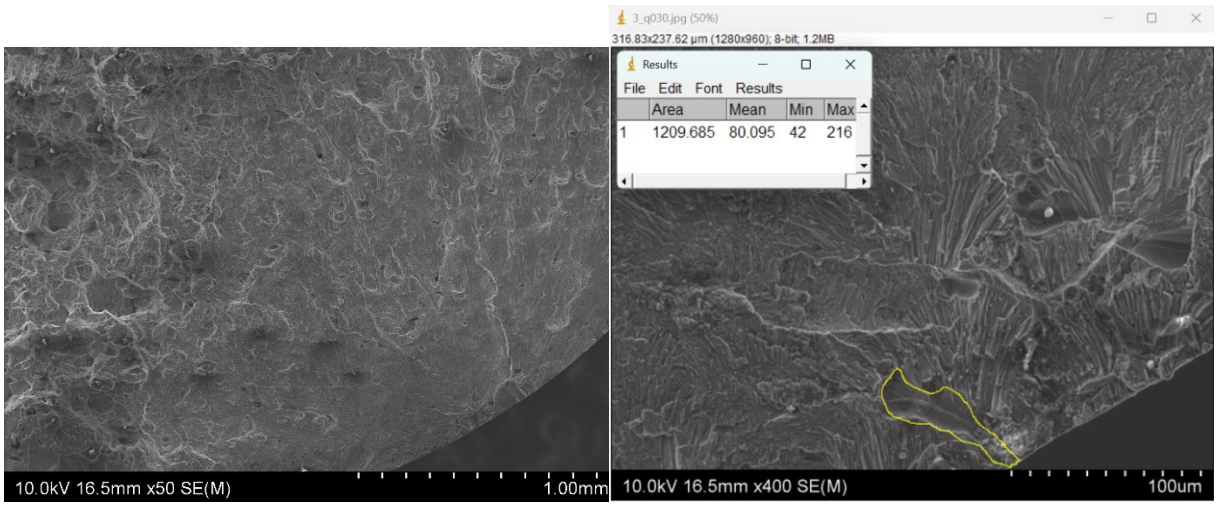

a) b)

Figure D.6. Fracture surface of sample CD//BD-HT-2 a) x50, b) x400.

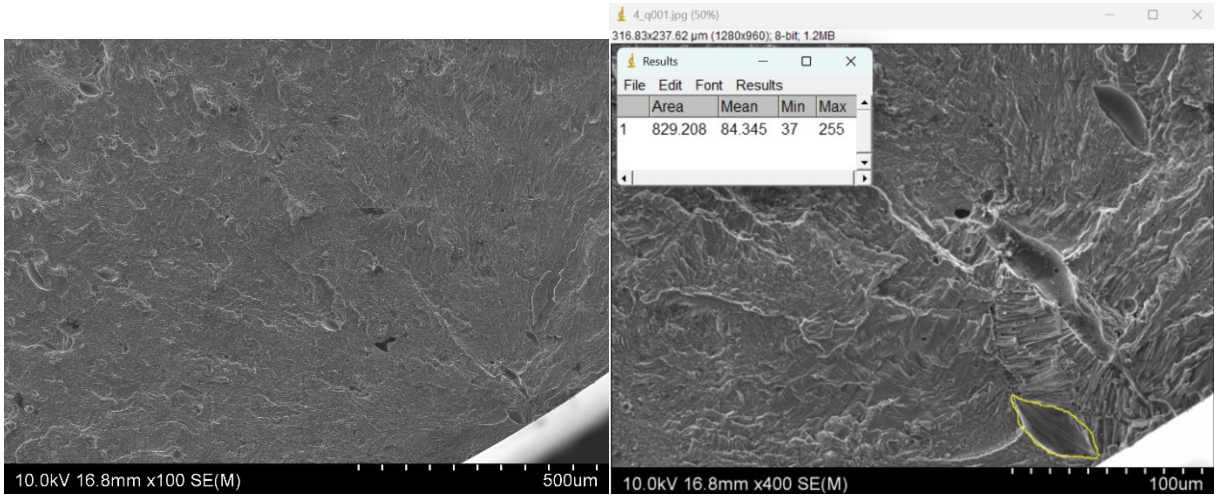

a) b)

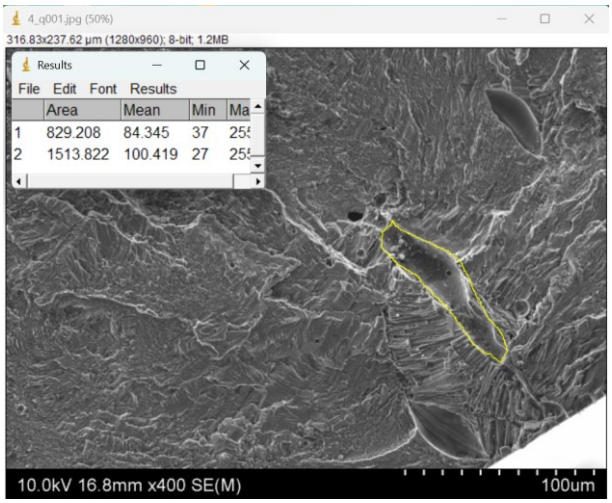

c)

Figure D.7. Fracture surface of sample CD//BD-HT-3 a) x100, b) x400, c) x400.

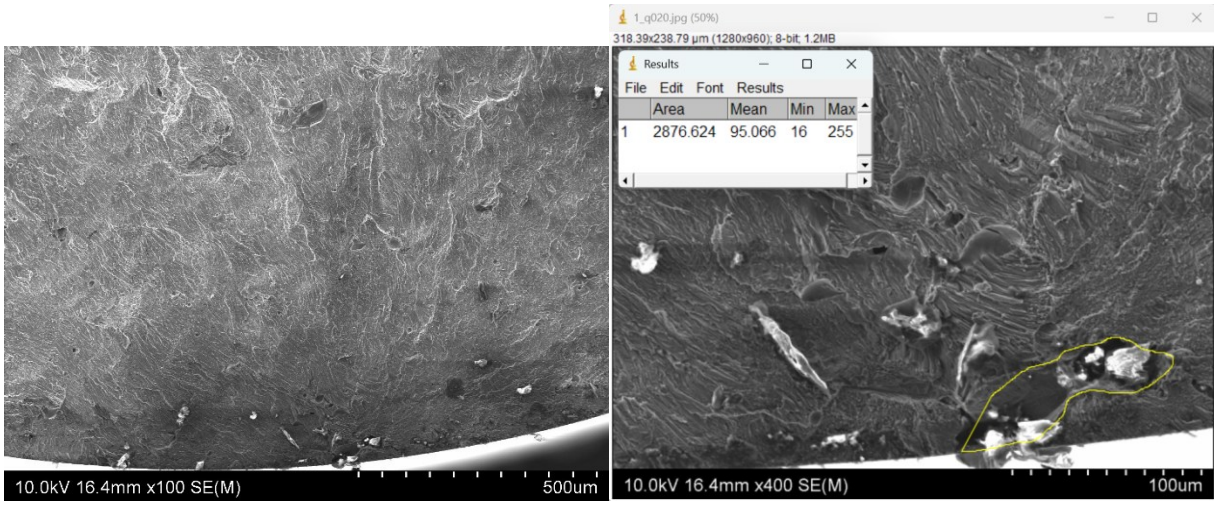

a) b)

Figure D.8. Fracture surface of sample CD//BD-HT-4 a) x100, b) x400.

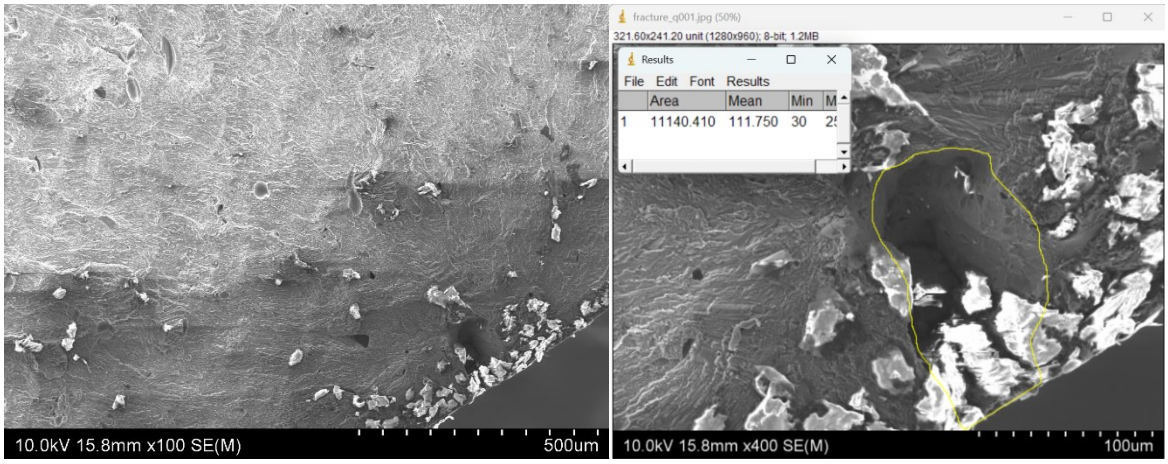

a) b)

Figure D.9. Fracture surface of sample CD//BD-HT-5 a) x50, b) x400.

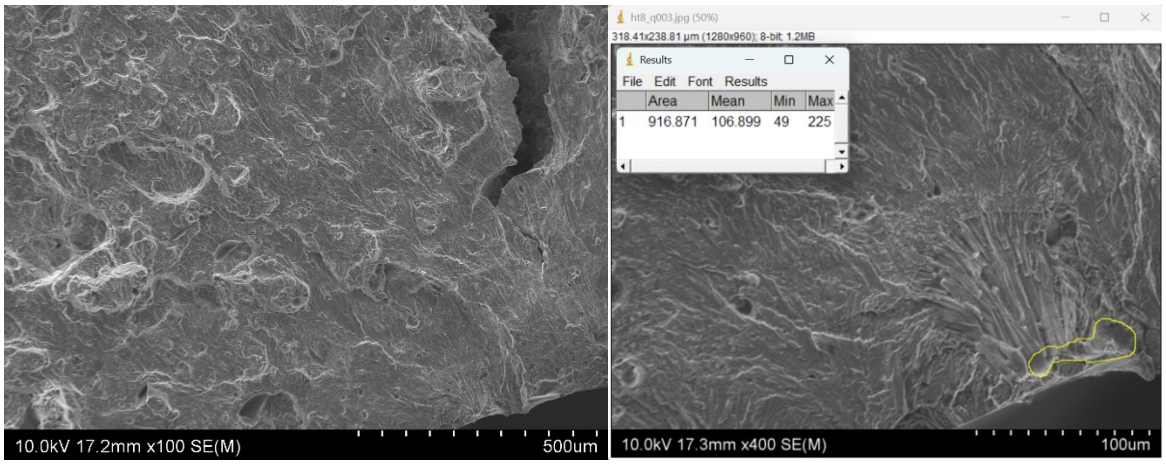

a) b)

Figure D.10. Fracture surface of sample CD//BD-HT-6 a) x50, b) x400.

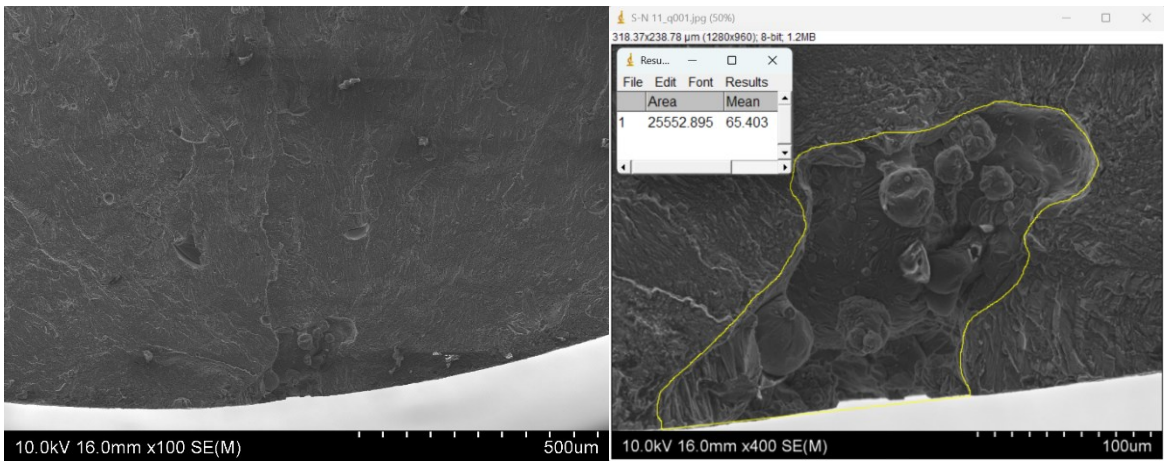

a) b)

Figure D.11. Fracture surface of sample CD//BD-HT-7 a) x100, b) x400.

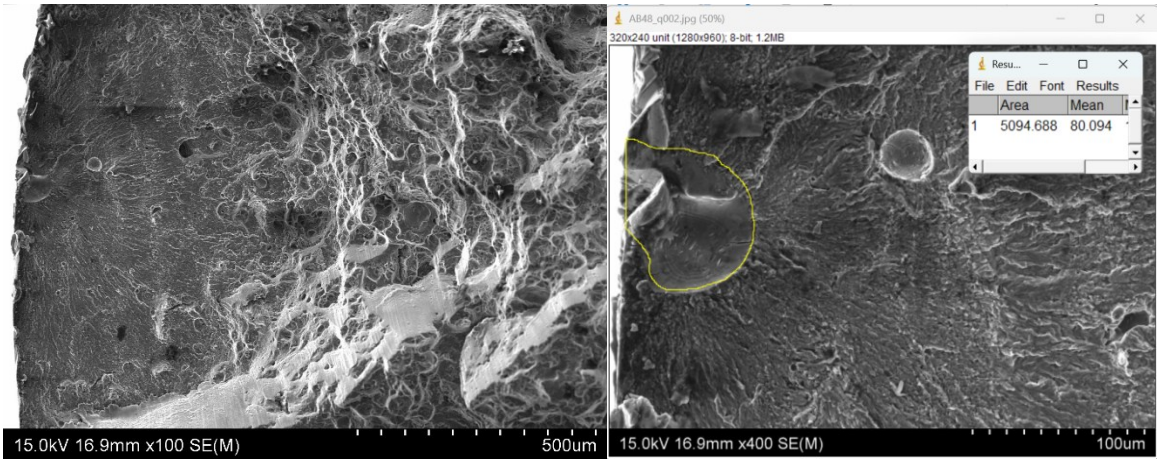

a) b)

Figure D.12. Fracture surface of sample CD⊥BD-AB-1a) x100, b) x400.

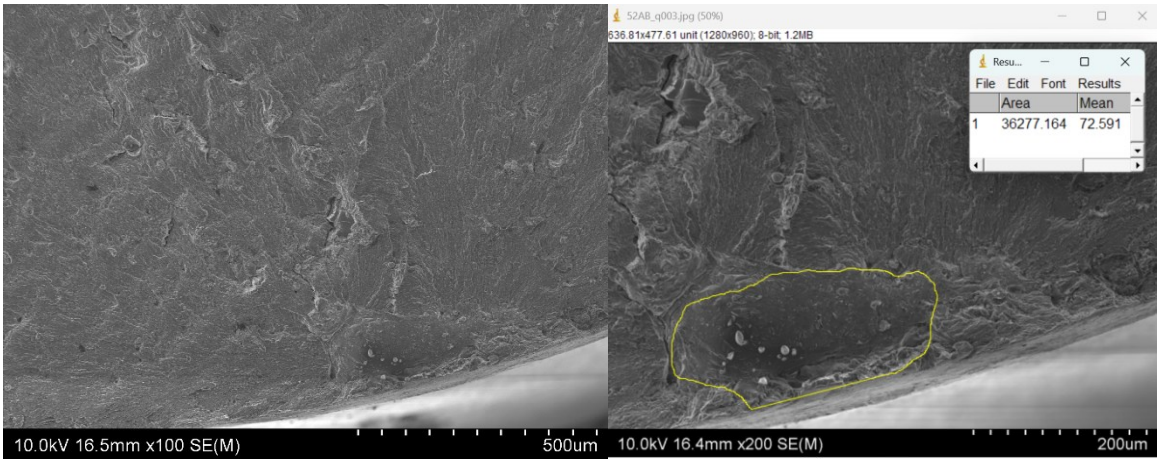

a) b)

Figure D.13. Fracture surface of sample CD⊥BD-AB-2 a) x100, b) x200.

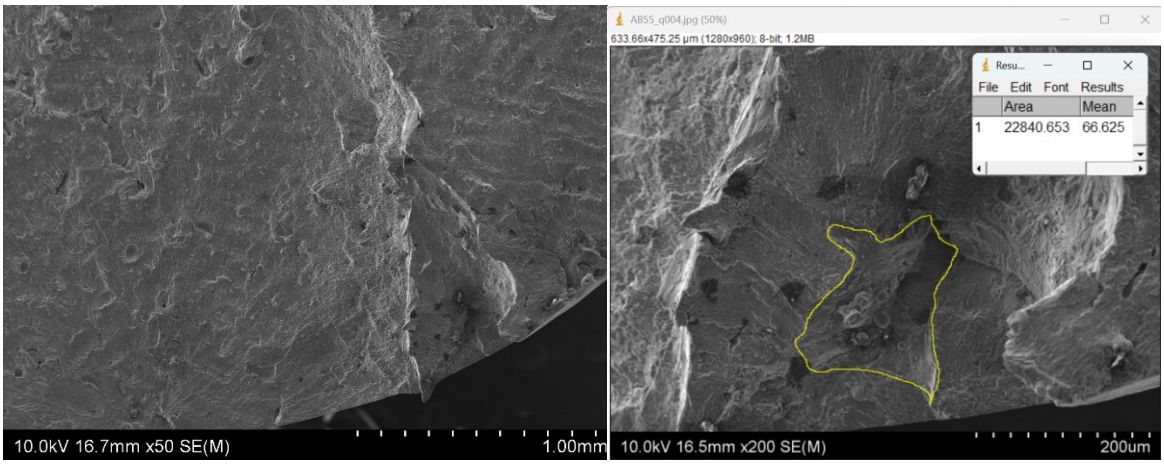

a) b)

Figure D.14. Fracture surface of sample CD⊥BD-AB-3 a) x50, b) x200.

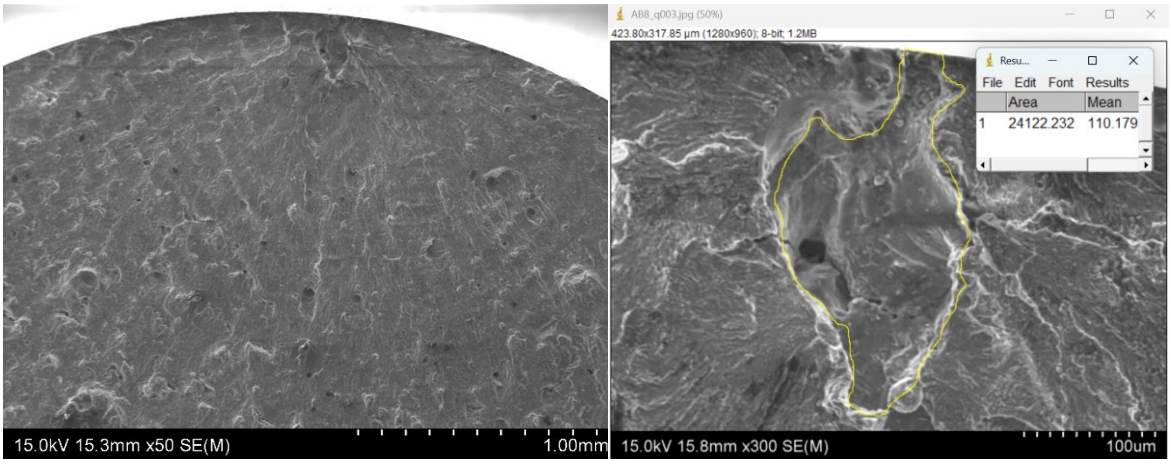

a) b)

Figure D.15. Fracture surface of sample CD⊥BD-AB-4 a) x50, b) x300.

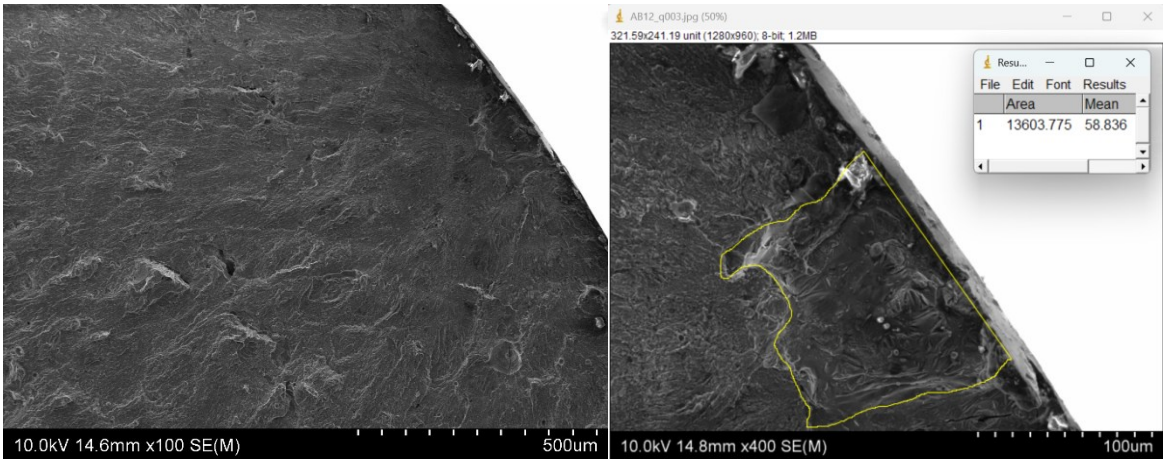

a) b)

Figure D.16. Fracture surface of sample CD⊥BD-AB-5 a) x100, b) x400.

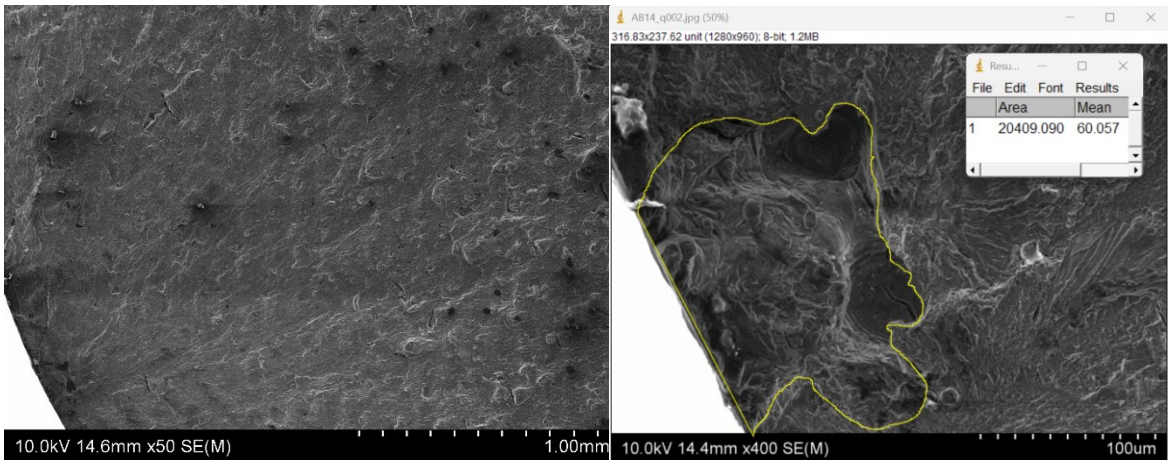

a) b)

Figure D.17. Fracture surface of sample CD⊥BD-AB-6 a) x50, b) x400.

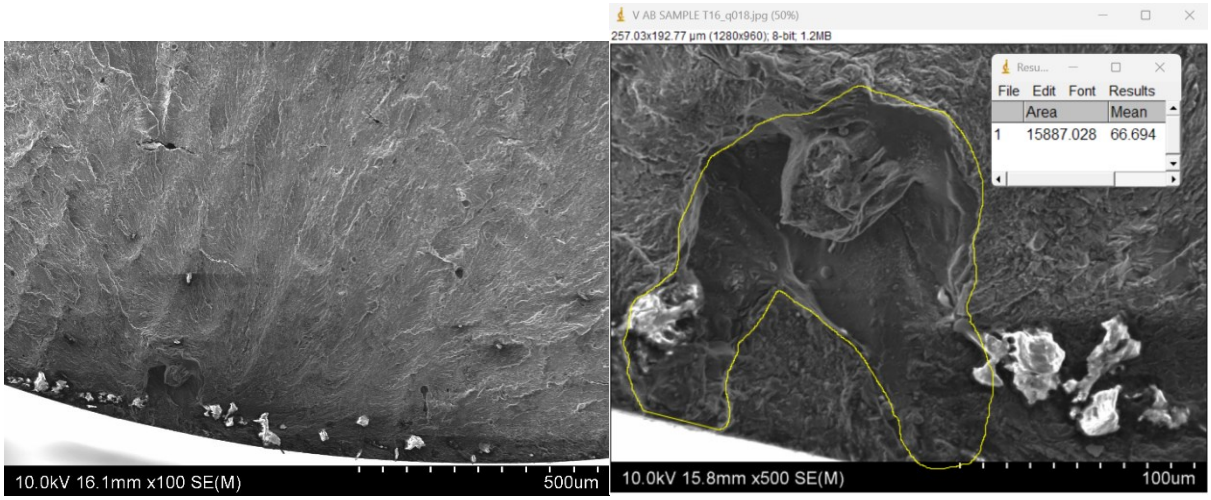

a) b)

Figure D.18. Fracture surface of sample CD⊥BD-AB-7 a) x100, b) x500.

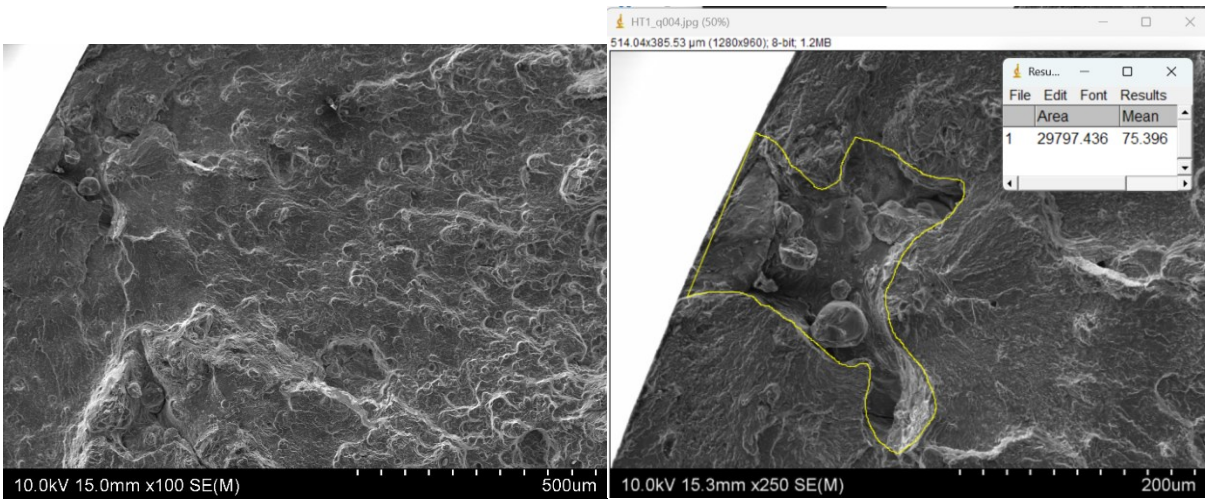

a) b)

Figure D.19. Fracture surface of sample CD⊥BD-HT-1 a) x100, b) x250.

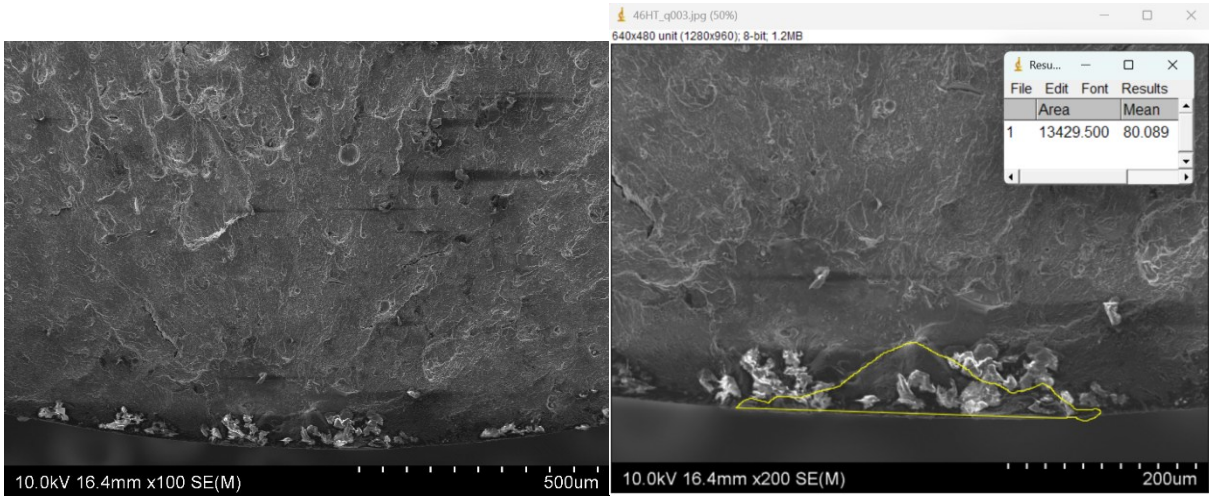

a) b)

Figure D.20. Fracture surface of sample CD⊥BD-HT-2 a) x100, b) x200.

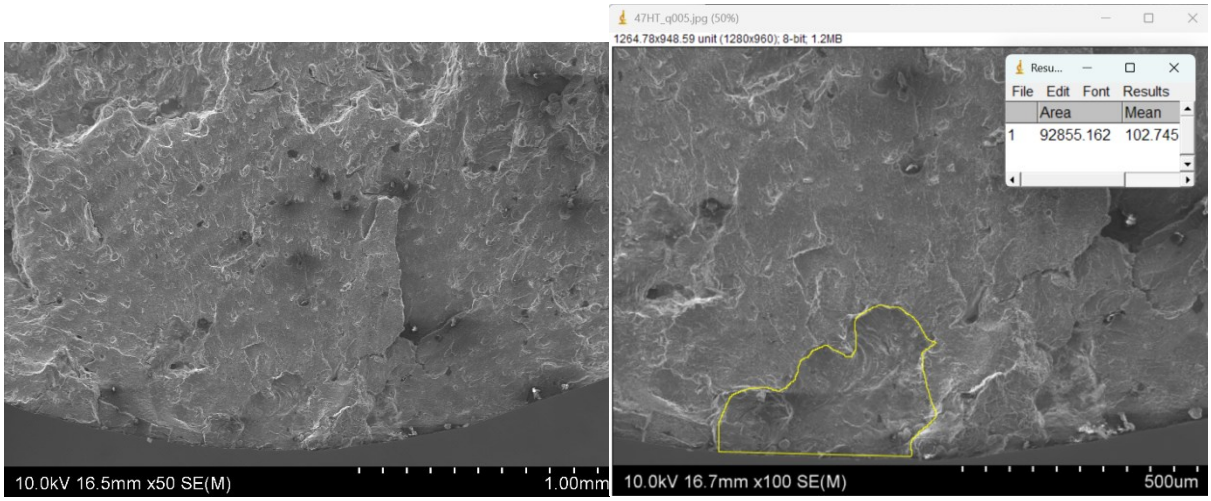

a) b)

Figure D.21. Fracture surface of sample CD⊥BD-HT-3 a) x50, b) x100.

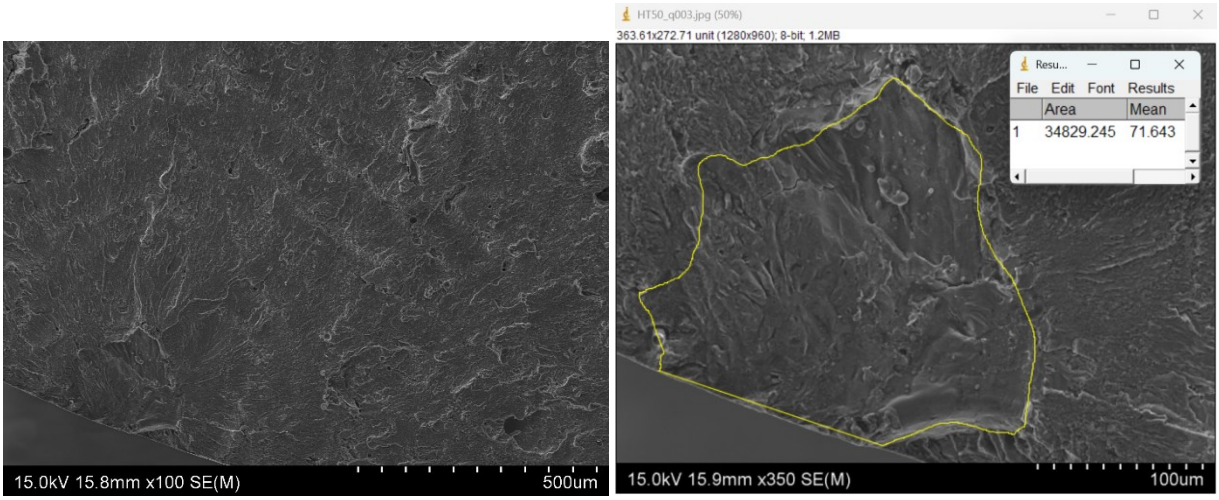

a) b)

Figure D.22. Fracture surface of sample CD⊥BD-HT-4 a) x100, b) x350.

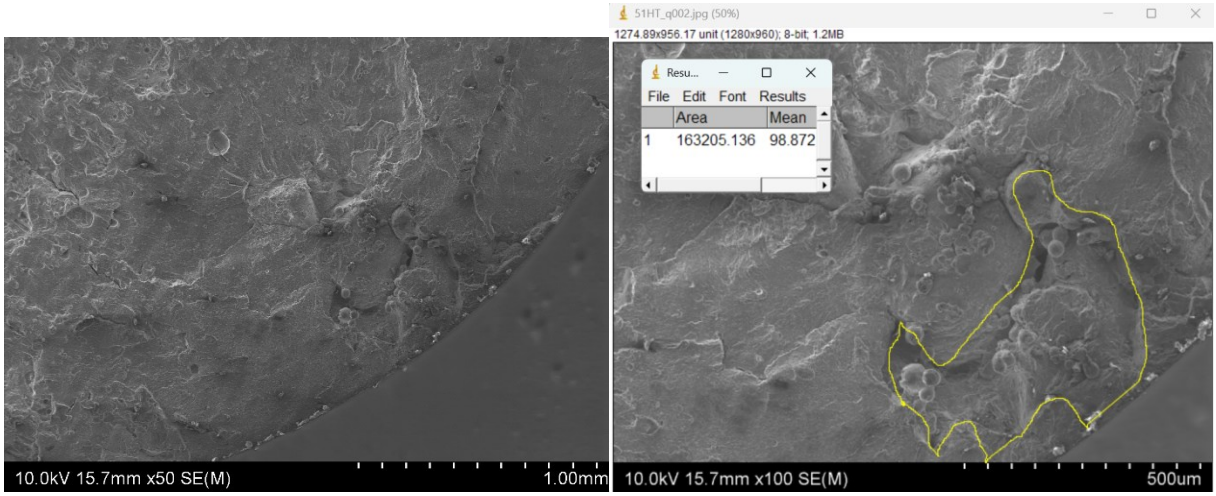

a) b)

Figure D.23. Fracture surface of sample CD⊥BD-HT-5 a) x100, b) x100.

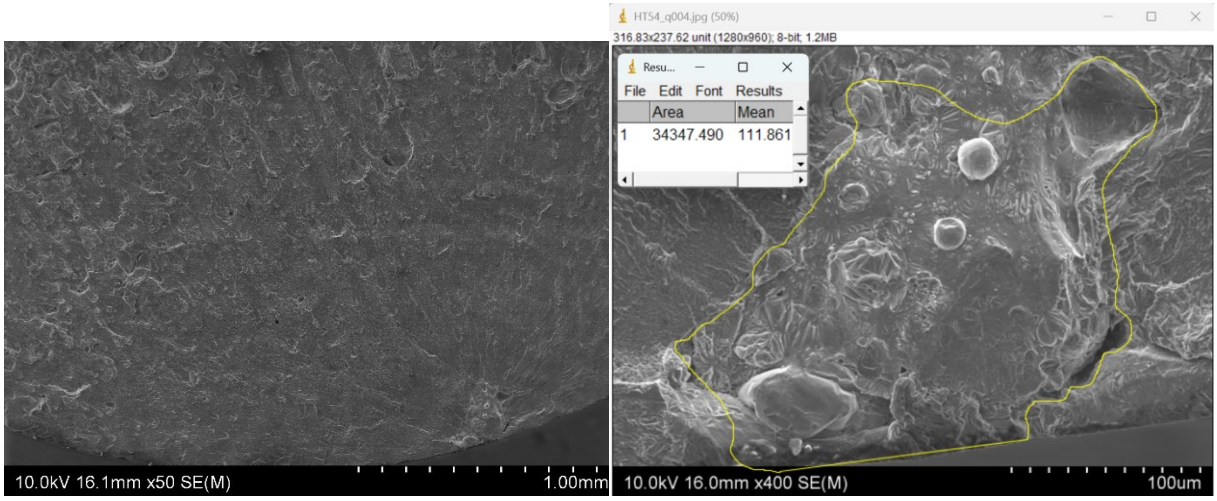

a) b)

Figure D.24. Fracture surface of sample CD⊥BD-HT-6 a) x100, b) x400.

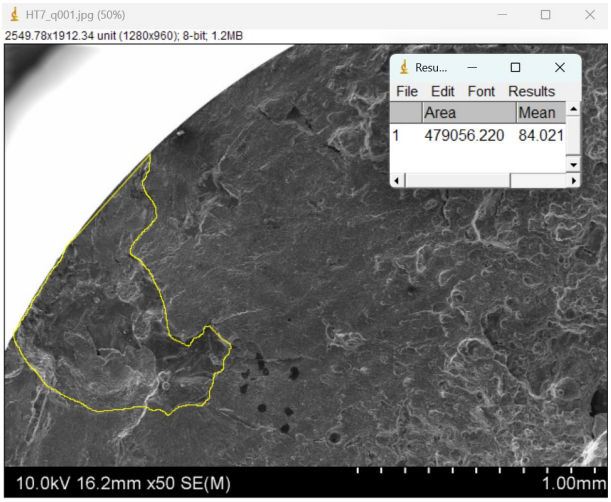

Figure D.25. Fracture surface of sample CD⊥BD-HT-7, x50